An experimental and computational study of tokamak plasma turbulence

Aylwin IANTCHENKO

A species set on endless growth is un-(Unsustainable).
— Muse

To my family...

Abstract

Turbulence driven by small-scale instabilities results in strong heat and particle transport, which significantly shortens the confinement time and prevents the formation of a self-sustained plasma reaction in magnetic confinement devices. Control and possible mitigation of this transport is critical to achieve controlled fusion, which requires a proper understanding of the underlying physics of turbulent processes.

This thesis explores both computational and experimental methods to study turbulent fluctuations, focusing on modelling and the use of the Tangential Phase Contrast Imaging (TPCI) diagnostic that measures electron density fluctuations. On the experimental side of this work, the TPCI diagnostic is upgraded with new equipment to perform ion scale measurements. The diagnostic is used in an initial study of turbulence when the shape of the plasma changes from positive to negative triangularity in a diverted configuration, and to study the effects of an electron cyclotron beam on turbulence.

However, the main part of the thesis is devoted to gyrokinetic GENE simulations of turbulence and modelling of TPCI signals. The simulated density fluctuations are post-processed with a synthetic diagnostic that has been developed to model measurements from TPCI, taking into account the effect of a spatial filter for selecting the measured wave-vector directions. Modelling, with GENE and the synthetic diagnostic, is performed for several TCV plasma scenarios with the aim of improving the interpretation of the TPCI signals. The synthetic diagnostic is used to establish a link between the TPCI signals and the underlying modes, and to find new ways to apply the TPCI diagnostic to measure Ion Temperature Gradient (ITG) and Trapped Electron Mode (TEM) turbulence. It is also demonstrated how computationally cheap linear simulations can be used to predict certain aspects of the TPCI signals.

In the final part of this work a computational study of turbulent fluctuations in the JT-60SA machine is also carried out, motivated in part by the concomitant design of a TPCI diagnostic for that device. Turbulence in a representative, planned, high-performance JT-60SA plasma discharge, scenario 1, is modelled with local gyrokinetic flux-tube simulations. The discharge features a double-null separatrix, 41 MW of combined Neutral Beam Heating (NBH) and Electron Cyclotron Heating (ECH), and a high predicted ratio β of the plasma kinetic to magnetic pressure. Electromagnetic effects, in particular compressional magnetic field fluctuations, are essential in this scenario due to the large β. A detailed linear and nonlinear study of the fluctuations is performed and conclusions are drawn on the capability of reduced transport models to predict profiles in reactor-relevant conditions and on the projected performance of the JT-60SA machine. Finally, predictions are provided of the characteristics of the TPCI measurement, using the results

Abstract

---

from the gyrokinetic study and the planned diagnostic setup on JT-60SA.

Sinossi

La turbolenza, dovuta alle instabilità che si sviluppano su scale microscopiche, provoca un elevato trasporto di calore e particelle nelle macchine per la fusione a confinamento magnetico, riducendo notevolmente il tempo di confinamento e impedendo al plasma il raggiungimento di una reazione autosostenuta. Il controllo e la possibile mitigazione di questo tipo di trasporto è fondamentale per realizzare la fusione controllata, la quale richiede una esaustiva comprensione della fisica che è alla base dei processi turbolenti.

In questo lavoro di tesi, si è svolto uno studio delle fluttuazioni di turbolenza sia dal punto di vista numerico che sperimentale. Si è posta l'attenzione sulla diagnostica Tangential Phase Contrast Imaging (TPCI), la quale è in grado di misurare le fluttuazioni di densità elettronica. Dal punto di vista sperimentale, la diagnostica TPCI è stata migliorata ai fini di poter misurare la scala ionica. Questa evoluzione della diagnostica TPCI ha permesso di misurare la variazione della turbolenza nel passaggio dalla triangolarità positiva a quella negativa del plasma in configurazione divertore, oltre a studiare l'effetto del riscaldamento tramite Electron Cyclotron Heating sulle fluttuazioni di densità.

Dal punto di vista numerico, si sono eseguite simulazioni girocinetiche di turbolenza con il codice GENE. Le fluttuazioni di densità così ottenute sono state post-processate con una diagnostica sintetica, sviluppata proprio per modellizzare le misure del sistema TPCI, tenendo conto anche dell'effetto di un filtro spaziale per selezionare le direzioni dei vettori d'onda misurati. Con l'obiettivo di migliorare la nostra conoscenza sui segnali TPCI, le simulazioni sono state eseguite per diversi scenari del plasma in TCV. L'uso della diagnostica sintetica ha permesso di associare i segnali TPCI alle instabilità del plasma e, dunque, di misurare con applicazioni innovative della diagnostica TPCI la turbolenza dovuta alle instabilità di tipo Ion Temperature Gradient (ITG) e Trapped Electron Mode (TEM). Inoltre, viene così illustrato come alcuni aspetti dei segnali prodotti dal sistema TPCI possano essere predetti con simulazioni lineari meno dispendiose dal punto di vista computazionale.

In aggiunta, è stato effettuato uno studio numerico sulle fluttuazioni turbolente in JT-60SA, in parte motivato dal presente design della diagnostica TPCI da utilizzare in quel device. Attraverso simulazioni girocinetiche locali, ovvero di tipo flux-tube, si è modellizzata la turbolenza in JT-60SA per una scarica di plasma a prestazioni elevate che è prevista nel Research Plan ed è indicata come scenario 1. La scarica presenta la separatrice a doppio punto a X, 41 MW di riscaldamento a fascio di neutroni (NBH) e un alto β, ovvero il rapporto tra la pressione cinetica e la pressione magnetica del plasma. A causa dell'alto β, è essenziale considerare gli effetti elettromagnetici, e in particolare le fluttuazioni del campo magnetico di compressione. Così, si è

svolto uno studio di tipo lineare e non lineare delle fluttuazioni e si sono tratte delle conclusioni sulla capacità dei modelli ridotti di trasporto di prevedere i profili radiali in condizioni di plasma rilevanti per un reattore e sulle prestazioni della macchina JT-60SA. Infine, tramite i risultati delle analisi girocinetiche, si sono predette le caratteristiche delle misure TPCI con l'impostazione della diagnostica pianificata per JT-60SA.

Parole chiave: plasma, tokamak, fusione, imaging a contrasto di fase, turbolenza, diagnostica sintetica, ion temperature gradient mode, trapped electron mode, modalità acustica geodetica, fluttuazioni elettromagnetiche

Résumé

Dans le plasma, les instabilités à petite échelle peuvent créer de la turbulence qui engendre le transport d´une grande quantité de particules et de chaleur, réduisant ainsi le temps de confinement, ce qui a pour effet d´empêcher la création d´un plasma brûlant. Pour parvenir à la fusion contrôlée, il est impératif de trouver des solutions pour réduire ce transport induit par la turbulence, ce qui nécessite une bonne compréhension de la physique sous-jacente.

Cette thèse explore à la fois les méthodes computationnelles et expérimentales pour étudier les fluctuations turbulentes, en se concentrant sur la modélisation et l'utilisation d'un diagnostic du type Tangential Phase Contrast Imaging (TPCI) permettant de mesurer les fluctuations de densité électronique. Durant la partie expérimentale de ce travail, une mise à jour du diagnostic TPCI a été réalisée pour pouvoir effectuer des mesures à l'échelle ionique. Dans une étude préliminaire, ce diagnostic a été appliqué lorsque la forme du plasma évoluait d'une triangularité positive à une triangularité négative dans une configuration déviée. Le diagnostic a également été appliqué pour étudier l'effet du chauffage par résonance cyclotronique électronique.

La majeure partie de cette thèse est consacrée aux simulations gyrocinétiques de la turbulence et à la modélisation des signaux TPCI. Les simulations des fluctuations de densité sont post-traitées avec un diagnostic synthétique qui a été développé pour modéliser les mesures de TPCI, en prenant en compte l'effet d'un filtre spatial pour sélectionner la direction des vecteurs d'onde mesurés. La modélisation de la turbulence avec le code gyrocinétique GENE et le diagnostic synthétique sont réalisés pour plusieurs scénarios de plasma dans le tokamak TCV, avec le but d'améliorer l'interprétation des signaux TPCI. En utilisant le diagnostic synthétique, un lien est établi entre les signaux TPCI et les modes sous-jacents. Ainsi, de nouvelles façons d'utiliser le diagnostic TPCI pour mesurer la turbulence du Ion Temperature Gradient (ITG) et du Trapped Electron Mode (TEM) sont présentées. Il est également démontré comment des simulations linéaires, nécessitant de faibles ressources en termes de calcul numérique, peuvent être utilisées pour prédire certains aspects des signaux TPCI.

Dans la dernière partie de ce travail, une étude numérique des fluctuations turbulentes dans la machine JT-60SA a également été réalisée. Cette étude a été en partie réalisée pour un projet de conception de diagnostic TPCI prévu pour cet expérience. À l'aide de simulations gyrocinétiques locales, la modélisation de la turbulence dans une décharge de plasma JT-60SA représentative, planifiée et à haute performance, appelée scénario 1, est réalisée. La décharge comporte un point double X, 41 MW de chauffage par faisceau de neutres (NBH) et de chauffage par resonance cyclotronique électronique (ECH) combinés et un rapport β prédit élevé de la pression cinétique du plasma et la pression magnétique. Les effets électromagnétiques, en particulier les fluctuations

Resume

du champ magnétique de compression, sont essentiels dans ce scénario en raison du grand β. Des étude linéaire et non linéaire détaillées des fluctuations sont réalisées. Les conclusions de cette étude sont présentées quant à la capacité des modèles réduit de transport à prédire les profils dans les conditions pertinentes du réacteur, ainsi que sur les performances projetées de la machine JT-60SA. Enfin, à l'aide des résultats de l'étude gyrocinétique, les prédictions des caractéristiques des mesures TPCI sont fournies pour la configuration prévue de ce diagnostic sur JT-60SA.

Mots clefs: plasma, tokamak, fusion, phase-contrast-imaging, turbulence, diagnostic synthétique, ion temperature gradient mode, trapped electron mode, geodesic acoustic mode, fluctuations electromagnétique.

Contents

Contents

1 Introduction

The free energy available in a gas that deviates from thermodynamic equilibrium can lead to chaotic motion and the formation of irregular structures called *turbulence*. This can be observed in the sky, where velocity and pressure gradients lead to chaotic motion of particles within clouds, creating a cascade of ever smaller swirls. It can also be observed in fusion plasmas, where large pressure gradients form as the very hot core is separated from the edge to prevent the walls of the fusion reactor from melting. These gradient-driven small-scale instabilities saturate through nonlinear interactions, creating a cascade of turbulent eddies. Although turbulence is a beautiful phenomenon to observe, it is often undesirable. Even if the turbulence structures are small, their collective effects can lead to large transport of particles and energy within the gas that is very difficult to control. In the sky, turbulence within the clouds can shake an aircraft in an uncontrollable way. In fusion plasmas, turbulence can lead to rapid transport of particles and energy out of the plasma, reducing the energy confinement time and effectively limiting the performance of fusion reactors.

This thesis investigates turbulence in fusion plasmas. In this chapter, the reader is introduced to the main concepts related to fusion, turbulence and plasmas.

1.1 Fusion plasmas

A *plasma* is a gas at very high temperature, large enough to exceed the binding energy of electrons to the atom nucleus, allowing the electrons to escape from the atom and form a gas of charged particles. If the ion particles in the hot gas move fast enough to overcome the repulsive Coulomb force they might fuse, releasing energy in the process since the resulting product is in a more stable state. These reactions, known as fusion reactions, constitute a fundamental energy source in the universe, and are what makes stars, such as our Sun, shine. Over the last 100 years we have been trying to recreate this process also on Earth, that is, to create an artificial star. In the stars, the large mass generates a strong enough gravitational field that keeps the particles in the plasma from escaping into space and being lost. On Earth it is not possible to rely on the same

mechanism but a different approach has to be taken. One possibility is to compress fuel pellets and apply heat using high energy beams. This is the case of inertial fusion. Another option, which is the case of magnetically confined fusion that is studied in this work, we can instead use magnetic fields to create a cage to hold the hot plasma together.

Globally, the plasma gas remains neutral but locally it consists of rapidly moving, positively charged ions and negatively charged electrons that respond to electromagnetic forces. In the presence of a magnetic field $\boldsymbol{B}$ a particle of charge q and velocity $\boldsymbol{v}$ is influenced by the Lorentz force

$$\boldsymbol{F} = q\left(\boldsymbol{v} \times \boldsymbol{B}\right). \tag{1.1}$$

Solving the equations of motion $m\,\mathrm{d}\boldsymbol{v}/\mathrm{d}t = \boldsymbol{F}$ for a constant $\boldsymbol{B}$-field leads to a circular motion perpendicular to the field as shown in Fig. 1.1. The particle traces out a circle of Larmor radius $\rho = v_\perp/\Omega$ and rotates with the gyration frequency $\Omega = qB/m$ known as the Larmor frequency. Here m is the mass of the particle and $v_\perp$ is the velocity perpendicular to the magnetic field.

Since the charged particles move unhindered along the magnetic field lines, such a configuration of a straight and constant $\boldsymbol{B}$-field is unsuitable for a fusion reactor, where particles and energy need to remain confined sufficiently long to generate self-sustaining fusion reactions. An alternative is to restrict the parallel motion by relying on the magnetic mirror effect, arising from the variation in the magnetic field strength. An even better option is to bend the field lines to form a torus. This magnetic field line configuration would have a strong toroidal magnetic field component, forcing the particles to follow the field lines in a circular loop. A second component, a weaker poloidal field component, would compensate for the centrifugal drift of the particles, forcing them to stay inside the fusion device. There are two main contestants for confining the plasma with such a toroidal magnetic field topology. In a stellarator [1] the field line geometry is generated predominantly by external magnets that usually have complicated non-planar structure to produce an optimised magnetic field. A second, more studied option, is the tokamak, which is an acronym in Russian that translates into "toroidal chamber with magnetic coils". Unlike a stellarator, the helicoidal twist of the magnetic field in a tokamak is achieved by actively driving a toroidal current in the plasma. The toroidal current generates the poloidal field which together with the toroidal magnetic field creates the desired torus topology. The first tokamak machine was built in 1959 in Moscow and had the name Moscow torus 5. Since then, many tokamak machines have been built around the world, for example JET, DIII-D, ASDEX Upgrade, JT-60, Alcator C-mod, TCV and JT-60SA. The International Thermonuclear Experimental Reactor (ITER), currently under construction in Cadarache, France, will be the largest tokamak experiment yet. The aim of the experiment is to demonstrate the physical feasibility of fusion energy production, by generating an output power ten times the input power [2]. There is also research being done in developing smaller fusion reactors, notably the SPARC device [3] that uses the recent development in high temperature superconductors to generate a stronger toroidal magnetic field.

In an axisymmetric toroidal magnetic field geometry it is possible to write the magnetic field in
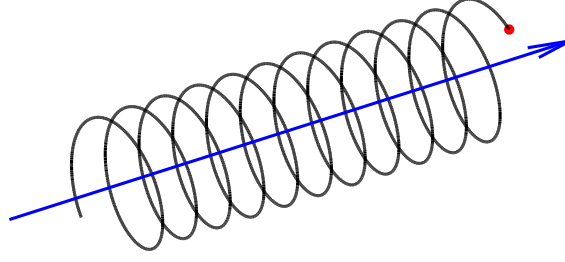
Figure 1.1 – The motion of a charged particle in a spatially constant magnetic field. Source: [4].

the form

$$\boldsymbol{B} = F\nabla\varphi + \nabla\varphi \times \nabla\psi, \tag{1.2}$$

where φ is the toroidal angle measured clock-wise as seen from the top, $F = RB_\phi$ and ψ is a stream function proportional to the poloidal magnetic flux, $\psi = 1/(2\pi)\int_S \mathrm{d}S B_\theta$ where B_θ is the poloidal component of the magnetic field. Also, R is the major radius and B_ϕ is the toroidal component of the magnetic field. From Eq. (1.2) it can directly be seen that magnetic field lines must lie on surfaces of constant pressure, labelled as *flux surfaces*. Thus $p = p(\psi)$ and $F = F(\psi)$, and transport in the radial direction, perpendicular to the magnetic field lines, is synonymous with transport across flux surfaces. There are several ways to label the flux surfaces, apart from using ψ. In this thesis we mainly use the toroidal magnetic flux Φ to compute $\rho_t = \sqrt{\Phi/\Phi_{\mathrm{LCFS}}}$, where Φ_{LCFS} is the toroidal magnetic flux through the Last Closed Flux Surface (LCFS). In few cases we will use the alternative label $\rho_\psi = \sqrt{\psi/\psi_{\mathrm{LCFS}}}$.

The characteristics of the flux surfaces, their shape and radial locations, are defined by the balance between pressure gradients in the plasma and the $\boldsymbol{J} \times \boldsymbol{B}$ force, where $\boldsymbol{J}$ is the current density. In a stationary equilibria without strong flows, $\nabla p = \boldsymbol{J} \times \boldsymbol{B}$. This equation leads to the Grad-Shafranov equation [5], describing how the pressure and current affect the shape and distribution of the flux surfaces

$$-R^2 \nabla \left(\frac{1}{R^2} \nabla \psi \right) = \mu_0 R^2 \frac{\mathrm{d}P(\psi)}{\mathrm{d}\psi} + F(\psi)\frac{\mathrm{d}F(\psi)}{\mathrm{d}\psi}. \tag{1.3}$$

The flux surface shape in the cylindrical R, Z coordinates can be described by a Fourier decomposition in the poloidal angle θ

$$R(\theta) = R_0 + r\cos\theta - \Delta(r) + \sum_{m=2}^{\infty} S_m(r)\cos\left[(m-1)\theta\right] \tag{1.4}$$

$$Z(\theta) = r\sin\theta - \sum_{m=2}^{\infty} S_m(r)\sin\left[(m-1)\theta\right], \tag{1.5}$$

3

where r is the minor radius, another flux surface label, measuring the horizontal distance along the outer midplane of the flux surface relative to the magnetic axis, which is at the major radius $R = R_0$. The Shafranov shift $\Delta(r)$ is a measure for the radial compression of the flux surface while $S_m(r)$ are the shaping coefficients. For $S_m = 0$ the flux surface shapes are circular. The second harmonic gives rise to an elongation of the plasma, $\kappa = r - S_2/(r + S_2)$ while the third harmonic gives the plasma a triangularity, $\delta = 4S_3/r$. In experiments it is possible to generate poloidal harmonics S_m using dedicated shaping coils. The elongated vessel and multiple independently driven poloidal field coils make the TCV machine [6] in SPC, Lausanne, Switzerland, particularly suited for studying the effect of plasma shaping on the performance of fusion reactors.

Ideally, particles would be constrained to move along the field lines and remain on the flux surfaces. However there are various mechanisms that lead to radial transport, causing particles and energy to move across the flux surfaces. In fusion plasmas, the most problematic one is the radial transport arising from anomalous, turbulent transport.

1.2 Turbulence in fusion plasmas

Turbulence is believed to account for most of the radial particle and energy transport measured in fusion plasmas. It is driven by microinstabilities: unstable modes with wavelengths λ of the order of the Larmor radius scale that are driven unstable. The frequency and growth of these instabilities can be modelled with linear physics, after assuming a form of the perturbation $\sim \exp[i\omega t + \gamma t]$, where ω is the real frequency of the oscillation, generally much slower that the gyrofrequency but much faster than that of the variation of background parameters, and γ is the growth rate of the mode. Gradients in temperature and density may lead to $\gamma > 0$, causing the mode to grow unstable.

1.2.1 Main instabilities in toroidal fusion plasmas

At the ion Larmor radius scale $\lambda \sim \rho_i$ the **Ion Temperature Gradient** (ITG) [7] mode is believed to account for most of the turbulent ion heat transport. It is a drift-wave type mode with a phase velocity of the order of the ion diamagnetic drift velocity

$$v_d = \frac{1}{qB^2}\left(\frac{-\nabla p}{n} \times \boldsymbol{B}\right), \qquad (1.6)$$

arising due to a gradient in the pressure.

The pressure gradient is in the radial direction and the diamagnetic drift in Eq. (1.6) is therefore in the poloidal direction, perpendicular to the magnetic field. For a given poloidal wave number k_θ the diamagnetic drift corresponds to a mode fluctuating with the diamagnetic frequency $\omega \sim v_d k_\theta$. Notice that the sign of ω depends on the charge q, and is therefore different for ions and electrons. In this thesis the convention is that the electron diamagnetic direction corresponds to $\omega < 0$ while

ions have $\omega > 0$. For ITG, $q > 0$ and therefore $\omega > 0$.
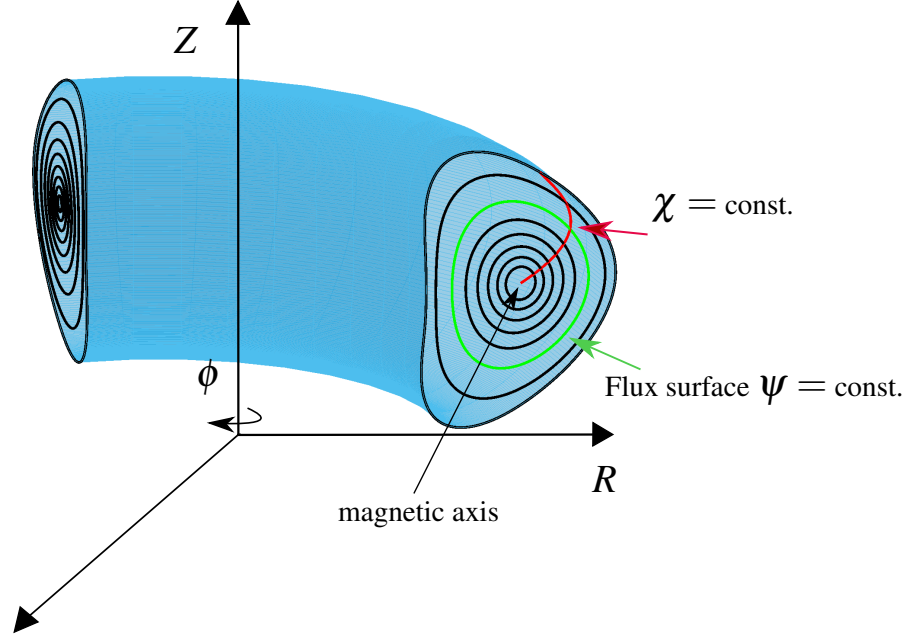
Figure 1.2 – Cartoon illustrating a positive triangularity plasma in the cylindrical coordinate system (R, Z, ϕ). The magnetic axis is indicated at the center of the flux surfaces labelled by Ψ. The straight field line poloidal angle χ will be defined in chapter 3.

The ITG instability can develop even without the presence of any external force, as long as there is a temperature gradient. However in toroidal magnetic geometry there are external forces arising due to the variation in the magnetic field direction and strength, which gives the ITG mode more of an interchange-like character. A simple illustration of the mechanism for this toroidal-ITG instability is as follows. The variation in the magnetic field vector leads to two additional drifts of the particles: the ∇B-drift

$$\boldsymbol{V}_{\nabla B} = \frac{\mu}{m\Omega} \left(\boldsymbol{b} \times \nabla B \right) \tag{1.7}$$

and the curvature drift

$$\boldsymbol{V}_c = \frac{v_{\parallel}}{\Omega} \left(\nabla \times b \right)_{\perp}. \tag{1.8}$$

In the above equations, $\mu = mv_{\perp}^2/(2B)$ is the magnetic moment and $v_{\parallel}$ is the particle velocity along the magnetic field. Since these two drifts are charge dependent, they separate electrons from ions which generates an electric field. This field in turn activates the charge independent

$E \times B$ drift

$$V_E = \frac{E \times B}{B^2}.\tag{1.9}$$

Depending on the direction of this drift it can either reinforce or stabilise an initial perturbation in the temperature (this reflects the interchange-like nature of this instability). In the inboard midplane of the tokamak the curvature and ∇B drift are such that the $E \times B$ drift is stabilising, while in the outboard midplane it will reinforce an initial perturbation, leading to the toroidal ITG instability. These two stabilising/destabilising regions of the tokamak are therefore known as the good, respectively bad curvature regions of the plasma. Perturbations generated by the ITG instability have thus a ballooning like character, reaching a maximum at the outboard midplane and a minimum at the inboard midplane.

In general the onset of the ITG instability does not only depend on the ion temperature gradient, but also on the density gradient. The critical threshold depends on the ratio between two gradient length scales, $\nabla \ln T / \nabla \ln N$.

While the toroidal ITG mode is responsible for turbulent transport in the ion channel, the **Trapped Electron Mode** (TEM) [8] instability is believed to drive most of the electron heat and particle transport. The instability arises due to the presence of trapped particles in the plasma. These particles do not complete a full toroidal orbit but are trapped inside a magnetic well, forming trajectories that take the shape of a banana, as illustrated in Fig. 1.3. This trapping mechanism is a consequence of conservation of the kinetic energy and of the magnetic moment $\mu = mv_\perp^2/(2B)$, and the variation of the magnetic field strength that varies between a maximum at the inboard and a minimum at the outboard mid-plane of the plasma ($B \sim 1/R$). Increasing magnetic field strength and conservation of μ implies that $v_\parallel$ has to decrease in order to conserve the kinetic energy $\mathscr{E} = \frac{1}{2}mv_\parallel^2 + B\mu$. If the ratio between the parallel and perpendicular velocity of the particle $v_\parallel/v_\perp$ is too small, particles might reach $v_\parallel = 0$ and get trapped.

The average toroidal position of the banana trajectories of trapped particles is not constant. These particles drift gradually in the toroidal direction with a precession velocity $\langle \dot{\varphi} \rangle_b$. Here $\langle \cdot \rangle_b$ denotes the average of the particle velocity over many banana periods. An electrostatic perturbation generated from a pressure perturbation might resonate with the precessional frequency of the trapped particles, leading to the TEM instability.

The TEM propagates in the electron diamagnetic direction, $\omega \sim \omega_{T,e}$ where $\omega_{T,e} < 0$ is the diamagnetic frequency generated by a gradient in the temperature. A simple estimate of the growth rate of the mode is given by [9]

$$\gamma \sim \sqrt{\frac{3}{2}\alpha_t n \langle \dot{\varphi} \rangle_b \omega_{n,e} \left(1 + \frac{d\ln T_e}{d\ln n_e}\right)},\tag{1.10}$$

where α_t is the fraction of trapped particles in the plasma. In contrast to ITG that is driven
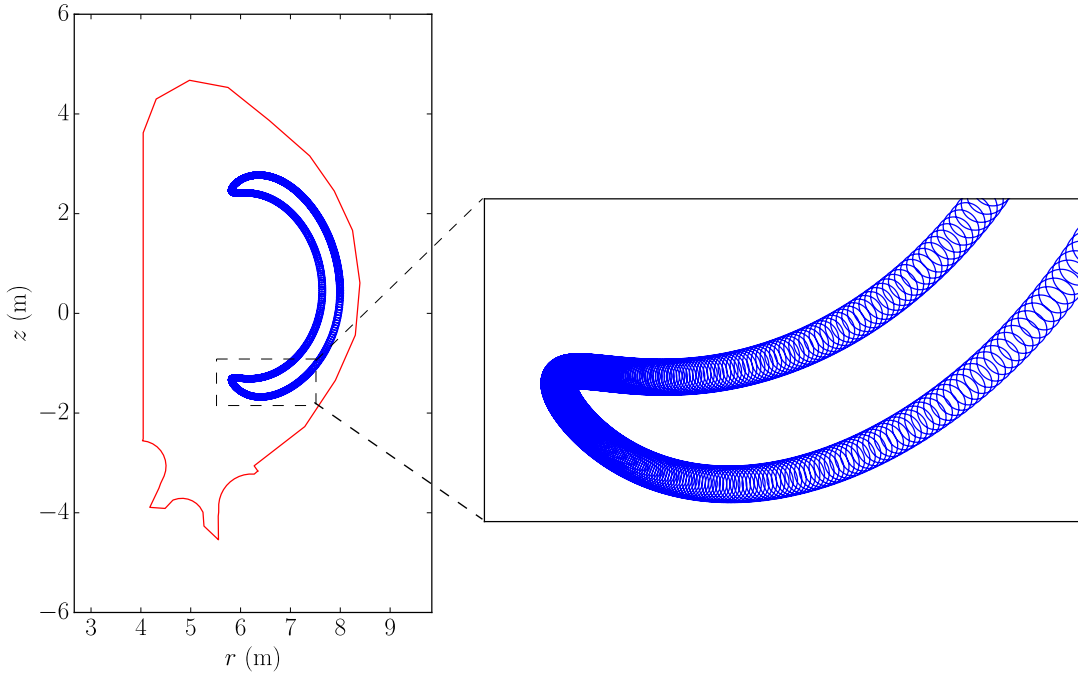
Figure 1.3 – The motion of a charged particle in a ITER-like magnetic field, projected on a poloidal cross-section of the tokamak. The particle gyrates rapidly around its guiding center while slowly drifting along a banana shaped trajectory. Source: [4].

by the ion temperature gradient, the TEM instability is driven by the electron temperature or density gradient. By reducing the ratio between the density and electron temperature gradients or changing the precessional drift (thus moving away from resonance) it is possible to stabilise the TEM instability, and thus reduce transport in the electron channel. The precessional drift can in particular be modified by changing the plasma magnetic geometry, for example by going from a positive to a negative triangularity plasma. This type of reduction in the TEM growth rate is one of the main candidates believed to explain the reduction in the turbulent heat flux observed when modifying the plasma triangularity [9, 10].

At very small scales, of the order of the electron gyroradius scale, $\lambda \sim \rho_e$, the very short wavelength **Electron Temperature Gradient** (ETG) [11] mode can appear. In fact, future fusion devices such as ITER will operate with substantial electron heating and in a regime when ion-scale modes are near marginal stability. In such a scenario, it is expected that ETGs will strongly influence the turbulent transport by greatly increasing the sensitivity of the electron heat flux Qe to variations in the electron temperature gradient (stiffness) [12–15]. ETG modes are usually described as being isomorphic to ITGs, with the role of ions and electrons swapped: the ETG mode propagates in the electron diamagnetic direction, and are driven by the electron temperature gradient. Despite their short spatial scale, ETGs might have an influence on the electron heat transport by developing radially elongated streamers [16] and by interacting with the ion scale

7

modes.

ITG,TEM and ITG are all electrostatic in nature; they are driven by perturbations in the electrostatic potential only. There are also electromagnetic modes driven by perturbations in the magnetic field, such as the Micro Tearing Mode (MTM) [17] and Kinetic Ballooning Mode (KBM) [18], appearing at large enough values of β. In this thesis we use β_e as the ratio between the normalised *electron* plasma kinetic to magnetic pressure

$$\beta_e = \frac{8\pi n_e T_e}{B_{\text{ref}}^2}, \tag{1.11}$$

where n_e, T_e is the electron density and temperature respectively and B_{ref} is the magnetic field at the magnetic axis.

1.2.2   Saturation of turbulence: Zonal flows

Linear physics leads to an exponential growth of the instabilities but it is nonlinear effects that saturate the growth of the perturbations, lead to spectral spreading and ultimately generate turbulence. The best known and one of the most common mechanisms for saturation of electrostatic turbulence are the zonal flows [19].

A fluctuating, radial variation in the electrostatic potential may lead to a flow, different from the mean $E \times B$ flow in the plasma, known as zonal flows. Zonal flows have a dominant, stationary component, with respect to the ion transit frequency $v_{t,i}/(qR)$ where v_t is the ion thermal velocity, and correspond to radially varying $E \times B$ flows that very efficiently shear large turbulent eddies into smaller structures, and thus acts as a saturation mechanism for turbulence. This is illustrated in Fig. 1.4. Indeed, at least for ITG driven turbulence, such zonal flows are the main saturation mechanism. They are of pure nonlinear character and interact with the turbulence through three wave interactions. The zonal flows are in fact self-consistently driven by the turbulence and can be seen as the decay via a resonant interaction of a microinstability eigenmode ($n \neq 0$), into a zonal mode ($n = 0$) and a sheared eigenmode ($n \neq 0$). Zonal flows have toroidal and poloidal mode numbers $n = 0$ and $m = 0$ respectively, and are therefore also constant along the magnetic field, with $k_\parallel = 0$. Here $k_\parallel$ is the wave number along the magnetic field line. The zonal $E \times B$ drift is thus always perpendicular to $\nabla \psi$ and zonal flows do therefore not cause any radial transport and are unable to respond to a gradient in the pressure.

Due to $k_\parallel = 0$, electrons, even with their high velocity, are unable to respond adiabatically to the zonal flows. The sheared flows therefore have very low inertia, leading to large amplitudes - making them very efficient in saturating ion scale turbulence. This is different at electron scales, where the large ion gyroradius means that the ion gyro-orbits averages over any zonal perturbation, giving the ions an adiabatic-like response to the zonal perturbations. This means that zonal modes are less efficient in shearing ETG turbulence. There are also situations when the Zonal flows are unable to saturate the turbulence levels even at ion scales. This means that
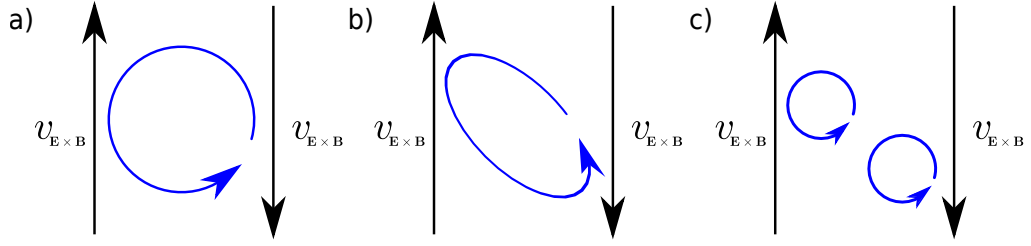
Figure 1.4 – An illustration of the shearing of turbulent eddies by zonal flows. An eddie that is subject to strong poloidal $\boldsymbol{E} \times \boldsymbol{B}$ flows (a) is sheared (b) and eventually breaks up into smaller eddies (c). Source: [9].

the fluxes generated by turbulence may reach very large values. This is the so called Non-Zonal Transition (NZT) [20] which might occur for simultaneously large values of the pressure gradient and β.

In experiments one can usually only distinguish finite frequency components, as the stationary components are very difficult to distinguish from background noise and offsets. Due to the stationary structure of the zonal flows, they are therefore very difficult to observe experimentally. However, the zonal mode usually also develops a time dependent $m = 1$ harmonic, density perturbation, known as the Geodesic Acoustic Mode (GAM). For zonal flows $\partial n / \partial t = 0$ implies incompressibility and the poloidal $E \times B$ drift is balanced by a flow along the magnetic field line. The GAM instead varies in time, $\partial n / \partial t \neq 0$, which leads to an oscillatory density flow. The GAM mode has been observed experimentally, using for example the TPCI diagnostic, and matches well the predictions by gyrokinetic simulations [9, 21, 22].

1.3 Why fusion ?

Turbulence is a major limiting factor in present fusion reactors, but why is it worth spending time, money and energy to try and solve this issue ? The main reason why research in fusion is important is because of the high energy density of the fusion reactions and the abundance of the fuel. Future fusion reactors are foreseen to use Deuterium and Tritium in the fusion reactions:

$$D + T \Longrightarrow He + n + 17.6 \text{ MeV}, \tag{1.12}$$
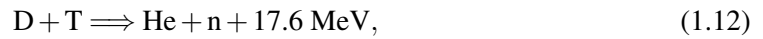
as this reaction is the most practical one to achieve. Most of the energy, 14 MeV, is carried by the neutron and can be used to produce steam, driving a turbine and yielding electric power [23]. The other 3.6 MeV is carried by He that remains in the magnetic case, and can be used for heating the plasma. If we produce enough fast He particles we might reach ignition, and a self-sustained plasma. The reaction in Eq. (1.12) is extremely energy dense, 1 kg of D-T could cover the need of one GW power plant for one day. Deuterium can easily be extracted from seawater and Tritium, although more complicated, as it is radioactive and will decay with time, can be extracted by having the neutron from the fusion reaction react with Lithium. Lithium in turn can be found in

the lithosphere and can alternatively be extracted, at a higher cost, from the oceans. Therefore the only input to the fusion reactor, after an initial amount of Tritium, is Deuterium and Lithium, which are both readily available. The available resources of Deuterium and Lithium would be enough to power fusion reactors that could satisfy our total energy demand for millions of years.

Furthermore, fusion reactors do not have the safety issues of a fission reactor, where chain reactions have to be carefully controlled and contained to avoid accidents, and where the radioactive waste has to be safely stored for generations. Fusion reactions are instead difficult to initiate but are easy to control. While overcoming the difficulties of initiating and containing a sufficient amount of fusion reactions is certainly challenging, keeping the fusion reactor safe afterwards is much simpler.

Fusion might not arrive in time to save us from the consequences of climate change; the catastrophes are imminent, happening right now. But once we have fusion, it does have the potential to resolve the global energy crisis, providing us with clean and sustainable energy that would satisfy out electricity demands for millions of years.

1.4   Scope and outline of the thesis

The goal of this thesis is to study turbulence in fusion plasmas. We concentrate on using the Phase-Contrast Imaging (PCI) [24–29] diagnostic for collecting information on electron density fluctuations. This diagnostic provides information on small-scale electron-density fluctuations, integrated along the path of a laser beam that is injected through the plasma. PCI measurements are not dependent on specific plasma conditions and can be performed from edge to core, which makes the technique an ideal choice for validation and comparison with theory.

A computational and experimental approach is necessary for a systematic study of turbulence. Theory is necessary for understanding and predicting turbulence phenomena, which, due to their complexity, often involves carrying out numerical simulations and modelling. While this approach gives an understanding of turbulence from first principles physics, it always relies on assumptions and simplifications of the real-life event. To ensure that the simplified models are valid and the theoretical predictions are accurate, the modelled turbulence should be compared with experimental measurements of the fluctuating quantities. Apart from validating the theory such a comparison, just as importantly, helps to interpret experimental measurements that are often complex and difficult to link to the underlying physical mechanisms. For example measurements can give information on fluctuations integrated over a laser beam path (case of PCI) or the change in the shape of a pulse after being reflected by the turbulent structures (case of short pulse reflectometry [30]), thus providing an indirect observation of the underlying turbulence. The result is also dependent on the measurement system geometry and procedure (such as optical components, passage of a laser beam through the plasma, etc.), and includes the combined effect of a range of fluctuation contributions. This is especially true for PCI. The PCI measurement is an average over various fluctuation contributions, including for example those driven by the ITG

modes or TEM, or caused by GAMs. Distinguishing the contributions from the different type of modes is difficult, and further complicated by the effect of the measurement geometry and the optical set-up of the diagnostic.

In this thesis work we perform both an experimental and computational study of the turbulent fluctuations to build on the community's present understanding of the turbulence processes. On the experimental side we use the PCI diagnostic that was installed [27] and already used successfully to probe ion scale turbulence in a wide range of plasma scenarios in TCV [21, 31]. During this work we upgraded the experimental set-up to provide more accurate measurement of ion scale turbulence, and made preparatory work for measurement of ETG-driven turbulence at the very small, electron scales.

On the computational side we have developed a synthetic diagnostic that models measurements from PCI, by post-processing nonlinear flux-tube gyrokinetic simulations performed with the Eulerian (grid-based) GENE code [11, 32, 33]. A key element included in the synthetic diagnostic is the effect of a spatial filter that is used in experiments to select preferential wave vector components that contribute to the measurement. Since the measured wave vector rotates along the laser beam path, the filter leads to a localisation of the PCI signal. Optimal localisation is achieved for a tangentially propagating PCI beam (i.e approximately tangential to the magnetic field), such as the one employed on TCV and the one planned for JT-60SA.

We use the synthetic PCI diagnostic for making predictions of future PCI measurements and to help interpret experimental observations. The modelling of the PCI signals is mainly done for the TCV machine but we also make predictions of future PCI measurement on JT-60SA, where PCI is planned to be one of the most important turbulence diagnostics [34].

The remainder of this thesis is organised as follows:

- Chapter 2 describes the TCV machine, which is the focus of this thesis for investigating turbulence. We present the general characteristics of the machine, the heating systems and the main diagnostics used for measuring the plasma profiles and shape. We also explain how profiles and magnetic geometry are computed from the various diagnostics, as it is important both for measuring relative fluctuation levels with PCI and for generating the input parameters for simulations of turbulence. Finally, we present the main diagnostic used to measure and study turbulence: the PCI diagnostic.

- Chapter 3 deals with the modelling aspect of this dissertation. We present the principles of the GENE code and the gyrokinetic equations for modelling turbulence. We then present the details of a synthetic diagnostic that is used for modelling PCI measurements, taking as input the electron density fluctuations computed with GENE.

- Chapter 4 is dedicated to showing how the synthetic PCI diagnostic and GENE modelling can be used for improving our interpretation of PCI measurements. First we model past PCI measurements that were performed to investigate the effect of plasma triangularity on

turbulence. These and past result showed that negative triangularity stabilises turbulence by increasing the critical threshold for the onset of instabilities, and by reducing the stiffness of the profiles. For the discharges we analyse, with the synthetic diagnostic we find that the main difference when changing from positive to negative triangularity, for the radial filter configuration that was used, is in the contribution from the GAM. Then by varying the filter orientation we show how PCI can be used to measure also the characteristics of TEM and ITG modes.

- In chapter 5 we turn to the experimental side of this thesis work. We show the upgrades in the TPCI hardware on TCV, and give details on the tests of the equipment that were carried out, in particular tests of the frequency response of the photovoltaic and photoconductive detectors. We then test the new set-up on first measurements at TCV.

- In chapter 6 we change the machine and focus on turbulence in the JT-60SA tokamak. We carry out GENE simulations to model the electromagnetic turbulence in the machine, and then use the synthetic PCI diagnostic to make predictions of future measurements with PCI in JT-60SA.

- Finally, in chapter 7 we offer conclusions and suggest future work that can be carried out with PCI and the synthetic diagnostic.

The initial idea with the modelling aspect of this thesis work was to predict and explain corresponding measurements. However, due to issues with the diagnostic, as will be explained in chapter 5, a direct comparison between modelling and experiments could not be done. Therefore, before we begin, the author would like to emphasise that the modelling and experimental side of this work are independent from each other. The purpose of the modelling of TPCI signals, in particular presented in chapter 4, is to improve our interpretations and make predictions of *future* TPCI measurements, *not* included in this work. Several TPCI measurements will be discussed in chapter 5, but these scenarios are different from the ones considered in the modelling aspect of this work.
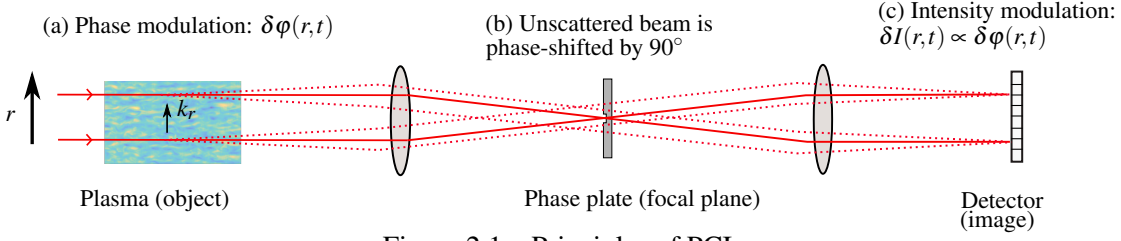
2 Experimental apparatus

The Phase-Contrast Imaging (PCI) diagnostic is used in this thesis to study turbulence, and the main focus is on the diagnostic installed on the Tokamak à Configuration Variable (TCV) device: chapters 3,4 and 5 all use the diagnostic set-up on TCV. A different set-up will however be examined in chapter 6, where predictions of TPCI signals in future JT-60SA experiments will be made.

This chapter is dedicated to introducing the general principles of PCI, the TCV machine and its main diagnostics used to measure the species profiles and to reconstruct the magnetic equilibrium. These measurements will be important in chapters 3,4 and 5 as they provide input parameters for gyrokinetic simulations of turbulence and are used to calculate relative fluctuation levels from the PCI signals.

The remainder of this chapter is structured as follows. The PCI technique for measuring electron density fluctuations is presented in section 2.1, including the routines for data analysis that are used to analyse the frequency and wave-number content of the density fluctuations from the PCI signals. The TCV machine, followed by the various diagnostics that measure the species profiles and for reconstructing the magnetic equilibrium, are described in 2.2. The procedure for preparing the measured profiles and input parameters for simulations is discussed in section 2.3, and a summary of the chapter is given in section 2.4.

2.1 The Phase-Contrast Imaging diagnostic

The phase-contrast imaging diagnostic is an internal reference interferometry technique, that transforms variations in the phase of the scattered component of a laser beam into variations in the amplitude. The principle of the diagnostic is depicted schematically in Fig. 2.1. We consider a laser beam with a frequency ω much larger than the electron plasma frequency and the electron gyration frequency, and a wavelength λ_0 shorter than the scale of the density fluctuations in the plasma. Under these conditions, when a laser beam is sent through a plasma, the intensity and shape of the beam are preserved, but variations in the refractive index introduce a small phase

(a) Phase modulation: $\delta\varphi(r,t)$

(b) Unscattered beam is phase-shifted by 90°

(c) Intensity modulation: $\delta I(r,t) \propto \delta\varphi(r,t)$

r

k_r

Plasma (object)

Phase plate (focal plane)

Detector (image)

Figure 2.1 – Principles of PCI.

shift $\delta\varphi$ that is proportional to the line integral of the density fluctuations over the beam path L, according to the relation

$$\delta\varphi = r_e\lambda_0 \int_L \delta n_e \, \mathrm{d}\ell, \tag{2.1}$$

where λ_0 is the laser wavelength and r_e is the classical electron radius [25]. Let $\varphi = \varphi_0 + \delta\varphi$ be the total phase shift due to variation in the refracting index in the plasma, where φ_0 is the phase shift due to the slow spatial variation in the background density ($|k| \approx 0$) while $\delta\varphi$ is due to fluctuations ($|k| > 0$). We assume that $\delta\varphi \ll \varphi_0$. The electric field of the scattered laser beam wave can be represented by

$$E_s = E_0 e^{i\delta\varphi} \sim E_0(1 + i\delta\varphi) \tag{2.2}$$

where we expanded to first order in $\delta\varphi$, and where the phase shift due to variation in the background density, φ_0, has been reabsorbed in the electric field component $E_0 = E_i \exp i\varphi_0$, where E_i is the incident electric field. If the scattered and unscattered components are directly recombined on an image plane, a set of square-law detector elements would measure an amplitude $|E_s| = E_i$, which is independent of the fluctuating phase shift that we try to quantify. However, if the unscattered components of the wave could be phase-shifted by 90° with respect to the scattered components, the total scattered field would become

$$E_s = E_0(1 \pm \delta\varphi), \tag{2.3}$$

and the intensity is then a function of $\delta\varphi$

$$|E_s|^2 \sim |E_0|^2(1 + 2\delta\varphi). \tag{2.4}$$

In this case, by recombining the scattered and unscattered components in an image plane, the temporal and spatial variation of the phase shift is transformed linearly into an intensity modulation that can be measured by a square-law detector.

The phase shift can in practice be effected by using the fact that the scattered and phase shifted component travels at a small angle to the laser beam propagation direction. A transmitting or reflecting optic, termed a *phase plate* [24, 35], placed in the focal plane of a lens can therefore be used for phase shifting the two components of the laser beam relative to each other. An illustration of a phase plate is given in Fig. 2.2. Such a phase plate is simply a mirror with a groove of $\lambda_0/8$ depth at the optical axis. A lens placed after the object causes the unscattered component affected by electron density fluctuations to pass though the optical axis on the focal plane, and into the
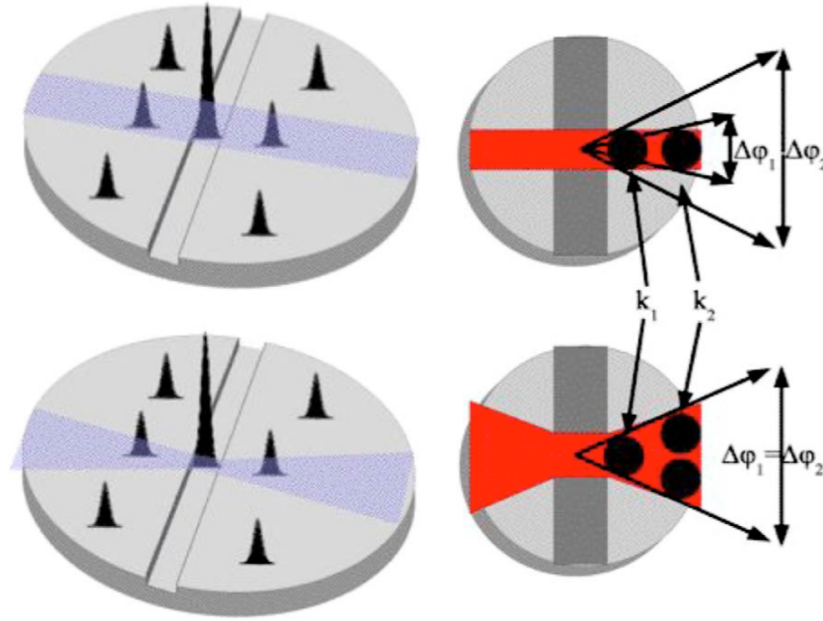
Figure 2.2 – An illustration of the PCI phase plate together with the spatial filter used for selecting the fluctuation direction. The phase plate is a mirror with a groove of $\lambda_0/8$ depth at the optical axis. Unscattered components that fall into the groove are phase shifted by $90°$ with respect to the scattered components that fall outside the groove. The partially reflecting groove also attenuates the much stronger unscattered component, thus enhancing the contrast between the two components of the beam. The purple horizontal band (left) and the red segments (right) illustrate the spatial filters used for selecting the fluctuation direction. Only peaks within these bands are selected by the filter. At the top is shown the configuration that optimises localisation at all values of k, rendering the integration length a function of k; at the bottom is the configuration that preserves the true imaging quality of PCI. Reproduced from [10].

groove, while scattered components are focused onto a distance $\delta x = F k / k_0$ from the optical axis, where k_0 is the laser wave number and F is the focal length. This is illustrated in Fig. 2.1. Contrast is achieved by using a partially reflecting material for the groove which decreases the amplitude of the unscattered part of the wave by a factor $\sqrt{\rho}$ such that the measured intensity becomes $|E_0|^2(\rho + 2\sqrt{\rho}\varphi)$, and contrast has been enhanced by $\sqrt{\rho}$.

The phase plate groove needs to be wide enough to accommodate the full diffraction spot of the unscattered component. The diffraction limited focal spot width is $\sim (F/a)\lambda_0$ where a is the optical aperture, and is typically $0.15 - 0.5$ mm in practical applications, for the most commonly used laser wavelength, $10.6\,\mu$m, corresponding to a CO_2 laser.

The drawback of the phase plate is that it now acts as a high-pass filter, preventing the detection of wave numbers for which the distance from the optical axis $|\delta x|$ is smaller than the width of the groove. This is in fact a fundamental limit of the technique, as the lack of an external reference precludes the measurement of absolute phase changes: only phase *differences* across the width of

the beam can be measured. The longest perpendicular *wavelength* that can be resolved is then of the order of the beam diameter, $\delta x = F\boldsymbol{k}/k_0 > \lambda_0 F/a$ which implies that $|\boldsymbol{k}| > 2\pi/a$.

There is no strict upper wave-number limit. However, beyond a certain wave-number threshold, there occurs a transition from the Raman-Nath (or geometric-optics) to the Bragg regime, giving rise to the so-called Talbot effect, where the medium under investigation is no longer imaged as a whole. This can be restated by saying that the depth of focus of the measurement becomes shorter than the depth of the medium (i.e., the length of plasma traversed). This threshold is $k_{\max} \approx (\pi k_0/L)^{1/2}$, where L is the effective integration length. Normally, the limit is very generous, as is the case for the PCI set-up used in this work and it is always possible to operate the diagnostic in the Raman-Nath regime.

In practice, the maximum *wave number* that can be resolved unambiguously is set by the Nyquist condition on the spatial sampling, i.e., by the number of detector elements and their spacing in the object plane. For a given beam width and detector dimension, spatial resolution can be increased by enhancing the magnification through a set of lenses placed before the detector, and projecting only a fraction of the beam onto the detector. The cost is, however, a reduced field of view and a reduced diameter of the cylindrical interaction volume in the plasma.

The transfer function for PCI can be written as [25]

$$T(\boldsymbol{k}) = 2\sqrt{\rho}\,u_0(0)\int_{-a}^{a}\frac{\sin(k_x x)}{\pi x}e^{-x^2/w_0^2}\left[1 - \cos(k_x x)\right]\mathrm{d}x, \tag{2.5}$$

where $u_0(0) = 2P/(\pi M^2 w_0^2)$ is the power flux in the centre of the image, ω_0 is the half-width of the incident laser beam wave, which is assumed to be Gaussian, M is the total magnification of the optical set-up and P is the laser power. When PCI is designed one tries to optimise the transfer function in Eq. (2.5) for the two dimensionless parameters $Q = k_c\omega_0/2$ and $\alpha = w_0/a$, and the optimal case gives $Q \approx 1.4 - 1.8$ and $\alpha = 1$. An example of a transfer function with these parameters is shown in Fig. 2.3. Here we also assumed that the phase plate has a reflectivity $\rho = 0.17$ and leads to a cut-off $k_c = 1.01$ cm^{-1}. For wave numbers larger that the cut-off k_c the transfer function is a essentially flat and PCI is thus a true imaging function of the density fluctuations.

Because of the line integration, the measured intensity modulation will be a sum of all fluctuating components along the beam path. In this set-up PCI will therefore not have any longitudinal localisation. However, by using the anisotropy of turbulent structures in magnetically confined fusion plasmas along with the twist of the magnetic field, longitudinal localisation can in fact be achieved, as discussed next.

Longitudinal localisation

Fluctuations with sufficiently large wave number in the direction of beam propagation are averaged out upon integration, in Eq. (2.1). It follows that the measured intensity modulation
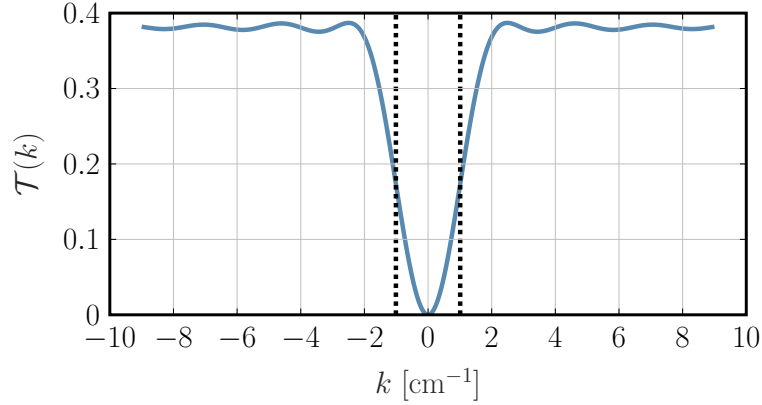
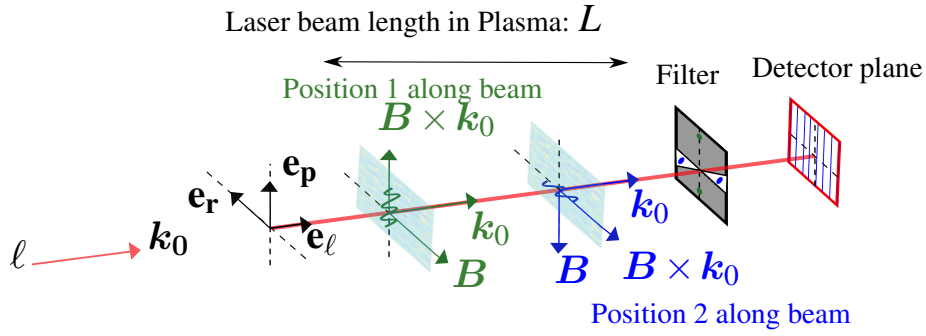Figure 2.3 – An example of the PCI transfer function.

Figure 2.4 – Principle of the magnetic field curvature technique to achieve longitudinally localised measurements.

is mainly sensitive to wave vectors perpendicular to the beam, i.e $\boldsymbol{k} \sim \boldsymbol{k}_{\perp,0}$. Furthermore, the turbulent structures are elongated along the field lines and the wave vector of the turbulent fluctuations is predominantly perpendicular to the magnetic field, $k_{\perp,B} \gg k_{\parallel}$. The wave vector detected by the PCI diagnostic, $\boldsymbol{k}_{\mathrm{meas}}$, is therefore due to fluctuation contributions that are mainly perpendicular to both the beam propagation direction and the total magnetic field, i.e., $\boldsymbol{k}_{\mathrm{meas}} \parallel \boldsymbol{B} \times \boldsymbol{k}_0$. Since the magnetic field in the fusion device twists, $\boldsymbol{k}_{\mathrm{meas}}$ will rotate by an angle that is a function of the linear coordinate ℓ along the beam path [27], as is indicated in Fig. 2.4.

The scattered components of the beam in the focal plane and the propagation direction in the image plane will rotate accordingly. By placing a narrow angular filter in a focal plane, measurements will be limited only to wave vectors that fall inside this range, which in turn corresponds to a specific segment of the full beam path in the plasma. The integration is then effectively performed over a reduced length, yielding some degree of spatial localisation.

The minimum selectable wave-vector range - regardless of how it is selected - is limited by diffraction. This is because the focal spot on the spatial filter has a finite size. If w_0 is the $1/e$ half-width of the laser beam amplitude profile, the angular resolution $\Delta\alpha$ required to measure the

scattering of the laser beam due to a density fluctuation with wave number k is

$$\Delta\alpha = 2\arctan\left(2/(kw_0)\right). \tag{2.6}$$

The angular resolution thus improves with larger wave number k. As it is the *direction* of the wave vector that defines the measurement location, in order for the measurement to access the same longitudinal range for all values of k and thus retain its strict imaging properties, one must select a specific angular range in k space. The corresponding spatial filter (in the case of 1D detection) would then have a transmission region in the shape of a wedge (as shown in Fig. 2.2, bottom). The angular resolution in Eq. (2.6) would then be set by the cut-off wave number k_c. The optimal longitudinal localisation for any given k, however, is obtained by selecting a *band* in k space with width equal to that of the diffraction spot. The corresponding spatial filter would then have a transmission region in the shape of a rectangle (Fig. 2.2, top). In this configuration, the angular resolution in k space is inversely proportional to k as shown by Eq. (2.6), and the longitudinal resolution thus improves with k.

The spatial filters modifies the transfer function of the PCI set-up in Eq. (2.5). Further details on how the spatial filters modify the response of the PCI transfer function will be given in the next chapter, where we present the synthetic PCI diagnostic.

2.1.1 The Tangential Phase Contrast Imaging system on TCV

In this work we focus on the PCI system installed on the TCV tokamak (TCV will be introduced in detail in the next section). In TCV the TPCI laser beam is sent nearly tangentially through the plasma, with respect to the toroidal magnetic field. The path of the laser beam through the plasma, projected on a poloidal cross-section and subdivided into a set of detector chords, is shown in Fig. 2.5. The corresponding projection on the toroidal cross-section of TCV is shown in Fig. 2.6.

The tangential configuration leads to a fast rotation of the measured wave-vector, and consequently very good localisation of the measurement, down to 1% of the minor radius. The rotation angle of the measured wave vector is a monotonic and steep function of a linear coordinate ℓ along the laser beam path. Optimal localisation is achieved when the measurement is performed near the tangency point, $\ell = \ell_{\text{tangency}}$, where ℓ_{tangency} is the position along the laser beam where it is tangent to the magnetic surface and coincides with the point along the ray where $\partial\rho_t/\partial\ell = 0$, as is illustrated in Fig. 2.7. At the tangency point the measured wave-vector rotates the fastest, and furthermore, the radial flux coordinate ρ_t varies the slowest, thus leading to very good localisation in ρ_t.

At the tangency point, the measured wave-vector is mostly radial. Therefore, for measurement at the tangency point the spatial filter has to be oriented along the radial direction. For a tangency point near the core this corresponds to a filter angle of about $160°$ relative to the inboard mid plane.
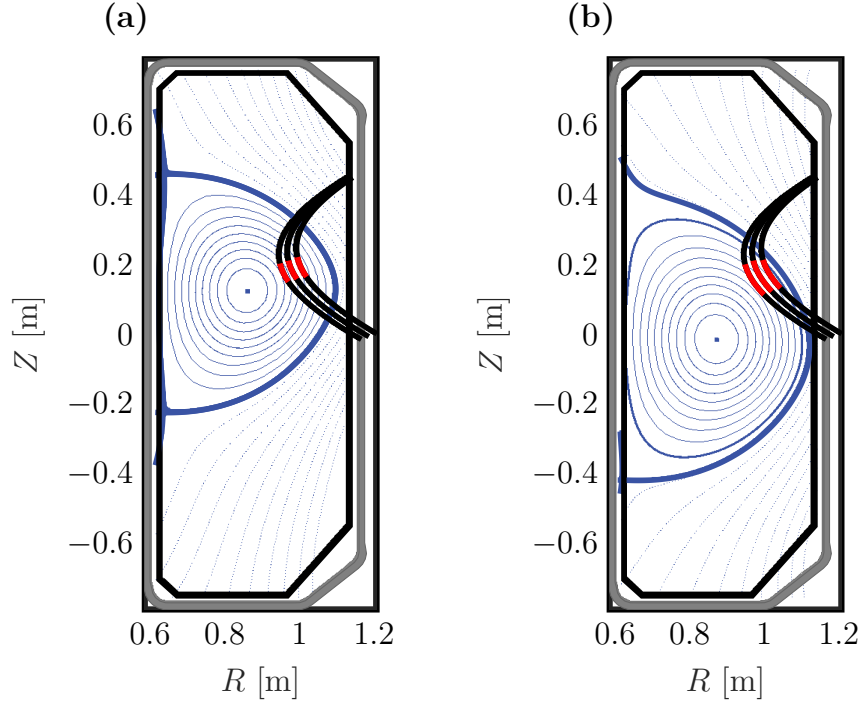
Figure 2.5 – Three examples of TPCI laser beam rays (black curves) projected onto the poloidal plane of TCV. The region selected by the spatial filter is indicated in red. By changing the location of the magnetic axis it is possible to access different regions of the plasma: a high magnetic axis (a) is for measurements closer to the core while a low magnetic axis (b) gives turbulence measurements closer to the edge.

A wedge shaped filter, with a 30° wedge half angle and a 160° filter angle, is the standard set-up used for turbulence measurements with TPCI in the past [21, 22, 31, 36, 37]. The measurement in this case is localised to the red segments indicated in Fig 2.5. The TPCI beam is fixed, however, as is illustrated in Fig 2.5 by moving the plasma vertically it is possible to vary the measurement location. If the magnetic axis is moved from its highest point to the lowest possible, it is possible to access fluctuations from the core $\rho_t = 0.4$ all the way to the LCFS. To retain optimal localisation the filter angle should be adjusted for each position of the plasma. Otherwise also other wave-vector directions, not only the radial, will start to contribute to the measurement, thus yielding a worse localisation. The measured wave-vector directions for the two positions of the magnetic axis is shown in Fig. 2.5, are illustrated in Fig. 2.8. In red again we show the directions selected by the wedge filter.

Further details on the TPCI set-up on TCV will be given in chapter 5 where we will present the work done in this thesis for upgrading the diagnostic.
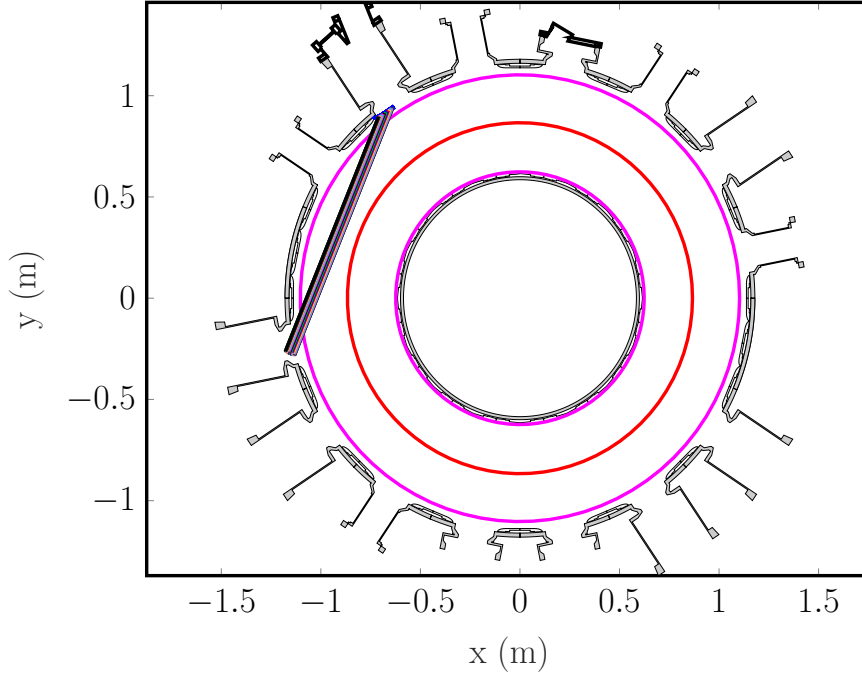
Figure 2.6 – The toroidal cross-section of the TCV tokamak, illustrating the tangential beam geometry of the TPCI diagnostic. The inner and outer positions of the LCFS are shown in purple, while the magnetic axis is indicated in red.

2.1.2 Routines for data analysis

Before finalising this section on the PCI diagnostic, we will also briefly summarise the main data analysis tools that will be used in the next chapters to analyse the PCI signals.

The analysis of turbulence is mainly carried out in frequency space by computing a range of spectral functions. For a signal $Y(t,x)$ we compute the Auto-power and Cross-spectral densities, defined as

$$P(f,x) = \hat{Y}(f,x)\hat{Y}^*(f,x), \tag{2.7}$$

and

$$P(f,\delta x) = \hat{Y}(f,0)\hat{Y}^*(f,\delta x), \tag{2.8}$$

respectively, where $\hat{Y}(f,x)$ is the Fourier-transform of $Y(t,x)$ and $\hat{Y}(f,x)^*$ is its complex conjugate. The complex coherence function is defined as

$$C(f,\delta x) = \frac{P(f,\delta x)}{\sqrt{P(f,x)P(f,0)}}. \tag{2.9}$$

The conditional wave-number spectrum is the spatial Fourier transform of the complex coherence $S(k|f) = \hat{C}(f,k_x)$. The spectrum is normalised such that the integral over the frequency, for each

Figure 2.7 – Radial ρ_t coordinate as a function of beam propagation length ℓ, starting from the point of entry into the plasma, for three TPCI rays (red, blue and green). The position $\ell = \ell_{\text{tangen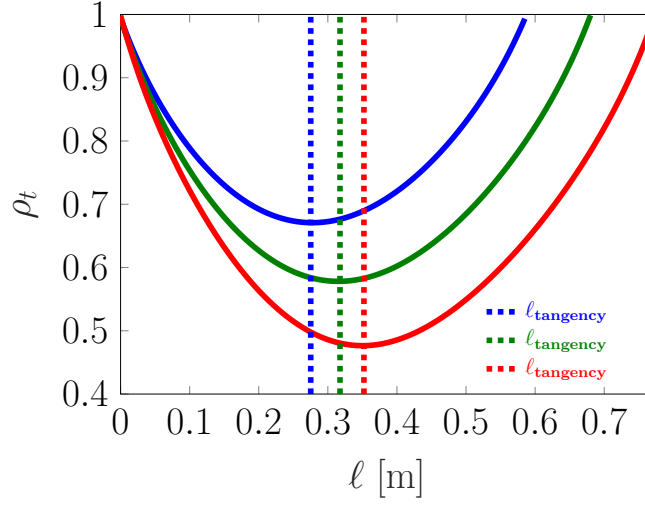cy}}$ denotes the tangency point and coincides with the point along the ray where $\partial \rho_t / \partial \ell = 0$. For purely radial modes it is equal to the position $\ell_\perp$, where the wave vector is perpendicular to the laser beam propagation direction $\boldsymbol{k}_0$.

k_x, equals one. If we assume that the fluctuations are stationary in space, we may estimate the absolute wave-number and frequency by multiplying the conditional spectra by the Cross-power spectral density $S(k,f) = S(k|f)P(f,0)$. The integral over the wave number gives an estimate of the frequency spectrum $S(f)$, and correspondingly, an integral over frequency gives an estimate of the wave-number spectrum $S(k)$.

Because of the very few spatial samples, which might also be unevenly spaced, using standard numerical Fast Fourier Transform techniques for evaluating the Fourier transforms may lead to inaccurate estimates of the wave numbers. In this work we employ the method previously used Refs [21, 25, 27, 36], and estimate the spatial transform using an iterative row-action method whose aim is to find a Fourier transform whose inverse transform matches the complex coherence function within error bars.

The reference channel in Eqs. (2.8) and (2.9) is held fixed and corresponds to the central ray used in the TPCI set-up.

2.2 The TCV device

In this thesis we study turbulence mainly in the TCV machine, located at the Swiss Plasma Center in Lausanne, Switzerland. The main parameters of the device are summarised in Table 2.1 and a sketch of the tokamak with its various magnetic coils is shown in Fig. 2.9. It is a highly elongated, medium sized, Tokamak with 16 independently powered magnetic shaping coils, which give
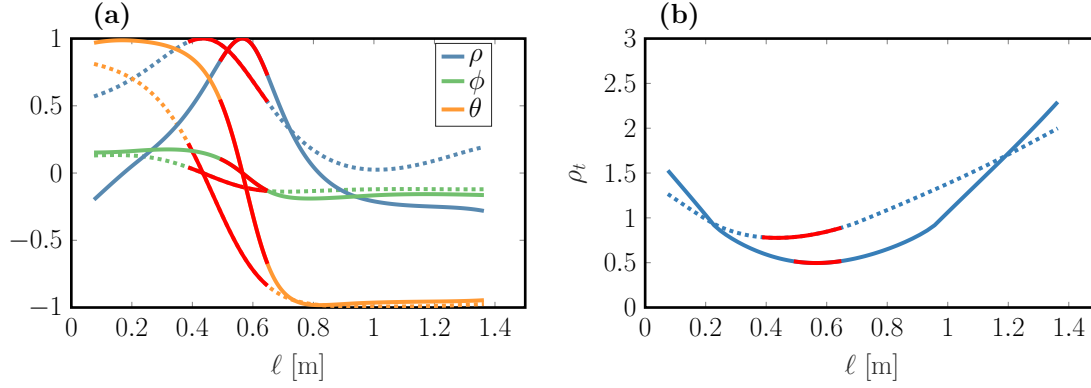
Figure 2.8 – The selected wave-vector direction of the fluctuations (a) and the radial flux surface coordinate ρ_t (b). We show the projection of the normalized wave vector onto the radial direction ρ (blue), poloidal direction θ (orange) and toroidal direction ϕ (green). In both subfigures the abscissa is the linear coordinate ℓ along the laser beam path. In red we indicate the segment that is selected by a wedge filter, with a 30° wedge half angle and a 160° filter angle with respect to the inboard midplane. The two different types of lines illustrate the measurement geometry for two positions of the magnetic axis. Solid lines correspond to a high magnetic axis (for turbulence measurements closer to the core, see Fig. 2.5 (a)) while the dashed lines are for a low magnetic axis (for turbulence measurements at the edge, see Fig. 2.5 (b)).

TCV the capability to create plasmas in a large variety of shapes, some of which are shown in Fig. 2.10. In particular, this includes plasmas with negative triangularity and extreme elongation. These shaping coils are evenly distributed on the LFS and HFS and are placed external to the vacuum vessel. As shown in Fig. 2.9, two additional poloidal field coils are placed inside the vessel to stabilise the plasma vertically, in particular in highly elongated plasmas. The central solenoid generates a current inside the plasma that in turn creates the poloidal magentic field component. The flux swing of the central solenoid can sustain a plasma for about two seconds. Finally, TCV is separated into 16 sectors, each with a set of toroidal field coils that generate the toroidal field.

The main source of ion heating is from two Neutral beam injectors installed on TCV, which can be used to vary ion-to electron temperature ratios as well as temperature gradients. In the NBI set-up, neutral particles are ionised and accelerated to high energies, then neutralised again before being sent towards the core of the plasma where they deposit their energy.

TCV is equipped with two NBI systems for ion heating. One is co-current and may deliver up to 1.3 MW of ion heating. Because of the tangential direction, this beam is also a strong source of momentum and can be used to study the effect of plasma rotation. A second NBI system was recently installed in the counter-current direction, and can deliver up to 900 kW of power. For a given direction of the plasma current, only the co-current beam can be used efficiently, as the second beam will have strong orbit losses, in particular at high energies of the injected neutrals.

Normally, both beams use deuterium atoms, but hydrogen is also possible. The beams can be

Table 2.1 – Main physics parameters of TCV.

| Parameter	Symbol	Value
Major radius	R_0	0.88 m
Minor radius	a	0.255 m
Vessel height	h	1.54 m
Vessel elongation	κ	3
Toroidal field on axis	B_0	1.54 T
Plasma current	I_p	$\leq$ 1 MA
Ohmic heating power	P_{OH}	$\leq$ 1 MW
NBI heating	P_{NBH}	$\leq$ 2 MW
ECR X2 heating	P_{ECH}	$\leq$ 3 MW
ECR X3 heating	P_{ECH}	$\leq$ 2.9 MW
Plasma species		D (He,H)
Main impurity		C
Plasma elongation	κ	0.9 - 2.8
Plasma triangularity	δ	-0.8 - 0.9
Electron density	n_e	$\leq 2 \times 10^{20}$ m^{-3}
Electron temperature (OH)	T_e	$\leq$ 2 keV
Electron temperature (ECRH)	T_e	$\leq$ 15 keV
Ion temperature (OH-ECRH)	T_i	$\leq$ 1 keV
Ion temperature (+ NBH)	T_i	$\leq$ 3.7 keV
Plasma frequency	ω_p	30-120 GHz
Electron Larmor radius	ρ_e	$50 - 60\ \mu$m
Ion Larmor radius	ρ_i	$1.5 - 6$ mm
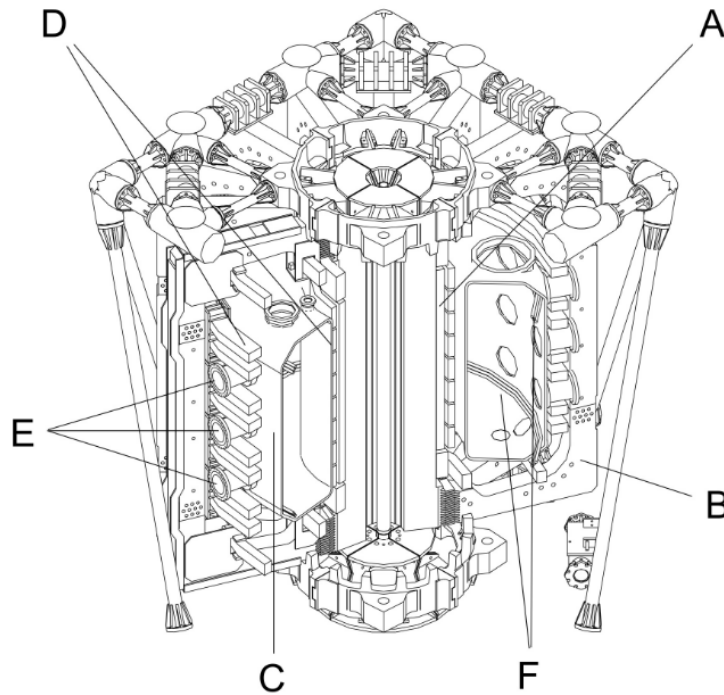
Figure 2.9 – A sketch of the TCV device showing the centrail solenoid (A), toroidal field coils (B), vacuum vessel (C), shaping coils (D), ports for access to TCV (E) and in-vessel poloidal field coils (F).

modulated up to 200 Hz for low power and up to 50-100 Hz for higher, ~ 1 MW, beam power. The beams are directed towards the magnetic axis, but off-axis heating can be achieved by vertical plasma displacement.

Electron Cyclotron Heating (ECH) is used to directly heat the electrons, by generating high frequency waves that resonate with harmonics of the electron cyclotron motion. The heating can in particular be used to increase the ratio T_e/T_i as well as affect the electron temperature gradient. TCV is equipped with several systems capable of heating at different harmonics and with different power. An illustration of the ECH system in TCV is shown in Fig. 2.11. Two single frequency systems heat at the second harmonic and may deliver a total power of 680 kW. Another two systems heat at the third harmonic and may deliver up to 480 kW of power. Finally, two dual frequency gyrotrons heat at either the second or third harmonic and may each deliver up to 1 MW of power.

Each gyrotron may operate for two seconds and usually has the polarisation of the extraordinary wave (X polarisation). Variable poloidal and toroidal injection angles allow one to vary the location of the heat deposited by the gyrotrons (poloidal), as well as to vary the amount of current drive (toroidal).

TCV has several diagnostics for measuring the various characteristics of the plasma. This includes the pressure profiles of electrons, ions and impurities, MHD analysis and the measurement of

#9849, $t = 0.50$ s

(a)

Limited $\kappa = 1.2$,
$\delta = 0.0$, $I_{\mathrm{p}} = 230$ kA

#6010, $t = 0.80$ s

(b)

SND upper
$I_{\mathrm{p}} = 330$ kA

#5650, $t = 0.80$ s

(c)

SND lower
$I_{\mathrm{p}} = 335$ kA

#8856, $t = 0.29$ s

(d)

DND
$I_{\mathrm{p}} = 325$ kA

#11368, $t = 0.65$ s

(e)

Highest current,
$I_{\mathrm{p}} = 1.06$ MA

#18548, $t = 1.50$ s

(f)

Highest fully ECCD
driven current, $I_{\mathrm{p}} = 210$ kA

#6442, $t = 0.50$ s

(g)

Pear shape
$I_{\mathrm{p}} = 360$ kA

#10159, $t = 0.01$ s

(h)

Doublet shape
$I_{\mathrm{p}} = 115$ kA

#19373, $t = 0.42$ s

(i)

Highest elongation,
$\kappa = 2.80$

#8890, $t = 0.75$ s

(j)

Highest triangularity,
$\delta = 0.86$

#11928, $t = 0.67$ s

(k)

Lowest triangularity,
$\delta = -0.77$

#11962, $t = 1.00$ s
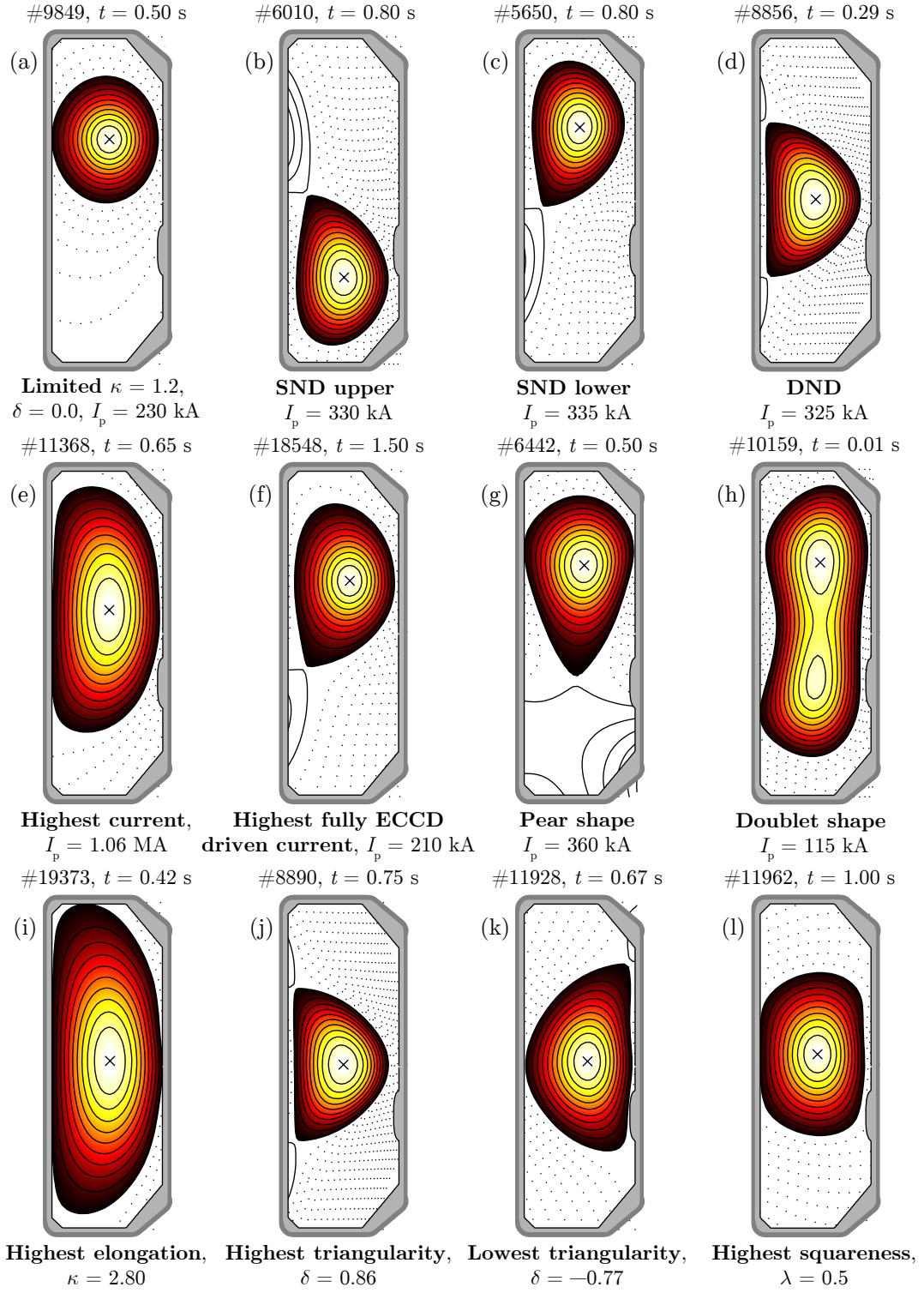
(l)

Highest squareness,
$\lambda = 0.5$

Figure 2.10 – Various plasma shapes that have been obtained in TCV.
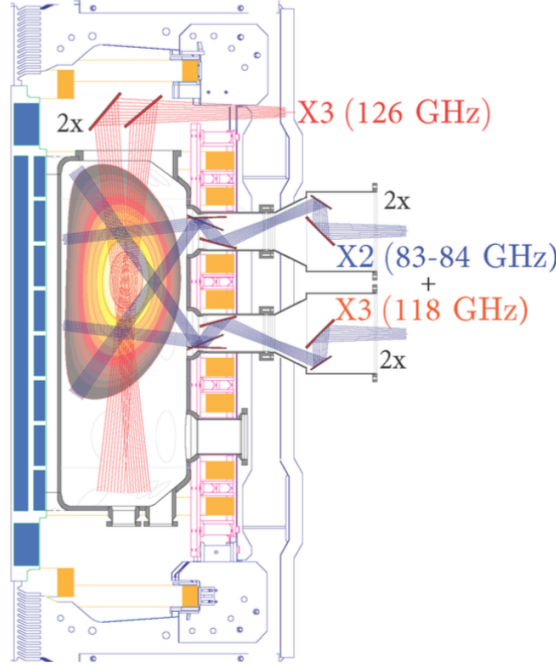
25

Figure 2.11 – TCV with EC heating.

fluctuations in the density or temperature of the plasma. As will be described in section 3.1 for simulating turbulence we need information about the main ion density and temperature, the electron density and temperature, impurity density as well as potentially the fast ion density and the external flow shear. Finally we also need an equilibrium reconstruction to map our measurements onto radial flux surface quantities, generally ρ_t. The diagnostics used to measure these quantities are presented below.

2.2.1 Thomson scattering diagnostic - measurement of n_e and T_e

For measurement of the electron density and temperature, we use the Thomson scattering diagnostic. The diagnostic operates with three sets of independent laser beams at 1.06 micronwavelength. In the presence of the electromagnetic wave, the electrons accelerate and re-emit radiation. Since the laser wave length is shorter than the Debye length, the radiation is uncorrelated and we therefore have incoherent Thomson scattering. Analysing the total scattering power along the laser beams allows one to determine the electron density, while the broadening of the scattered radiation spectra permits the derivation of the electron temperature. In TCV, there are a total of 109 observation systems, probing the locations from $Z = -69$cm to $Z = 55$cm, at mid-radius ($R = 0.9$m) and providing temperature and density profiles from core to the edge. The temperature range that can be measured is 6 eV to 20 keV. Each laser operates at a 20 Hz repetition rate, but since they are triggered individually, it is possible to achieve an even higher rate. An absolute calibration is carried out routinely using Raman scattering. The calibration is corrected during experimental campaigns by using special reference shots.

2.2.2 Charge Exchange Recombination Spectroscopy - measurement of n_C, T_i, Z_{eff} and $\mathrm{d}\Omega/\mathrm{d}\rho$

The Charge Exchange diagnostic (CXRS) [38, 39] on TCV is used to obtain local measurements of the carbon density, temperature and velocity profiles. Since the relaxation rates of the impurity ions with main ion species is fast, the temperature measurement is considered a proxy of main ion temperature. The walls of TCV are covered with graphite tiles, making therefore carbon the most abundant impurity. The temperature and density of carbon are measured with the CXRS diagnostic, consisting of four systems: two toroidal ones, looking at the plasma from the LFS and HFS respectively, and two poloidal ones, one of which is specifically designed to take measurements in the plasma edge. A diagnostic neutral beam, with low enough power that it does not perturb significantly the plasma, generates charge exchange reactions between the impurities and neutral particles. These reactions lead to radiation that can be detected with spectrometers, and the carbon C6+ line at 529.1 nm is the principal one measured. Local measurements of temperature and density are then performed through the analysis of spectral moments. Poloidal and toroidal rotation are measured though the Doppler shift of the C6+ line. In particular, systems three and four give information about the poloidal $\boldsymbol{E} \times \boldsymbol{B}$ rotation of the plasma, which is important for turbulence simulations that consider external flow shear, induced for example via NBI.

2.2.3 Magnetic probes - magnetic equilibrium reconstruction

The free boundary equilibrium LIUQE [40] code is used for equilibrium reconstruction, based on the magnetic measurements from TCV magnetic probes, flux loops and the measurement of the coil currents themselves. The magnetic probes are pick-up coils that measure the electric field induced by the time derivative of the magnetic field along the probe axis. The probes are aligned with the vessel wall and are placed between the wall and the graphite tiles. As they are located inside the vacuum vessel, the time resolution is not limited by the magnetic diffusion time of the conducting vessel. In addition to equilibrium reconstruction, their fast frequency response ($> 100 \text{kHz}$) and the fact that they are absolutely calibrated, make the probes also suitable for studying MHD phenomena.

There are 228 magnetic probes, arranged in poloidal and toroidal arrays in TCV. Three pairs of toroidal arrays are installed at the mid-plane, and 35 cm below and above it respectively. Each set includes 8 magnetic probes on the High Field Side (HFS) and 16 probes on the Low Field Side (LFS) located at equidistant toroidal angles. Four poloidal arrays at four poloidal cross-sections, toroidally separated by 90 degrees, are equipped with 38 almost evenly spaced magnetic probes each.

The flux loops provide measurement of the poloidal magnetic flux. They are wound outside the vacuum vessel in a poloidal location that is in correspondence with the magnetic probes.

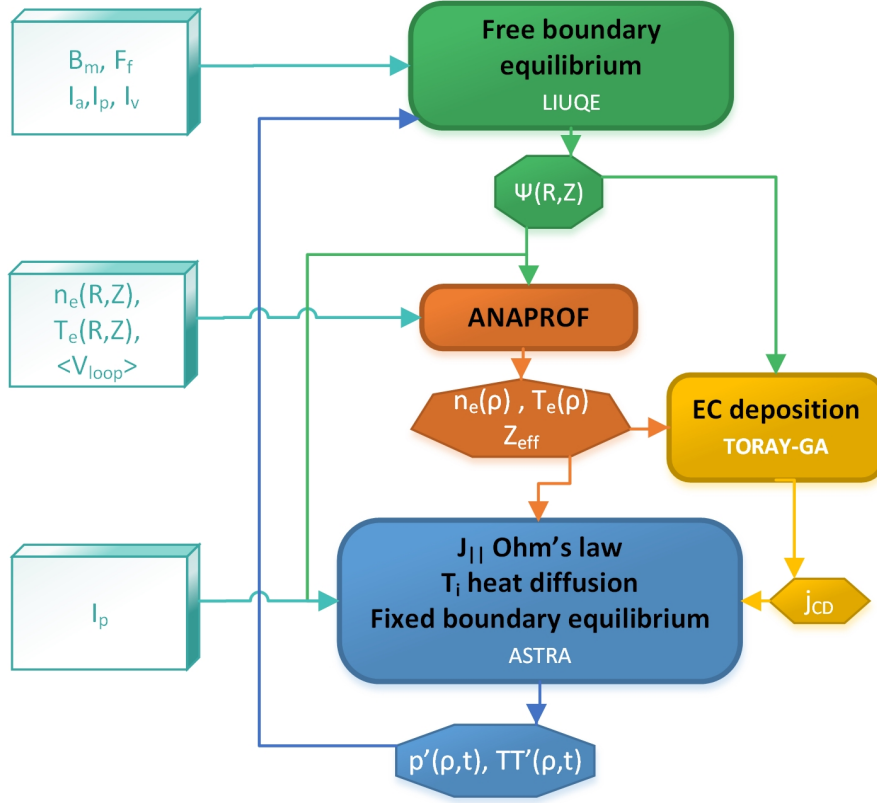## 2.3   Preparing input parameters for turbulence simulations

Figure 2.12 – The iteration procedure of the KER method for finding the best fit of parameters. Source: [41].

To simulate turbulence we need to provide parameters of the plasma, including species density and temperature profiles, the effective charge as well as the magnetic equilibrium. These are all obtained or inferred from experimental measurements. As mentioned earlier, the ion temperature is obtained from CXRS, the Thomson measurements provide the electron temperature and density, while the ion and impurity densities are obtained from the effective charge and quasineutrality. As we will explain in the next chapter, in this work the gyrokinetic simulations are gradient driven, and the simulation results are therefore very sensitive to even small variations in the profiles. It is therefore very important that the input parameters be computed as accurately as possible. In this work we normally follow the following procedure

1. First we check the quality of the data. For example, for CXRS we individually compute the profiles from all four systems. Systems that behave strangely are removed from further analysis.

2. Fitting raw measurements

   (a) If the discharge does not contain NBH we fit the various profiles using in-house available scripts such as `proffit_to_node` and `chie_tcv_to_node`. The results

are stored in MDSPlus nodes for later use. Once we have the fits we run the Automatic System for TRansport Analysis (ASTRA) code and compute a magnetic equilibrium consistent with the total kinetic pressure provided by the measurements.

(b) If the discharge contains NBH it is not sufficient to run ASTRA to compute the magnetic equilibrium, as the effect of NBH on the flux surface position cannot be neglected. Instead, for this case, we use the results computed from the Kinetic Equilibrium Reconstruction (KER) method [41]. KER is an iterative method for identifying the plasma state given available measurements of profiles and/or first principle modelling. This is achieved by iterating over pressure profiles combined with a calculation of the deposited heat and current drive, and a reconstruction of the plasma equilibrium. The computation is run until convergence when all results match the available constraints in a least-squares sense.

The iterative procedure of KER is demonstrated in Fig. 2.12. Using measurements of the magnetic field and currents, LIUQE is used to reconstruct the flux surfaces on a R,Z grid. Together with the electron density and temperature measured with the Thomson diagnostic, as well as the measured loop voltage, the ANAPROFS suite of codes provides the electron profiles on the flux surfaces. The effective charge Z_{eff} is estimated from the icdbseval routine to match the plasma current and loop voltage measured with the magnetic probes. We assume that the only impurity present is carbon and thus, by knowing Z_{eff}, we can estimate the ion density. Then, the TORAY code is run if the discharge contains ECH to calculate the current drive. In the next step the ion temperature is either computed by solving the heat diffusion equation or computed from CXRS measurements (the preferred choice). Together all parameters are provided to the transport code ASTRA that gives the functions pp' and tt' that are fed back to the LIUQE code for recalculating the equilibrium. This loop is repeated until convergence is reached.

3. For any of the fitting routines, we choose a tension that can be used to adjust the smoothness of the profiles. A low tension gives profiles that closely follow the experimental measurements, but might have unphysical local variations in the gradients. To have a smooth gradient, we normally choose a larger tension. No matter which option we choose to fit the profiles, we always make sure the result remains within the experimental error bars before moving on to the next step.

4. Once we have obtained the profiles and magnetic equilibrium we run the CHEASE code to map the kinetic profiles from a ρ_ψ grid to a ρ_t grid, which we normally use in the gyrokinetic simulations. Note that CHEASE otherwise does not have any effect on the profiles or equilibrium. It is simply used here as a conversion tool.

5. At this point we have all the input parameters required to run the gyrokinetic simulations.

2.4 Chapter summary

In this chapter we have introduced the reader to the PCI diagnostic, and shown the details of the diagnostic set-up in the TCV machine. We also gave details on other diagnostics installed on TCV that will be used in chapters 3 and 4 for generating the input for simulations of turbulence in TCV and for processing the experimental TPCI signals in chapter 5. In subsection 2.1.2, we also defined the statistical tools that will be used in the remainder of this thesis for analysing modes and turbulent density fluctuations from the TPCI data.

3 Modelling PCI measurements with gyrokinetic simulations and a synthetic diagnostic

This chapter explains how measurements of electron density fluctuations with the PCI diagnostic can be modelled. The first step is to generate realistic fluctuations that take into account the actual plasma geometry and profiles from the experiment. Nowadays, several gyrokinetic codes [11, 32, 42–49] capable of taking into account multiple kinetic species, collisions and electromagnetic fields, as well as the experimental MHD geometry and global effects, can be used for this task. The second step is to model the experimental measurement procedure itself through a synthetic diagnostic that takes into account the exact measurement geometry and the response of the diagnostic set-up and optical equipment. The same analysis procedures can then be applied to both the synthetic diagnostic results and the corresponding experimental data, allowing valid one-to-one comparisons between the two.

This chapter presents the details of a synthetic diagnostic developed to model measurements from PCI, by post-processing nonlinear gyrokinetic flux-tube simulations performed with the Eulerian (grid-based) GENE code [11, 32, 33]. A novel key element in the synthetic diagnostic is the effect of a spatial filter, used in experiments to select preferential wave vector components that contribute to the measurement. As explained in subsection 2.1, since the measured wave vector rotates along the laser beam path, the filter leads to a localisation of the PCI signals. Optimal localisation is achieved for a tangentially propagating PCI beam (i.e approximately tangential to the magnetic field), such as the one employed on TCV and the one planned for JT-60SA. In this chapter we present the implementation of such a filter and show how it affects the TPCI measurement.

This chapter is organised as follows. Section 3.1 introduces the gyrokinetic description of turbulence and provides details of the code GENE, which is used to solve the gyrokinetic equation and generate turbulence fluctuations. The principle of the synthetic diagnostic, which includes the implementation and effects of a spatial filter, is then explained in section 3.2. A property of this filter is that it reduces the effective integration length and thus localises the measurement. A first-principles test of the localisation is performed by generating density fluctuations for two TCV discharges using nonlinear gyrokinetic GENE simulations. The details of these simulations

together with first principle estimates of the localisation will be given in subsection 3.2.2.

The gyrokinetic simulations presented in this and the following chapter have been carried out with the aim of matching reality as close as possible, but some simplifications still have to be made for practical reasons. Due to these simplifications as well as the inaccuracy of the input parameters, the predicted heat fluxes will not always match the experimental values. This might discourage the reader, as the agreement of the heat fluxes between simulations and experiments is usually considered a measure of the quality of the simulation. However, matching heat fluxes with experiments is a very complicated task and not the purpose of this work. Rather, the aim here is to identify trends and changes in the modelled TPCI signals when the diagnostic configuration and simulation parameters are varied. Even if the heat fluxes differ from the experiments, it is still useful to investigate the properties of the underlying turbulence and compare these fluctuations with the experiments. Even if the amplitudes of the fluctuations are not quite correct, much can be learned from the frequencies, wave numbers and propagation directions of the fluctuations. Indeed, by looking more in depth at the wave-number and frequency content of the fluctuations, rather than just the amplitudes, we go beyond the standard comparison of heat fluxes between simulations and experiments.

3.1 Simulating plasma fluctuations with the GENE code

Based on actual experiments [50–52], turbulent fluctuations in core magnetized plasmas have several particular characteristics. First of all is the very small fluctuation amplitude, normally just a few percent of the background parameters, $|\delta f| \ll f$. Here δf is the fluctuating part of the particle distribution function $f(\boldsymbol{x}, \boldsymbol{v}, t)$ that describes the probability of finding at time t a particle at a spatial $\boldsymbol{x}$ and with velocity $\boldsymbol{v}$. The second property is an anisotropic structure of the turbulent eddies. Particles in the plasma move very fast along the magnetic field lines but drift slowly across them. The consequence is that turbulent eddies tend to have an elongated structure that is aligned with the magnetic field lines. In other words, they have a very long correlation length along the magnetic field line but a very short correlation length, of the order of a few Larmor radii, perpendicular to the field lines. Finally, the third property is that the frequency of the turbulent oscillations is of the order of the diamagnetic frequency i.e much slower compared to the gyrofrequency, but much faster compared to the time variation of the background profiles.

Thanks to these separations in spatial and temporal scales it is possible to derive a set of equations that focuses on describing the turbulent fluctuations, known as the *gyrokinetic equations*. There are several existing gyrokinetic codes that solve the gyrokinetic equations but in this work we use the Eulerian code GENE [11, 32, 33]. It is a δf code that evolves in time the fluctuating distribution function in phase space, while the background distribution f_0 remains static. We mainly use the local flux-tube version of the code, but it has also the possibility of including radial variation in the background profiles, together with particle and heat sources [33, 53] for carrying out global simulations. In its flux-tube version, it can include the effect of background sheared flows [54–56], as well as various forms of the linearised Landau collision operator [57–

59]. Linear simulations can be run as an initial value problem, or as an eignevalue problem to determine the characteristics of the most unstable as well as subdominant modes present in the considered plasma scenario.

In the following subsection we summarise the gyrokinetic description of turbulence and present in more detail the gyrokinetic code GENE. This will be heavily based on Refs. [9, 60], however, as will be seen, here we retain both electrostatic fluctuations ϕ and electromagnetic fluctuations, accounting for both perpendicular $\delta A_{\parallel}$ and parallel (compressional) $\delta B_{\parallel}$ terms.

3.1.1 The gyrokinetic description of turbulence

The spatial and temporal properties of turbulence can be summarised into the following scaling

$$\frac{|\delta f_s|}{|f_{s,0}|} \sim \frac{|e\phi|}{|T|} \sim \frac{|\delta B|}{|B_0|} \sim \frac{|k_{\parallel}|}{|k_{\perp}|} \sim \frac{\omega}{\Omega_s} \sim \frac{\rho_s}{a} = \rho^* \ll 1, \tag{3.1}$$

known as the gyrokinetic ordering. This states that the rapidly spatially and temporally varying fluctuating part of the particle distribution function δf_s, electrostatic potential ϕ and magnetic field δB are much smaller compared to the corresponding slowly varying background reference values $f_{s,0}, T_e/e, B_0$. Furthermore, as already mentioned, the turbulent fluctuations are elongated along the magnetic field lines $|k_{\parallel}| \ll |k_{\perp}|$ and have a frequency of oscillation ω much slower than the cyclotron frequency Ω_s. This ordering is set by ρ^*, the Larmor radius normalised to the minor radius a of the tokamak (stands as a measure for characteristic length of variation of equilibrium), such that $\rho^* \ll 1$ is assumed.

In a collisionless plasma, the time evolution of the full particle distribution function in phase space of each species s is governed by the Vlasov equation

$$\left[\frac{\partial}{\partial t} + \boldsymbol{v} \cdot \frac{\partial}{\partial \boldsymbol{x}} + \frac{q_s}{m_s}\left(\boldsymbol{v} \times \boldsymbol{B} + \boldsymbol{E}\right) \cdot \frac{\partial}{\partial \boldsymbol{v}}\right] f_s = 0. \tag{3.2}$$

Henceforth we drop the indexing s, labeling the species dependent quantities, to lighten the notation.

By applying the gyrokinetic ordering, Eq. (3.1), it is possible to derive an equation that describes the evolution of the fluctuating part of the distribution function, while neglecting the large scale and slow time evolution of the background parameters. This is done by first considering the unperturbed system, whose distribution conveniently expressed in the Guiding Center coordinates $(\boldsymbol{X}_{GC}, v_{\parallel,GC}, \mu_{GC}, \alpha_{GC})$, assuming $\rho^* \ll 1$. As mentioned in the introduction, section 1.1, particles in the plasma gyrate in near circular orbits with gyro-radius ρ_s and a gyration frequency Ω_s. The guiding-center position $\boldsymbol{X}_{GC}$ is the centre of that orbit. The other terms are the velocity $v_{\parallel}$ parallel to the magnetic field of the guiding center, the magnetic moment $\mu = mv_{\perp}^2/(2B)$ at the Guiding centre and finally, α_{GC} is the fast gyration angle, where $v_{\perp}$ is the component of the velocity perpendicular to the magnetic field and $B = |\boldsymbol{B}|$.

At equilibrium, α_{GC} is a cyclic variable, i.e the equations of motion of the particles are independent of α_{GC} and the associated canonical momentum μ_{GC} is therefore constant. However, in the presence of fluctuating fields with wavelengths of the order of the Larmor radius ρ, α_{GC} is not cyclic anymore. To treat the fluctuating fields, one defines through a perturbative approach using Lie transforms a near identity transformation from the Guiding-Center coordinates to the gyrocenter coordinates $(X_{GC}, v_{\parallel,GC}, \mu_{GC}, \alpha_{GC}) \rightarrow (X, v_\parallel, \mu, \alpha)$, such that α remains cyclic. Note that in the absence of fluctuations, guiding center variables are equal to the gyro-center coordinates.

The Vlasov equation states that the distribution is invariant along the particle trajectories. Written in the gyrocenter coordinates it therefore reads

$$\frac{\mathrm{d}f}{\mathrm{d}t} = \frac{\partial f}{\partial t} + \dot{X} \cdot \frac{\partial f}{\partial X} + \dot{v}_\parallel \frac{\partial f}{\partial v_\parallel} + \dot{\mu} \frac{\partial f}{\partial \mu} + \dot{\alpha} \frac{\partial f}{\partial \alpha} = 0. \tag{3.3}$$

By applying the gyro-averaging operator $\langle A(X, \mu) \rangle$, which for a field A is given by

$$\langle A(X, \mu) \rangle = \frac{1}{2\pi} \oint \mathrm{d}\alpha \, A(X + \rho(X, \mu, \alpha)), \tag{3.4}$$

it is possible to remove the dependence on the gyro angle α in Eq. (3.3). Considering then only the fluctuating part of the distribution function and expanding to first order in ρ^* leads to the effectively 5-dimensional $(X, v_\parallel, \mu)$ *gyrokinetic* equation

$$\begin{aligned}
\frac{\partial \delta g}{\partial t} = &-\frac{B_0}{B_{0,\parallel}^*} \left(v_{\langle \chi \rangle} + v_{\nabla B} + v_c \right) \cdot \left[\nabla f_0 - \mu \nabla B_0 \frac{f_0}{T_0} \right] \\
&-\frac{B_0}{B_{0,\parallel}^*} \left((v_{\langle \chi \rangle} + v_{\nabla B} + v_c) \cdot \left[\nabla \delta f - (q\nabla \langle \phi \rangle + \mu \delta \langle B_\parallel \rangle) \frac{f_0}{T_0} \right] \right. \\
&+ v_\parallel \cdot b \left[\left(q\nabla \langle \phi \rangle + \mu \langle \delta B_\parallel \rangle \right) \frac{F_0}{T_0} + \nabla \delta f - \frac{1}{mv_\parallel} \mu \nabla B_0 \frac{\partial \delta f}{\partial v_\parallel} \right) \right],
\end{aligned} \tag{3.5}$$

where the effective magnetic field is defined as $B_{0,\parallel}^* = \nabla \times A_0^*$ with the effective vector potential $A_0^* = A + \frac{m}{q} v_\parallel b$. All fluctuating quantities are written in gyrocenter coordinates, while the equilibrium quantities are in the Guiding Center coordinates.

Eq. (3.5) describes the evolution of the modified fluctuating distribution function $\delta g(t)$, related to the fluctuating particle distribution function δf and fluctuating parallel component of the vector potential $\delta A_\parallel$ through

$$\delta g = \delta f + q v_\parallel \langle \delta A_\parallel \rangle \frac{f_0}{T_0}, \tag{3.6}$$

where T_0 is the background temperature. The zeroth order particle distribution function is a

solution to the zeroth order gyrokinetic equation, and is given by the Maxwellian

$$f_0 = \frac{n(\psi)}{\pi^{3/2} v_{th}^3} e^{-\frac{\frac{1}{2} m v_\parallel^2 + \mu B}{T(\psi)}}, \tag{3.7}$$

where the temperature $T(\psi) = m v_{th}^2(\psi)$ and v_{th} is the thermal speed. This is a so-called local Maxwellian, and is a solution to the zeroth order gyrokinetic equation in the limit of zero finite orbit width.

In Eq. (3.5) $\boldsymbol{v}_{\nabla B}$ and $\boldsymbol{v}_c$ are the ∇B and curvature drift terms respectively, already introduced in Eq. (1.7) and Eq. (1.8). The fluctuating drift $\boldsymbol{v}_{\langle \chi \rangle}$ is given by

$$\boldsymbol{v}_{\langle \chi \rangle} = \frac{1}{B_0} \boldsymbol{b} \times \nabla \delta \langle \zeta \rangle, \tag{3.8}$$

where $\delta \zeta = \phi - v_\parallel \delta A_\parallel + \frac{\mu}{q} \delta B_\parallel$ is the modified fluctuating potential.

In the gyrokinetic Eq. (3.5) the term ∇f_0 involves the density and temperature gradients of each species, thus driving the turbulence. The quadratic nonlinear term $\frac{B_0}{B_{0,\parallel}}^* \boldsymbol{v}_\chi \nabla \delta f$ in particular leads to the ultimate saturation of the exponentially growing instabilities and the associated turbulence cascade development. By removing this term, it is possible to run linear simulations that are relatively computationally inexpensive and determine the most unstable modes, for example ITG and TEM, in the considered scenario.

The time evolution of δg is linked to the fluctuating electrostatic potential ϕ through the following form of the Poisson equation

$$-\nabla^2 \phi = \frac{1}{\varepsilon_0} \sum_s q_s \delta n_s(\boldsymbol{x}) = \frac{1}{\varepsilon_0} \sum_s q_s \int \delta f_s(\boldsymbol{x}, \boldsymbol{v}, t) \, \mathrm{d}\boldsymbol{v}, \tag{3.9}$$

and to the fluctuating magnetic field $\delta \boldsymbol{B} = \nabla \delta A_\parallel \times \boldsymbol{b} + \delta B_\parallel \boldsymbol{b}$ via Ampère's law:

$$\nabla \times \delta \boldsymbol{B} = \mu_0 \sum_s \delta \boldsymbol{j}_s(\boldsymbol{x}) = \mu_0 \sum_s q_s \int \delta f_s(\boldsymbol{x}, \boldsymbol{v}, t) \boldsymbol{v} \, \mathrm{d}\boldsymbol{v}, \tag{3.10}$$

neglecting the displacement current. The density and current sources in the above field equations are expressed in terms of the gyro-centre coordinates using a pull-back operator. For further details we refer to, for example, Refs. [9, 60].

Typical ion-scale turbulence has a correlation length that is much larger than the Debye length. Therefore one can neglect the Laplacian of ϕ on the left hand side of Eq. (3.9) which thus reduces to the quasi-neutrality equation for the densities and the density gradients. For electron-scale turbulence, such as driven by electron temperature gradient instabilities, this term needs to be kept as the wavelength of the fluctuation is of the order of the electron gyroradius which in turn is of the order of the electron Debye length, $\rho_e \sim \Lambda_{D,e}$.

For low β simulations one usually neglects solving for the parallel component of the magnetic field, $\delta B_\parallel$ in Eq. (3.10), and simply considers only $\delta A_\parallel$. This is the case for the TCV-relevant simulations that are carried out in this work, see chapters 3 and 4. However, as will be shown in chapter 6, β can be very large in the JT-60SA machine, and then one cannot neglect compressional magnetic field fluctuations.

It is possible to include the full radial variation of background profiles, such as densities, temperatures and the safety factor, in the gyrokinetic Eq. (3.5). However in this work we take the local flux-tube limit $\rho^* \to 0$, assuming that the turbulence is a local process and depends mostly on the local profiles and their gradients. The gradients are retained but these also assumed to be constant across the simulation domain. Instead of solving for the whole core plasma, the simulation domain is a narrow flux-tube [61], following a field line, with a small perpendicular extension. An example of a flux-tube is illustrated in Fig. 3.1. To be able to simulate the turbulence and obtain saturated heat fluxes, one has to make sure that the size of the flux-tube is sufficiently large to fit the turbulent eddies. Therefore for small machines there is a risk that the flux-tube will be larger than the minor radius of the device. This is for example the case when studying TCV discharges, where global simulations are thus a priori more appropriate [9].

Global simulations have the additional benefit that they can be run in a flux-driven mode, rather than gradient driven mode, which is the case of local simulations. Local simulations therefore have to face the *stiffness problem*. Turbulent transport in the core of magnetised fusion plasmas usually leads to very stiff temperature profiles such that the profile gradients reach a critical value which is not substantially exceeded even when more heating - even very strong heating - is applied. Stiffness is usually associated with the temperature profile, but if the turbulence is very sensitive to the density gradients, such as density gradient driven TEMs, stiff density profiles could in theory also be obtained. Experimentally this would be manifested in a similar density profile, despite strong particle sources. Stiffness is usually taken as a measure of the local slope of the flux as a function of normalised gradient, and speaking of very stiff profiles means that fluxes vary strongly with gradients. Therefore, for gradient driven simulations, simulated fluxes vary strongly even for very slight variations in the input gradients within their experimental error bars, yielding potentially very different results. Flux driven simulations avoid this stiffness problem, although they are computationally very expensive as one has to wait for the profiles to evolve.

Despite its limitations, in this work we take the local approximation in all of our simulations. Even with recent performance improvements of global simulations, local simulations remain computationally more affordable and are sufficient for our purpose, which is to study the nature of the underlying fluctuations rather than exactly reproducing the experimental heat flux levels.

The collision operator

Particles in the plasma do not interact with each other only through the electromagnetic fields related to collective phenomena (waves), as so far described by Eqs. (3.5), (3.9) and (3.10), but
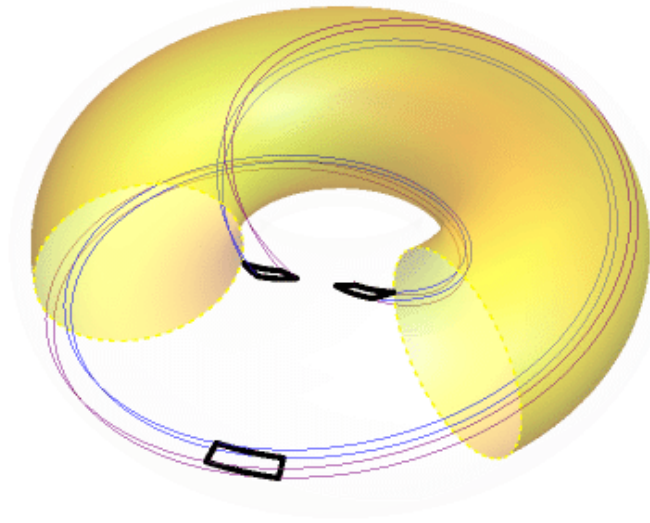
Figure 3.1 – An example flux-tube (thin blue and purple lines) that is one poloidal turn long with its cross-sectional shape indicated on the outboard midplane (thick black rectangle) and at both locations on the inboard midplane (thick black parallelograms). Also shown is the central flux surface of the flux-tube (transparent yellow) with a toroidal wedge removed for visual clarity. Source: [62].

also via binary interactions i.e collisions. Although at sufficiently high temperatures and low densities as found in core magnetic fusion plasmas, the collision frequency is smaller than the typical frequencies of the microinstabilities, collisions can still affect both ITG [63] and TEM [64] instabilities, as well as affect the regulation of turbulence via zonal flows [65]. Collisions are also responsible for the ultimate dissipation of energy at the end of the turbulence cascade, which otherwise has to be handled by imposing an artificial hyperdiffusion. In TCV cases, including collisions is essential in order to stabilise the microinstabilities and bring the simulated turbulence heat flux down to experimental levels [9].

In GENE one normally uses the linearised Landau intra-and inter-species collision operator [66], but neglecting the slow thermalisation process between the background distribution functions, and higher order nonlinear contributions coming from the collisions between two fluctuating distributions. Instead, only the contributions related to collisions between a fluctuating and a background distribution function are considered. Finally, although they can be included in GENE, we neglect finite Larmor orbit effects and only use the gyrophase independent part of the linearised operator.

The first simulations in this work, presented in the next section 3.2 as well as in the beginning of chapter 4, use the standard form of the linearised Landau collision operator, which does not satisfy the H-theorem for entropy production [67] for non-isothermal cases. However, later in the second part of chapter 4 and in chapter 6, we use the so called Sugama collision operator [68], where this problem has been corrected.

GENE coordinate system and boundary conditions

The coordinates used in GENE take into account the field line following properties of turbulent fluctuations. The field aligned coordinates are x, y, z where x is the radial and y the binormal coordinate, while z is the straight-field-line poloidal angle parametrising the position along a given field line (note that $\boldsymbol{B} \parallel \nabla x \times \nabla y$ so that $x = $ const and $y = $ const defines a magnetic line). The curvilinear coordinate system (x, y, z) is clearly non-orthogonal. The expressions for these coordinates in terms of the radial position ρ_t, the toroidal angle φ and the straight-field line poloidal angle χ are given by

$$
\begin{aligned}
x &= \rho_t - \rho_{t,0}, \\
y &= C_y \left[q(\rho_t)\chi - \varphi \right], \\
z &= \chi,
\end{aligned}
\tag{3.11}
$$

where $q(\rho_t)$ is the safety factor profile, $C_y = r_0/q_0$, $q_0 = q(\rho_{t,0})$ and $r_0 = a\rho_{t,0}$ is the radial position of the centre of the flux-tube. The straight field line poloidal angle is defined in terms of the geometrical poloidal angle θ as

$$
\chi = \frac{1}{q(\rho_t)} \int_0^\theta \frac{\boldsymbol{B} \cdot \nabla \phi}{\boldsymbol{B} \cdot \nabla \theta'} \, \mathrm{d}\theta',
\tag{3.12}
$$

where the safety factor is defined as

$$
q(\rho_t) = \frac{1}{2\pi} \int_0^{2\pi} \frac{\boldsymbol{B} \cdot \nabla \phi}{\boldsymbol{B} \cdot \nabla \theta} \, \mathrm{d}\theta.
\tag{3.13}
$$

The size of the flux-tube in the perpendicular direction comprises several turbulent eddy lengths, corresponding to tens of Larmor radii, and in the limit $\rho^* \to 0$ one has scale separation between eddy size and equilibrium scale. By involving statistical equivalence periodic boundary conditions can be imposed in x and y. Denoting L_x as the radial length of the flux-tube, and L_y the binormal length, periodicity in x reads

$$
\Phi(x + L_x, y, z) = \Phi(x, y, z),
\tag{3.14}
$$

and periodicity in y reads

$$
\Phi(x, y + L_y, z) = \Phi(x, y, z),
\tag{3.15}
$$

with $L_y = C_y \Delta\phi$ and where $\Delta\phi$ is the toroidal angle extension of the flux-tube. If the flux-tube covers the full magnetic surface $L_y = 2\pi C_y = 2\pi r_0/q_0$, but this is in general not the case.

Because of periodicity in the radial and binormal directions, fluctuations are conveniently represented in Fourier space along x and y with associated wave numbers k_x and k_y respectively. Toroidal symmetry is reflected in (x, y, z) coordinates by invariance with respect to y as it is the

only coordinate which depends on φ (see Eq. (3.11)). Linear eigenmodes thus have fixed k_y related to toroidal mode number n by the relation: $k_y = -n/C_y = -nq_0/r_0$. Since microinstabilities are field-aligned with $nq_0 \approx m$, where m is the poloidal mode number, $k_y \approx m/r_0$ is an estimate of the poloidal wave number. Note that k_y might not necessarily correspond to an integer toroidal mode number n if the flux-tube does not cover an integer division of the toroidal angle. However, in this work, for properly mapping the flux-tube onto the synthetic volumes in the synthetic diagnostic, in all simulations L_y was chosen such that k_y translates to an integer toroidal mode number n.

With respect to $z \in [-\pi, \pi]$, fluctuations are however represented in direct space considering a finite difference scheme based on a mesh $\{z_{j=0,\dots,n_z-1}\}$ (usually chosen equidistant). For this parallel direction, according to Eq. (3.11) periodicity in the poloidal coordinate $\Phi(\psi, \chi + 2\pi, \phi) = \Phi(\psi, \chi, \phi)$ translates to

$$\Phi(x, y, z + 2\pi) = \Phi(x, y - 2\pi C_y q, z). \tag{3.16}$$

A slightly different form of the parallel coordinate is considered in this work, $z' = \frac{1}{N}\text{arcsinh}(kz)$ where the normalisation factor $N = \text{arcsinh}(k\pi)/\pi$. In this work we use $k = 2$. When transforming to this new coordinate system, all the metric coefficients as well as the Jacobian are evaluated consistently. The parallel boundary conditions is unchanged. This new parallel coordinate is convenient to model turbulence in very shaped plasmas, as they might reduce the requirement on the number of z points required for convergence [54].

In the local representation, the parallel boundary condition Eq. (3.16) translates into coupling of radial k_x modes in Fourier space

$$\hat{\Phi}(k_x, k_y, z + 2\pi) = \hat{\Phi}(k_x + 2\pi k_y \hat{s}, k_y, z). \tag{3.17}$$

The periodicity in Eq. (3.16) is exactly ensured only when considering a radial shift Δx for the radial coordinate x appearing in the q profile:

$$q(x) = q_0 \left(1 + \hat{s}\frac{x - \Delta x}{r_0}\right) = q_0 \left(1 - \hat{s}\frac{\Delta x}{r_0}\right) + \frac{\hat{s}x}{C_y}, \tag{3.18}$$

which can be seen as follows. From the definition of the binormal coordinate in Eq. (3.11) and by representing a fluctuating quantity $\Phi(x, y, z)$ in Fourier space and using the parallel boundary condition in Eq. (3.16) we obtain

$$\Phi(x, y, z + 2\pi) = \sum_{k_x} \sum_{k_y} \hat{\Phi}(k_x, k_y, z + 2\pi) e^{ik_x x} e^{ik_y y} \tag{3.19}$$

and

$$\Phi(x, y - 2\pi C_y q, z) = \sum_{k_x}\sum_{k_y} \hat{\Phi}(k_x, k_y, z) e^{ik_x x} e^{ik_y(y - C_y 2\pi q(x))}$$

$$= \sum_{k_x}\sum_{k_y} \hat{\Phi}(k_x, k_y, z) e^{ix(k_x - k_y 2\pi\hat{s})} e^{ik_y y} e^{-ik_y C_y 2\pi q_0\left(1 - \hat{s}\frac{\Delta x}{r_0}\right)}$$

$$= \sum_{k_x}\sum_{k_y} \hat{\Phi}(k_x + \hat{s}k_y 2\pi, k_y, z) e^{ik_x x} e^{ik_y y} e^{-ik_y C_y 2\pi q_0\left(1 - \hat{s}\frac{\Delta x}{r_0}\right)}. \tag{3.20}$$

By comparing Eq. (3.19) and Eq. (3.20) we recover the coupling (Eq. (3.16)) between modes $k_x = k_{x0} + pk_y 2\pi\hat{s}$, $p \in \mathbb{Z}$, as a consequence of the parallel boundary condition. GENE assumes that the last phase factor in Eq. (3.20) is unity, i.e $k_{y,min}C_y q_0 \left(1 - \hat{s}\Delta x/r_0\right) \in \mathbb{Z}$, where $k_{y,min} = 2\pi/L_y$. This corresponds to choosing the radial shift such that

$$\Delta x = \frac{C_y}{n_0 \hat{s}}\left(\text{NINT}(n_0 q_0) - n_0 q_0\right), \tag{3.21}$$

where $n_0 = -C_y k_{y,min}$ and $\text{NINT}(y)$ provides the nearest integer to y. Eq. (3.21) in fact corresponds to shifting the origin of the simulation box to the nearest mode rational surface. Also, n_0 corresponds to the lowest toroidal mode number for the considered simulation box. We will therefore always have continuity in the parallel coordinate even if the flux-tube does not correspond to a rational fraction of a full toroidal turn.

GENE observables and normalisation

A GENE simulation one usually does not output the entire fluctuating particle distribution function, but instead saves moments of the distribution function. In particular we compute the fluctuating species density

$$\delta n_j(\boldsymbol{x}) = \int \delta f \, d\boldsymbol{v}. \tag{3.22}$$

This is the main output we need from GENE for modelling TPCI measurements, which is presented next in this chapter. Later in this work, we will also study the heat flux from our simulations, which is given by

$$\boldsymbol{Q}_j(\boldsymbol{x}) = \int \frac{1}{2}mv^2 \boldsymbol{v}_D \delta f \, d\boldsymbol{v}, \tag{3.23}$$

where $\boldsymbol{v}_D = \boldsymbol{v}_\chi + \boldsymbol{v}_{\nabla B} + \boldsymbol{v}_c$ is the generalised drift velocity. Note that we normally only consider the radial contribution of the heat flux, $\nabla x \cdot \boldsymbol{Q}_j(\boldsymbol{x})$.

All quantities in GENE are normalised. The spatial variables, such as the wave numbers k_x

and k_y are expressed in terms of the particle gyroradius. The heat fluxes in GENE are given in GyroBohm units $Q_{GB} = p_e c_s \rho_s^2 / L_{ref}^2$ where $p_{ref} = n_e T_e$ is the reference pressure, $c_s = \sqrt{T_e/m_i}$ is the sound speed, $\rho_s = c_s/\Omega_i$ is the reference gyroradius with $\Omega_{ref} = eB_{ref}/m_i$ the gyrofrequency.

3.2 The synthetic PCI diagnostic

In this section we present the details of the synthetic diagnostic that models the experimental PCI measurements. This is largely taken from Ref. [69]. The first step in the modelling procedure, already presented in section 3.1, is to generate electron density fluctuations with gyrokinetic simulations. In the following examples we will take simulations from the GENE code, but the synthetic diagnostic can easily be adapted to other gyrokinetic codes by appropriately modifying the mapping of the coordinates between the simulation and the diagnostic volumes as explained in Appendix B. To demonstrate the working principle of the synthetic diagnostic, we generate electron density fluctuations for an example positive and negative triangularity TCV scenario, details of which will be described in subsection 3.2. In subsection 3.2.1 we show how we post-process these fluctuations to obtain the unfiltered PCI signals, including how we implement the spatial filtering in the synthetic diagnostic. Then in subsection 3.2.2 we finally compute estimates of the "true" integration length and localisation. We compare our results with the theoretical expectation when the measured wave vector strictly satisfies $k_{\mathrm{meas}} \parallel k_0 \times \mathbf{B}$, as was discussed in section 2.1. Note that throughout this section the subscript $\perp,0$ refers to a wave vector perpendicular to the laser beam while $\perp,B$ refers to the wave vector perpendicular to the magnetic field.

Throughout this section we illustrate the synthetic PCI diagnostic by modelling measurements from the PCI system installed on the TCV tokamak, where the laser beam is sent nearly tangentially through the plasma. The path of the laser beam through the plasma, projected on a poloidal cross-section and subdivided into a set of detector chords, is shown in Fig. 3.2. Here we show an example of three detector chords, distinguished by the coordinate r, which will be introduced later in Fig. 3.6. In practice, the number of chords should equal to the number of detector elements used in the measurement. Later in this section we will consider 9 detector elements, thus 9 chords. In this example the PCI beam covers a radial coordinate going from edge to midradius, as shown in Fig. 2.7. In subsection 3.2.2 we will see however that the spatial filtering can reduce the contributions to the PCI signals down to a small segment near midradius. The tangential configuration leads to a fast rotation of the measured wave-vector, and consequently very good localisation. This will be confirmed from first principles in subsection 3.2.2.

Generating δn_e

Electron density fluctuations δn_e are generated with the Eulerian (grid-based) local (flux-tube) version of the GENE [9, 11] code, already introduced in the previous chapter.
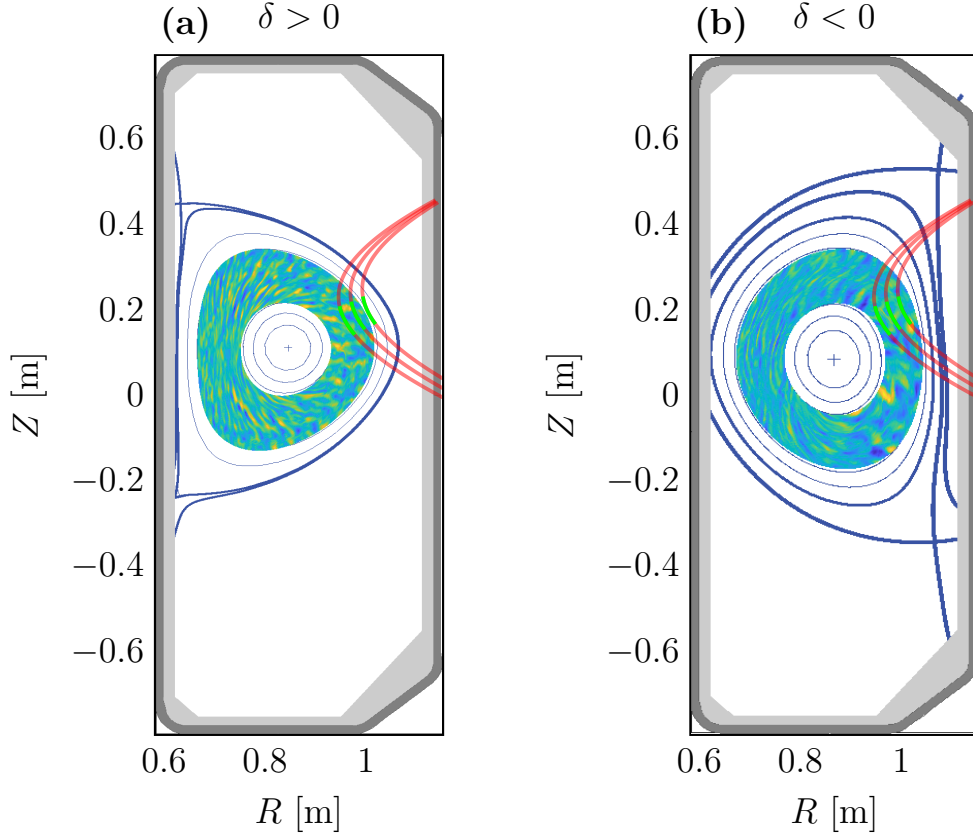
Figure 3.2 – PCI set-up in TCV: laser beam (red) divided into several rays on top of a snapshot (in the poloidal plane in a flux-tube centered around the tangency point) of electron density fluctuations generated by GENE. In the actual set-up used until now there are 9 non-equidistant rays corresponding to 9 non-equidistant detector elements. Both a positive (a) and a negative (b) triangularity scenario are shown.

In this chapter we generate electron density fluctuations for a positive and a negative triangularity TCV discharge. For a proper modelling of a TCV scenario it is necessary to consider three kinetic species in our simulations: main deuterium ions, electrons and carbon impurities. Furthermore, collisions also have to be retained while electromagnetic effects can be neglected for these TCV-relevant simulations where $\beta_e \sim 0.1\%$. Finally, we consider also an experimental magnetic geometry provided with the MHD code CHEASE [70].

Density and temperature profiles for the positive triangularity scenario #49052 and negative triangularity scenario #49051, both with an equal amount of 460 kW central ECH power, are shown in Fig. 3.3. These profiles have been generated by using the Kinetic Equilibrium Reconstruction method presented in section 2.3. As input to KER we provide the electron pressure measured by the Thomson scattering diagnostic, while the ion density is estimated from quasi-neutrality and the ion temperature is estimated using the PRETOR formula. We center the flux-tube in the GENE simulations at $\rho_{t,0} = 0.6$ (= tangency point of central ray $r = r_2$, see Fig. 2.7) where parameters
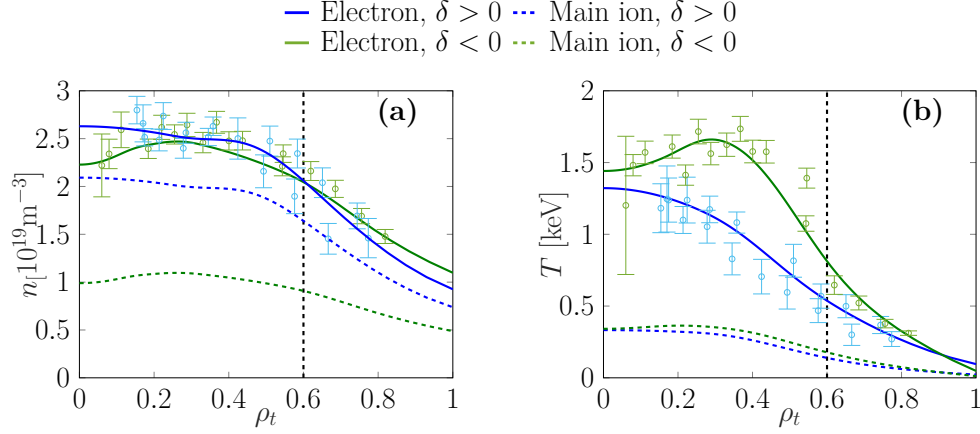
Figure 3.3 – Density (a) and temperature (b) profiles for electrons (solid lines) and ions (dashed lines) for positive (blue) and negative (green) triangularity cases.

for the two discharges are shown in Table 3.1. The triangularity at this radius is $\delta = 0.18$ for #49052 and $\delta = -0.1$ for #49051. This radial localisation corresponds to the tangency point of the PCI beam. The input parameters differ between the two scenarios as a consequence of the equal ECH heating but different transport properties. The experimental heat flux values are $Q_e = 658 \pm 70$ kW, $Q_i = 10 \pm 5$ kW for $\delta > 0$ and $Q_e = 616 \pm 70$ kW, $Q_i = 11 \pm 5$ kW for $\delta < 0$. Since for $\delta < 0$ the electron heat flux is similar to $\delta > 0$, but the electron temperature is larger, it suggests that TEMs are weaker. The stabilisation of TEMs could be due to the increased collisionality and dilution in the $\delta < 0$ case due to increased impurity density. This in turns leads to a more peaked T_e profile and thus an increased electron temperature gradient. Another explanation for the similar heat fluxes but different parameters could also be a stabilisation of ITG turbulence, also due to impurities. The contribution of ITG to Q_e would then also be lower. An increased impurity density in $\delta < 0$ is typically observed in TCV plasmas, but the reason for this effect is not yet understood. Because of this effect it is often difficult to distinguish the stabilising role of the negative triangularity equilibrium, from the stabilising effect of increased n_c.

We consider the grid $N_x \times N_y \times N_z \times N_{v_\parallel} \times N_\mu \times N_s = 256 \times 64 \times 48 \times 30 \times 16 \times 3$, where the resolutions refer to the number of discretization points along the three spatial directions (x, y, z), the two velocity space directions $(v_\parallel, \mu)$, and the number of particle species s respectively. The radial and binormal simulation box sizes are different for the two scenarios, with $L_x = 128 \, \rho_i$, $L_y = 112 \, \rho_i$ for $\delta > 0$ (ρ_i is the ion Larmor radius), and $L_x = 142 \, \rho_i$, $L_y = 152 \, \rho_i$ for $\delta < 0$ as a consequence of the different values of $\hat{s}$ and q_0. For the same number of radial and binormal wave numbers we therefore have $\max(k_y \rho_i) = 3.54$, $\max(k_x \rho_i) = 6.24$ for $\delta > 0$ and $\max(k_y \rho_i) = 2.6$, $\max(k_x \rho_i) = 5.6$ for $\delta < 0$.

Adaptive hyperdiffusivities [71] in x and y are used to simulate damping provided otherwise by small-scale modes that are not included in this simulation. All nonlinear simulations are performed for a sufficiently long time, $t_{sim} > 900$ a/c$_s$ where $c_s = \sqrt{T_e/m_i}$ is the sound speed, to

Table 3.1 – Parameters of the positive triangularity shot #49052 and negative triangularity shot #49051 (blue font and in parentheses) at $\rho_t = 0.6$ used as input to the GENE simulations, obtained from the MHD equilibrium code CHEASE [70] and species profiles shown in Fig. 3.3. The reference magnetic field is provided at the magnetic axis. The parameter a is the minor radius and R is the major radius. In bold we show important parameters undergoing a large change when changing from positive to negative triangularity.

n_e $[10^{19}\mathrm{m}^{-3}]$	2.10 (2.12)	T_i/T_e	0.26 (0.22)	q_0	**1.47 (1.21)**
T_e [keV]	0.54 (0.88)	$a/L_{n,e}$	1.48 (1.14)	$\hat{s}$	**1.44 (1.22)**
B_0 [T]	1.55 (1.50)	$a/L_{n,i}$	1.48 (1.14)	R/a	3.12 (3.17)
a [m]	0.27 (0.28)	$a/L_{T,e}$	**2.81 (3.62)**	β_e $[10^{-3}]$	0.18 (0.34)
n_i/n_e	**0.76 (0.36)**	$a/L_{T,i}$	3.75 (3.42)	ν_c $[10^{-3}]$	**0.78 (0.27)**

generate enough statistics of the density fluctuations.

For the considered parameters, we find the simulated ion and electron heat flux $Q_e = 152$ kW, $Q_i = 10$ kW for $\delta > 0$ and $Q_e = 504$ kW, $Q_i = 3$ kW for $\delta < 0$. In both cases, but especially for $\delta > 0$, we see that GK simulations that used KER to generate input profiles underestimate the experimental heat flux values. We can better understand the change in the heat fluxes by looking also at linear GENE simulations, and compute the growth rate γ and frequency ω of the most unstable mode, as shown in Fig. 3.4. For $\delta > 0$ we see TEMs ($\omega < 0$) at large scales ($k_y\rho_i < 0.6$) and ITG modes ($\omega > 0$) at smaller scales ($k_y\rho_i > 0.6$). For now we focus on the modes for $k_y\rho_i \leq 2$. If we keep the parameters (such as gradients and densities) of the $\delta > 0$ case but using the equilibrium of $\delta < 0$ we clearly stabilise both ITG and TEMs at these scales. Adding also the actual parameters of $\delta < 0$ leads to a slight increase of the TEM growth rates, due to the larger T_e and $a/L_{T,e}$. The orange line shows the stabilisation due to the increased impurity content in $\delta < 0$. For this case we kept all the parameters of $\delta > 0$, including the equilibrium, but then took the carbon impurity density n_c from the $\delta < 0$ (adjusting n_i for quasineutrality) case. This clearly stabilises both TEM and ITG modes. Finally, we yet again illustrate the stabilising role of triangularity by changing the equilibrium to $\delta > 0$ but keeping the parameters of $\delta < 0$ case, showing an increase in the growth rates.

In view of these observations we can interpret the change of the nonlinearly simulated ion heat flux going from $\delta > 0$ to $\delta < 0$. The reduction in the heat flux is due to a stabilisation of TEM and ITG modes at the considered scales, which is a combined effect of an increased impurity content and the change in the plasma shape. Q_i underestimates the experimental value for the $\delta < 0$ case, since the ITG suppression due to carbon is most likely overestimated for this case. An increased electron temperature gradient is observed for the $\delta < 0$ case, where TEMs are
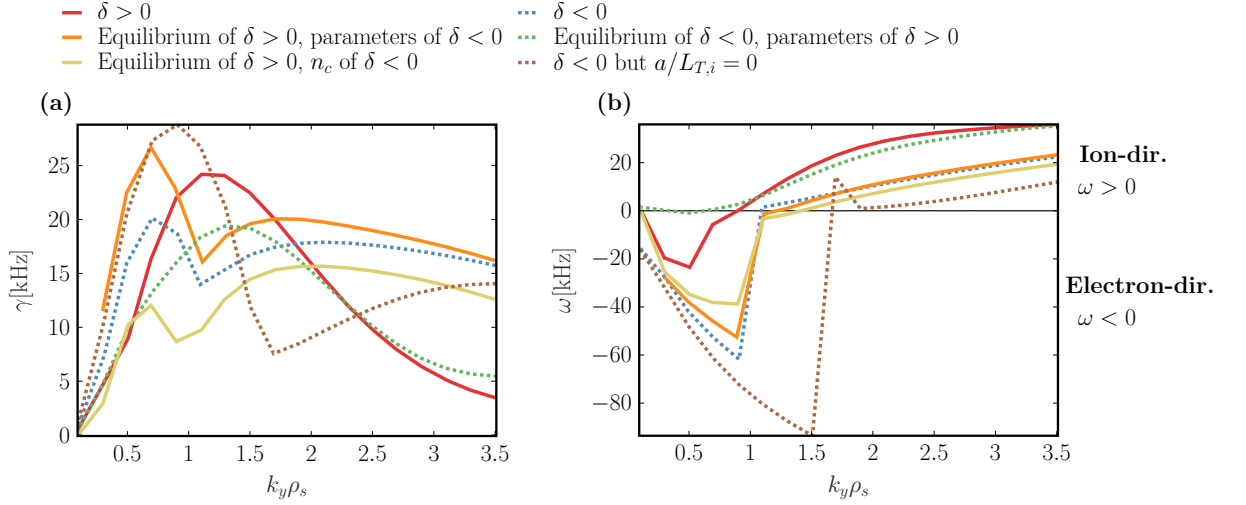
Figure 3.4 – Linear simulations illustrating at $\rho_t = 0.6$ the growth rate (a) and frequency (b) for the $\delta > 0$ case (red, TCV #49052) and $\delta < 0$ case (blue, TCV #49051). Also shown is the result (green) obtained when taking the equilibrium from $\delta < 0$ but the parameters (temperatures and densities, gradients) from $\delta > 0$. The opposite is shown in orange. Finally, we show what we obtain when we take the case of $\delta > 0$ but the carbon impurity density n_c from $\delta < 0$ (yellow) and also the case of $\delta < 0$ but with the ion temperature gradient set to 0 (brown).

stabilised by increased collisionality, reduced T_i/T_e ratio, and the negative triangularity. Better agreement with experiments could be achieved by varying input parameters within experimental error bars. This was not done in the present work where the aim of the simulations was to make a first test of the synthetic diagnostic, rather than exactly reproducing the experimental heat flux levels

Finally, in Fig. 3.4 we note that at smaller scales, above $k_y\rho_i > 2$ the effect of changing from $\delta > 0$ to $\delta < 0$ is very different, in fact the growth rates have increased substantially. Even though this mode is propagating in the ion diamagnetic direction ($\omega > 0$) this appears to be an instability of different nature than the ITG mode seen for $k_y\rho_i \leq 2$, as it appears even if the ion temperature gradient $a/L_{T,i}$ is set to zero. We did not investigate further the nature of this mode, as in the nonlinear simulations it has little effect given that the heat fluxes usually peak around γ/k_y. We confirm this in Fig. 6.12 where it is clearly seen that the main contribution to the density fluctuations, apart from the zonal flow $k_y = 0$ component, is for $k_y\rho_i < 1$ while for larger scales there is a cascade in k_y of decreasing fluctuation amplitude.

Electron density fluctuations obtained from nonlinear GENE simulations are post-processed with a synthetic diagnostic to model measurements from TPCI as discussed in the next section.
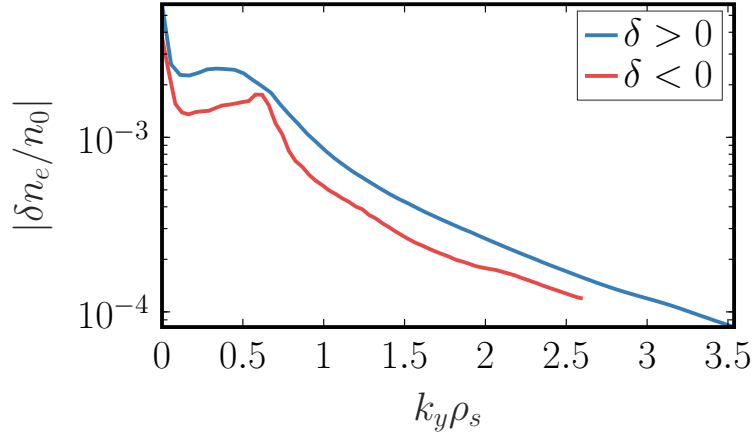
Figure 3.5 – k_y spectra, averaged over all k_x and z, of the electron density fluctuations simulated with nonlinear GENE simulations. In blue is the $\delta > 0$ case, while in red is the case with $\delta < 0$.

3.2.1 Generating the synthetic signals

The synthetic diagnostic aims to model the intensity of the electron density fluctuations measured by the square-law detectors. As described in section 2.1, the measured fluctuating intensity originates from an incident laser beam field that is scattered by the electron density fluctuations. Let $E_{p0}(r, p)$ represent the distribution of the incident laser field. The coordinates r and p represent the Cartesian space perpendicular to the laser beam propagation direction, k_0, and are introduced in Fig. 3.6. After scattering, the laser beam field is focused onto the focal plane where a phase plate is used to create the phase contrast between scattered and unscattered components. A spatial filter is also used for longitudinal localisation of the PCI signal and to select the measured wave-vector direction. The action of the phase plate and the spatial filter can be described with the transfer function T that acts on the scattered laser beam field $P_a E_{p0}(1 + \delta\varphi)$ through the circular convolution operator $\circ$: $[T \circ (P_a E_{p0}(1 + \delta\varphi))](r, p)$. Here $P_a(r, p)$ represents the effect of the aperture that is the most restrictive optical component limiting the perpendicular size of the laser beam to size, a, of the aperture. To first order in the fluctuating phase, $\delta\varphi$, the measured fluctuating intensity can then be written as [24]

$$
\begin{aligned}
\tilde{\mathscr{E}}(Mr, Mp, t) &= \frac{c}{4\pi M^2} \mathrm{Im}\left\{[T \circ (P_a E_{p0})](r, p) \times \right.\\
&\quad \left. [T \circ (P_a E_{p0} \delta\varphi)]^*(r, p, t - t_d)\right\} = \\
&\frac{c}{4\pi M^2} r_e \lambda_0 \int_L \mathrm{d}\ell \, \mathrm{Im}\left\{[T \circ (P_a E_{p0})](r, p) \times \right.\\
&\quad \left. [T \circ (P_a E_{p0} \delta n_e)]^*(r, p, t - t_d)\right\}
\end{aligned}
\tag{3.24}
$$

where we made use of Eq. (2.1). The intensity is evaluated at the coordinates (Mr, Mp) in the detector plane that corresponds to the coordinates (r, p) in the object plane. Here M is the aggregate magnification of the optical set-up.

We implement Eq. (3.24) in subsection 3.2.1 taking into account a finite aperture, $P_a(r, p)$, and a Gaussian distribution of the incident laser field, $E_{p0}(r, p)$. While this gives the most proper estimate of the PCI signals, in this approach it is difficult to see the contribution from individual GENE k_x and k_y modes to the PCI signals. It is more insightful to write the synthetic signals directly in terms of their GENE k_x and k_y contributions, as presented in subsection 3.2.1. To make it computationally efficient, in this approach we simplify, by assuming the aperture a to be infinite and describing the incident laser beam as a plane wave. Further simplifications are made thanks to the separation of scales, with the beam diameter being larger than the size of a typical turbulence eddy which in turn is larger compared to the size of the detector elements. As will be shown in the end of subsection 3.2.1, these simplifications do not alter the main signatures of the synthetic signal, yet the approach reveals useful information on the role of different k_x and k_y modes.

The time delay t_d in Eq. (3.24), between the scattering event and the measurement in the detection plane, can for the parameters we consider be treated as a constant and will therefore henceforth be omitted.

Gaussian beam and finite aperture

We consider the proper case first, and describe the laser beam E_{p0} with a Gaussian

$$E_{p0}(r, p) = \left(\frac{8\pi}{c}P\right)^{1/2} \left(\frac{2}{\pi}\right) \frac{1}{w_0} e^{-\left(\frac{r^2+p^2}{w_0^2}\right)}, \tag{3.25}$$

where P is the total beam power, and w_0 is the $1/e$ half-width of the laser beam. The Gaussian field is truncated by the pupil function P_a

$$P_a(r, p) = \begin{cases} 1, & \text{if } \sqrt{r^2 + p^2} \leq a \\ 0, & \text{otherwise.} \end{cases} \tag{3.26}$$

Here a is the radius of the most restrictive optical component in the laser beam path and is normally of the order of the laser beam half-width, $a \sim w_0$.

From the gyrokinetic GENE simulations we have obtained the electron density fluctuations $\delta n_e(x, y, z)$ inside a flux-tube, centred around the radial position $\rho_0 = 0.6$, the laser beam being tangent to the corresponding magnetic surface. These density fluctuations have to be interpolated onto a coordinate system aligned with the PCI laser beam before we can conveniently compute the measured intensity in the detector plane, given by Eq. 3.24, and compute the synthetic signals.

To compute the synthetic PCI signal we represent the laser beam in the Cartesian coordinate system e_r, e_p, e_ℓ where ℓ is the coordinate along the beam direction while r, p represent the two coordinates perpendicular to the beam, as shown in Fig. 3.6.
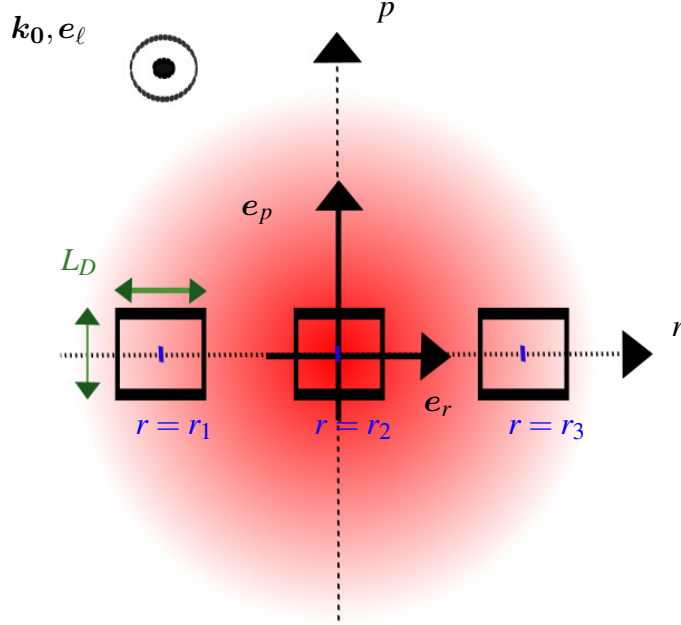
Figure 3.6 – Cartesian coordinate system composed of the vectors e_r, e_p perpendicular to the beam and e_ℓ aligned with the PCI laser beam propagation direction k_0. A detector element i occupies a subvolume that is centered at $r = r_i, p = 0$. In this case we show three detector elements, thus $i = 1, 2, 3$. The detector elements are square with side L_D.

From the equilibrium generated by CHEASE, we may transform the detector coordinates r, p, ℓ to the magnetic coordinates $\chi(r, p, \ell), \phi(r, p, \ell), \rho_t(r, p, \ell)$ as well as compute the safety factor, $q(r, p, \ell)$ which then through Eq. (3.11) can be transformed to the field-aligned GENE coordinates $x(r, p, \ell), y(r, p, \ell), z(r, p, \ell)$. We then interpolate the electron density fluctuations generated by GENE to obtain the fluctuations $\delta n_e(x(r, p, \ell), y(r, p, \ell), z(r, p, \ell))$ within the laser beam.

The next step is to apply the effect of the phase plate to obtain the phase contrast between scattered and unscattered components. As discussed in section 2.1, the phase plate is placed in the focal plane where it introduces a 90° phase change to components of the laser beam passing through a central groove. In Fourier k_r, k_p space the phase plate can be described with the function

$$\hat{T}_G = 1 + P_{k_c}(k_r, k_p)\left(i\sqrt{\rho} - 1\right), \tag{3.27}$$

where the pupil function P_{k_c} is given by Eq. (3.26) and $\rho \leq 1$ is the power transmissivity that enhances the contrast by attenuating the unscattered component of the beam. The hat is used to indicate that we now consider the Fourier transform of the real space transfer function T appearing in Eq. (3.24). The cut-off wave number, $k_c = k_0 v / F$, is related to the half-width of the groove, v, which is of the order of the diffraction half-spot of the unscattered component. The role of $\hat{T}_G$ for calculating the intensity in Eq. (3.24) can be understood with the help of the Fourier-transforming property of lenses. A lens placed after the object is used to focus scattered and unscattered components of the laser beam onto the phase plate. The unscattered component
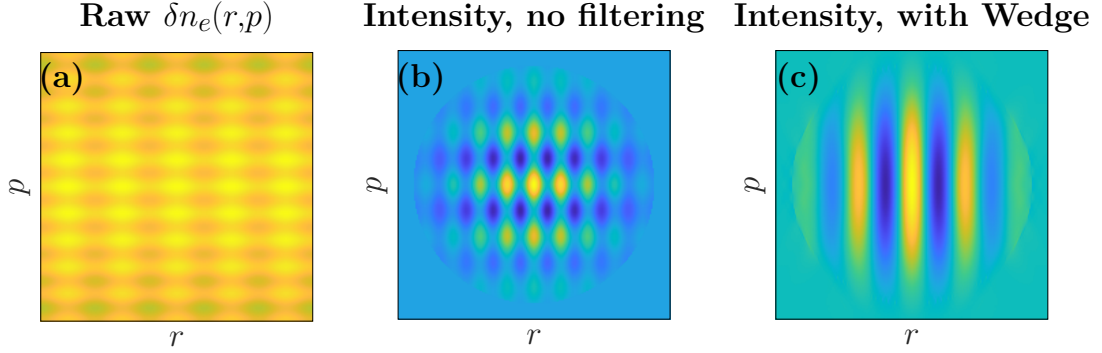
Figure 3.7 – An artificial electron density fluctuation composed of three fluctuation components (a), the corresponding intensity calculated with Eq. (3.24) when applying the effect of a phase plate (b) and the intensity when also including a wedge filter (c). The filters are represented in wave-number space (k_r, k_p) but could equally be represented in real space (r, p), where they would have the same shape.

is given by the term $P_a E_{p0}$ in Eq. (3.24) whose field distribution in the focal plane is proportional to $\mathscr{F}[P_a E_{p0}](k_r, k_p)$, where $\mathscr{F}[\cdot](k_r, k_p)$ denotes the spatial Fourier transform. Correspondingly, the distribution in the focal plane of the scattered part of the beam, which is affected by the electron density fluctuations, is proportional to $\mathscr{F}[P_a E_{p0} \delta n_e](k_r, k_p)$. The effect of the phase plate can thus be written as a simple multiplication of both scattered and unscattered components with $\hat{T}_G$. In real space this operation is represented as a convolution, as written in Eq. (3.24).

We demonstrate the effect of the phase plate on an artificial density fluctuation composed of three fluctuating components, $\delta n_e(r, p) = 10\cos(0.25 k_c p) + \cos(10 k_c p) + \cos(5 k_c r)$ as illustrated in the leftmost plot in Fig. 3.7. When applying $\hat{T}_G$ the part of the density fluctuation with $k < k_c$ that scatters the laser beam into the groove, is filtered out, while the remaining components lead to a measurable intensity, as shown in the central plot in Fig. 3.7. The reduction of the fluctuation amplitude towards the borders is a consequence of the Gaussian form of the incident laser beam, while the circular cut is due to the Pupil function P_a

Given the actual density fluctuations generated by GENE, $\delta n_e(x(r, p, \ell), y(r, p, \ell), z(r, p, \ell))$, the scattered and unscattered field distributions are calculated using the Fourier transform, before applying Eq. (3.27), transforming back to real space and finally evaluating the intensity through Eq. (3.24).

In addition to the phase plate, in this work we include the effect of a spatial filter that is also placed in the focal plane. As discussed in section 2.1 such a spatial filter can be used to restrict the wave vectors that contribute to the PCI signals. If we assume that the measured wave vector satisfies $k \parallel k_0 \times \mathbf{B}$ and this direction varies along the laser beam, each wave vector direction translates to a specific position ℓ along the beam. The spatial filter therefore selects both which wave vector directions contribute to the PCI signal, and where in the plasma the signal is coming

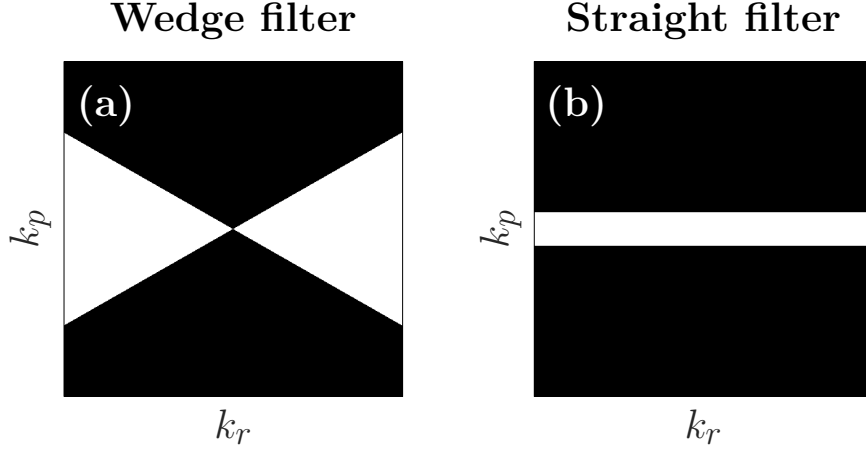## Wedge filter   Straight filter

Figure 3.8 – The wedge (a) and straight (b) configurations used for spatial filtering in the PCI set-up. Fluctuations that scatter the laser light onto the filter domain (white colors) contributes to the PCI signals while other components are strongly damped (black).

from. Our goal now is to derive the selection rules naturally by performing the line integration directly, i.e., by implementing a truly faithful synthetic diagnostic.

We will consider two different spatial filtering configurations, the wedge and the straight filter, which are alternately used in the PCI set-up. Similarly to the phase plate, the action of the spatial filter is included through a multiplication of the field distribution of unscattered and scattered components in Fourier space, with a mask function. In the case of a straight filter only the part of the focal spot falling inside the width $\pm k_S$, of the filter contributes to the PCI signals. Thus k_S is the upper cut-off wave number in this filter configuration. The straight filter can in Fourier space be represented with the mask function

$$\hat{T}_S(k_r, k_p) = \begin{cases} 1, & \text{if } |k_p| \leq k_S \\ 0, & \text{otherwise.} \end{cases} \tag{3.28}$$

An example of the straight filter is shown on the right-hand side of Fig. 3.8. Optimal localisation is achieved when k_S is minimum, and thus equal to k_c. Since the measured wave-vector rotates along the laser beam path, the straight filter configuration thus leads to an optimal localisation for each wave number $|\boldsymbol{k}_{\perp,0}|$. Fluctuations with larger $|\boldsymbol{k}_{\perp,0}|$ fall more quickly outside the filter domain and are therefore more localised. The filter therefore leads to a non-uniform localisation of the fluctuation contributions.

The wedge filter configuration instead provides a uniform localisation by including any contribution falling inside a wedge, with a wedge half angle θ_W. In this case the mask function is given

by

$$\hat{T}_W(k_r, k_p) = \begin{cases} 1, & \text{if } \left| k_r / \sqrt{k_r^2 + k_p^2} \right| \geq \cos \theta_W \\ 0, & \text{otherwise.} \end{cases} \tag{3.29}$$

Similarly as for the straight filter configuration, the smallest wedge half angle is limited by diffraction. From the illustration of the wedge filter in Fig. 3.8 we see that a given $|\boldsymbol{k}_{\perp,0}|$ stays within the filter over a larger angle and thus over a larger portion of the laser beam. The wedge filter thus provides uniform localisation for each $|\boldsymbol{k}_{\perp,0}|$ that falls inside the filter. In this fashion, this filtering choice retains the strict imaging properties of the technique. In this case the localisation will be limited by the smallest $|\boldsymbol{k}_{\perp,0}|$ that is included in the measurement, and thus this leads to a worse localisation compared to the straight filter case that optimises the integration length for each $|\boldsymbol{k}_{\perp,0}|$.

Notice that the straight and wedge filters in Fig. 3.8 are represented in wave-number space (k_r, k_p). They could equally well be represented in real space r, p on a focal plane, where they would have the same shape.

Both filter configurations are aligned along $\boldsymbol{e}_r$, meaning that any rotation of the filter necessarily involves a corresponding rotation of the image and consequently, the detector elements. The direction of $\boldsymbol{e}_r$ can thus be used to select the preferential (k_x, k_y) components. Normally we choose $\boldsymbol{e}_r \parallel \nabla x(\ell = \ell_{\text{tangency}})$ where ℓ_{tangency} is the position along the laser beam where it is tangent to the magnetic surface, which corresponds to the point in Fig. 2.7 where the derivative $\mathrm{d}\rho_t/\mathrm{d}\ell$ goes to zero. The effect of the spatial filter, in this case the wedge filter, is illustrated in the rightmost plot in Fig. 3.7. It filters out the high k component of the artificial density fluctuation, propagating purely in the $\boldsymbol{e}_p$ direction. After applying both the phase plate groove and the spatial filter the remaining part of the artificial density fluctuation is the component $\cos(5k_c r)$ that scatters the laser beam both outside the phase plate groove, and within the spatial filter.

The total effect of the phase plate and spatial filters is thus given by a multiplication of scattered and unscattered field distributions in the focal plane with the total transfer function. In the case of the straight filter configuration it is $\hat{T} = \hat{T}_G \hat{T}_S$ and $\hat{T} = \hat{T}_G \hat{T}_W$ in the case of the wedge filter configuration.

Finally, to obtain the synthetic PCI signals we have to average over the detector area. The synthetic signal for a given detector element, i centred at $r = r_i$ and $p = 0$ (as illustrated in Fig. 3.6)) is given by

$$\langle I \rangle (r_i, t) = \int_{-L_D/2 + r_i}^{L_D/2 + r_i} \int_{-L_D/2}^{L_D/2} \mathrm{d}r \, \mathrm{d}p \, \tilde{\mathscr{E}}(Mr, Mp, t), \tag{3.30}$$

where L_D is the square length of the detector elements as is illustrated in n Fig. 3.6.

Synthetic PCI signal in terms of GENE k_x and k_y modes

The procedure described in the previous subsection gives the most proper estimate of the PCI signals. However, starting from the point when we computed the electron density fluctuations on the Cartesian grid, $\delta n_e(r, p, \ell, t)$, we lost track of how the different k_x and k_y GENE fluctuation components individually contribute to the PCI signals. Of course, it is possible to retrieve this information by artificially modifying the input GENE fluctuations when calculating Eq. (3.24) (for example by removing all but one k_x, k_y component, and then repeating the procedure for all k_x and k_y values), however it is more convenient and insightful to directly write the synthetic signal in terms of the GENE k_x and k_y modes.

To make this computationally efficient, we make several simplifications. First, instead of a Gaussian we assume the incident beam to be an infinite plane wave, and thus equal to a constant, $E_{p0}(r, p) = E_{p0}$. The aperture is also assumed to be infinite. In this case the measured intensity in Eq. (3.24) can be rewritten as [24]

$$\tilde{\mathscr{E}}(Mr, Mp, t) = \frac{\sqrt{\rho} c E_{p0}^2}{4\pi M^2} r_e \lambda_0 \int_L d\ell \left[T \circ \delta n_e\right](r, p, t), \tag{3.31}$$

where the transfer function T here is slightly different from T appearing in Eq. (3.24).

Consider then the electron density fluctuations represented as a Fourier sum with respect to time and summed over the radial k_x and binormal k_y GENE components

$$\delta n_e(r, p, \ell, t) = \sum_{k_x} \sum_{k_y} \delta n_e(t, k_x, k_y, z(r, p, \ell), t)$$
$$\times e^{i k_x x(r, p, \ell) + i k_y y(r, p, \ell)}, \tag{3.32}$$

such that the intensity, Eq. (3.31), averaged over each detector element i is given by

$$\langle I \rangle (r_i, t) = \frac{\sqrt{\rho} c E_{p0}^2}{4\pi M^2} r_e \lambda_0 \int_L d\ell \int_{-L_D/2 + r_i}^{L_D/2 + r_i} \int_{-L_D/2}^{L_D/2} dr\, dp$$
$$\times \sum_{k_x} \sum_{k_y} \hat{G}(k_r(k_x, k_y, r, p, \ell), k_p(k_x, k_y, r, p, \ell))$$
$$\times \delta n_e(k_x, k_y, z(r, p, \ell), t) e^{i k_x x(r, p, \ell) + i k_y y(r, p, \ell)}. \tag{3.33}$$

Here we have introduced the function $\hat{G}$ that is related to the Fourier transform of $T(r, p)$ appearing in Eq. (3.31) but contains the necessary terms to make the coordinate transformation from (r, p, ℓ) to (x, y, z), valid. A proof on the existence of such a function is given in Appendix A. In the following we will actually not explicitly compute $\hat{G}$ by defining $T(r, p)$. Instead we directly choose $\hat{G}$ such that it correctly captures the effect of the various filters on a given k_x and k_y mode.

To simplify further we assume that the Fourier amplitudes of the fluctuations are constant across the transverse width of the detectors, e.g $\delta n_e(k_x, k_y, z(r, p, l), t) \sim \delta n_e(k_x, k_y, z(r_i, 0, \ell), t) \equiv$

$\delta n_e(k_x, k_y, z(r_i, \ell), t)$. Furthermore we expand the phase term such that

$$k_x x(r, p, \ell) + k_y y(r, p, \ell) \sim k_x x(r_i, 0, \ell) + k_y y(r_i, 0, \ell) + r k_r(r_i, 0, \ell, k_x, k_y) +$$
$$p k_p(r_i, 0, \ell, k_x, k_y) \equiv k_x x(r_i, \ell) + k_y y(r_i, \ell) + r k_r(r_i, \ell, k_x, k_y) + p k_p(r_i, \ell, k_x, k_y), \quad (3.34)$$

meaning that we regard the detector volumes as one dimensional rays. Both these simplifications are justified since the size of the detector elements (in the object plane, thus L_D is magnified by the magnification $1/M$) are very small compared to the typical size of a turbulence structure. In the end of this subsection we verify that indeed, after these simplifications, the synthetic signals retains the main signatures that are obtained in the proper case, subsection 3.2.1.

The wave numbers k_r and k_p appearing here are computed for each GENE wave number, k_x and k_y, and for every position along the laser beam. For a given k_x and k_y, the wave numbers k_r and k_p are computed using $k_r(r_i, \ell, k_x, k_y) = \boldsymbol{k}_{\perp,B}(r_i, \ell, k_x, k_y) \cdot \boldsymbol{e}_r$ and $k_p(r_i, \ell, k_x, k_y) = \boldsymbol{k}_{\perp,B}(r_i, \ell, k_x, k_y) \cdot \boldsymbol{e}_p$. The full wave vector is $\boldsymbol{k}_{\perp,B}(r_i, \ell, k_x, k_y) = k_x \nabla x(r_i, \ell) + k_y \nabla y(r_i, \ell)$ where the radial $\nabla x(r_i, \ell)$ and binormal $\nabla y(r_i, \ell)$ unit vectors for the GENE coordinates are evaluated at every position r_i, ℓ along the laser beam. The wave vector is then projected onto the unit vectors $\boldsymbol{e}_r$ and $\boldsymbol{e}_p$ in the r and p directions respectively. Unlike Eq. (3.30) the intensity in Eq. (3.33) thus only includes the wave numbers k_r and k_p that correspond to a mode k_x and k_y that actually exists in the GENE simulation. Henceforth, the dependence of k_r and k_p on k_x, k_y, r_i and ℓ is assumed, and therefore omitted in writing to simplify the notation.

Eq. (3.33) can thus be written as

$$\langle I \rangle (r_i, t) =$$
$$\frac{\sqrt{\rho} c E_{p0}^2}{4\pi} r_e \lambda_0 \int_L \mathrm{d}\ell \sum_{k_x} \sum_{k_y} \hat{G}(k_r, k_p) \mathscr{T}_{\mathrm{av}}(k_r, k_p) \delta n_e(k_x, k_y, z(r_i, \ell), t) e^{i k_x x(r_i, \ell) + i k_y y(r_i, \ell)}, \quad (3.35)$$

where the function $\mathscr{T}_{\mathrm{av}}(k_r, k_p)$ takes into account the effect of averaging the measured intensity over the detector area. It is derived from the integration of the intensity over the detector area and is given by

$$\mathscr{T}_{\mathrm{av}}(k_r, k_p) = \frac{4M^2}{L_D^2 k_r k_p} \sin\left(k_r \frac{L_D}{2M}\right) \sin\left(k_p \frac{L_D}{2M}\right). \quad (3.36)$$

Just as in the previous subsection, the transfer function $\hat{G}(k_r, k_p)$ contains the combined effect of the phase plate and spatial filters and is given by $\hat{G}(k_r, k_p) = \hat{G}_G \hat{G}_W$ for the wedge filter case and $\hat{G}(k_r, k_p) = \hat{G}_G \hat{G}_S$ for the straight filter case. The transfer function of the spatial filters, $\hat{G}_S$ and $\hat{G}_W$ are the same as T_S and T_W defined earlier, given by Eq. (3.29) and Eq. (3.28) respectively.
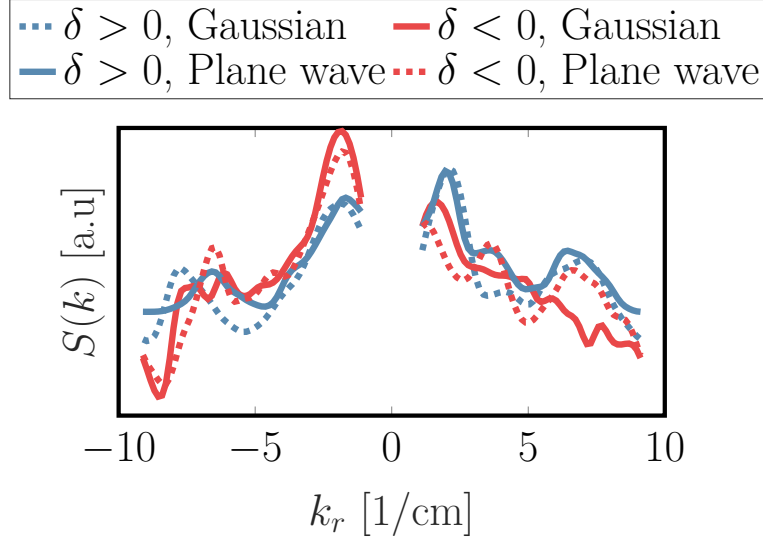
Figure 3.9 – Comparison of the wave-number spectrum when using either the proper approach with a Gaussian laser beam (solid lines) with the simplified approach of a plane wave (dashed lines). We show the comparison for both positive (blue) and negative (red) triangularities.

The phase plate, however, is in this case described by the mask function, $\hat{G}_G$, given by

$$\hat{G}_G(k_r, k_p) = \begin{cases} 1, & \text{if } \sqrt{k_r^2 + k_p^2} \geq k_c \\ 0, & \text{otherwise.} \end{cases} \tag{3.37}$$

To verify the assumptions and approximations made in this subsection we compare the wave number spectrum calculated for the synthetic signals when considering the proper synthetic signals, computed using the approach in subsection 3.2.1, with the simplified approach described in this subsection. We consider δn_e generated for the positive and negative triangularity cases, using the parameters shown in Table 3.1. The result, shown in Fig. 3.9, demonstrates that the simplified approach is able to reproduce the main trends of the synthetic signals: in particular, the asymmetry in the amplitudes of fluctuations propagating with $k_r > 0$ and $k_r < 0$, for both positive and negative triangularity cases. Henceforth we will rely on the results obtained using the simplified approach only, which allows us to study the contribution of each k_x, k_y GENE fluctuation to the synthetic signals. Since we are mainly interested in reproducing the relative amplitudes of the fluctuations we have chosen E_{p0} in the plane wave approximation Eq. (3.35) to obtain similar amplitudes to the Gaussian beam case.

As pointed out in subsection 2.1, the consequence of selecting the wave vector directions is also a reduction in the integration length. Under the assumption that the measured wave vector satisfies $\boldsymbol{k}_{\text{meas}} \parallel \boldsymbol{k}_0 \times \mathbf{B}$, each of the fluctuation components $\delta n_e(k_x, k_y, z(r_i, \ell))$ is a delta function, which is non-zero only at the point $\ell = \ell_\perp$ where that (k_x, k_y) component is perpendicular to the laser beam.

If we set θ equal to the fast varying phase in Eq. (3.32), $\theta(k_x, k_y, r_i, \ell) = k_x x(r_i, \ell) + k_y y(r_i, \ell)$, we define $\ell_\perp$ such that

$$\left. \frac{\partial \theta(k_x, k_y, r_i, \ell)}{\partial \ell} \right|_{\ell=\ell_\perp} = k_x \left. \frac{\partial x(r_i, \ell)}{\partial \ell} \right|_{\ell=\ell_\perp} + k_y \left. \frac{\partial y(r_i, \ell)}{\partial \ell} \right|_{\ell=\ell_\perp}$$

$$= (k_x \nabla x(r_i, \ell) + k_y \nabla y(r_i, \ell)) \cdot \boldsymbol{e}_\ell \Big|_{\ell=\ell_\perp} \quad \boldsymbol{k}_\perp \cdot \boldsymbol{e}_\ell \Big|_{\ell=\ell_\perp} = 0. \quad (3.38)$$

For purely radial modes with $k_y = 0$ this position is at the tangency point, $\ell_\perp = \ell_{\text{tangency}}$ as illustrated in Fig. 2.7. At a given point ℓ along the laser beam we therefore have contributions from all (k_x, k_y) modes that satisfy $k_x \nabla x(r, \ell) + k_y \nabla y(r, \ell) \parallel \boldsymbol{k}_0 \times \mathbf{B}$. When the filter axis is along the radial direction at the tangency point, wave vectors that are mostly radial will contribute to the PCI signal, meaning that the contribution to the integral in Eq. (2.1) should mainly come from a small segment near the tangency point. In the next subsection we will ignore the assumption $\boldsymbol{k}_{\text{meas}} \parallel \boldsymbol{k}_0 \times \mathbf{B}$ and seek to rederive it directly, by estimating the "true" integration length we obtain and its relation to the dominant k_x, k_y components in the PCI signals.

3.2.2 Localisation of the synthetic signals

When computing the localisation of the PCI signals we will rely on the simplified approach for computing the synthetic signals, described in subsection 3.2.1. This will allow us to study the localisation and the contribution of each individual GENE k_x and k_y fluctuation components and thus see the effect of the geometrical mode structure of the various contributions.

Localisation relies on the two criteria, $\mathbf{k}_{\text{meas}} \perp \mathbf{B}$ and $\mathbf{k}_{\text{meas}} \perp \mathbf{k}_0$. The criterion $\mathbf{k}_{\text{meas}} \perp \mathbf{B}$ is already a built-in assumption in gyrokinetics and can be verified by noting that the variation along the parallel direction is much slower compared to the variation across a field line $\mathrm{d}\ln \delta n_e / \mathrm{d}z \ll \mathrm{d}\ln \delta n_e / \mathrm{d}x \sim \mathrm{d}\ln \delta n_e / \mathrm{d}y$. By representing the fluctuations in terms of their k_x and k_y wave numbers we therefore automatically consider fluctuations that satisfy $\mathbf{k}_{\text{meas}} = \mathbf{k}_{\perp,\mathbf{B}} \perp \mathbf{B}$. The wave vector perpendicular to the magnetic field, for every k_x and k_y, is given by

$$\boldsymbol{k}_{\perp,B}(\ell, r) = \nabla x(\ell, r) k_{x,\text{eff}}(\ell, r) + k_y C_y (q_0 \nabla \chi(\ell, r) - \nabla \phi(\ell, r)), \quad (3.39)$$

where the effective radial wave number is $k_{x,\text{eff}}(\ell, r) = k_x + \chi(\ell) \hat{s} k_y$ and where the dependence on χ shows how the radial wave number increases as we move in the poloidal direction, due to the magnetic shear. This wave vector is a function of the coordinate along the beam due to the gradients, $\nabla x(\ell)$ and $\nabla y(\ell)$. Notice that $\boldsymbol{k}_{\perp,B}(\ell)$ is everywhere continuous while $\nabla y(\ell)$ has a jump once we cross the inner midplane. This is again a consequence of the parallel boundary conditions and the connection of the k_x modes, since the jumps in ∇y and k_x cancel.

The second property that the measured fluctuations have to satisfy in order to contribute to the PCI signals is $\mathbf{k}_{\text{meas}} \perp \mathbf{k}_0$, and is a consequence of the line averaging. Away from $\ell = \ell_\perp$ a given k_x, k_y mode generates a large component along $\boldsymbol{k}_0$ and is therefore averaged over once we carry

out the integration. This implies that the integral over the whole laser beam path L in Eq. 3.31 can be replaced by an integral over a shorter segment, $\Delta L_{k_x,k_y} < L$, centred at $\ell = \ell_\perp$, provided that the rest term is small compared to the contribution around $\ell = \ell_\perp$. This property should be satisfied in a *statistical sense* such that the analysis of the PCI signals does not change when we integrate over the shorter segment. Since the analysis of the PCI signals is often performed by computing the Power-Spectral Density (PSD) we aim to find $\Delta L_{k_x,k_y}$ that preserves the PSD. We therefore compute the PSD of the cumulative integral around $\ell = \ell_\perp$ and sum over the frequency components to estimate the total power contribution from a given segment of length $\Delta L_{k_x,k_y}$

$$S_{k_x,k_y}(r_i,\Delta L) =$$
$$\left(\frac{\sqrt{\rho}cE_{p0}^2}{4\pi}r_e\lambda_0 M^2\right)^2 \times \sum_f \left|\int_{\ell_\perp(k_x,k_y)-\Delta L/2}^{\ell_\perp(k_x,k_y)+\Delta L/2} \mathrm{d}\ell \hat{G}\mathscr{T}_{\mathrm{av}}\delta n_{e_{k_x,k_y}}(z(r_i,\ell),f)\right|^2 \tag{3.40}$$

where

$$n_{e_{k_x,k_y}}(z(r_i,\ell),f) = \delta n_e(k_x,k_y,z(r_i,\ell),f)e^{ik_xx(r_i,\ell)+ik_yy(r_i,\ell)}$$

and where we have carried out a Fourier transform over the relevant frequencies f of the density fluctuations. In this case we consider f between 10 and 300 kHz which has been commonly used when analysing the PCI signals in this work.

In Eq. (3.40) $\Delta L_{k_x,k_y}$ is defined such that, when the integral is calculated over the segment $\Delta L_{k_x,k_y}$, the PSD is preserved, implying that for larger integration lengths, $\Delta L > \Delta L_{k_x,k_y}$, the value of $S_{k_x,k_y}(\Delta L)$ should not change. We therefore define

$$\Delta L_{k_x,k_y} = \min(\Delta L):$$
$$\left|\frac{S_{k_x,k_y}(\Delta L_{k_x,ky})}{S_{k_x,k_y}(\Delta L)} - 1\right|^2 \leq \varepsilon \ \forall \ \Delta L \geq \Delta L_{k_x,k_y}, \tag{3.41}$$

where $\varepsilon = 0.1$, meaning that the reduced segment, with length $\Delta L_{k_x,k_y}$, includes at least 90% of the total signal power. Note that $\Delta L_{k_x,k_y}$ will be different for modes with different propagation directions, and should therefore be evaluated for each k_x and k_y mode (thereof the k_x, k_y subscript). Note that $\Delta L_{k_x,k_y}$ in Eq. (3.41) will include both the effect of localisation due to line averaging, and due to the selection done by the spatial filters. To illustrate this method we take as an example a $k_x = k_{x0}$ component of a purely radial $k_y = 0$ mode. A snapshot of the PCI signal from this component is shown in the top plot in Fig. 3.10, with and without applying a straight filter. The considered component is perpendicular to the PCI laser beam at the tangency point, $\ell_\perp \approx 0.3$ m. When evaluating Eq. (3.40) for this case we obtain the result in the bottom plot in Fig 3.10. The straight thick lines in both plot shows the chosen integration length. It is clearly seen how the narrow straight filter suppresses the considered fluctuation component once its wave vector falls outside the filter, leading to a much more localised measurement. For a general PCI geometry we might have multiple values of $\ell_\perp$ and therefore potentially multiple localised segments that should be taken into account when we carry out the integration. In this case we compute a value
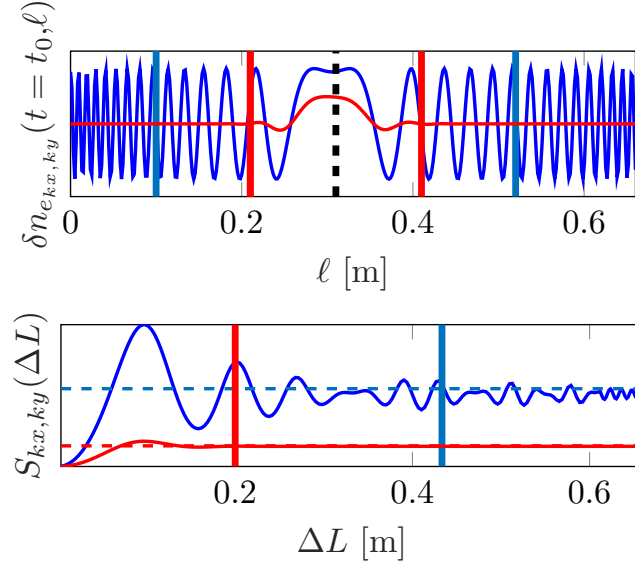
Figure 3.10 – On the top: Electron density fluctuation, along the central chord of the PCI beam ($r_i = r_0$) for a purely radial electron density fluctuation component $k_x = k_{x,0} \neq 0, k_y = 0$ without applying any filter (blue) and with a straight filter (red). The black dashed line indicates the $\ell_\perp$ point and the solid line for each component shows the calculated integration length. On the bottom: the result from Eq. (3.40) for both cases.

of $\Delta L_{k_x,k_y}$ separately for each segment by centering the integration interval in Eq. (3.40) around each $\ell_\perp$. In this subsection we will focus on the localisation of the PCI signals in TCV, where we only have a single segment. The case of multiple $\ell_\perp$ values will be discussed in detail later in chapter 6 where we will look at the PCI geometry proposed for JT-60SA.

We will carry out the analysis of the localisation for the central PCI ray only, with $r_i = r_0$, since other rays will lead to similar results. In the following it is assumed that all quantities are evaluated at $r_i = r_0$ and we henceforth omit writing this variable to simplify the notation. We focus the analysis of the localisation properties for TCV on the positive triangularity case, and in the end we make a comparison with results for the negative triangularity case.

There are three different features of the density fluctuation in Eq. (3.32) that can have an effect on the localisation. The most important is localisation due to the geometrical structure of a k_x and k_y mode. To study this we assume that he electron density fluctuation takes the form

$$\delta n_e(\ell)_{k_x,k_y} = e^{i(k_x x(\ell) + k_y y(\ell))} = e^{i\theta(k_x,k_y,\ell)} \tag{3.42}$$

with constant fluctuation amplitude along the laser beam. The subscript indicates that we now consider just one k_x, k_y fluctuating component. The fluctuation in this case is independent of time and the PSD in the analysis of the localisation can therefore be replaced by just evaluating the absolute value of the line integrated fluctuations. Fluctuations of the form described by Eq. (3.42)

have been the basic assumption in the past when making estimates of the PCI localisation [21, 34, 72]. The result in this case can be compared with an estimate of the integration length which is derived by performing a second order Taylor expansion of the fast-varying phase θ around the tangency point $\ell_\perp$

$$\theta(k_x, k_y, \ell) \sim \theta(k_x, k_y, \ell_\perp) + \frac{1}{2} \left. \frac{\partial^2 \theta(k_x, k_y, \ell)}{\partial \ell^2} \right|_{\ell = \ell_\perp} (l_\perp - l)^2,$$

where we used Eq. (3.38) to remove the first order derivative. For some constant C we thus find

$$\Delta L_{k_x, k_y} \sim \sqrt{2C \Big/ \left| \partial^2 \theta(k_x, k_y, \ell) \Big/ \partial \ell^2 \right|_{\ell = \ell_\perp}}. \tag{3.43}$$

The value of C is chosen such that $\Delta L_{k_x, k_y}$ calculated through Eq. (3.43) matches Eq. (3.41) at low $k_\perp \sim 1 \text{ cm}^{-1}$.

In addition to the geometrical structure described by the fast varying phase in Eq. (3.42) there are two more features of the fluctuations that have to be taken into account for a proper estimate of the localisation. The first is the effect of the phase of the complex Fourier amplitudes, $\hat{\theta}(k_x, k_y, \ell, t)$, which can be defined from the relation

$$e^{i\hat{\theta}(k_x, k_y, \ell, t)} = \delta n_e(\ell, t)_{k_x, k_y} \Big/ \left(\left| \delta n_e(\ell, t)_{k_x, k_y} \right| e^{i\theta(k_x, k_y, \ell)} \right). \tag{3.44}$$

This phase is in general dependent both on time and position along the beam, and reflects the field aligned nature of the fluctuations. The more realistic signal thus becomes

$$\delta n_e(\ell, t)_{k_x, k_y} = e^{i\hat{\theta}(k_x, k_y, \ell, t)} e^{i\theta(k_x, k_y, \ell)}. \tag{3.45}$$

Finally, we can also have a time and spatial variation of the Fourier amplitude $\left| n_e(\ell, t)_{k_x, k_y} \right|$, which in a local simulation mainly reflects the ballooning structure of the fluctuations. The actual simulated fluctuations thus take the form

$$\delta n_e(\ell, t)_{k_x, k_y} = \left| \delta n_e(k_x, k_y, z, t) \right| e^{i\hat{\theta}(k_x, k_y, \ell, t)} e^{i\theta(k_x, k_y, \ell)}, \tag{3.46}$$

which is equal to Eq. (3.32) when only considering a single k_x, k_y mode. The effect of both the phase ϕ and the spatial variation of the Fourier amplitudes can only be addressed in part in a local simulation. In reality, both amplitude and phase will vary along the laser beam due to variation in the background profiles and their gradients, as well as change in the magnetic geometry. These effects could properly be addressed with a global simulation, but in this work we limit the analysis to the local case, while a comparison with a global simulation is left for future work.

We carry out the exercise of calculating $\Delta L_{k_x, k_y}$ for all three forms of the density fluctuations, and with and without applying the filter in Eq. (3.40). We illustrate the localisation properties for two
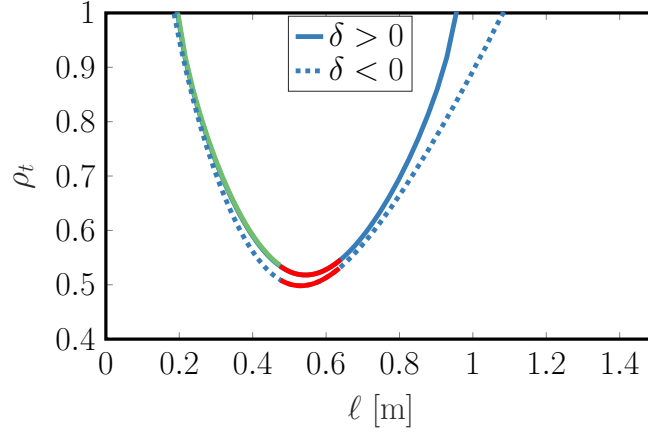
Figure 3.11 – The flux surface ρ_t coordinate as a function of the linear beam coordinate ℓ, for $\delta > 0$ (solid blue curve) and for $\delta < 0$ (dashed blue curve). Assuming that the measured wave vector perfectly satisfies $k_{\mathrm{meas}} \parallel k_0 \times \mathbf{B}$, the red segment indicates the measurement location in the case of a $f_a = 160°$ filter angle (as used in Fig. 3.12 and Fig. 3.17) and the green segment is the case of $f_a = 100°$ (as used in Fig. 3.14). Note that the green and red segments do not overlap.

different filter angles: 160 degrees and 100 degrees (the angle is calculated relative to the outer plasma midplane). For the positive triangularity discharge, #49052, a 160 degree filter angle corresponds to the radial direction at the tangency point. A straight filter with a width equal to the Gaussian width of the focal spot, which leads to optimal localisation, will be compared with the wedge filter. The wedge half angle is $\theta_W = 30$ degrees, which has been commonly used in the experiments. We will consider only the main fluctuating components falling inside the filter, whose power is larger than 1% of the RMS value when averaging over all k_x, k_y contributions. Finally, we will only show the results for $k_y \geq 0$, but taking into account the complex conjugate contribution at $k_y \leq 0$ so as to properly reproduce the contribution from each k_x and k_y component in the sum, Eq. (3.32).

Note that apart from selecting different wave-vector directions, changing the equilibrium and/or the filter angle will also change the measurement location. This is clearly shown in Fig. 3.11 where we illustrate the flux surface ρ_t coordinate as a function of the linear beam coordinate ℓ, for the two filter configurations considered in the positive triangularity case and the $f_a = 160°$ configuration in the negative triangularity case. If we assume that the property $k_{\mathrm{meas}} \parallel k_0 \times \mathbf{B}$ is perfectly satisfied it is clear that $f_a = 160°$ primarily selects fluctuation contributions from the tangency points: $\rho_t = 0.55$ for $\delta > 0$ and $\rho_t = 0.5$ for $\delta < 0$. Instead, for $f_a = 100°$ the localisation is clearly worse and almost the entire first half of the beam path in the plasma, from core to edge, is contributing to the measurement.

For the positive triangularity case and a 160 degree filter angle we obtain the power levels as shown in the two first columns in Fig. 3.12. The top row (a) includes only geometrical effects (i.e a density fluctuation given by Eq. (3.42)) while the middle row (b) also includes the effect of the

phase, Eq. (3.45). In the third row (c) we show the result obtained when considering the true form of the simulated density fluctuation, Eq. (3.46), but normalised by its RMS value. Finally, the actual simulated, unnormalised, fluctuations have been used to obtain the result in the bottom row (d). For a 160 degree filter angle the filters clearly preferably select components with low k_y. In the case of Eq. (3.42) the $k_y = 0$ component is perfectly symmetrical, while there is a very slight asymmetry appearing for larger k_y. Adding the effect of the phase $\hat{\theta}$, Eq. (3.45), leads to a slight asymmetry in the $k_y = 0$ components that have now a dominant contribution that is propagating radially outward, $k_x > 0$. The largest component overall is still $k_y \neq 0$ with $k_x < 0$. When adding also the effect of the amplitude, thus considering the actual but normalised density fluctuation given by Eq. (3.46), the $k_y = 0$ component stands out even more. Finally, when including the actual amplitude it clearly becomes the dominant feature in the PCI signal. As will be shown in the next chapter, section 4.1, this component in fact corresponds to a radially outward propagating GAM and is dominating the synthetic PCI signals for the considered positive triangularity TCV scenario.

Next, in Fig. 3.13, we show the corresponding localisation along the laser beam, after applying Eq. (3.40) and using the criterion in Eq. (3.41), for each type of density fluctuation. Instead of ΔL we show the equivalent segment length in $\Delta \rho_{k_x,k_y}$, i.e the corresponding extent of the segments across the flux surfaces. The case without any filter (red circles) tests the property, $\boldsymbol{k}_{\mathrm{meas}} \perp \boldsymbol{k}_0$ which we can see is poorly satisfied. For $k_\perp(\ell_\perp) < 7 \text{ cm}^{-1}$ essentially the whole laser beam path length, $\Delta \rho_{k_x,k_y} \sim 0.4$, is required to be able to reproduce a power level above 90% of the actual value. For increasing $k_\perp(\ell_\perp)$ however we start to see a reduction in the integration length. This indicates that the spatial variation of the fluctuation is fast enough and the contribution to the PSD away from $\ell = \ell_\perp(k_x, k_y)$ is being averaged out. Applying a wedge filter (blue squares) leads to only slightly better localisation at low $k_\perp$. We conclude that while the wedge filter does have the effect of restricting the wave-vector directions, it has nonetheless little effect on the localisation. Very good localisation is however seen when we consider the optimal case, i.e apply a straight filter (green asterisks). Most components in this case have $\Delta \rho_{k_x,k_y} \sim 0.1$. In the straight filter case, lighter shades of green indicates an increase in the k_y wave number which seems to lead to worse localisation. The reason is that the $\ell_\perp$ locations of $k_y \neq 0$ components are away from the tangency point, where ρ and the angle between the fluctuation wave vector and laser beam is varying the most. For $k_y \neq 0$ the same integration length along the laser beam path thus translates to a larger $\Delta \rho_{k_x,k_y}$. The different values of k_y are also responsible for the large spread seen in the unfiltered case. Finally, with black crosses we compare our calculated localisation with the simple estimate given by Eq. (3.43). We see that it agrees well with the trend of the unfiltered case, and even with the case of a wedge filter.

The localisation is similar for all three forms of the density fluctuation, Eq (3.42), Eq (3.45) and Eq (3.46), with the main difference coming from the fact that in the latter two fewer components are considered in the calculation of the localisation, because of their very low amplitudes. In the actual synthetic signal, as shown in subfigure (d), most components have a relatively low value of $k_{\perp,B}(\ell) < 8 \text{ cm}^{-1}$.

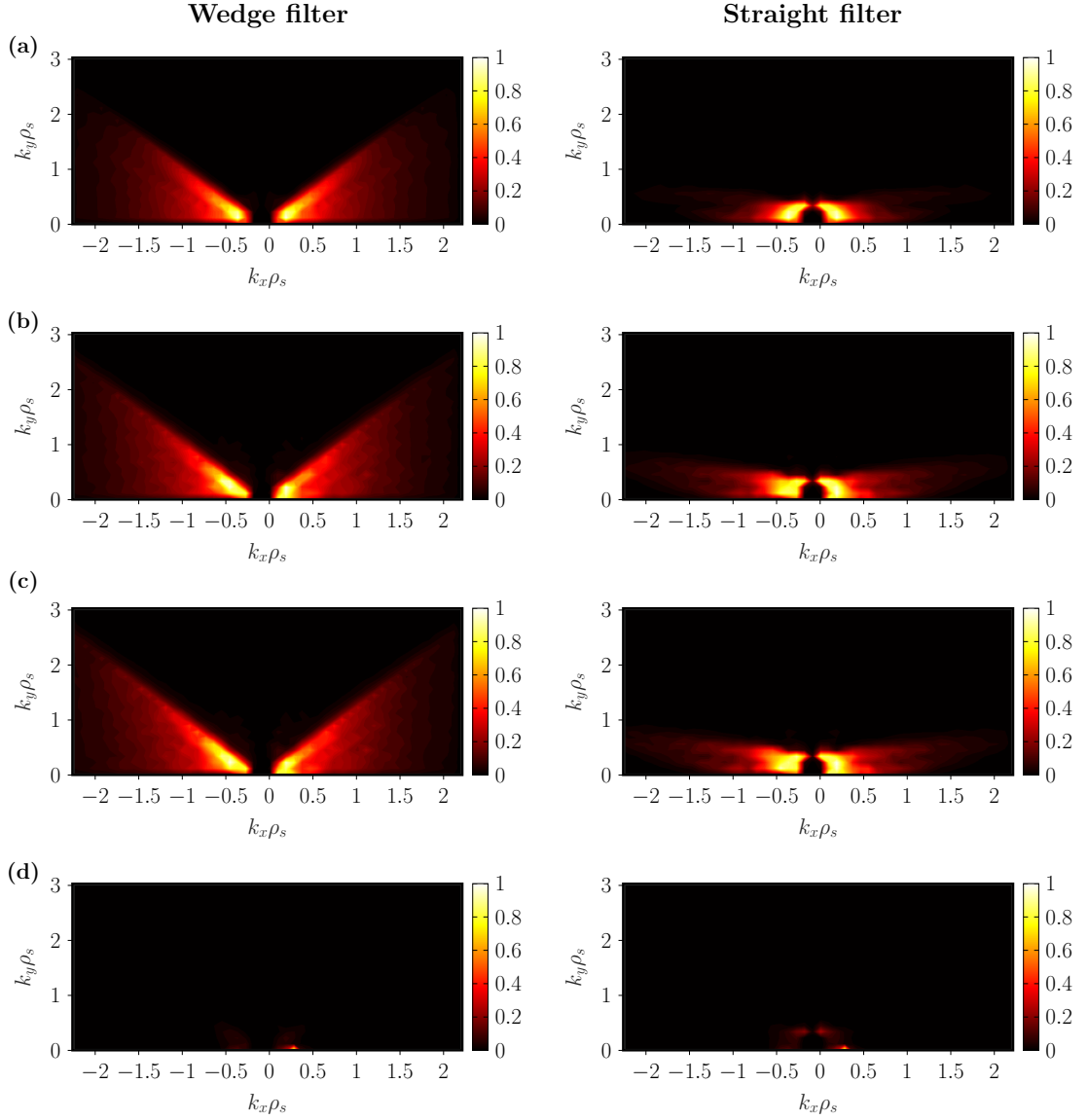**Wedge filter**   **Straight filter**

(a)

(b)

(c)

(d)

Figure 3.12 – Total power of each GENE k_x, k_y component when integrated over the whole laser beam propagation length in the case of a wedge filter (first column) and a straight filter (second column). The fluctuating data used to generate these plots comes from the positive triangularity case, discharge #49052. Both filters have a filter angle equal to 160 degrees, which corresponds to the radial direction at the tangency point. The power levels are shown of a density fluctuation of the form given in Eq. (3.42), (a), when including the effect of the phase $\hat{\theta}(k_x, k_y, \ell, t)$, Eq. (3.45) (b) when considering the actual simulated density fluctuation but normalised with its RMS value, Eq. (3.46) (c), and finally when including the actual amplitude of the simulated density fluctuations (d). The color scale is such that darker green colors indicate large amplitudes.
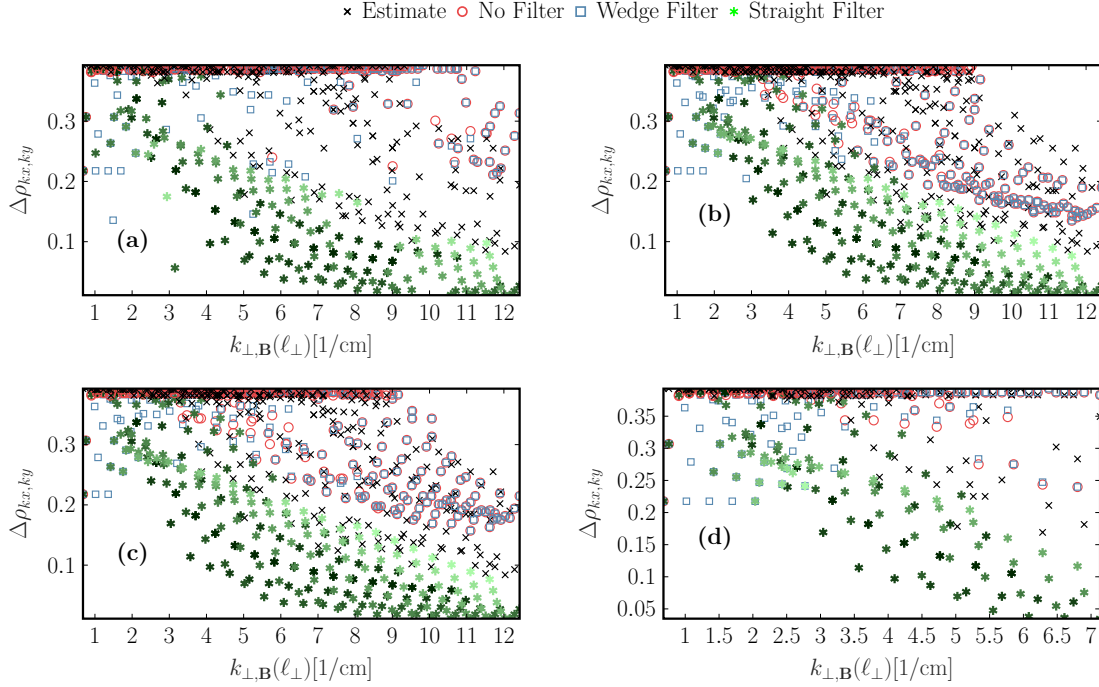
Figure 3.13 – The localisation in terms of the radial coordinate $\Delta\rho_{k_x,k_y}$ after applying Eq. (3.40) and using the criterion in Eq. (3.41) for the components. The four boxes (a-d) correspond to the four rows in Fig. 3.12. We show the unfiltered (red circles), the wedge filter (blue squares) and the straight filter (green stars) case. A comparison is done with the estimated integration length calculated from Eq. (3.43) (black crosses). For the straight filter case, the color gradient indicates different values of k_y; dark colors corresponds to low values of k_y while lighter colors show an increase in k_y. The large scattering of $\Delta\rho_{k_x,k_y}$ at similar values of $k_{\perp,B}(\ell)$ is due to the different k_y modes considered. Generally, modes with larger k_y tend to give worse localisation compared to low k_y modes, at similar values of $k_{\perp,B}(\ell)$.

If we rotate the filter by 60 degrees, to a 100 degrees angle, we obtain the power levels shown in Fig. 3.14 and the corresponding localisation as shown in Fig. 3.15. The $k_y = 0$ components are not at all included now and the form of the PCI signals is essentially dictated by the poloidal $k_y \neq 0$ fluctuating components. The lighter green colors for the straight filter case now indicate an increase in $k_{\perp,B}(\ell_\perp)$. Thus, unlike Fig. 3.13, increasing $k_{\perp,B}(\ell_\perp)$ corresponds now to an increase in k_y rather than an increase in k_x as was previously the case. The localisation for this filter configuration is considerably worse, than in the case of the other filter configurations, which included a large fraction of k_x values. The absence of any markers in the case of the filter for $k_{\perp,B}(\ell_\perp) > 8$ cm^{-1} shows how restrictive this filter configuration is. When including the effect of phase and amplitudes, a radially outward component with $k_y\rho_i \sim 1$ becomes dominant. Although we get worse localisation, in this configuration TPCI can be used to study ITG and TEM turbulence. The configuration used in Fig. 3.13 is instead more appropriate for studying purely radially propagating modes with $k_y = 0$, such as the GAM.
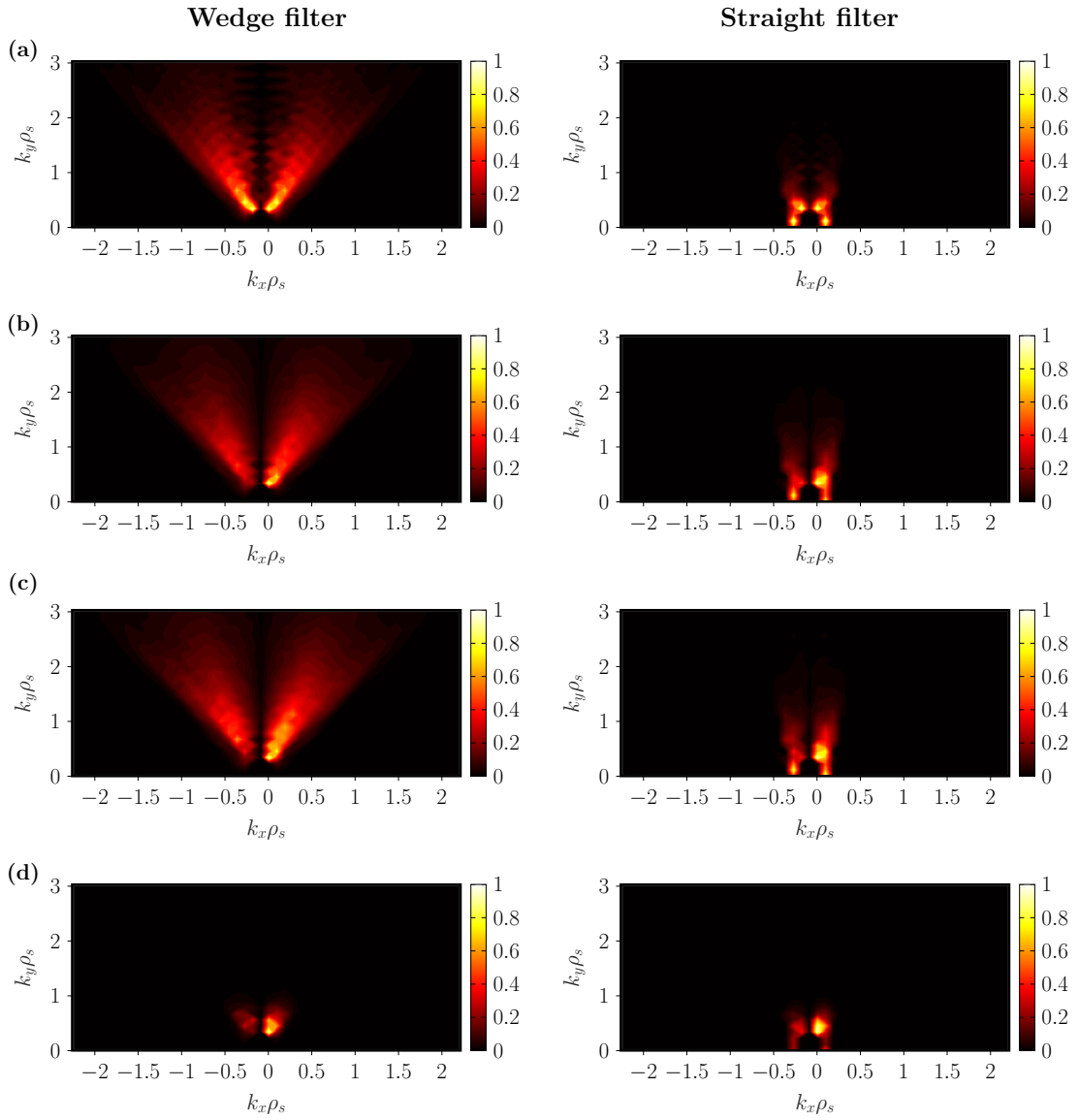
Wedge filter   **Straight filter**

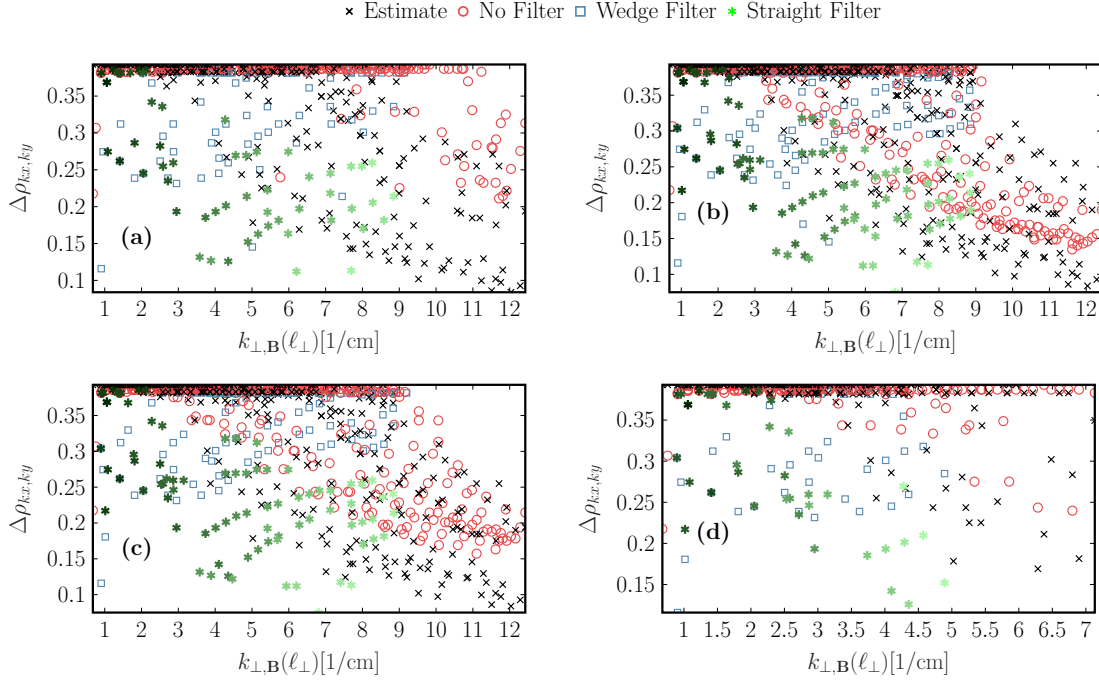Figure 3.14 – Same as Fig. 3.12 but for the case of a 100 degree filter angle.

Figure 3.15 – Same as Fig. 3.13 but for the case of a 100 degree filter angle.

All of these results have to this point been computed for the positive triangularity case only. When comparing with experiments, we will also evaluate the synthetic signals for the $\delta < 0$ case. Just as for the positive triangularity case in Fig. 3.17, the measurement with PCI in $\delta < 0$ was carried out with a wedge filter with a 160 degree filter angle. However, due to the change in the magnetic geometry, the 160 degree filter angle no longer corresponds to the radial direction at the tangency point. As was seen in Fig. 3.17 the contribution is now more from $k_y \neq 0$ modes and consequently, as shown in Fig. 3.16, the localisation is worse than for the corresponding positive triangularity case, Fig. 3.13. The power levels in Fig. 3.17 show that the filters still include $k_y = 0$ components, but poloidal components with $k_y \neq 0$, propagating radially inward, are favoured in the measurement. Because of these k_y components, the signals in the negative triangularity case have lesser localisation. Notice that larger k_x values in the case of a straight filter (seen by following the green markers with a constant color) lead to slightly worse localisation in this case. This is because in this particular case the larger k_x components stay within the filter for a slightly longer length along the laser beam. This effect is most visible for the larger k_y values (lighter green colors). From the plots of the PSD levels, it is clear that, unless the raw fluctuation data contains a strong purely radial component, the measurement will be dominated by $k_y > 0$ components, propagating radially inward.

To conclude, in contrast to past predictions of the PCI localisation [21, 31, 73] we find that the property $\boldsymbol{k}_{\text{meas}} \perp \boldsymbol{k}_0$ is not perfectly satisfied and consequently the localisation is not as good as previously believed when no spatial filter is used. Also, while in the case of a narrow straight filter the localisation is indeed very good, especially in the radial coordinate, the wedge filter,
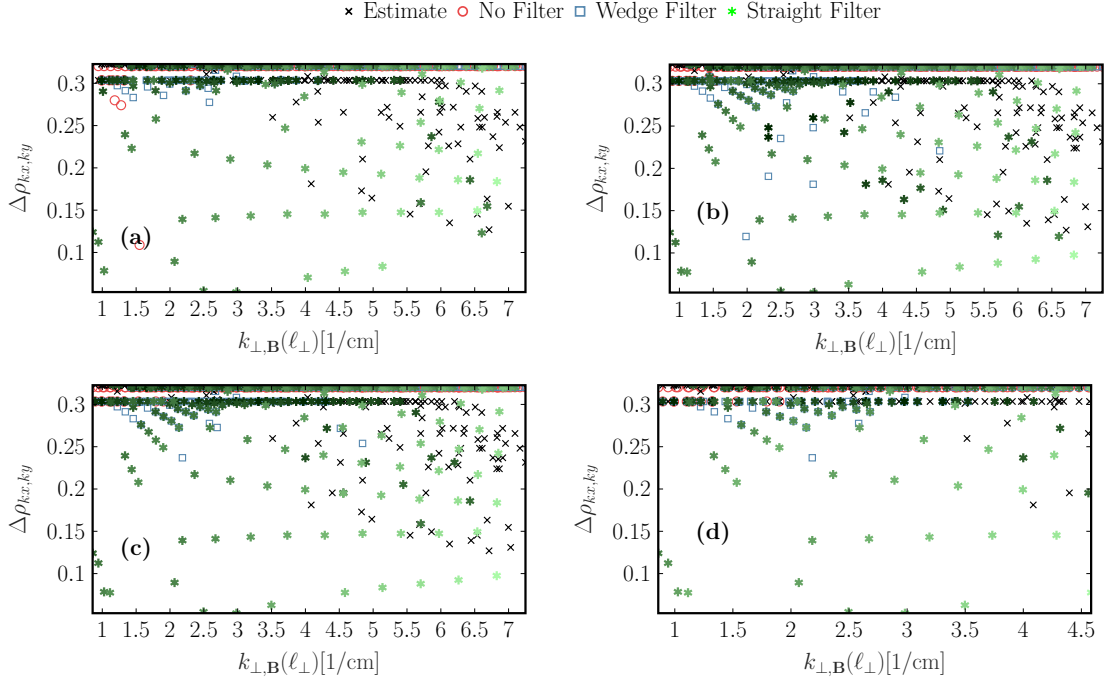
Figure 3.16 – Same as Fig. 3.13 but for the negative triangularity case.

which has also been commonly used in the experiments, provides relatively poor localisation. For this case, stating that the signal only comes from the tangency point is therefore inaccurate. It is interesting to note that the increasing complexity in the description of the density fluctuations (including phase and amplitudes) has little effect on the localisation. This could mean that global effects also will play little role on the localisation. However, this does not mean that global effects can be neglected. For example, the contribution to the PCI signals could be localised to a portion of the plasma where fluctuation levels are small (such as close to the core) which can only properly be accounted for by making a global simulation.

3.3 Chapter summary

In this chapter we introduced the gyrokinetic framework and presented the details of a synthetic diagnostic that models measurement with PCI by post-processing electron density fluctuations generated by gyrokinetic simulations. In its present state it uses GENE simulations but can easily be adapted also to other gyrokinetic codes. An important feature included in the synthetic PCI is the possibility to apply a filter in wave-number space. This filter selects the measured wave vector direction and this translates into a longitudinal localisation of the signal in space. Such a filter must be taken into account when modelling PCI measurements on TCV, and in the future also on JT-60SA. We implemented two different versions of the synthetic diagnostic. The first properly takes into account the Gaussian form of the PCI laser beam which is required to accurately compute the synthetic PCI signals. We also considered a simplified approach, approximating the

PCI laser beam as an infinite plane wave which allowed us to write the synthetic signals in terms of the GENE k_x and k_y modes. Using the plane wave approximation we have shown from first principles how the spatial filters affect the PCI signals and the localisation we obtain for different k_x and k_y modes. In general we find that the localisation is good for large enough $k_{\perp,B}$ but not as good as was predicted from simplified analytical considerations.
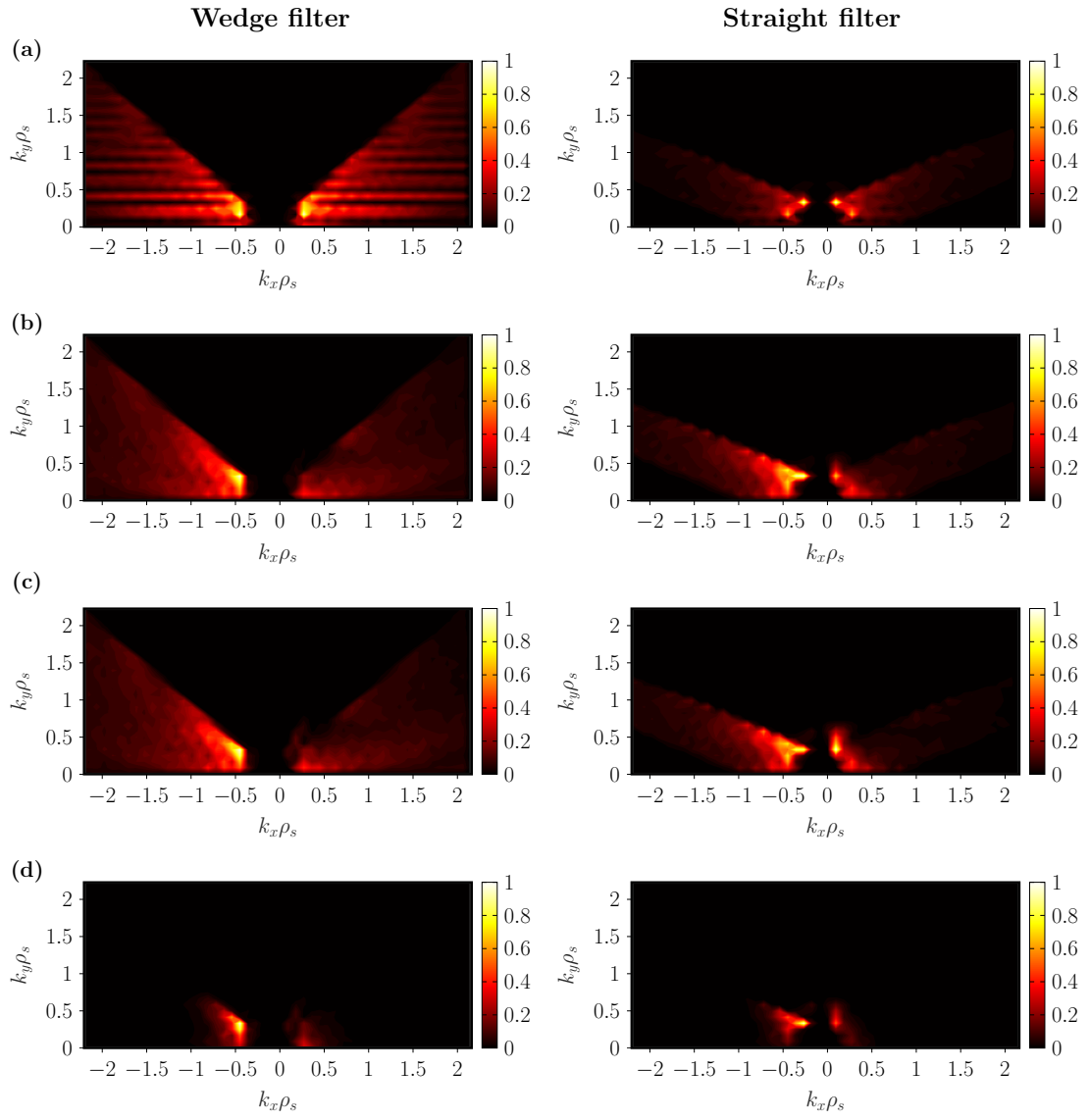
Figure 3.17 – Same as Fig. 3.12 but for the negative triangularity case.

4 Prediction and interpretation of TPCI measurements in TCV

The details of the synthetic diagnostic for modelling measurements with TPCI were presented in the last chapter. In this chapter, the synthetic diagnostic is now used to improve the interpretation of the TPCI measurements and link the diagnostic signals to the physics of the underlying turbulent fluctuations. First, in section 4.1, an analysis of the positive and negative triangularity TCV discharges, #49052 and #49051, will be performed. These two discharges were already introduced in the previous chapter, section 3.2. The density fluctuations modelled with GENE simulations for the two cases are taken and post-processed with the synthetic tool. Both #49052 and #49051 have been analysed in the past with actual TPCI measurements [74]. By using the same set-up of TPCI in the synthetic diagnostic as in the actual experiments, a comparison is made between the modelled and measured TPCI signals. As will be shown, the spatial filter configuration used in #49051 and #49052 is such that purely radial components of the $k_y = 0$ modes dominate the measurement.

A spatial filter oriented along the radial direction is commonly chosen in the TPCI set-up because it provides very good localisation. Although the localisation is worse, it is possible to learn about the non-radial components of the turbulence by rotating the filter. This is explored in the next part of this chapter, section 4.2, where the spatial filter will be rotated so that the TPCI measurement becomes dominated by $k_y \neq 0$ contributions. As will be seen, this configuration allows to study ITG/TEM turbulence and distinguish modes propagating in the ion direction (ITG) from modes propagating in the electron direction (TEM). The dependence of the TPCI signals on the ITG/TEM fluctuations is more clearly shown by considering a more recent pair of positive and negative triangularity discharges, #69508 and #69340, respectively. NBH was used to raise the ion temperature in these two scenarios, thus enhancing the ITG drive of the turbulent fluctuations and leading to a more pronounced transition from a TEM to ITG regime when changing the plasma triangularity. These two new scenarios are presented in subsection 4.2.1. The new TPCI set-up which allows to focus the measurement on the $k_y \neq 0$ modes while damping the contribution from purely radial modes ($k_y = 0$), is presented in subsection 4.2.2.

Another useful feature of TPCI measurements sensitive to $k_y \neq 0$, is that some properties of
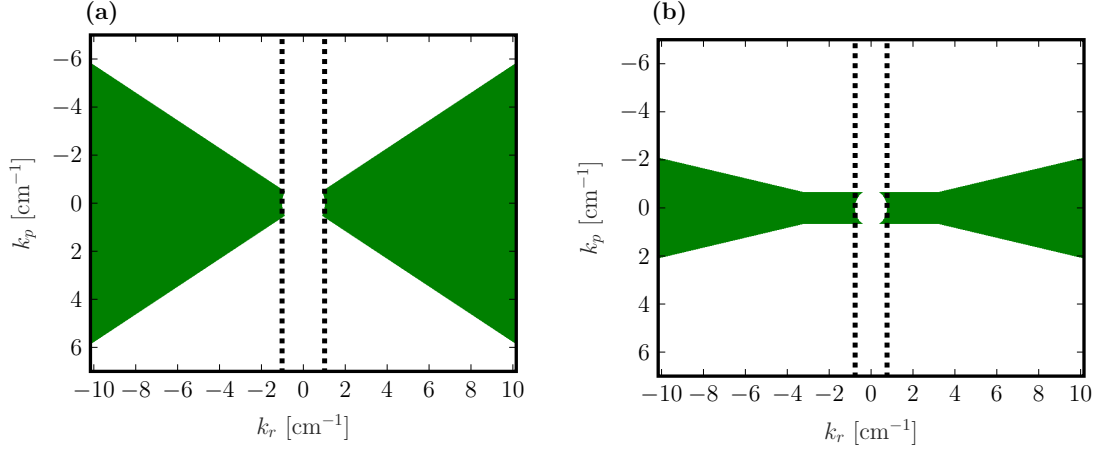
Figure 4.1 – The spatial filter used for shots #49051 and #49052 (a) and the new filter (b) used for predicting future TPCI measurements. The dashed black line indicates the cut-off wave number.

the measurements can already be predicted from simple and fast linear GENE simulations. This is in contrast to a measurement of $k_y = 0$ components, which can only be modelled with computationally intensive and time-demanding fully nonlinear simulations. In subsection 4.2.4 it is shown how linear GENE simulations can be used to predict certain aspects of the TPCI signals when the measurement mainly comes from $k_y \neq 0$. This is demonstrated in practise at the end of this chapter, in section 4.3, by predicting TPCI measurements in a plasma undergoing a transition from a Linear Ohmic Confinement (LOC) regime to a Saturated Ohmic Confinement (SOC) regime.

Much of section 4.1 comes from Ref. [69].

4.1 Interpretation of past experimental TPCI measurements in TCV

In this section we further consider the two discharges #49052 and #49051, already introduced and discussed in the previous chapter, section 3.2. We recall that these discharges have positive and negative triangularity, respectively, and equal ECH power, and were performed in the past to study the effect of triangularity in TCV [74]. For modelling the TPCI signals we make use of the electron density fluctuations obtained from the GENE simulations, and post-process them with the synthetic diagnostic, using the method described in section 3.2.1. The set-up of the diagnostic is the same as considered in the corresponding experiments: nine unevenly spaced detector elements (and therefore nine values of $r = r_1, r_2 \ldots r_9$), with a 5 cm diameter beam. The lower wave-number cut-off is at $k_c = 1.01$ cm^{-1} and the maximum measurable wave number is at $\max(k_r) \sim 9$ cm^{-1}. The spatial filter is illustrated in subfigure (a) in Fig. 4.1 with respect to the inboard midplane, and is a wedge with half angle $\theta_W = 30$ degrees and oriented along the radial direction at the tangency point (160 degree filter angle).
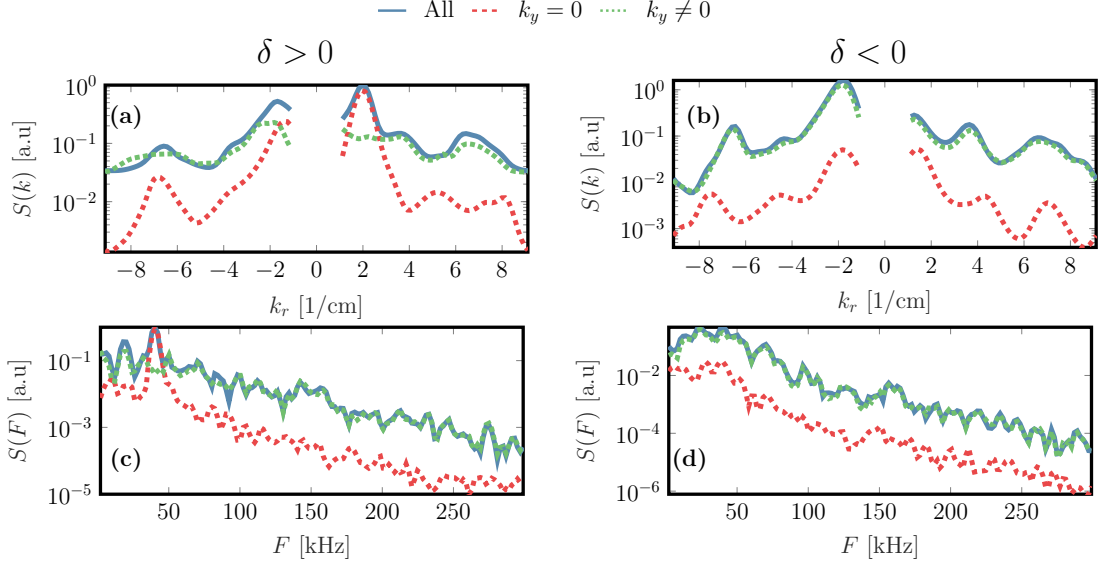
Figure 4.2 – Synthetic wave-number spectrum $S(k_r)$ (a,b), frequency spectrum $S(F)$ (c,d) for #49052 with $\delta > 0$ (a,c) and for #49052 with $\delta < 0$ (b,d) cases. The result is shown when including all k_y contributions in Eq. (3.35) (solid blue), only $k_y = 0$ (dashed red) and only $k_y \neq 0$ (dotted green).

Based on the analysis carried out in subsection 3.2.2 we can expect that the effective integration length for this case with wedge-like filter will be similar to the unfiltered case, shown in blue and red respectively in Fig. 3.13; i.e $\Delta\rho_{k_x,k_y} \approx 0.3$, which essentially corresponds to the whole laser beam propagation length ≈ 50 cm, at the maximum (Nyquist limited) wave number $|\boldsymbol{k}_{\perp,B}|$. As pointed-out in the previous chapter, the consequence of this is that the contribution to the TPCI signal is coming from the whole laser beam path and not only from the tangency point, which both complicates the interpretation of the TPCI results and makes the flux-tube approximation less appropriate for modelling the TPCI signals. Since a global simulation that would generate sufficient time statistics was outside the scope of this thesis, we pursue here with the flux-tube approximation. As we will see, even with this reduced modelling, the synthetic diagnostic is nevertheless able to reproduce the main features seen in the corresponding experimental signals.

Wave-number spectra and frequency spectra of the synthetic data are shown in Fig. 4.2 for both the positive and negative triangularity cases. We use the plane wave approximation and compare between different contributions to the TPCI signals. We either include all k_x and k_y components in the sum in Eq (3.35), only purely radial components with $k_y = 0$ or finally only components with a non-zero binormal wave number, $k_y \neq 0$. This is a convenient way to split the contributions since $k_y = 0$, corresponds to purely zonal-type modes, while $k_y \neq 0$ includes contributions from non-zonal modes only, such as ITG modes and TEM.

The wave-number spectra in Fig. 4.2 $S(k_r)$ for $\delta > 0$ (a) suggest that the density fluctuations propagate mostly outward, $k_r > 0$, with the dominant contribution coming from $k_r \sim 2$ cm^{-1}. We

71

can see that this actually corresponds to the purely radial $k_y = 0$ fluctuation contributions. Notice that the dominance of this component in the synthetic result was already predicted from the plots of the PSD in Fig. 3.12. The $k_y = 0$ components also lead to a peak in frequency at $F \sim 40$ kHz, which is typical for a GAM in TCV [37]. An analysis of the raw GENE output has revealed that the $k_y = 0$ density fluctuation component indeed has the poloidal $m = 1$ structure of a GAM. Although $k_y = 0$ provides the dominant contribution in the $\delta > 0$ case, modes with $k_y \neq 0$ are instead responsible for a power cascade in frequency as shown in the frequency spectrum $S(F)$ in Fig. 4.2.

The asymmetry of the $k_y = 0$ component is due to the structure of the complex Fourier amplitudes of the raw density fluctuations generated by GENE, combined with the effect of the measurement geometry. This was already suggested by the rows (b,c) in Fig. 3.12. If we look at the frequency and k_x spectra of the $k_y = 0$ components coming from the raw GENE density fluctuations we notice that the $k_x > 0$ components are dominant above the midplane, $z > 0$, as shown in subfigures (a),(b) and (c) of Fig. 4.3. In a flux-tube, and assuming up-down symmetric equilibrium, the $k_y = 0$
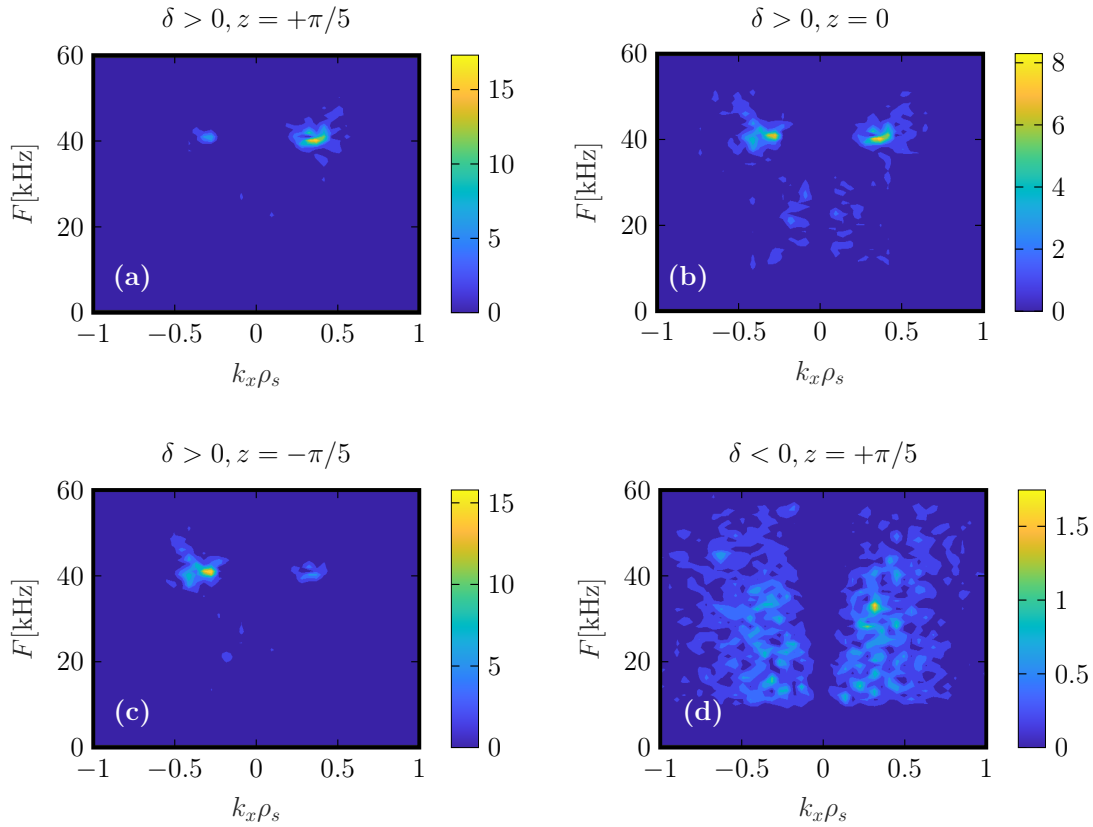

Figure 4.3 – The k_x and frequency spectra of the raw GENE $k_y = 0$ density fluctuation component, for $\delta > 0$, shown above the midplane (a), at the midplane (b) and below the midplane (c). For comparison, the spectra for $\delta < 0$ above the midplane (d) is also shown.

component has to satisfy the symmetry $\Phi(k_x, z) = \Phi(-k_x, -z)$ [75]. Therefore once averaged over

the whole flux surface the GAM will not have any preferential propagation direction. However, in our case the TPCI laser beam only passes through the upper part of the plasma, as was shown in Fig. 3.2. This means that the TPCI beam picks up only a larger $k_x > 0$ than $k_x < 0$ contribution for the $k_y = 0$ fluctuations, explaining the asymmetry seen in Fig. 3.13 and Fig. 4.2. Instead, if the TPCI beam passed through the lower portion of the plasma, it would pick up the dominant $k_x < 0$ component and the wave-number spectrum $S(k)$ in Fig. 4.2 (a) would show the opposite propagation direction for the dominant $k_y = 0$ component.

Contrary to $\delta > 0$, fluctuations seem to propagate radially inward for the negative triangularity, $\delta < 0$, case. This is suggested by the wave-number spectrum $S(k_r)$ shown in the bottom of Fig. 4.2, which has a dominant component at $k_r \approx -2$ cm^{-1}. It is also clear from this plot that the zonal $k_y = 0$ component provides a very modest contribution and the signal is almost entirely dominated by fluctuations with $k_y \neq 0$. Based on the results in Fig. 3.16 we can directly conclude that the low contribution of $k_y = 0$ components is both due to the different plasma geometry and different characteristics of the fluctuations. Indeed, it is clearly seen in subfigure (d) of Fig. 4.3 that the amplitudes of the k_x components for $k_y = 0$ above the midplane are significantly smaller than in the $\delta > 0$ case (notice the different scale of color bars between subfigure (a) and (d) of Fig. 4.3). There is also no clear GAM structure, which was the reason for the positive k_x asymmetry seen for the $\delta > 0$ case. This explains the synthetic results, but we stress that we do not yet have a clear physical understanding what makes the GAM contribution disappear in the $\delta < 0$ case.

More details on the fluctuations in the TPCI signals are given by the conditional wave-number and frequency spectrum $S(k_r|f)$, defined in section 2.1.2, which is shown in Fig. 4.4. In addition to the plane wave approximation we also show the synthetic result when using the true, Gaussian beam approach presented in subsection 3.2.1. Apart from a very slight difference in some frequency and wave-number components we see that the two approaches give very similar results. There is a slightly larger frequency spread in the Gaussian beam case, and the left leg with $k_r < 0$ is also slightly more prominent.

We now show the experimental results from the actual corresponding TPCI measurements. The conditional wave-number and frequency spectra for the $\delta > 0$ and $\delta < 0$ cases are shown in Fig. 4.5. In the $\delta > 0$ case, the measurement is clearly dominated by fluctuating components with $k_r > 0$, with the largest component having $k_r \sim 2$ cm^{-1} and $F \sim 40$ kHz. The negative triangularity case on the other hand is dominated by components with $k_r < 0$. All these observations are in good semi-quantitative agreement with the results from modelling with the synthetic diagnostic shown in Fig. 4.4. Our interpretation of the difference between measurements in $\delta > 0$ and $\delta < 0$ is therefore a change in the contribution from the zonal type modes, which in particular includes the GAM. While the wave number of the dominant contribution is in good agreement with experiments, more analysis is required to understand the larger frequency spread seen in the experimental case. A potential explanation could be the radial variation of the GAM frequency, not accounted for in the analysis performed here based on a single local flux-tube simulation.

$\delta > 0$ $\delta < 0$
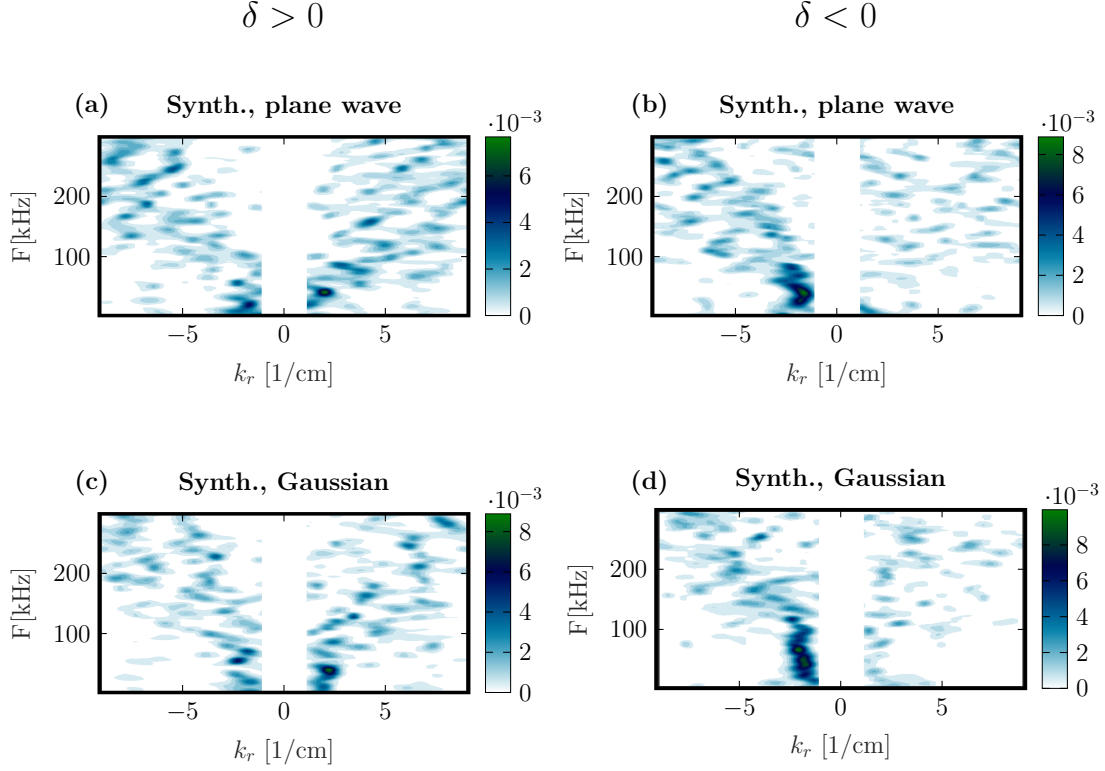

Figure 4.4 – The conditional spectrum for $\delta > 0$ (left column) and $\delta < 0$ (right column). The top row (a,b) shows the synthetic results when applying the plane wave approximation and the bottom row (c,d) shows the synthetic results when accounting for a Gaussian laser beam.
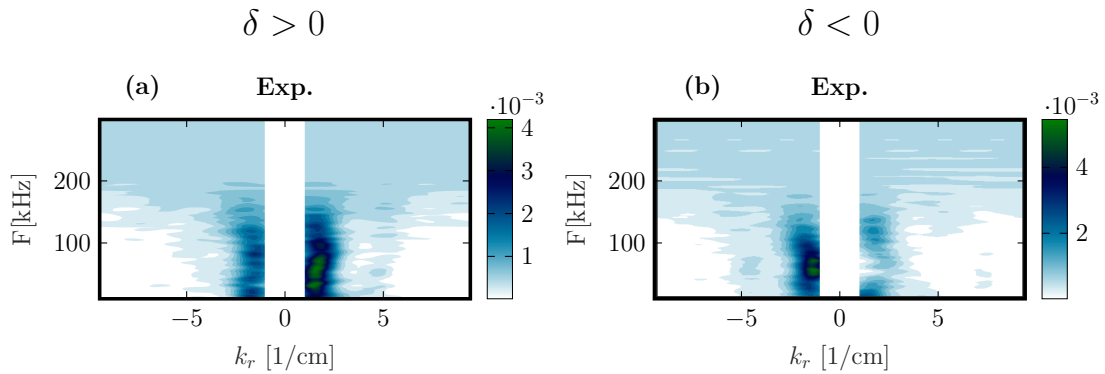
$\delta > 0$ $\delta < 0$

Figure 4.5 – Same as Fig 4.4 but calculated from the actual TPCI measurement in the $\delta > 0$ #49052 discharge (a) and $\delta < 0$ #49051 discharge (b).

In conclusion, we have seen that the synthetic diagnostic appears to be able to reproduce the main signatures of the TPCI signals, in particular the change in the TPCI $S(k_r)$ spectra when we transition from $\delta > 0$ to $\delta < 0$. More detailed gyrokinetic simulations, varying input parameters and radial positions, are required to better understand the difference between synthetic and experimental results.

Because of the orientation of the spatial filter, all the cases shown above have focused on the effect of purely radial fluctuations $k_y = 0$ on the TPCI signals. In the next section we will illustrate what we can learn about $k_y \neq 0$ modes, in particular ITG versus TEM turbulence, when we rotate this filter slightly.

4.2 Measuring ITG and TEM turbulence

We will now investigate what information about turbulence can be obtained if the spatial filter is rotated such that the contribution from $k_y \neq 0$ modes dominate the measurement over the contributions from $k_y = 0$. To better recognise trends in the TPCI signals, a new set of TCV scenarios is introduced: discharges #69508 and #69340. In these two cases, ITG turbulence is more pronounced, making it easier to identify changes in the TPCI signals when we vary the ITG and/or TEM drive. Nevertheless, the discharges considered earlier, #49052 and #49051, are still included in the following analysis to illustrate the effect of the different filter configuration (the wedge angle in the new set-up is smaller).

The new scenarios, including linear and nonlinear GENE simulations, will be introduced in subsection 4.2.1. The new TPCI set-up and signals will be presented in subsection 4.2.2. In subsection 4.2.3, based on simulations, we will show how the changes in the TPCI signals can be linked to the $k_y \neq 0$ fluctuations and how the diagnostic can be used to identify whether the plasma is ITG or TEM driven. Finally, in subsection 4.2.4, we will show that certain aspects of our results can, in fact, already be predicted from computationally cheap and fast linear simulations.

4.2.1 Simulation and filter configurations

We consider the positive triangularity discharge #69508 and its negative triangularity equivalent #69340. Both these shots have a diverted equilibrium and are NBI heated. The heating is stronger in #69508 (735 kW) than #69340 (362 kW) in order to keep the profiles as similar as possible, once again illustrating the stabilising role of negative plasma triangularity on turbulent transport. We compute the profiles for these two scenarios using the KER approach described in section 2.3, and the results, including the normalised gradient length scales, are shown in Fig. 4.6. All profiles are indeed similar, except the carbon density n_c, which is slightly lower in the negative triangularity case, and the ion temperature gradient $a/L_{T,i}$ which is clearly larger for $\delta < 0$ outside $\rho_t = 0.7$.

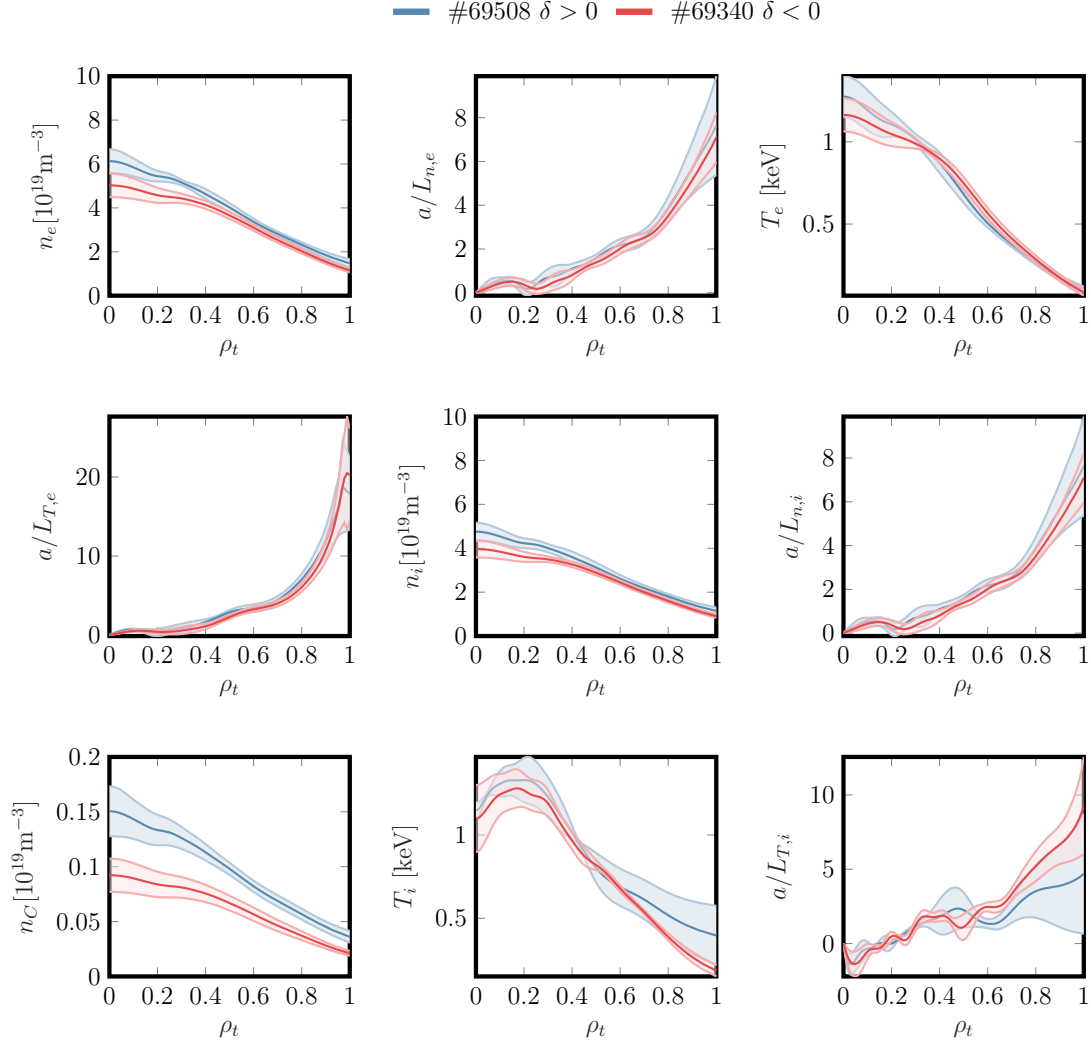We focus on $\rho_t = 0.7$, as local linear GENE simulations showed that a transition from the TEM

Figure 4.6 – Profiles for the positive triangularity shot #69508 (blue) and negative triangularity shot #69340 (red). Error bars are represented by colored bands.

dominated case, #69508, to the ITG dominated case, #69340, is most pronounced at this radius. The physical input parameters to the simulations at this radius are given in Table 4.1. The triangularity of the considered flux surface is $\delta = 0.1$ for #69508 and $\delta = -0.1$ for #69340. As for the previous simulations, we consider the most important parameters necessary to lower the simulated heat flux levels to experimental values: kinetic electrons, ions and carbon impurities. We account as well for collisions and electromagnetic effects, although β is small. As already confirmed by previous studies [9, 76], collisions, in particular on impurities, are most important in TCV to bring down the simulated heat flux from tens of MW to the experimental range of hundreds of kW. Due to NBI, fast ions are present in the scenarios. However, their density at $\rho_t = 0.7$ is very low and therefore it is expected that they should not significantly alter our results.

Table 4.1 – Physical parameters of the positive triangularity shot #69508 (black font) and negative triangularity shot #69340 (blue font and in parentheses) at $\rho_t = 0.7$ used as input to the GENE simulations, obtained from the MHD equilibrium code CHEASE [70] and species profiles shown in Fig. 4.6. The reference magnetic field is provided at the magnetic axis. The parameter a is the minor radius and R is the major radius. Important parameters undergoing a large change when changing from positive to negative triangularity are shown in bold.

n_e [10^{19}m^{-3}]	2.94 (2.64)	T_i/T_e	**1.56 (1.3)**
q_0	**1.81 (1.6)**	T_e [keV]	0.42 (0.42)
$a/L_{n,e}$	1.70 (1.97)	$\hat{s}$	1.46 (1.34)
B_0 [T]	1.40 (1.39)	$a/L_{n,i}$	1.7 (1.97)
R/a	3.27 (3.43)	a [m]	0.28 (0.27)
$a/L_{T,e}$	2.52 (2.84)	β_e [10^{-2}]	0.25 (0.23)
n_i/n_e	0.91 (0.87)	$a/L_{T,i}$	**1.42 (3.61)**
ν_c [10^{-2}]	**0.78 (0.16)**	Z_{eff}	1.45 (1.65)

The total experimental heat flux value at $\rho_t = 0.7$, evaluated with ASTRA, and including the contribution from Ohmic heating and NBH, is 231kW for #69508 and 186 kW for #69340. These low heat flux values for the experiments, despite strong NBI heating, are due to large fast-ion losses. Consequently, only a fraction of the heating power is actually deposited in the plasma. The simulation performed considering the reference parameters for #69508 yields a heat flux of 280 kW, which reproduces the total experimental heat flux quite well. Very good agreement is also achieved for the heat flux ratios: $Q_{\text{ion}}/Q_{\text{electron}} \approx 0.35$ experimentally and $Q_{\text{ion}}/Q_{\text{electron}} \approx 0.37$ in the simulation. The same cannot be said for the $\delta < 0$ case where the simulated heat flux ~ 1.5 MW is much larger than the experimental heat flux. Even the heat flux ratio in the simulations , $Q_{\text{ion}}/Q_{\text{electron}} \sim 0.96$, is very different from the experimental value $Q_{\text{ion}}/Q_{\text{electron}} \sim 0.08$, suggesting that the ion transport is overestimated. In part, this discrepancy could be due to the absence of background flow shear in our flux-tube simulations. We do not include it here, but only mention that including flow shear measured by the CXRS diagnostic ($\omega_{E\times B} = -0.13$, considering a purely toroidal flow) indeed reduces the heat flux to 1.14 MW but it is not sufficient to match the experimental values. Instead, the main reason for the excessive heat flux in our simulations is probably due to an underestimation of the stabilising effect of negative triangularity, which, as has been previously discussed [9], can only be modelled properly if global effects are included in the simulations, especially further away from the LCFS given that radial penetration of δ is weak. In our case, however, this should not be a major concern, as we focus on identifying trends in the TPCI signals, rather than reproducing the heat fluxes in experiments. However, for later more detailed comparisons with experiments, global simulations might be required, in particular for the $\delta < 0$ case.

We notice that our results here differ from what we obtained previously in section 3.2 where we considered the other two TCV discharges, #49052 ($\delta > 0$) and #49051 ($\delta < 0$). There, in contrast to what we see here, a better match between simulated and experimental heat fluxes was observed for the $\delta < 0$ case, while for $\delta > 0$ we underestimated the heat flux values. Given the results from previous work [9] the effect of $\delta < 0$ is likely not properly accounted for in either case, each using the local flux-tube approximation, and the better match of the heat flux for $\delta < 0$ we obtained in section 3.2 is most likely a coincidence. Especially, since no CXRS measurement was available and the ion temperature, T_i, had to be inaccurately computed with the PRETOR formula. In this sense, the results obtained in this section, for #69508 and #69340 are more accurate since CXRS measurements were available to compute T_i.

In addition to the simulations at the nominal parameters, we vary the physical input parameters slightly to generate artificial scenarios where ITG modes or TEMs are more or less unstable. In Table 4.2 we show the 12 different runs considered in this section. The order in the table corresponds to increasing ITG content, as will be defined and shown later. In addition to the new runs, we also include the two cases studied before, #49051 and #49052, corresponding to runs one and four in Table 4.2. The reference #69508 and #69340 correspond to five and nine. Then we have runs seven and ten corresponding to #69508 and #69340 ,respectively, but without carbon impurities ($n_c = 0$), where the main ion density and density gradient are adjusted to satisfy quasineutrality. In runs six and eight we considered again #69508 and #69340, but took half the collisionality $\nu = \nu_0/2$, where ν_0 is the nominal value given in Table 4.1. In runs 11 and two we swapped the ion temperature gradient, thus decreased it in the $\delta < 0$ case and increased it in the $\delta > 0$ case. Finally, for the #69058 case, we set $a/L_{T,i} = 0$ corresponding to run three, and for run 12 set $a/L_{T,e} = 0$ while increasing the ion temperature gradient $a/L_{T,i} = 3$ to have enough turbulent transport.

The growth rate k_y-spectra results from the linear simulations for these cases (excluding runs 1 and 4 that were already shown in Fig. 3.4) are shown in Fig. 4.7. The reference case of #69508 (run five, shown in blue in subfigure (a)) has a mix of ITG ($\omega > 0$) and TEM ($\omega < 0$), while the corresponding reference $\delta < 0$ case #69340 (run nine, blue, subfigure (b)) has a broader k_y range which is ITG unstable. Taking half the collisionality (green lines) destabilises the modes for both $\delta > 0$ and $\delta < 0$, while not significantly altering the ITG/TEM mix, as shown by the little difference in the real frequency, ω. If we remove impurities in $\delta > 0$ (subfigure (a), red line) we increase the growth rates for $k_y\rho_s \lesssim 0.6$ and $k_y\rho_s \gtrsim 1.6$ and the real frequencies become more positive. Surprisingly, for $0.6 \lesssim k_y\rho_s \lesssim 1.6$ impurities instead seem to be destabilising, as γ at these scales decreases when $n_c = 0$. This effect is similar to what we saw in Fig. 3.4 (#49052, $\delta > 0$ red to yellow for $k_y\rho_s \gtrsim 2$) and suggests that the mode appearing at these scales, which propagates in the ion direction, is in fact not a standard ITG, but something different. Potentially, it could be a density gradient driven TEM. The same can be seen in the $\delta < 0$ case but there it appears in a more narrow range, $1.1 \lesssim k_y\rho_s \lesssim 1.4$. Finally, in orange, we show the case when the ion temperature gradients are swapped. In the $\delta > 0$ case, this means increasing $a/L_{T,i}$, leading to more ITG, while for $\delta < 0$ $a/L_{T,i}$ decreases, creating a scenario more dominated by TEM.
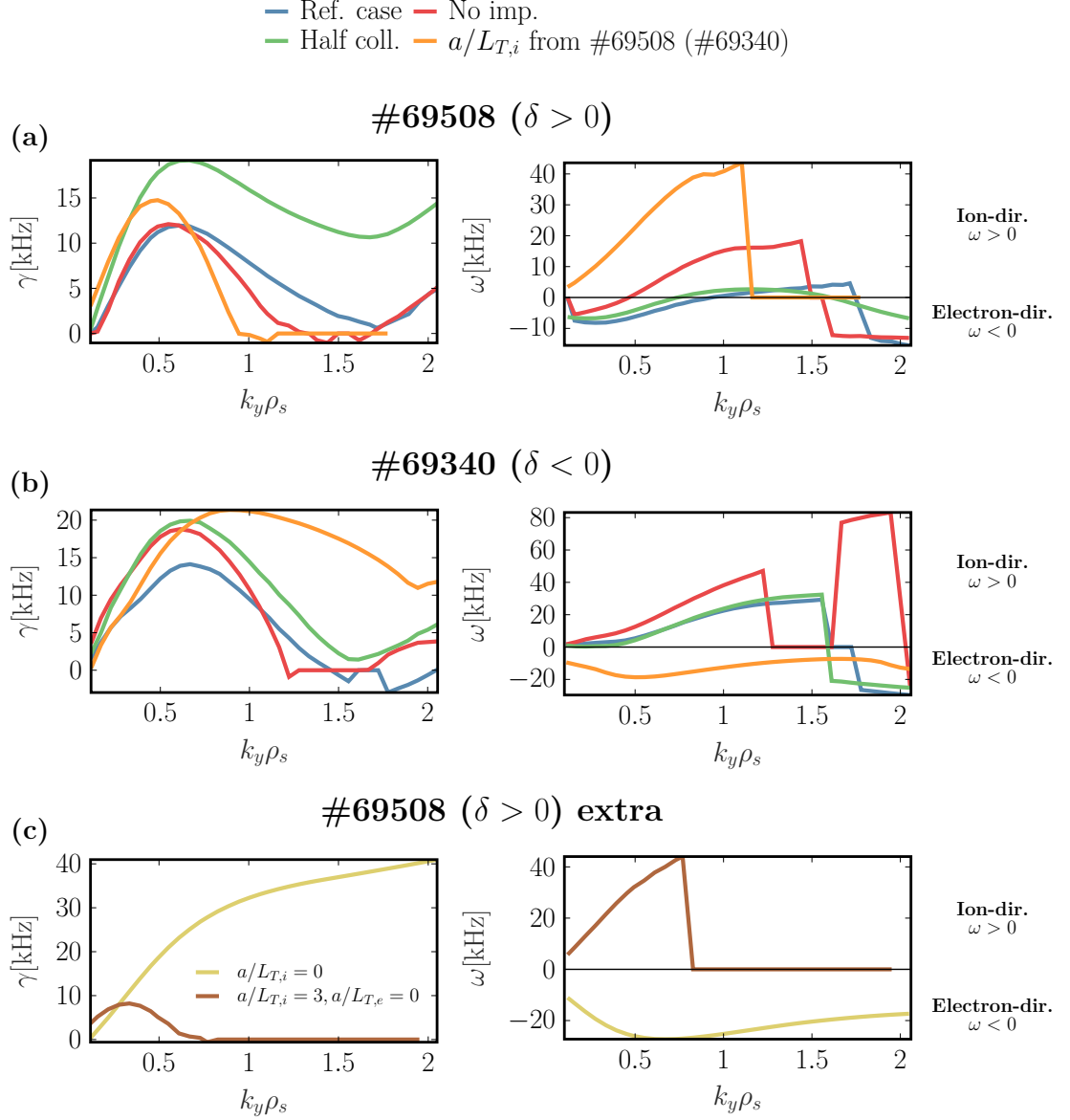
Figure 4.7 – Linear GENE results of the growth rate of the most unstable mode for the $\delta > 0$ case #69508 (a) and the $\delta < 0$ case #69340 (b). In the last row (c) we show the additional cases for #69508 corresponding to runs three and 12 described in Table 4.2.

Table 4.2 – Table of the various runs performed in this section to study ITG and TEM turbulence. The runs are ordered and indexed by increasing ITG content in the scenario, with run one completely dominated by TEM while run 12 is mostly ITG.

Run number	Title	Description
1	#49051, Ref.	Reference #49051 ($\delta < 0$) case
2	#69340, $a/L_{T,i}$ from #69508	#69340 but with $a/L_{T,i}$ from #69508
3	#69508, $a/L_{T,i} = 0$	#69508 but with $a/L_{T,i} = 0$
4	#49052 Ref.	Reference #49052 ($\delta > 0$) case
5	#69508 Ref.	Reference #69508 ($\delta > 0$) case
6	#69508, half coll	#69508 with half collisionality, $\nu = \nu_0/2$
7	#69508, No imp.	#69508 with $n_C = 0$
8	#69340, half coll	#69340 with half collisionality, $\nu = \nu_0/2$
9	#69340 Ref.	Reference #69340 ($\delta < 0$) case
10	#69340, No imp.	#69340 with $n_C = 0$
11	#69508, $a/L_{T,i}$ from #69340	#69508 but with $a/L_{T,i}$ from #69340
12	#69508, $a/L_{T,e} = 0, a/L_{T,i} = 3$	#69508 but with $a/L_{T,i} = 3$ and $a/L_{T,e} = 0$

In subfigure (c) of Fig. 4.7 we show two additional runs done for #69508. The yellow line corresponds to the third run, for which the ion temperature gradient was set to zero, such that a TEM, propagating in the electron direction, is found over the entire k_y spectrum. It is interesting to note that the growth rate increases when $a/L_{T,i} = 0$ (compare with the blue curve in subfigure (a) in Fig. 4.7). This could be related to the same mode that is destabilised when impurities are included. However, in the present case, it propagates in the electron direction, rather than in the ion direction, as was seen before. A similar effect was actually also seen in the $\delta < 0$ case when the temperature gradient was lowered (see orange curve in subfigure (b) in Fig. 4.7). Finally, the brown curve in subfigure Fig. 4.7 (c) shows the linear simulation for run 12, which is clearly completely dominated by an ITG-like mode.

We now move on to the nonlinear simulations, where we consider a similar grid resolution to what we used for the simulations of #49052 and #49051: $N_x \times N_{ky} \times N_z \times N_{v_{\parallel}} \times N_\mu \times N_s =$
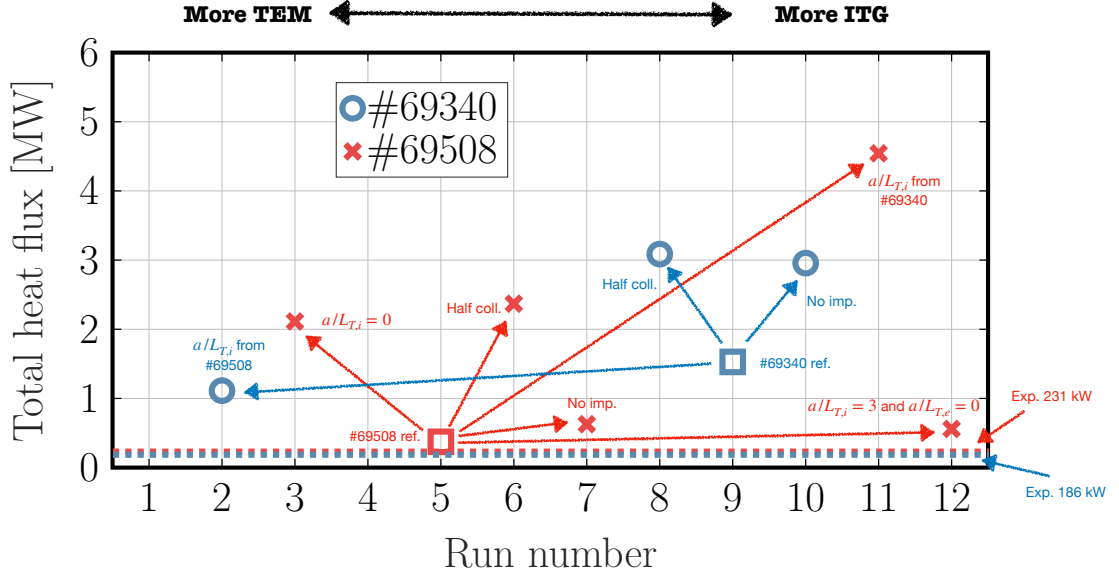
Figure 4.8 – The heat flux from the nonlinear GENE simulations for the runs in Table 4.2. The cases with $\delta > 0$ (#69508) are shown in red while the cases with $\delta < 0$ (#69304) are shown in blue. We use crosses and circles for the two equlibria respectively, apart from the reference cases which are shown as squares. The dashed lines indicates the experimental values. Note that run one and four correspond to the discharges #49051 and #49052, and are therefore not shown.

$256 \times 64 \times 30 \times 48 \times 16 \times 3$ with $k_{y,min}\rho_s = 0.059$ and $l_x = 127\rho_s$ for $\delta > 0$, and $N_x \times N_{ky} \times N_z \times N_{v_\parallel} \times N_\mu \times N_s = 256 \times 64 \times 50 \times 48 \times 16 \times 3$ with $k_{y,min}\rho_s = 0.055$ and $l_x = 134\rho_s$ for $\delta < 0$. For these parameters, the heat fluxes for the reference #69508 and #69340 cases are converged within 20%. We did not do additional resolution studies, but kept the grid resolution constant for the other runs in Table 4.2. The much larger values of N_z for the $\delta < 0$ case is due to the more complex magnetic geometry, which requires more grid-points in the straight field-line poloidal angle to be properly accounted for.

The simulated heat fluxes for each run are illustrated in Fig. 4.8. As already mentioned, the reference #69508 case reproduces the experimental heat flux value well, while the reference #69340 case overestimates the flux. Halving the collisionality increases the heat flux in both equilibria (see five to six and nine to eight respectively), the effect being the largest for $\delta > 0$ where ν is larger. Removing impurities has a destabilising effect in both $\delta > 0$ case (five to seven) and in $\delta < 0$ (nine to ten). Reducing $a/L_{T,i}$ gives a lower heat flux (nine to two) while increasing it increases the flux (five to 11). Setting the electron temperature gradient to zero, while increasing substantially the ion temperature gradient (five to 12), also corresponds to increased flux. We also see an increase in the flux (five to three) when we set $a/L_{T,i} = 0$, which is consistent with the increase in the linear growth rate seen in Fig. 4.7. This increase in the growth rate is consistent with the observations in Ref. [77], and supports the idea that the dominant mode is a density-driven TEM.
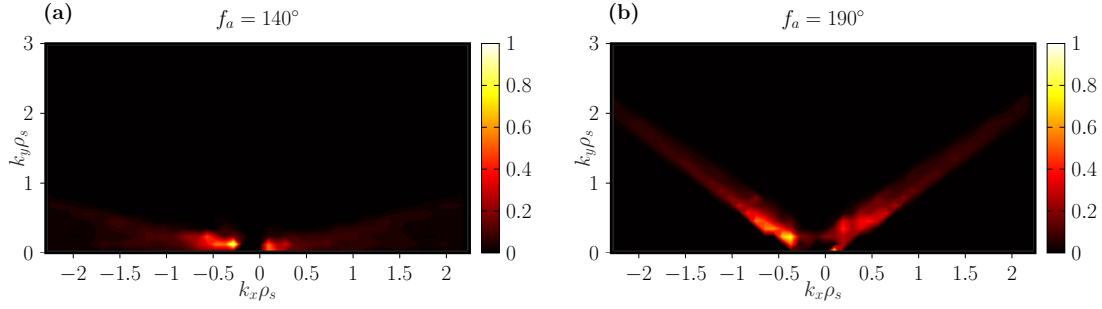
Figure 4.9 – The PSD illustrating the selected k_x and k_y components for two different orientations of the spatial filter. Mainly $k_y = 0$ components are selected when using $f_a = 140°$ (a), while for $f_a = 190°$ (b) the TPCI measurement is more dominated by $k_y \neq 0$ fluctuation components.

In the next subsection we will apply the synthetic diagnostic and continue to study these various runs through the predicted TPCI signals.

4.2.2 Applying the synthetic diagnostic

As in the first cases presented in this chapter, we generate electron density fluctuations for each simulation and then apply the synthetic diagnostic to model the measurements of TPCI. It is important to keep track of the individual contribution from each k_y mode and therefore we use the simplified, plane wave approach for the synthetic modelling presented in section 3.2.1. To be able to compare our results with future experiments, we use the updated set-up of the TPCI diagnostic, described in detail in the next chapter. In particular, instead of nine unevenly spaced detector elements, we consider 32 equally spaced elements. Furthermore, the beam size is increased to 5.9 cm. The dimensions of the spatial filter and the phase plate had to be changed to be compatible with the new set-up: the new filter, as illustrated in subfigure (b) in Fig. 4.1, has a smaller wedge angle, 23 degrees, and a straight filter part for the lowest k_r. The consequence of such a filter configuration is that the integration length becomes dependent on the wave number in the straight filter part. We consider two filter configurations: one with $f_a = 190°$, which focuses on the poloidal k_y contributions, and one with $f_a = 140°$ that predominantly has purely radial contribution (thus the filter is aligned with the normal of the flux surface at the tangency point), and for both discharges #69508 ($\delta > 0$, run five) and ($\delta < 0$, run nine). The selected k_x and k_y components for the two filter configurations are shown in Fig. 4.9. The measurement geometry, including the selected segments for the $f_a = 190°$ filter angle is shown in Fig. 4.10.

The localisation, estimated using the same method as for the past cases, using the true but normalised (by its RHS value) form of the density fluctuations given by Eq. (3.46), is shown in Fig. 4.11 for the $f_a = 140°$ filter angle. In subfigure (a) we include all k_y contributions that scatter light onto the filter. The localisation is very similar to what we already observed in the past (see Fig. 3.13), but in this case, much better localisation is achieved with the considered wedge filter because of the much smaller wedge angle. The unfiltered measurement (not shown) remains
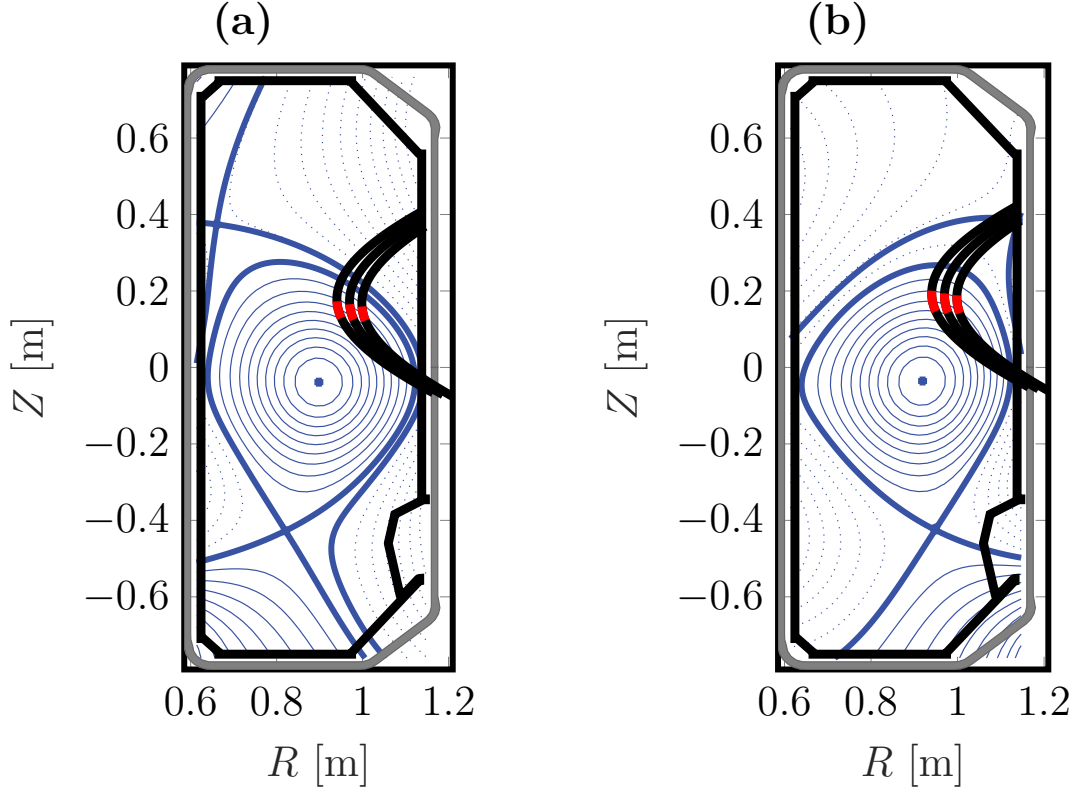
Figure 4.10 – The selected segment in the positive (a, #69508) and negative (b, #69340) triangularity discharges. The red segment indicates the regions along the beam selected by the spatial filter with a 190 degree filter angle.

poorly localised as was previously seen in Fig. 3.16. In subfigure (b) we show the localisation only for the $k_y = 0$ case to better illustrate the effect of the considered spatial filter configuration; localisation is improved with $k_{\perp,\mathbf{B}}(\ell_\perp)$ in the straight filter part, and becomes constant in the wedge part, $k_{\perp,\mathbf{B}}(\ell_\perp) \gtrsim 3$. As expected, localisation becomes worse when the measurement is focusing on the contribution from $k_y \neq 0$ fluctuation components, as is shown in Fig. 4.12.

We proceed by computing the synthetic signals for each of the runs in Table 4.2, using for now only the $f_a = 190°$ filter orientation. The conditional spectra are shown in Fig. 4.13 and Fig. 4.14. The corresponding wave-number spectra and frequency spectra are shown in Fig. 4.15 and Fig. 4.16. An interesting signature in the signals can already be observed in the conditional spectra, but is most clear in the wave number spectra: scenarios with increased ITG content tend to be dominated by $k_r > 0$ while TEM dominated cases mostly have structures with $k_r < 0$. For example, compare the reference $\delta > 0$ case in Fig. 4.15 (blue curve, run five) and the case with increased $a/L_{T,i}$ (orange, run 11). The latter is dominated by a peak at $k_r \sim 2$ cm^{-1} while the first has a peak at $k_r \sim -2$ cm^{-1}. Similarly, we can see a clear difference in the conditional spectra in Fig. 4.13 when we compare the reference cases with $\delta > 0$ (subfigure b) and $\delta < 0$ (subfigure a). The first has more TEM-like activity while the latter has more ITG.
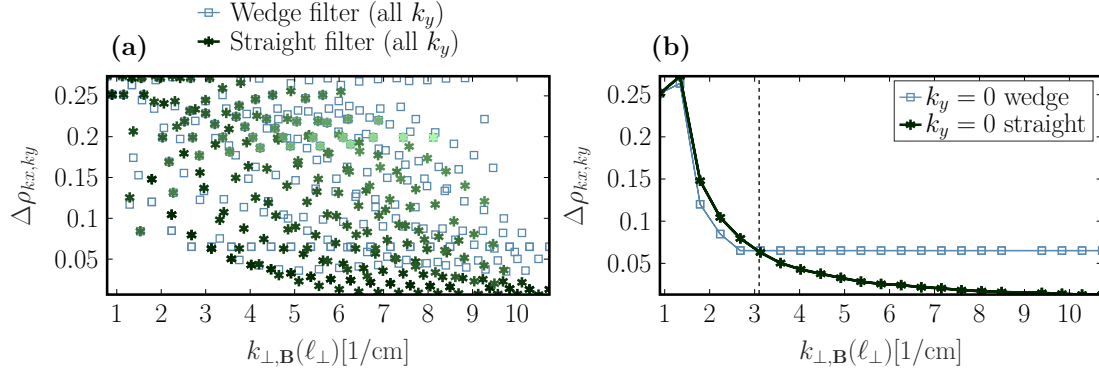
Figure 4.11 – The localisation estimated using the new TPCI set-up, which features a smaller wedge angle and a narrower straight filter near the center. Here we show the localisation when $f_a = 140°$. The localisation obtained when using this wedge filter (blue squares) is compared with the localisation that would be obtained if a narrow straight filter is used instead (green asterisks). In the latter, the gradient in color, from dark to light green, indicates an increase in the k_y wave number. All k_y contributions that scatter light into the filter are included in (a) while in (b) only the contribution from $k_y = 0$ is shown.

Halving the collisionality (subfigure c and d) seems to increase the phase velocities (see the left bands with $k_r < 0$), which is indicated by the slope of the black dashed lines, and which are a fit of the maximum frequency for each k_r. The steepening is due to a steep decay of the frequency spectra, as can be seen especially for the $\delta > 0$ case, in Fig 4.15 but also in the $\delta < 0$ case in Fig. 4.16. This could be explained by the increased dissipative effect collisions have at smaller scales. Because of this flattening, higher frequency components at low k_r have larger amplitudes in the conditional spectra, thus leading to an overall increase in the phase velocity, as is seen in Fig. 4.13, especially in subfigure (d). Halving the collisionality also leads to an increased amplitude of $S(k_r)$, in agreement with the increased growth rate in Fig. 4.7. Removing impurities also increases the amplitude of the TPCI signals. For $\delta > 0$ the frequency spectrum in Fig. 4.15 becomes slightly more peaked, leading to a reduced overall phase velocity as seen in Fig. 4.13 (f). In $\delta < 0$ instead, impurities seems to have a similar effect as collisions thus flattening the frequency spectra in Fig. 4.16 and increasing the phase velocities in Fig. 4.13 (e). From this we can conclude that the dilution effect of impurities is more pronounced in the $\delta > 0$ case, while in $\delta < 0$ their main effect is via collisions. Finally, increasing the main ion temperature gradient in the $\delta > 0$ case increases significantly the fluctuation amplitude and flattens the frequency spectra, again leading to increased phase velocities in Fig. 4.13, (h). Instead, when we lower the ion temperature gradient in the $\delta < 0$ case, the fluctuation amplitude decreases slightly, but the main difference is that fluctuations with $k_r < 0$ clearly becomes the dominant feature. As already mentioned, this seems to be a signature of an increased TEM content in the scenario. We will explore this in more detail in the next subsection, where we will directly compare the ITG/TEM content measured with TPCI with the characteristics of the modes in the corresponding nonlinear simulation.
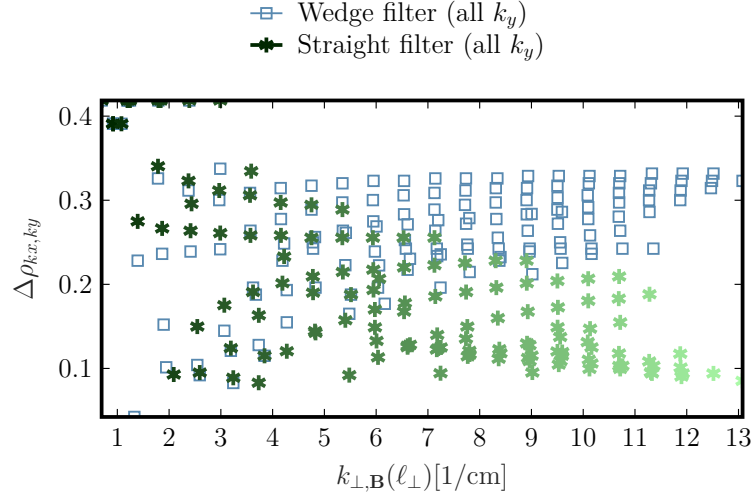
Figure 4.12 – Same as subfigure (a) in Fig. 4.11 but using $f_a = 190°$.

4.2.3 Estimating ITG/TEM content with TPCI

In the nonlinear simulations it is possible to identify the power of modes propagating in the ion direction or the electron direction, by computing the power spectral density for each k_y in the simulation. We define the frequency spectrum in the following way

$$P_{NL}(\omega, k_y, z) = \sum_{k_x} |\delta n_e(k_x, k_y, z, \omega)|^2, \tag{4.1}$$

where the sum is taken over all k_x modes and where we have carried out a Fourier transform over the relevant frequencies ω of the density fluctuations, considering the full nonlinear saturated phase of the simulation. We usually evaluate this quantity only at the outboard midplane, $z = 0$. An example of this quantity is shown in the first column in Fig. 4.17 for the TEM-dominated run five (subfigure (a)) and the ITG-dominated run 11 (subfigure (c)). We notice that most of the contribution to the power is coming from only a small number of k_y modes. In subfigure (a) there are clearly more modes propagating in the electron direction ($\omega < 0$), while in subfigure (c) there is a dominant contribution from ITG-type fluctuations ($\omega > 0$).

Let us define the ratio between the ITG and TEM contributions in the following way

$$R_{NL} = \frac{\sum_{k_y, \omega > 0} P_{NL}(\omega, k_y, z = 0)}{\sum_{k_y, \omega < 0} P_{NL}(\omega, k_y, z = 0)}. \tag{4.2}$$

For a TEM dominated case we thus have $R_{NL} < 1$ and for an ITG dominated case we have $R_{NL} > 1$, as is illustrated in Fig. 4.17. In comparison, in the right column of Fig. 4.17 (subfigure (b) and (d)), we show the corresponding wave-number spectra computed from the synthetic TPCI signals, when using the $f_a = 190°$ configuration (similar to subfigure (b) in Fig. 4.16 and
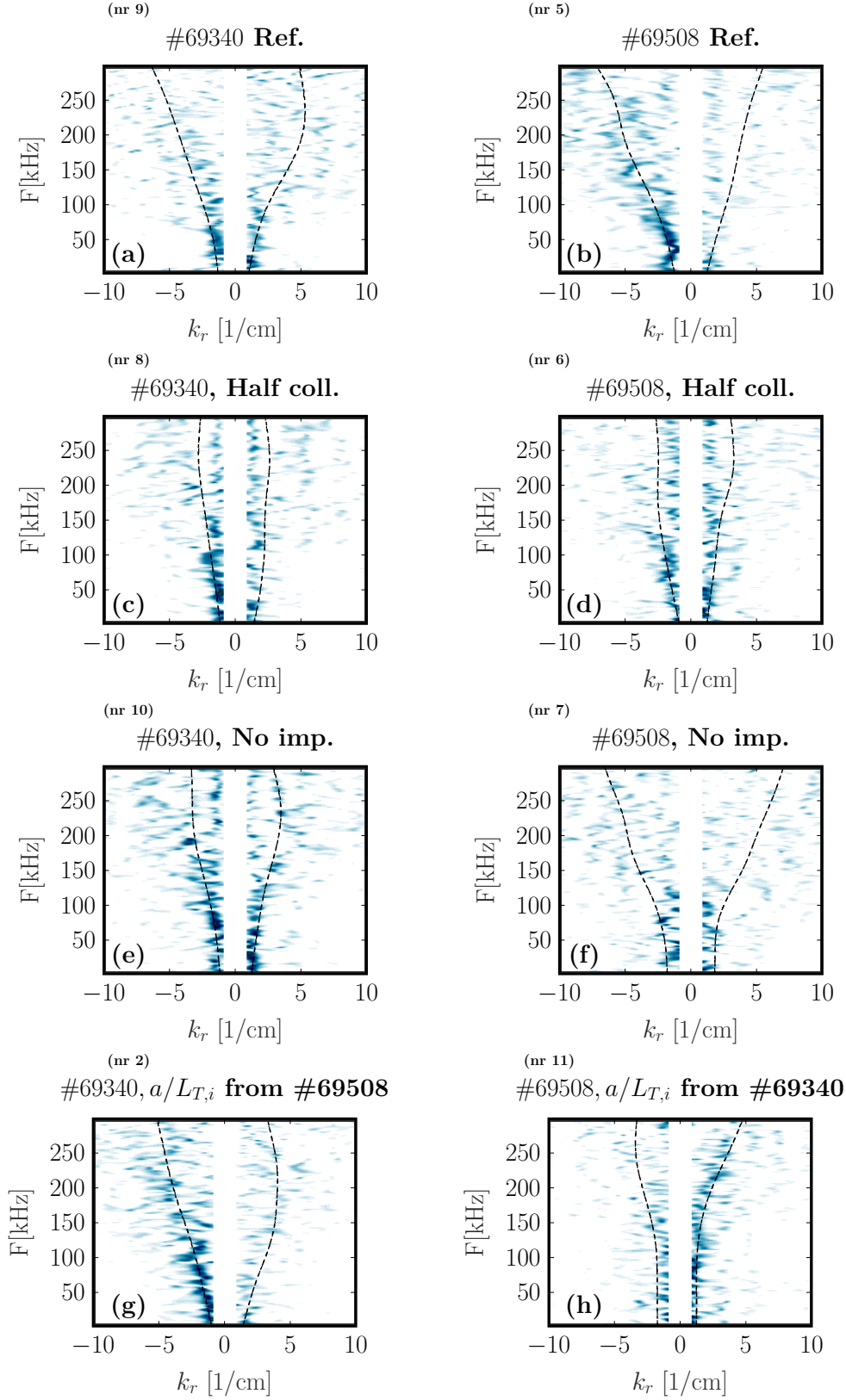
Figure 4.13 – Conditional spectra for $\delta > 0$, #69508 (left column) and for $\delta < 0$, #69340 (right column). The dashed black lines map out a fit of the maximum frequency at each wave number.

(nr 12)
$\#69508, r_a/L_{T,i} = 3, r_a/L_{T,e} = 0$
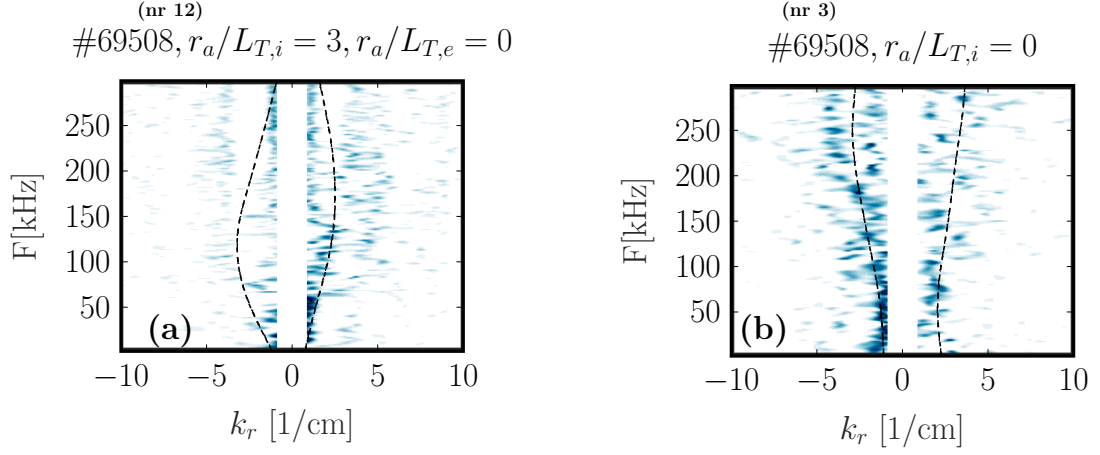
(nr 3)
$\#69508, r_a/L_{T,i} = 0$

Figure 4.14 – Conditional spectra for $\delta > 0$, #69508 for runs 12 (a) and three (b) from Table 4.2. The dashed black lines map out a fit of the maximum frequency at each wave number.
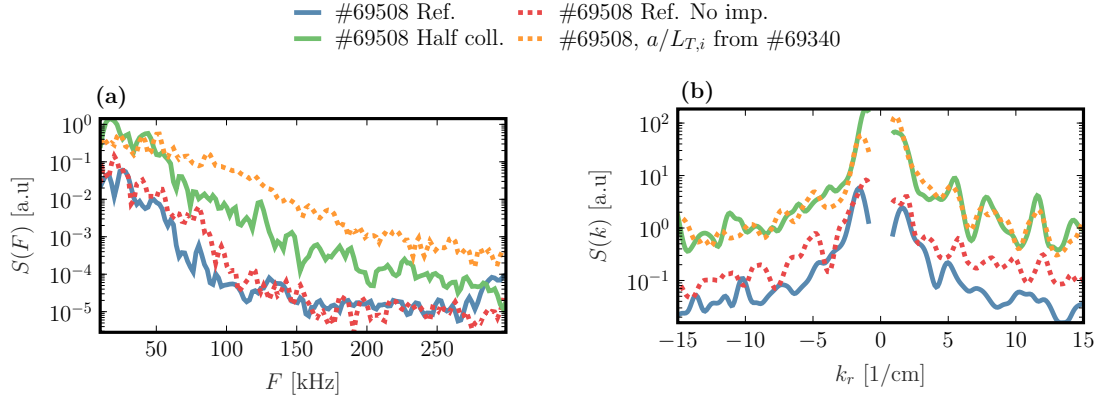
Figure 4.15 – Frequency (a) and wave-number (b) spectra for #69508 ($\delta > 0$).
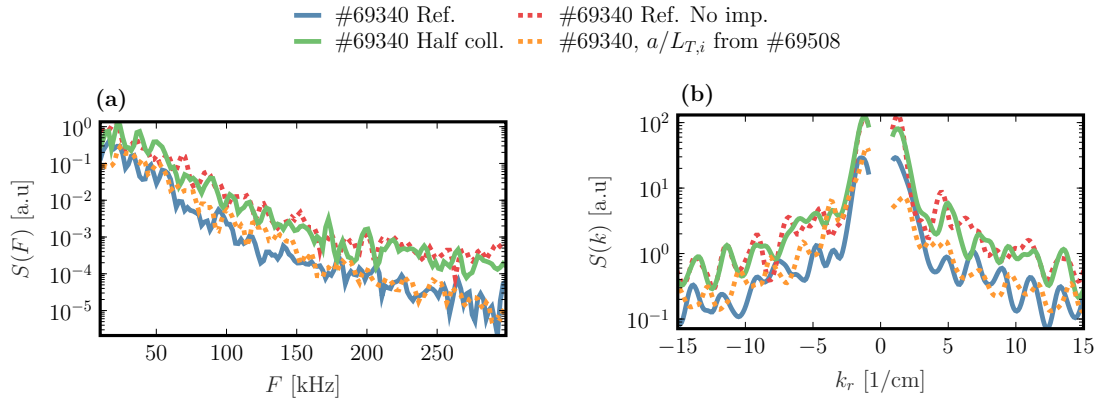
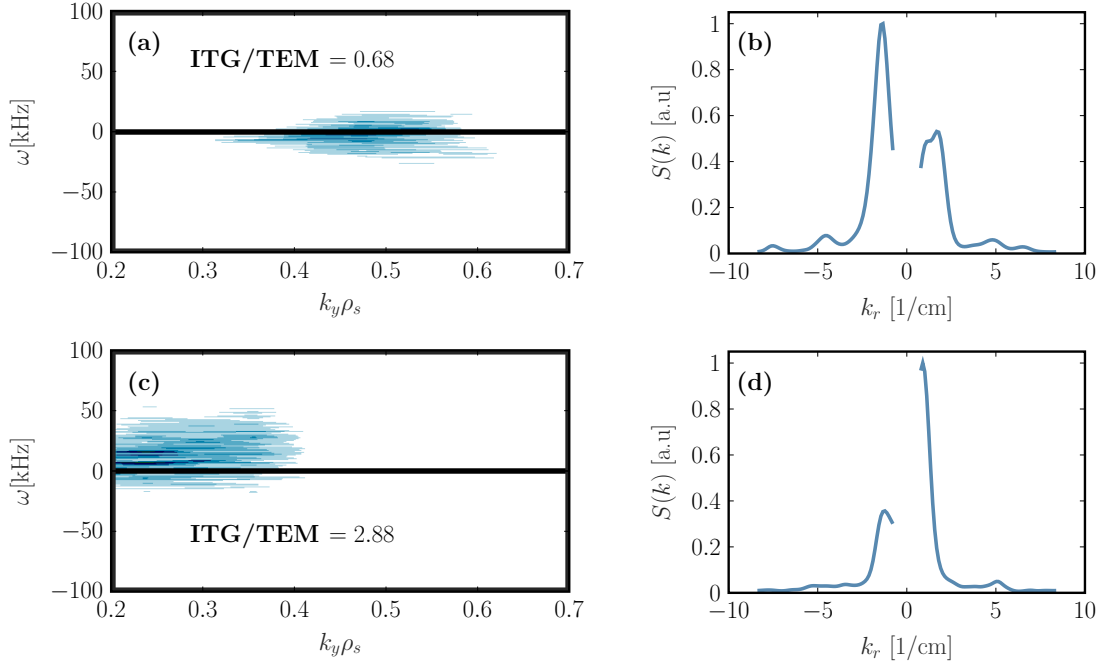Figure 4.16 – Frequency (a) and wave-number (b) spectra for #69340 ($\delta < 0$).

Figure 4.17 – An example of the frequency spectra $P_{NL}(\omega, k_y, z = 0)$, computed with Eq. (4.1) (a,c), and the wave-number spectra (b,d) computed from the synthetic signals (similar to right subfigure in Fig. 4.16 and Fig. 4.15) when using the $f_a = 190°$ configuration. The top row shows a case dominated by TEM type fluctuations, while the bottom is dominated by ITG. The top row shows the results for run five while the bottom row is for run 11.

Fig. 4.15). As was already observed in the previous subsection, the ITG cases have a dominant peak in $S(k_r)$ at $k_r > 0$, while the TEM cases are dominated by $k_r < 0$. Let us define the ITG/TEM ratio for TPCI as follows

$$R_{TPCI} = \frac{\sum_{k_r} S(k_r > 0)}{\sum_{k_r} S(k_r < 0)}. \tag{4.3}$$

When evaluating this ratio it is important to note the ion diamagnetic direction e_d and compare it to the orientation of the unit vector e_r. In the cases studied in this chapter $e_r \cdot e_d > 0$, meaning that $R_{TPCI} > 0$ corresponds to a case dominated by modes propagating in the ion-diamagnetic direction (for example ITG), while $R_{TPCI} < 0$ is dominated by modes propagating in the electron-diamagnetic direction (such as TEM). Reversing for instance the direction of the toroidal magnetic field would result in $e_r \cdot e_d < 0$ and ITG modes would appear on the left of the k_r wave-number spectra.

For a proper evaluation of the ITG/TEM content in the plasma it is also important to include the Doppler shift due to poloidal $E \times B$ rotation. In the simulations considered in this work we do not include the external rotation of the plasma, but it will, in general, be present in the experiments, especially when NBI is applied. The rotation will lead to a Doppler shift ω_d of the frequency components in the wave-number and frequency spectra $S(\omega \pm \omega_d, k_r)$. For large enough ω_d

fluctuating components might appear to propagate in the opposite diamagnetic direction (for example a TEM with $\omega < 0$ might appear as an ITG with $\omega > 0$). However, with knowledge of the Doppler shift ω_d it is straightforward to correct the wave-number and frequency spectra, such that k_r, once again reflects the diamagnetic propagation direction of the modes. In the remainder of this chapter we proceed by assuming that we work in the frame rotating with the plasma.

For each of the nonlinear simulations in Table 4.2 we evaluate the ratio R_{NL} from the nonlinear simulation and compare it to the ratio R_{TPCI} computed from the synthetic TPCI signals. The result is shown in Fig. 4.18, where the run numbers, as was indicated earlier, were chosen to reflect increasing content of ITG-like turbulence (thus ensuring a monotonic curve of R_{NL} versus run number). The ratio R_{TPCI} computed from the synthetic diagnostic reproduces the monotonic trend of the nonlinear result R_{NL} very well, with the exception of run number 12, where a decrease in the ratio is seen while R_{NL} is clearly increasing. We do not expect to get an exact match between R_{NL} and R_{TPCI} as it would require the spatial filter angle and width to be chosen such that the contribution from the most important fluctuations is properly taken into account. The difference between R_{NL} and R_{TPCI} for run 12 suggests that non-negligible contributions from fluctuating components are filtered out in the TPCI signals. A different filter angle could potentially give a better match. The importance of choosing the right filter angle can also be illustrated by computing R_{TPCI} for the alternative filter configuration, $f_a = 140°$, where the measurement is dominated by purely radial modes. As shown by the dashed orange line in Fig. 4.18, clearly, no clear trend is observed.

In the case of the $f_a = 190°$ configuration, we have separated the old runs, #49051 and #45052 (green curve), corresponding to run one and four, from the other cases because of the different equilibria and filter configuration. This again to stress that a good comparison of R_{TPCI} between scenarios should be done for a similar measurement geometry and a similar filter configuration that captures the effect of the most important modes.

The result obtained here shows that in the actual experiments, for a properly oriented filter, an increasing R_{TPCI} value can be interpreted as an indication of an increasing ITG content in the plasma. However, one always has to be very careful to not falsely interpret an increasing R_{TPCI} as a transition from TEM to ITG dominated plasma, when what is actually seen may be a transition from a measurement dominated by $k_y \neq 0$ to one case dominated by $k_y = 0$. This could for example happen if the measurement geometry is changing for a fixed filter angle, either because the magnetic equilibrium is changing or because the plasma is vertically displaced while the measurement position is changed. At the beginning of this chapter, we already saw that a $k_y = 0$ dominated plasma (#49052) features an outward propagating GAM, thus $R_{TPCI} > 1$. For the same filter configuration in the negative triangularity case we instead saw the measurement being dominated by $k_y \neq 0$ with $R_{TPCI} < 1$. In this case the transition does not mean a transition from ITG to TEM, but rather a transition from a measurement dominated by $k_y = 0$ to one dominated by $k_y \neq 0$, which in turn happens to be dominated by TEMs.

Regarding the k_y contribution to the TPCI signals, which was evaluated by computing the total
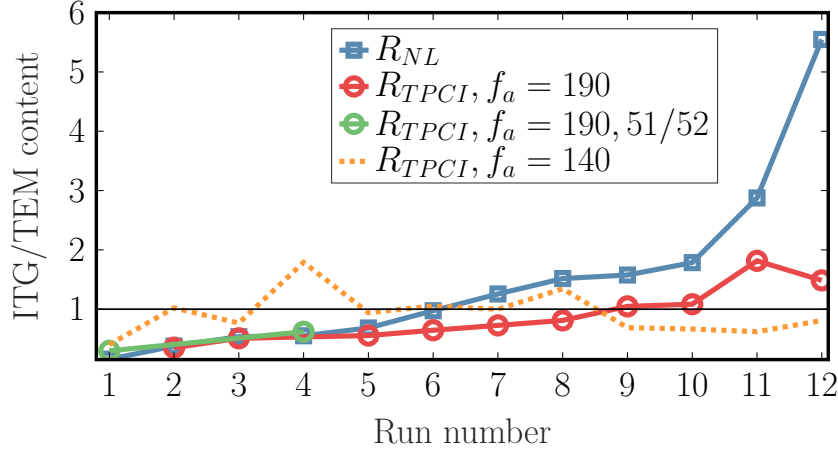
Figure 4.18 – The ITG versus TEM content estimated via the nonlinear ratio R_{NL} of Eq. (4.2) (blue squares), or the TPCI ratio R_{TPCI} of Eq. (4.3) when using a 190° (circles) or 140° (dashed orange curve) orientation of the filter. In red we show the new cases #69508 and #69304 while in green are the old ones related to discharges #49051 and #49052.

power in $S(k_r)$ when considering each k_y mode separately in the sum Eq. (3.35): it is very peaked and only a few k_y modes actually contribute to the measurement. This is shown by the red dotted curve in Fig. 4.19, for the 190° filter configuration. In all cases, it seems that all of the contribution to the signals comes from $k_y\rho_s < 1$. For comparison, we show the electrostatic heat flux spectra (blue solid curve) computed from the corresponding nonlinear simulation. We show the heat flux spectra rather than the density spectra because, later, in subsection 4.2.4, we will make a connection between nonlinear results and modelled TPCI signals, with the quasilinear predictions of the heat flux. In any case, the density spectra peak at similar k_y values as the heat flux spectra. We see that k_y corresponding to the peak contribution to TPCI matches the k_y related to the peak contribution in the heat flux very well. In Fig. 4.20, we show the same results, for the two example runs nine and five, but in the case of a 140° filter angle. Clearly, in this case the measurement is dominated by $k_y = 0$ and no information on the k_y spectra of the fluctuations can be obtained. In general, in Fig. 4.19 larger k_y modes tend to be more damped in the TPCI signals compared to the result from the nonlinear GENE simulations. This is because the higher k_y modes poorly satisfy the condition $\boldsymbol{k}_\perp \perp \boldsymbol{k}_0$ as was shown in the last chapter when we estimated the localisation, for example in Fig. 3.13. This means that the modes contribute to the TPCI measurement across the full laser beam path. However, by placing a narrow wedge filter in the laser beam path, we cut away this contribution, thus damping the larger k_y components. If we had a wider filter then the damping would be less, as is the case of runs one and four in Fig. 4.19 for the two old #49051 and #49052 cases, where a wider wedge filter was used.

Finally, in the 190° filter configuration, the TPCI wave number k_r is a function that varies with k_y. This means that through the TPCI signals it is possible to identify whether a scenario is dominated by larger or smaller k_y mode numbers. For example in subfigure (e) in Fig. 4.19 the dominant contribution is at $k_y\rho_s \sim 0.6$ while in subfigure (g) it is near $k_y\rho_s \sim 0.4$. The corresponding TPCI
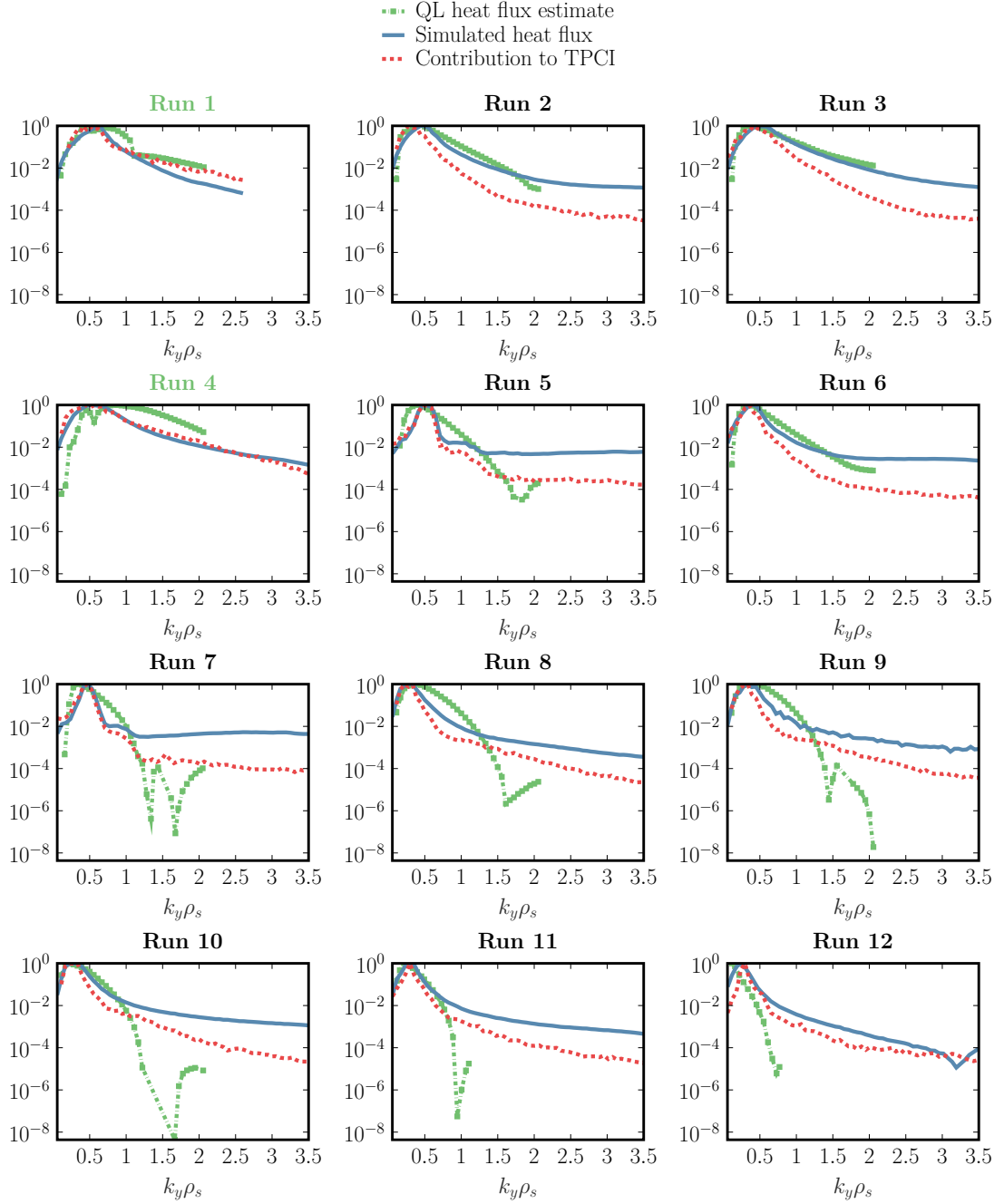
Figure 4.19 – The heat flux spectra $Q(k_y)$ computed from the nonlinear simulation (blue) and the contribution from each k_y to the TPCI signals (red) for a 190° orientation of the filter. In green we show the quasilinear estimates of the heat flux spectra. All curves are normalized to their maximum value with respect to k_y. The result is shown for all of the 12 runs in Table 4.2, with the cases highlighted in green (runs one and four), highlights the different magnetic geometry and the wider wedge-filter configuration that was used.
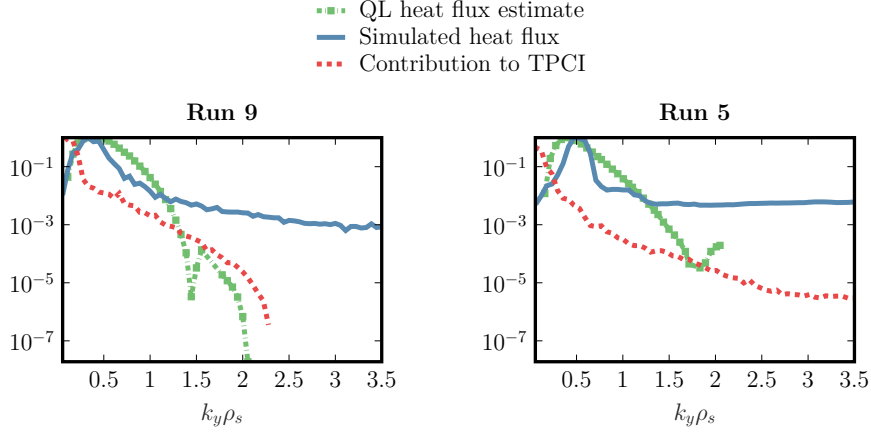
Figure 4.20 – Same as Fig. 4.19 but using a 140° orientation of the filter. In this case, the TPCI measurement is clearly dominated by low k_y components as shown with the two examples of run five (left) and run nine (right) from Table 4.2.

wave-number spectra are shown in Fig. 4.21, where we can clearly distinguish the case with dominant contribution from larger k_y (blue) from the case dominated by lower k_y (red).

To conclude, we have shown that it is indeed possible to use the TPCI diagnostic to understand whether the plasma is primarily driven by ITG modes or TEM, as long as the spatial filter is oriented such that the contribution from purely radial modes is damped. The contribution to the signal in this case matches well the dominant k_y modes, as seen in the k_y spectra computed directly from the corresponding nonlinear GENE simulations. The next step would be to test these predictions with actual experiments. We could do this by measuring the fluctuations in the two discharges, #69508 and #69340, that have been analysed in this chapter. However, we would then be constrained to measuring the fluctuations at $\rho_t = 0.7$, where the input parameters to our simulations have been computed. For measurement at other radial positions or for completely different discharges, we would need to carry out additional nonlinear simulations to be able to identify possible transitions from TEM to ITG. This is computationally very demanding and time consuming, making it unpractical for day to day analysis of TPCI measurements. Instead we are looking for a more efficient way of predicting TPCI signals. As we will see in the next subsection, much can already be inferred from simple linear simulations.

4.2.4 Predicting TPCI signals with quasilinear simulations

It is possible, to some extent, to predict nonlinear parameters by running computationally cheap linear simulations and applying a quasilinear method [78–82]. The QuasiLinear (QL) model is, in essence, an approximate method for predicting nonlinear heat and particle fluxes. This method consists of performing several linear simulations with varying input parameters and at several poloidal k_y mode numbers. For every set of input parameters, one makes an estimate of the heat or particle flux F_s for a given species s. This can be realised for a given species by computing a
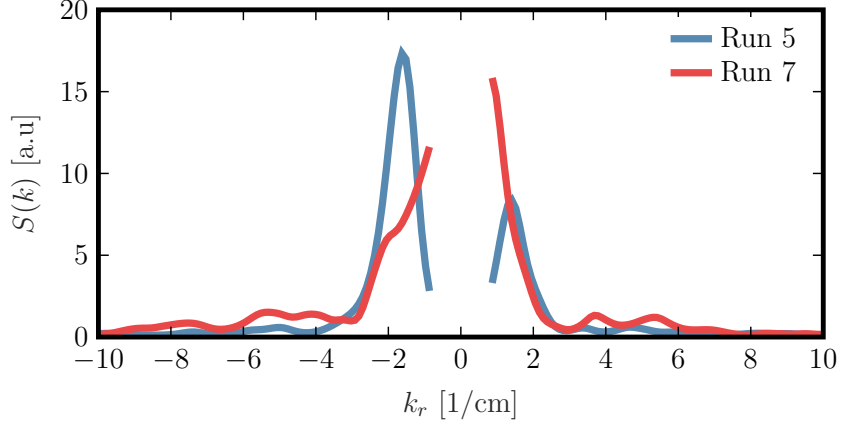
Figure 4.21 – Wave-number spectra with the peak contribution in the k_y spectra shown in Fig. 4.19 at low k_y (red) and larger k_y (blue).

sum over k_y mode contributions of the linear flux $F^L_{s,\mathrm{norm}}(k_y)$ weighted by the QL weight $w(k_y)^{QL}$. In the case of the heat flux, we thus have

$$Q_s^{QL} = A_0 \sum_{k_y} w^{QL}(k_y) Q^L_{\mathrm{norm},s}(k_y). \tag{4.4}$$

The quasilinear weights model the saturation of the fluxes in nonlinear simulations given by

$$w^{QL}(k_y) = \left(\frac{\gamma(k_y)}{\langle k_\perp(k_y)^2 \rangle} \right)^\zeta, \tag{4.5}$$

where γ is the growth rate of the linear mode. For $\zeta = 1$ the weights correspond to a 'mixing length' saturation rule, but we choose here $\zeta = 2$ which is the standard choice that normally yields the best agreement between the QL model and the corresponding nonlinear results. The flux-surface averaged perpendicular wave-number, further weighted by the eigenmode envelope, is given by

$$\langle k_\perp(k_y)^2 \rangle = \frac{\sum_{k_x} \int \mathrm{d}z \, k_\perp^2(k_x,k_y,z) |\phi(k_x,k_y,z)|^2 J(z)}{\sum_{k_x} \int \mathrm{d}z \, |\phi(k_x,k_y,z)|^2 J(z)} = \frac{\sum_{k_x} \langle k_\perp^2(k_x,k_y,z) |\phi(k_x,k_y,z)|^2 \rangle}{\sum_{k_x} \langle |\phi(k_x,k_y,z)|^2 \rangle}, \tag{4.6}$$

where $J(z) = [(\nabla x \times \nabla y) \cdot \nabla z]^{-1}$ is the Jacobian and $k_\perp^2 = |k_x \nabla x + k_y \nabla y|^2$.

The normalized linear heat flux contribution from a given k_y mode appearing in Eq. (4.4) reads

$$Q^L_{\mathrm{norm},s}(k_y) = \frac{\left\langle \frac{1}{C} \sum_{k_x} 2\mathscr{R} \left[i k_y \phi^* \int \mathrm{d}v^3 \, \delta f(k_x,k_y,v) \right] \right\rangle}{|\phi(k_x=0,k_y,z=0)|^2|}, \tag{4.7}$$

where $C = B_0/\sqrt{(\nabla x \cdot \nabla x)(\nabla y \cdot \nabla y) - (\nabla x \cdot \nabla y)^2}$. Here $\mathcal{R}$ stands for the real part and

$$\langle A \rangle = \frac{\int A(z)J(z)\,\mathrm{d}z}{J(z)\,\mathrm{d}z}, \tag{4.8}$$

for the flux-surface average. In both Eq. (4.6) and Eq. (4.7) we take the sum only over the three lowest order k_x contributions ($k_x = -\Delta k_x, 0, \Delta k_x$) which has been shown to give the best results [78]. Regarding the k_y sum, we have seen in our tests that it is important to keep the same $k_{y,\mathrm{min}}$ as in the corresponding nonlinear simulation, but that it is sufficient to stop the sum at half the corresponding $k_{y,\mathrm{max}}$.

In the k_y spectra in Fig. 4.19, discussed earlier, we added the QL estimate of the heat flux (green dotted lines). We see that in almost all of the cases, the peak of the heat flux is very well reproduced by the QL estimates. Given that contribution to the TPCI signals match the peak in the nonlinear k_y-spectra, it follows that we can use the QL estimates to predict the dominant contribution to the TPCI signals when the diagnostic is configured appropriately, i.e in the here considered case for the filter angle $f_a = 190°$. By taking the ratios between the ion and electron heat flux, the QL estimates can also be used to probe whether the scenario is dominated by ITG modes (typically $Q_{ion}^{QL}/Q_{electron}^{QL} > 1$) or TEMs (typically $Q_{ion}^{QL}/Q_{electron}^{QL} < 1$). In Fig. 4.22 we compare the nonlinear estimates R_{NL} of the ITG/TEM content, already shown in Fig. 4.18, with the QL estimates of the heat flux ratios (orange curve). Although the values are slightly different, we notice that the monotonic trend of increasing ITG content, as we move from run one to 12, is well reproduced (with run four as a (small) outlier). We also show the corresponding nonlinear heat flux ratio, which matches the QL predictions rather well. Even though it is a physically somewhat different quantity, the heat flux ratio thus appears as a good proxy to predict the trend of increasing ITG content in the TPCI signals. A slight exception is run four, which suggests that there is an increased ion heat flux which is, however, not as closely reflected by increased density fluctuations relative to modes propagating in the ion diamagnetic direction.

We can estimate the ratio R_{NL} more directly by noticing a remarkable feature in the frequency and k_y spectra in the nonlinear simulations. In Fig. 4.23 we compare the spectra evaluated at the beginning of the simulation i.e at time $t = 40a/c_s$, right after the linear phase, to the spectra after considering the full saturated phase of the simulation at time $t = 1200a/c_s$ for an example TEM-dominated case. The envelope of the blob formed in frequency and wave-number space remains similar. This is better illustrated in subplot (a) in Fig. 4.23 where we show the PSD for the dominant k_y contribution. This feature was observed for most of the runs in Table 4.2, suggesting that perhaps it is possible to predict the ITG/TEM ratio R_{NL} already through linear simulations.

To test this idea we consider the exponential growth of a linear mode at some k_y, with growth rate γ_{k_y} and frequency ω_{k_y} such that $\delta n(k_y, t) = A \exp\left[-i(\omega_{k_y} + \gamma_{k_y})t\right]$. Taking the Fourier transform
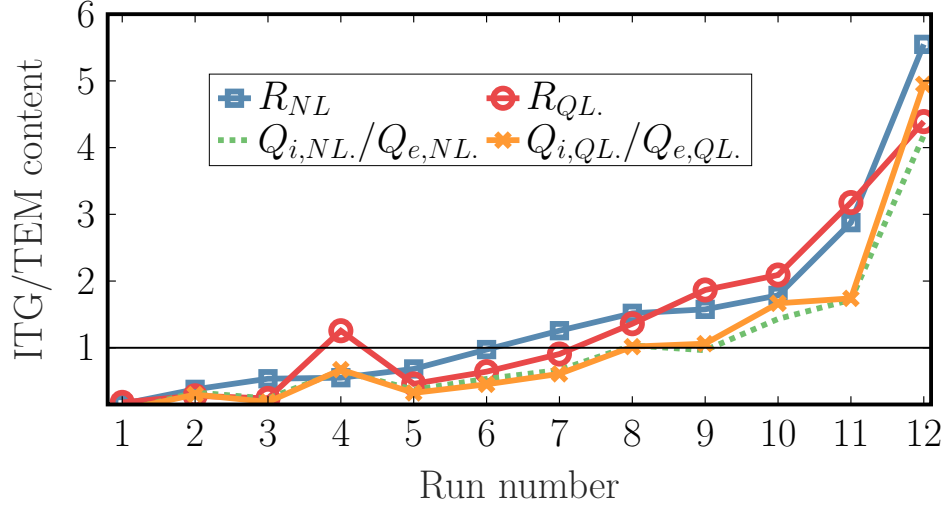
Figure 4.22 – The nonlinear estimate of the ITG/TEM content R_{NL} (blue squares) and the nonlinear ion-over-electron heat-flux ratio (dashed green line). These are compared to the QL heat flux ratio orange asterisks and the QL estimate of the ITG/TEM content R_{QL} (red circles).
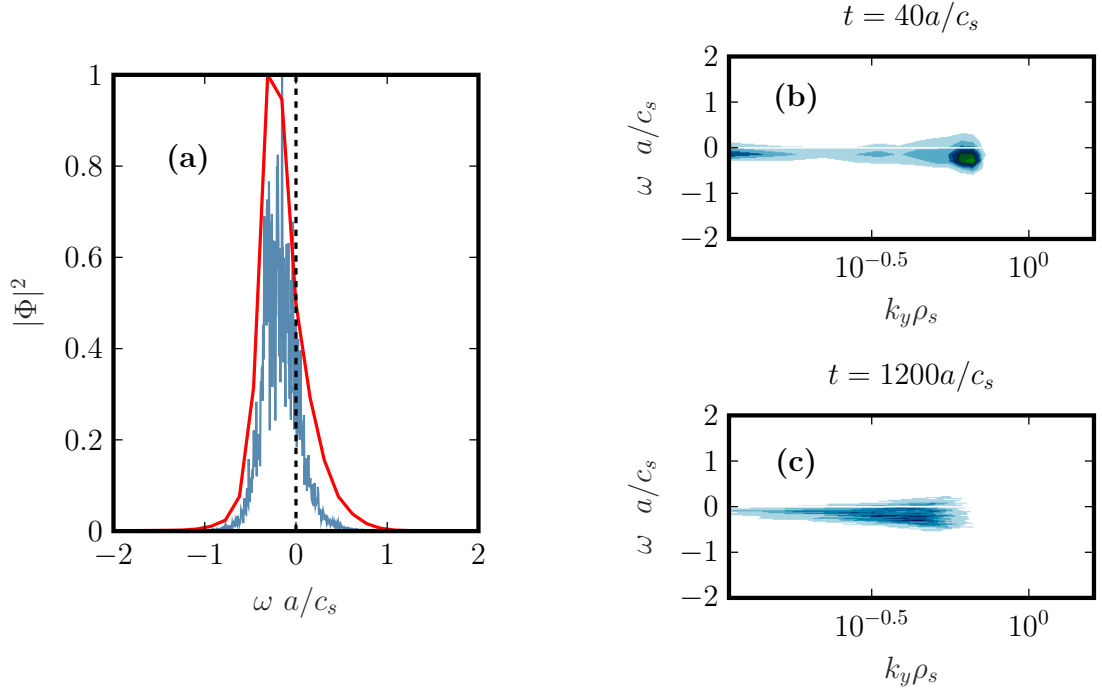

Figure 4.23 – PSD of the electrostatic potential $\left|\Phi^2\right|$ after just considering the initial linear phase (b) or the full saturated phase in the considered nonlinear simulation (c). In (a) we show the PSD for the dominant k_y mode, comparing again the linear phase (red) with the full nonlinear saturated phase (blue).

of this quantity gives,

$$\int_0^T A e^{i(\omega_{k_y}+\gamma_{k_y})t} e^{-i\omega t}\, dt = \frac{A}{\gamma_{k_y}+i(\omega_{k_y}-\omega)}\left[\left(e^{T\left(\gamma_{k_y}+i(\omega_{k_y}-\omega)\right)}-1\right)\right],$$

when evaluated over a time window T and the PSD is then

$$P_L(k_y,T,\omega) = \frac{A^2}{\gamma_{k_y}^2+(\omega-\omega_{k_y})^2}\left(e^{2T\gamma_{k_y}}+1-2e^{T\gamma_{k_y}}\cos(\omega_{k_y}-\omega)\right). \tag{4.9}$$

This corresponds to a peak in frequency around $\omega = \omega_{k_y}$ which is broadened because of the exponential growth γ_{k_y}. Because of this broadening, a purely ITG dominated scenario may still lead to frequency contributions interpreted as corresponding to modes propagating in the electron diamagnetic direction and vice-versa, just as is observed in a nonlinear simulation. The coefficient A is assumed to be a constant and can be removed by considering ratios of $P_L(k_y,T,\omega)$ as will be done in the following.

Based on Eq. (4.9) we develop a simple QL estimate R_{QL} of the nonlinear ratio R_{NL}

$$R_{QL} = \frac{\sum_{k_y} w^{QL}(k_y)\left(\sum_{\omega>0}P_L(k_y,T,\omega)\Big/\sum_{\omega}P_L(k_y,T,\omega)\right)}{\sum_{k_y} w^{QL}(k_y)\left(\sum_{\omega<0}P_L(k_y,T,\omega)\Big/\sum_{\omega}P_L(k_y,T,\omega)\right)}, \tag{4.10}$$

where we used the QL weights from before. The time T is fixed to $40\ a/c_s$ corresponding to the typical saturation time seen in the nonlinear simulations. This quantity is evaluated for each nonlinear run and shown in Fig 4.22 (red circles) and seems to provide a slightly improved estimate of R_{NL} compared to simply considering the heat-flux ratio. Again, run four is an exception where the QL weights clearly overestimate the ITG contribution. We do not yet have an explanation for this outlier, which shows that our proposed strategy is not yet completely robust, and should not be trusted fully. In fact, there is not a first-principle basis that could give a physical explanation that could motivate our observations. Nevertheless, for most cases considered here, it does seem that R_{QL} can be used to detect conditions where the ITG/TEM content seems to change. Once these conditions have been found, they can be verified with TPCI measurements and nonlinear simulations.

To conclude, in this section we have shown that we can predict certain aspects of the TPCI signals through simple linear simulations. We can see if the signals are dominated by $k_r > 0$ or $k_r < 0$, and whether the dominant contribution comes from low or high k_r mode number.

In the final section of this chapter we will summarise our findings and make an example of a prediction of TPCI signals using linear simulations, for future comparison with TCV experiments.

4.3 Chapter summary and discussion

In this chapter we have used the synthetic diagnostic to improve our interpretation of TPCI measurements. First in section 4.1 we focused on the two discharges #49052 and #49051 that had already been analysed in past experiments with TPCI. The filter configuration was such that the measurement mainly came from purely radial modes. Our conclusion was therefore that the main changes observed in the experiments are to be attributed to a change from a measurement dominated by the zonal modes, such as the GAM ($\delta > 0$, #49052) to a measurement where the $k_y = 0$ modes were suppressed. The GAM was seen to lead to a dominant peak at $k_r > 0$, while, without it, the measurement is dominated by $k_r < 0$.

In the next part of this chapter we investigated what we could learn about the ITG and TEM turbulence if the spatial filter in the TPCI set-up was rotated to damp the contribution from the $k_y = 0$ modes. We found that in this case, the TPCI measurement becomes indeed sensitive to the characteristics of ITG/TEM turbulence. We found for example collisions to be stabilising, thus leading to reduced amplitudes of the TPCI signals. We also found that by computing the ratio between the power of modes with $k_r > 0$ over the power of modes with $k_r < 0$ we can distinguish a plasma more dominated by ITG modes from a plasma dominated by TEM fluctuations. Finally, we found that the measurement accurately reproduced the main contribution in the nonlinear k_y heat-flux spectra.

In the final part of this chapter, we showed that certain characteristics may be estimated with fast and computationally-cheap linear simulations. In particular it appears possible to predict if the TPCI measurement will be dominated by $k_r > 0$ or by $k_r < 0$ and if the dominant k_r is large or small. Finally, a change in the linear growth rate also predicts a corresponding change in the amplitude of the TPCI signals. To illustrate the method with the linear simulations we conclude this chapter by making an example prediction of TPCI signals. We consider the discharge #68408 that was carried out in the past to investigate the transition of a plasma from a Linear Ohmic Confinement regime (LOC) to the Saturated Ohmic Confinement regime (SOC). This discharge has been studied in detail with the CXRS diagnostic and a publication is under preparation by F. Bagnato et al. There it is shown that a transition from LOC to SOC, by means of a density ramp, is due to a stabilisation of TEM turbulence in an initially TEM dominated plasma, which then becomes ITG dominated. Experiments are planned with the TPCI diagnostic to investigate the ITG to TEM transition in this scenario. This discharge is of particular interest for its absence of NBH which is normally required to raise the ion temperature and drive ITG modes.

The profiles for the low, middle and high density cases are illustrated in Fig. 4.24. We employ the method described in this chapter to make predictions for the TPCI signals in this scenario. Linear simulations during different times of the discharge are shown in Fig. 4.25. From top to bottom we show the low, middle and high density case, going from the LOC to SOC regime. The gradient in the color corresponds to a radial scan: dark to light colors indicate a radial scan from $\rho_t = 0.5$ to $\rho_t = 0.8$. From the growth rate in all cases we clearly see that modes become more unstable towards the edge, consistent with the increased gradients that are typically observed in
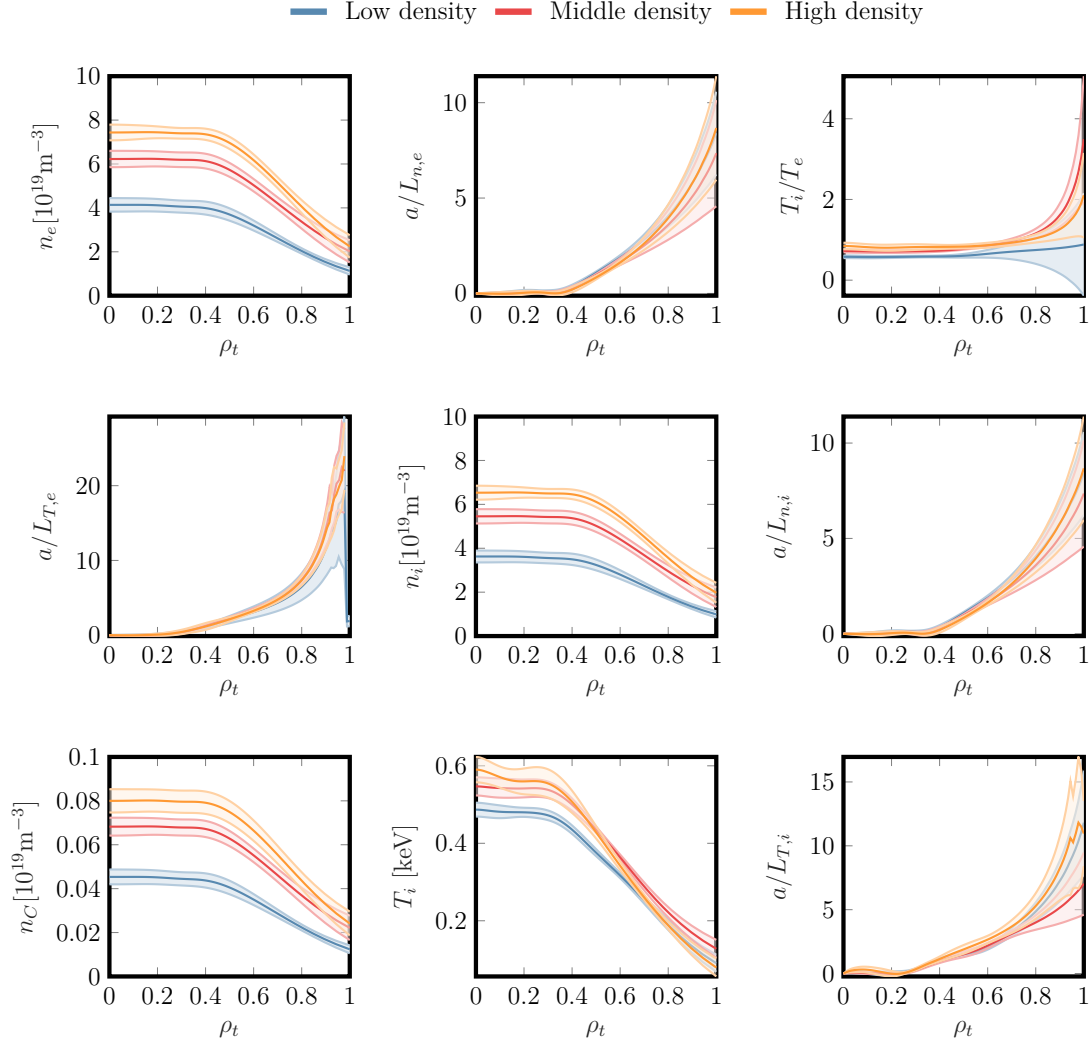
Figure 4.24 – Profiles for the low density (blue), middle density (red) and high density (orange) phases of the TCV discharge #68408.

the edge. If we compare the frequency we clearly see that the scenario transitions from a mostly TEM dominated case (low density, subfigure (a)) to an essentially purely ITG dominated case (high density, subfigure (c)). The growth rate seems to reach a minimum at the middle density (see dark lines in subfigure (b)) and increase again slightly while in the high density case. This is consistent with the plasma transitioning from the LOC to the SOC regime. It is also clear that the transition from TEM to ITG starts in the core and later propagates towards the edge. This is better illustrated if compute the ITG/TEM ratio R_{QL} which is shown in Fig. 4.26.

In the low density regime the discharge is already ITG dominated in the core, but otherwise TEM dominated towards the edge. At intermediate density, ITG dominates up to $\rho_t \sim 0.75$. The very high density is completely dominated by ITG from edge to core.

(a)
Low density
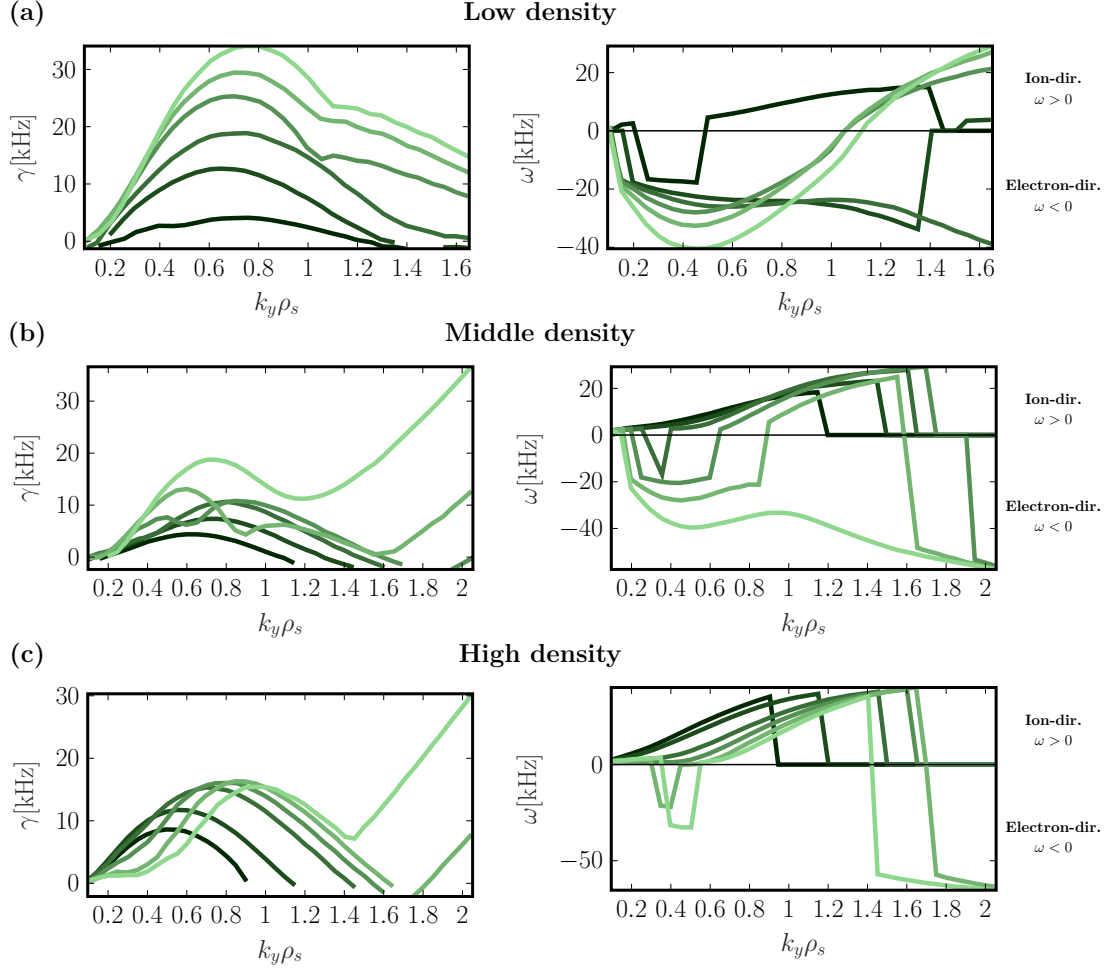

(b)
Middle density

(c)
High density

Figure 4.25 – Linear simulations of the low density (a), middle density (b) and high density (c) parts of the discharge #68408. The gradient in the color, from dark to light green, indicates an increase in the radial position considered in the linear simulations. The left column shows the growth rate while the right columns shows the real mode frequency.
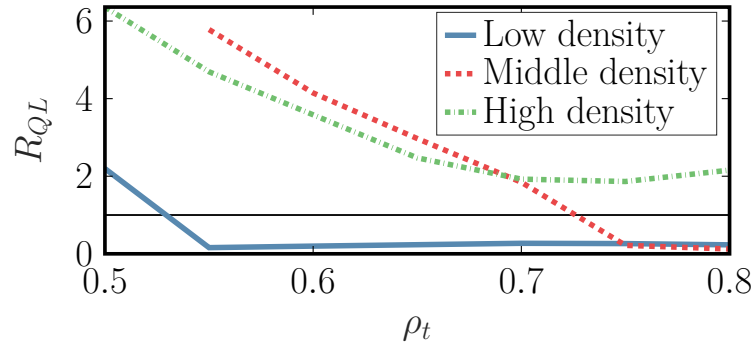

Figure 4.26 – An estimate of the ITG/TEM ratio in the low density (solid blue), middle density (dashed red) and high density (dotted green) part of the discharge #68408.

Finally, we can also estimate the heat flux spectra, shown in Fig. 4.27. We notice that there is a shift in the dominant k_y contribution. For the low density case the dominant contribution comes from decreasing k_y as we transition from core to edge. In the middle density case, when we move from core to edge, we first increase in the dominant k_y and then strongly decrease, reaching a dominant $k_y \rho_s$ around 0.4. In the high density case we see the opposite trend: the dominant contribution comes from increasing k_y as we transition towards the edge.

In view of our observations in this chapter we can then make the following conclusions regarding the TPCI signals in this scenario:

1. As a result of increased linear growth rates, the measured fluctuation amplitude are expected to increase as we move towards the edge. The overall amplitude will first decrease with density, but then slightly increase as we reach the SOC regime.

2. At low density, $S(k_r)$ will be dominated almost completely by $k_r < 0$, except in the core where the dominant contribution should come from $k_r > 0$. As we increase the density, the measurement will be dominated more and more by $k_r > 0$ ($\sim$ ITG). There should be a delay in the transition: measurements in the edge will move towards $k_r > 0$ later compared to measurements closer to the core.

3. There should be a clear variation in the dominant contribution to $|k_r|$. For low density, measurements from core to edge should see a decrease in k_r. At larger density we should first have an increase in k_r and then a decrease. Finally, for the high density case the opposite trend should be observed and $|k_r|$ should increase as we move towards the edge.

Since these predictions are very sensitive to the radial position in the plasma, they could also be used for validating the estimates of the localisation with experiments. In particular, by using a broad wedge filter, but which still nontheless damps the $k_y = 0$ components, one can test the property $\boldsymbol{k}_{\text{measured}} \perp \boldsymbol{k}_0$.
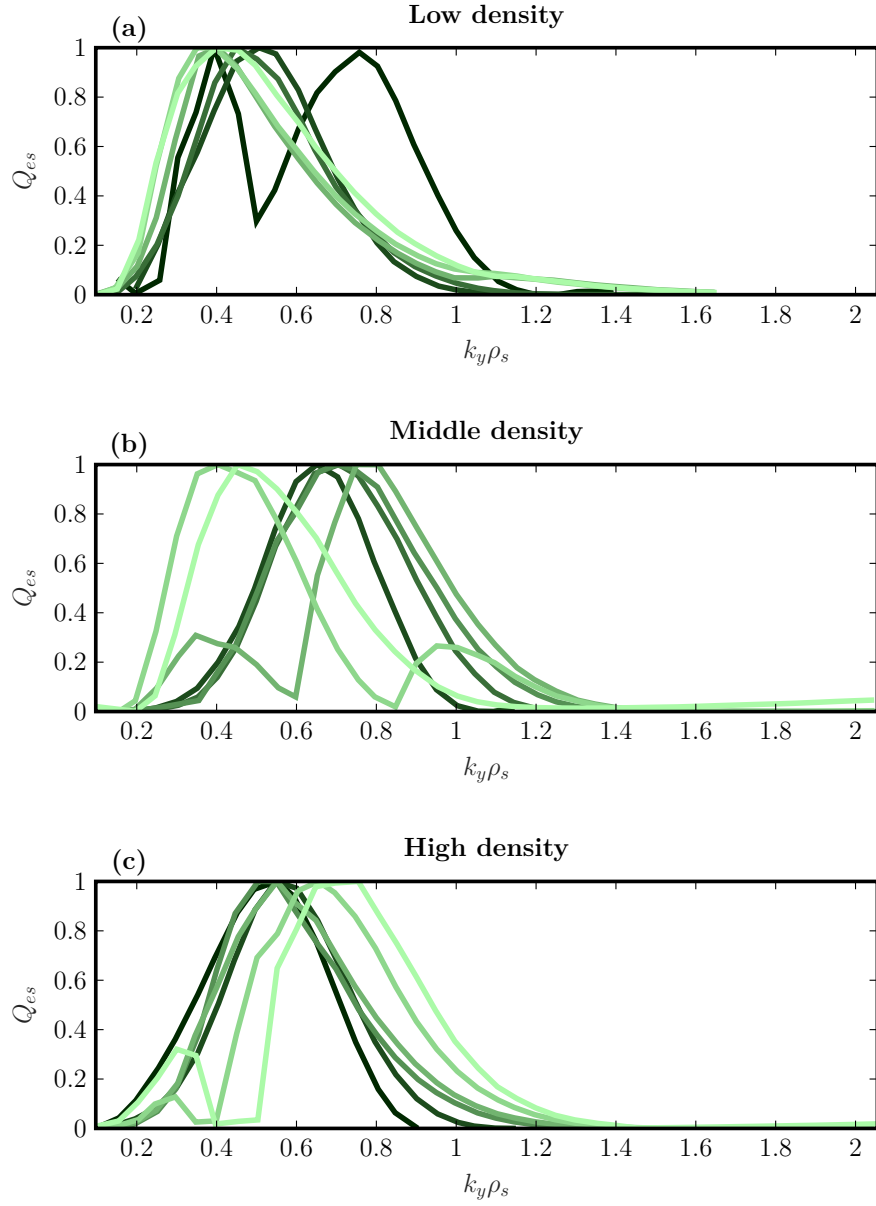
Figure 4.27 – The normalized quasilinear heat flux spectra for the low density (a), middle density (b) and high density (c) part of the discharge #68408. The gradient in the color, from dark to light indicates an increase in the radial position considered in the linear simulations.

5 Upgrades to the TPCI diagnostic on TCV and first measurements

The TPCI diagnostic on TCV has been developed [27] and extensively used in the past to probe ion-scale turbulence in different plasma scenarios [36, 37]: in particular, to study the effect of triangularity on turbulent transport, as well as to make first direct observations of the GAM. In this work, a general upgrade of the existing TPCI diagnostic was planned. Much of the old equipment exhibited very poor performance, in particular, less than 9 out of the 30 photoconductive detector elements previously used to measure the fluctuating phase, were still functioning. The CO_2 laser also showed strong temporal fluctuations, making it very difficult to perform even basic tests in the lab. The aim was to replace this old equipment; however, the main aspect of the TPCI upgrade was to implement a state-of-the-art photovoltaic 64 element detector with a very high bandwidth to make first measurements of electron-scale turbulence. Unfortunately, due to delays and problems, this detector could not be used in this work. Instead, a newly procured photoconductive detector with a lower bandwidth had to be implemented, to measure turbulence at the ion scale.

This chapter presents the experimental part of this thesis work. First, section 5.1 describes the new equipment that was purchased to upgrade the TPCI system, including the laboratory tests that were performed, especially of the detector bandwidth. Also shown is the slightly modified upgraded TPCI set-up, including the new equipment for performing ion-scale turbulence measurements. Due to vibration problems, only data from four TCV discharges could be acquired. The first two were used to further investigate the role of triangularity on turbulence, but in diverted equilibria, unlike previous studies. Next, two discharges were performed to study the effect of ECH on plasma turbulence. The TPCI measurements from these two experiments are presented in section 5.1 and finally a summary of this chapter is given in section 5.3.

5.1   Upgrading the TPCI system on TCV

In this section we will present the upgrade of the TPCI diagnostic. First in subsection 5.1.1 we give details of the new hardware procured for the upgrade and discuss the tests, in particular of

the detector bandwidth, carried out in preparation of the upgrade. Then, in subsection 5.1, we will discuss the new set-up of the diagnostic.

5.1.1   New equipment for the upgrade of the TPCI diagnostic

Several new pieces of equipment were acquired in preparation of the diagnostic upgrade. In particular, a new set of photovoltaic (PV) and photoconductive (PC) detectors were procured, as listed below:

- **Judson 64-element photovoltaic detector and preamplifier**
  A very high bandwidth, state-of the art photovoltaic detector with a linear array of 64 square elements with an area of 0.12×0.12mm^2 and 10μm spacing. The frequency response is designed to have a 3-dB point at 10 MHz. Each detector element has a responsivity of 4 A/W and is followed by a preamplifier with a 1kOhm transimpedance gain. The PV detector is reversed-biased at -0.3 V. Two temperature sensors are installed inside the Dewar for measuring the temperature, in particular the cooling rate, which should not be faster than 3 K/min. A Lakeshore temperature regulator with a controllable cooling rate was used for this task.

- **Sacrificial Judson 4-element PV detector**:
  A smaller, but otherwise identical (in theory) copy of the larger 64 element PV Judson detector. It was procured to perform first tests in the lab to make sure we avoid damaging the larger detector.

- **Infrared Associates 64 element photoconductive detector**:
  Another 64 element, but photoconductive, linear detector array. The square element size is slightly larger, 0.5×0.5 mm^2 with a 50μm spacing. The 3-dB point should be near 400 kHz, but then decay slowly, 10dB/decade, and there is therefore near 40% of the response remaining still at 1 MHz. The response is 20 kV/W with an adjustable preamplifier gain following. In the default state the amplification was 1400.

- **Single element PV Kolmar detector**:
  A very high bandwidth photovoltaic detector, albeit only with a single element. The 3-dB point should be near 60 MHz. Unlike the other detectors it is not AC coupled and can be used to measure the DC signals as well. The element size is 0.1×0.1 mm^2.

Because of its high bandwidth, the Judson detector could be used for measuring very small electron-scale fluctuations. As a backup for this detector, we also procured a lower bandwidth PC detector from Infrared Associates. Finally a single element PV detector from Kolmar was also purchased, for potentially measuring high frequency MHD modes and more generally for support in testing.

We also acquired a new laser, from Access. Just as in the previous set-up, it is a C02 laser, but of

higher power ~ 50 W. Since the phase-contrast signal scales with the laser power, this would increase the minimum detectable phase. The laser beam has a 2.4 mm diameter and 5.5 mrad divergence. The laser is driven by a RF driver, which is driven in turn by a 28 VDC power supply. Both the laser head and the RF driver are water cooled, using a 600-W SMC cooler. A set of new equipment had to be ordered that could sustain the very high power: in particular a water cooled attenuator (Sintec STC-MA-WJ) and a fan-cooled shutter (Lasermet LS-100-12).

Finally, another method for measuring high frequency fluctuations in the MHz range, but using a lower bandwidth detector, could be implemented by downshifting these higher frequency components to the measurable range, using a heterodyning component. Two Acousto-Optical cells were procured for this task (GEF-35-5-10600 WC and GEF-40-5-10600 WC from Brimrose). When a laser light enters the AOM cell at the Bragg angle (here 34 mrad) the laser beam is diffracted into a 0th order and a 1st order component. The diffraction efficiency is 60-70%, and can be regulated through the amplitude of the modulation signal applied to the RF driver connected to the cell. The 1st order component is frequency shifted by the center frequency of the AOM cell. By combining the two AOM cells that have slightly different center frequencies, 35 MHz and 40 MHz respectively in our case, it is thus possible to generate a local oscillator with a ± 5 MHz frequency shift. This component can in turn be used in a heterodyning set-up, to downshift electron-scale frequency fluctuations in the plasma to the measurable range. The AOM cells are water-cooled with the same cooler used for the laser.

The heterodyning set-up was kept available for possible future applications but was not planned to be deployed in the short term. However, we found an additional application for this equipment for testing purposes: by supplying a time varying modulation signal to the RF driver of the AOM cell, it is possible to modulate the power of the laser beam, up to tens of MHz. This offers a unique capability for measuring the frequency response of the various detectors with great accuracy. In particular, we needed to ensure that the Judson detector indeed reaches 10 MHz.

The AOM cell was implemented in a set-up in the lab for testing the response of the PV and PC detectors. This set-up is illustrated in Fig. 5.1. The laser beam first goes through a shutter and an attenuator to regulate its power. It then goes through the AOM cell at the Bragg angle. An Arbitrary Waveform Generator (AWG) sends a modulation signal to the RF driver, which in turn is connected to the AOM cell that diffracts the incident laser beam into a 0th and a 1st order component. The 0th order component is directed onto a beam dump (in practice a power meter), while the 1st order component is directed towards the detector. Just before reaching the detector, one-half of the beam power is split onto a second power meter to monitor the power incident on the detector.

To avoid damaging the 64 element Judson detector that is meant to be actually implemented in the TPCI set-up, first tests were carried out using the identical 4-element sacrificial detector. Importantly, for an accurate measurement of the detector bandwidth, the frequency response of the AOM cell had to be taken into account. The very high bandwidth Kolmar detector was used for this task. It is rated with a bandwidth of 60 MHz and a linear response up to 10 MHz could
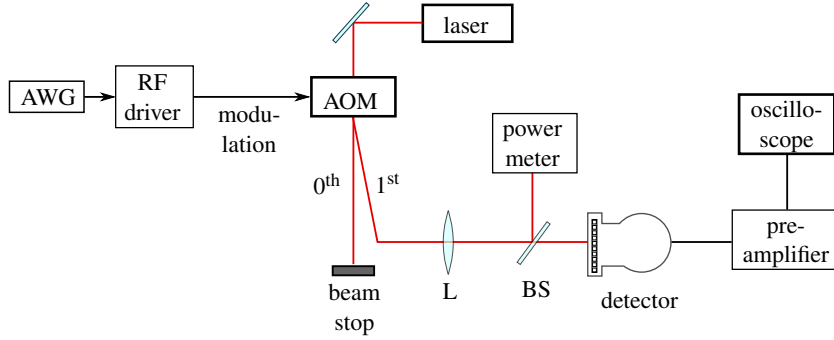
Figure 5.1 – Optical set-up for measuring the bandwidth of the detectors. Source: [83].

therefore safely be assumed. After including the correction of the AOM response, the 3-dB point of the Judson detector appears to be around 8MHz, which is quite close to the specifications. A similar test was then started for the corresponding 64-element detector: however it was seen that the absolute response was much lower than the response of the 4 element detector. Discussion with Judson revealed that a lower absolute response was due to poor thermal contact which does not allow the detector array to cool down to the required 77 K. This leads to a shift in the spectral response towards shorter wavelengths, and at 10.6 μm there is therefore already a significant drop in the response. The detector therefore had to be sent back for repairs, and could not be implemented in the final TPCI set-up, and thus electron-scale measurements, as previously planned, could no longer be performed in this thesis work.

Ion-scale measurements could however still be performed by implementing the 64 element PC Infrared Associates detector. The measured frequency response is shown in Fig. 5.2, confirming a 3-dB point near 300 kHz. This curve could now be used in experiments for adjustments to the signal at higher frequencies.

5.1.2 The upgraded TPCI diagnostic set-up

The TPCI set-up is very similar to what was already used in the past, apart from slight adjustements to include the new laser and detector. The details can for example be found in Refs. [36, 37]. A top view of the optical table used in the old set-up is shown in Fig. 5.4. Here we will mainly summarise the general set-up and point out the changes that were required to implement the new equipment.

The high power Access laser was set up on the optical table as illustrated in subfigure (b) in Fig. 5.5, followed by a shutter and an attenuator similarly to the old set-up shown in Fig. 5.4. As described in Ref. [36] the CO2 laser is co-aligned with a visible laser (Scitec model SDL-635-LM-100T) with a 635 nm wave length and 100 mW power, which is then mainly used for the alignment. The beam of the visible laser, before combined with the CO2 beam, is shown in blue in Fig. 5.4. The two co-linear beams are expanded through a telescope configuration. such that
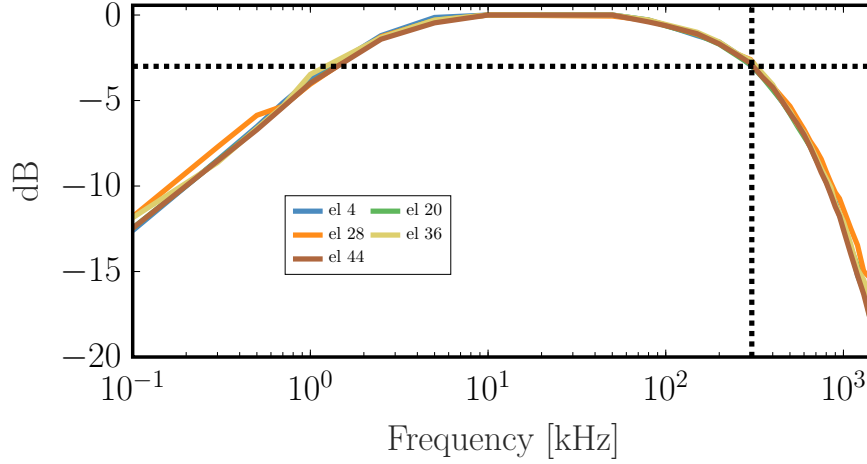
Figure 5.2 – The frequency response of four example elements of the 64 element Infrared Associates detector, corrected with the frequency response of the AOM cell.

the Gaussian beam diameter is 5.9 cm which is slightly smaller than the most restrictive optical component in the laser beam path, to avoid clipping. The laser beam is then sent tangentially through the TCV vessel as illustrated in Fig. 5.3 via a set of elliptical mirrors, five of which are supported on the vessel. The beam enters and exits the plasma through ZnSe windows.

A large off-axis parabolic mirror is used to collect all the light scattered by the plasma. As illustrated in Fig. 5.4, where the returning beam after having passed through the TCV vessel is shown in green, a lens L2 focuses the beam onto the phase plate groove. The beam propagates then through another 2 lenses (L3 and L4) creating a focus point at the spatial filter location, before reaching the detector array on a plane coinciding with the image of the median location in the plasma. The new 64 element PC detector array is shown in subfigure (a) in Fig. 5.5. In the new set-up, the focal lengths of the lenses are the same as the ones of the old set-up shown in Fig. 5.6, except $f_3 = 0.381$ m. The distances are $d_{12} = 4.93$ m, $d_{23} = 0.82$ m, $d_{34} = 1.69$ m and the detector is placed 0.81 m from the last lens. The magnification of the system is 0.4744. Out of the 64 available channels, in this initial set-up, only 29 were used, so that the maximum measurable wave number is about 12 cm^{-1}. The cut-off wave number is 0.76 cm^{-1}. The signal from the preamplifiers goes into two 16-channel ADCs (D-Tacq model ACQ216) with a sampling frequency of 12 MHz and built-in 5 MHz anti-aliasing filters. The acquisition time is 2.6 s, covering the duration of a typical TCV discharge.

The remaining 3 channels of the ADC are instead used for monitoring the focal-control feedback system. Because of the internal reference, TPCI is inherently insensitive to vibrations. However, due to the optics mounted on the TCV vessel, vibrations might shift the TPCI beam such that it misses the phase plate groove. A feedback vibration control system [24, 27] is used for damping these vibrations and keeping the TPCI laser beam on the groove. The feedback circuit relies on an observer based on a quadrant detector (also from Infrared Associates), which detects the error in
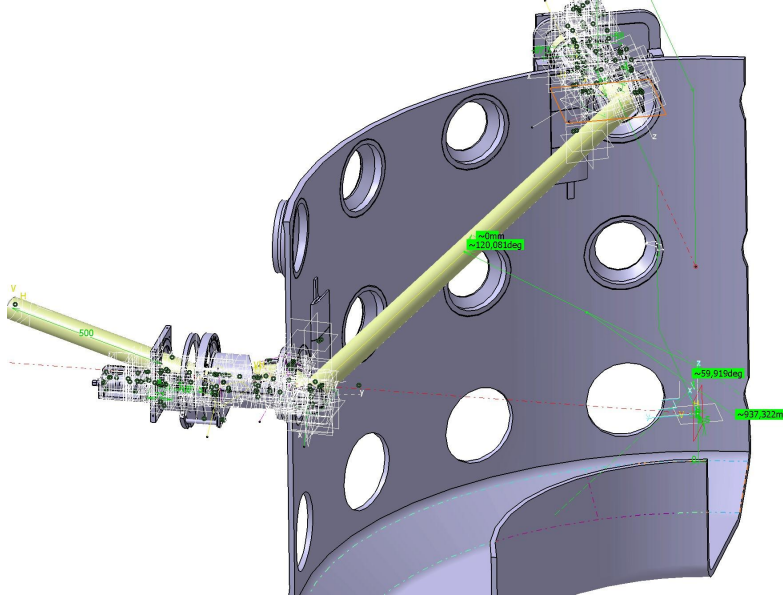
Figure 5.3 – The TPCI beam propagation in TCV. The propagation direction is from left to right. Source: [27].

position along the horizontal and vertical axes. The output from the detector is sent to a frequency compensation circuit that in turn generates two signals, that are used to drive two galvanometer drivers controlling two rotatable mirrors, which compensate for the vibrations. A very small fraction of the TPCI laser beam, depicted with the red lines in Fig. 5.4, is split off after L2 and focused onto the quadrant detector. A remotely driven function generator was implemented to remotely control the offset of the galvanometers. Before a discharge, this offset is varied until the position measured by the quadrant detector is close to the center. Only then could the feedback circuit be locked.

The poor performance of the vibration circuit is the main reason for the limited data that could be obtained in this thesis work. These issues will be further discussed in the next section.

Due the magnification required and constraints on available optics, the spatial filter had to be changed to satisfy the new constraint. The new wedge filter was already illustrated in the last chapter, subfigure (b) in Fig. 4.1. The filter consists of a straight filter part, where the integration length improves with k. For each k_r the angular resolution is given by

$$\theta = \arctan \frac{d_{\text{straight}}}{2y} \tag{5.1}$$

where d_{straight} is the width of the straight filter and $y = F|k_r|/k_0$ is the position along the wedge where a fluctuation with wave number k_r scatters the light. Here $F = 0.81$ is the effective focal length of all lenses up to the spatial filter. The width d_{straight} is in fact larger than the diameter of the diffraction spot. The integration length in the straight filter part therefore ends up being slightly longer compared to the wedge part. Note that all wedge filters in the TPCI set-up
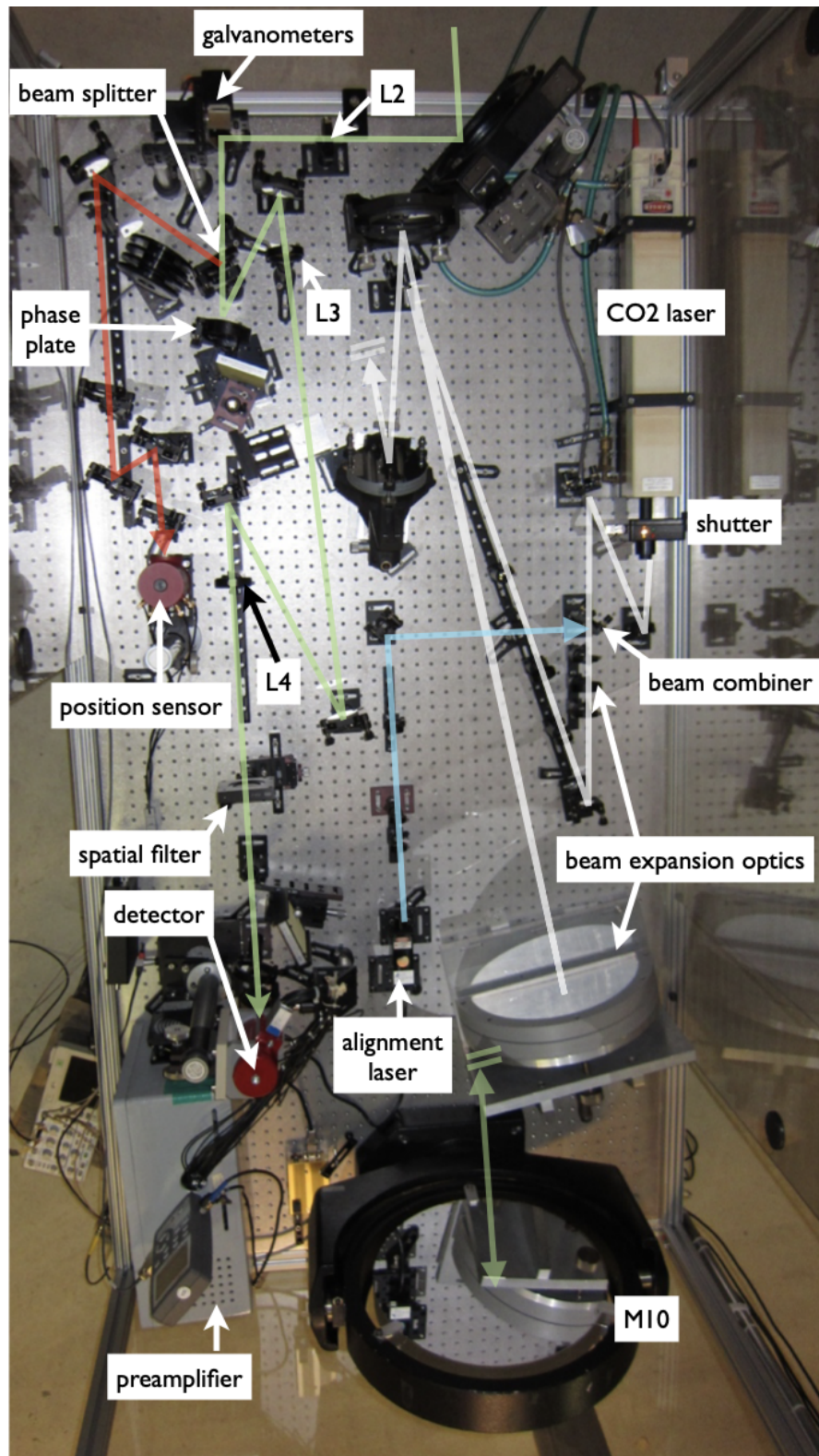
Figure 5.4 – Top-view of the optical table. Source: [37].
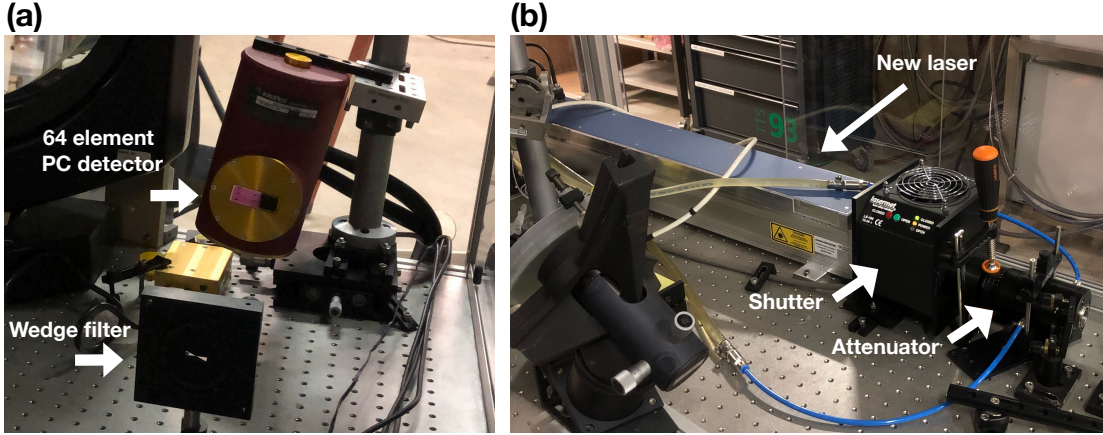
(a)

(b)

Figure 5.5 – A photo of the new 64 element PC detector (a) and the new laser (b), including a new shutter and attenuator that are capable of handling the much higher laser power.
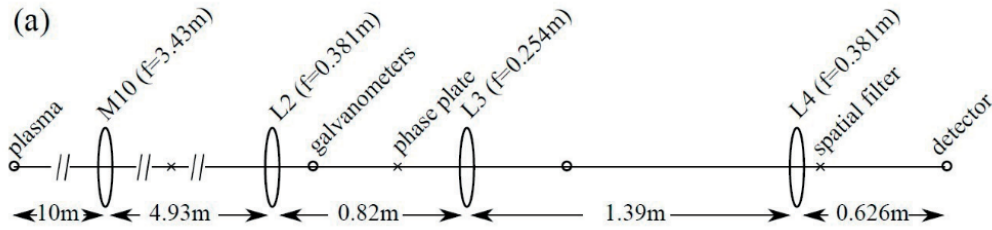

Figure 5.6 – The imaging optical system used in the TPCI set-up. Crosses denote the focal planes while circles denote the image planes. Source: [21].

generally consist of a straight filter segment before the wedge. However, normally the size of the straight filter part is equal to the size of the diffraction limited focal spot, such that only light that is scattered in the wedge part of the filter contributes to the measurement.

In the analysis routines of the TPCI signals, the integration length is computed for each k_r as well as for each ray. The user then has the choice to either average over all the rays and apply the correction of the varying integration length, in wave number space; or to average over k_r and apply the correction in real space.

5.2   First experimental results

The upgraded TPCI diagnostic was made operational in mid-summer 2022, however, because of difficulties with damping the vibrations, only very few measurements could be performed. For reasons that are still being investigated, the feedback circuit that is responsible for damping the oscillations is not performing as it should (and as it used to), and oscillations in particular around 300 Hz are essentially undamped. Furthermore, a drift in the alignment was observed and realignments of the laser beam had to be performed on a daily basis. The reason for this drift was

however not yet understood. Understanding and fixing the issues with the vibrations remains the main task for recommissioning the TPCI diagnostic.

Nevertheless, TPCI signals in four TCV discharges were acquired. Two of these were performed for the study of the role of plasma triangularity in turbulence. Unlike past experiments, these two discharges used diverted plasma configurations. Next, another two measurements were obtained for the study on the effect of EC heating on turbulent fluctuations. The TPCI results from these two studies will be discussed in subsection 5.2.1 and subsection 5.2.2 respectively.

The same analysis routines previously used for studying the synthetic TPCI signals and that were introduced in section 2.1.2, are applied for analysing the signals from the experiments. Out of the 29 detector channels that were in use, only 22 were selected for the analysis. All channels appeared to be sensitive to high-frequency pick-up signals, especially at 200 kHz. Seven of the 29 channels were severely affected and were therefore removed from the analysis. A low-pass and a high-pass filter, with a cut-off at 200 kHz and 20 kHz respectively, were applied to the remaining channels. The frequency response is corrected by the measured detector responsivity, previously shown in Fig. 5.2.

A relative calibration of the TPCI channels is carried out using the standard technique employing acoustic waves [25, 37]. Acoustic waves can conveniently be used for the calibration since they generate a periodic variation in the refractive index in air, with a wavelength similar to the wavelengths of ion-scale plasma turbulence. A transducer is mounted perpendicularly to the TPCI beam, before the last mirrors that send the laser beam inside the TCV vessel, and generates a 15 kHz wave 20 ms before the start of the discharge. Then, in the analysis routines, we apply a narrow, phase preserving, bandpass filter around the acoustic frequency to isolate the acoustic wave in the TPCI signals. Only the first 2 ms are used for analysis to avoid echoes and standing waves. The relative phase, evaluated by calculating the Cross-Spectral Density (CPSD) between channels, is then evaluated between the channels, providing an estimate of the laser beam size in the plasma, and thus the magnification. The relative response, calculated through the power spectral density, gives the calibration factor which is applied to signals of each channel. An absolutely calibrated microphone could be used for an absolute calibration of the TPCI signals, however, during this thesis work an absolute measurement of the sound pressure field was not available and therefore only a relative calibration between the different TPCI channels could be carried out.

In general we find an average magnification around 0.5 which is close to the design value: 0.47. However, the uncertainty is very large, up to ± 0.17, and is furthermore varying between discharges. This translates to a large uncertainty in the estimated wave numbers and correlation lengths of the measured turbulence. It is hypothesised that the reason for this large uncertainty is a change in the shape of the TPCI laser beam, potentially due to overheating of the attenuator used in the set-up. Improving the calibration is important to enhance the accuracy of future TPCI measurements. For the discharges analysed in this section, the average magnification however remained similar. Therefore, despite the uncertainty we still applied the relative calibration when

analysing the signals.

The signals are multiplied by the estimated integration length and normalised to the electron density, measured with the Thomson scattering diagnostic (see section 2.2.1), at the tangency point. Quantities that are shown in real space use the integration length averaged over all k_r. Quantities in wave-number space, such as the conditional spectra and related quantities, instead average over real space and take into account the varying integration length as a consequence of the combined straight-wedge filter configuration. The spectral quantities have 1 kHz frequency resolution and are evaluated by averaging the signals over several time-segments, after applying a Hanning window.

5.2.1 Change in fluctuations between positive and negative triangularity discharges in diverted equilibria

In a recent work [83] a first characterisation of core turbulence, when changing plasma triangularity from positive to negative, in a *diverted* configuration, was carried out. Three different fluctuation diagnostics were used, including the correlation electron cyclotron emission diagnostic for measuring electron temperature fluctuations [84], a pulse reflectometer diagnostic for detecting density fluctuations [85], and the TPCI diagnostic. No significant reduction in turbulence amplitudes was observed, which could be explained by the high collisionality in both scenarios ($v_{eff} = 0.1 R n_e Z_{\text{eff}} / T_e^2 = 2.5 - 4$), for which no significant improvement is expected based on observations of heat transport in TCV [86]. Nevertheless, a change in the nature of the underlying modes could be observed: Broadband features in the TPCI frequency spectra were found in the case of $\delta > 0$, but were less pronounced in the $\delta < 0$ equilibria. The broadband features in $\delta > 0$ were identified as Quasi-Coherent modes (QCMs), which are known to be a signature of strong TEM activity in the plasma [76, 87–89]. Thus, the conclusion was similar to that proposed in the past [76], that $\delta < 0$ stabilises TEM turbulence.

In this subsection we will build on the TPCI results already discussed in Ref. [83] and perform a more detailed analysis of the signals, complemented also by linear GENE simulations of the most unstable mode.

TPCI measurements were obtained for two Ohmic diverted discharges, #75530 with positive triangularity and #75529 with negative triangularity. The TPCI filter angle is $160°$ such that the measurement is close to the tangency point, focusing mostly on radial contributions. However, there is still a non-negligible contribution from poloidal fluctuating components. The TPCI measurement geometry is illustrated in Fig. 5.7, where it is evident that the TPCI rays for $\delta < 0$ pass closer to the core ($\rho_\psi \in [0.45, 0.69]$) compared to in $\delta > 0$ ($\rho_\psi \in [0.59, 0.81]$).

The profiles for the two discharges are shown in Fig. 5.8. Note that CXRS measurements were not available and the ion temperature was computed using the PRETOR formula. The profiles are very similar, with the exception of a slightly increased impurity content in $\delta < 0$ which suggests already that the stabilising effect of triangularity is small, as normally additional heating has to
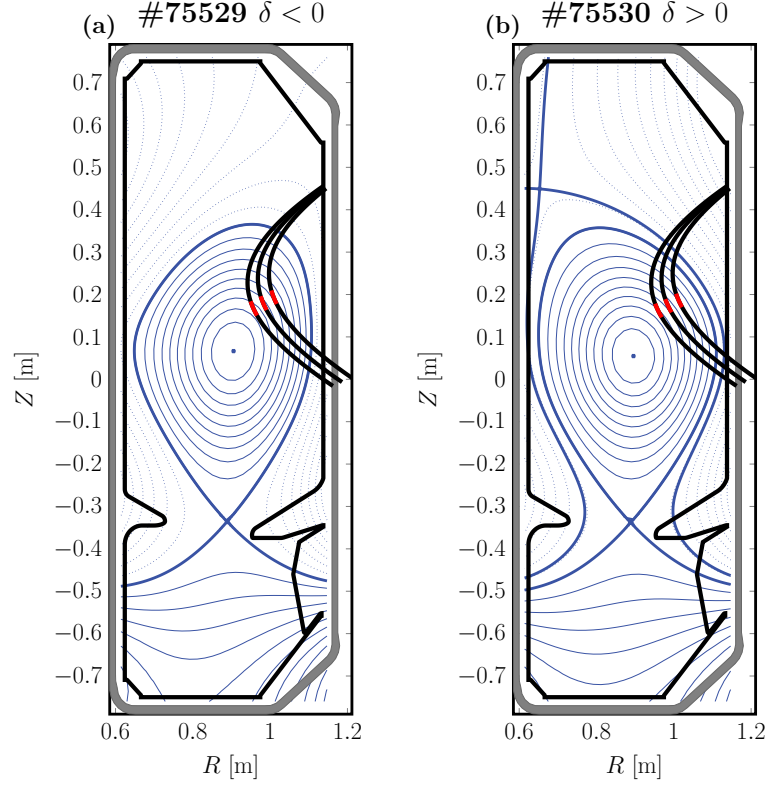
Figure 5.7 – The TPCI measurement geometry in the negative triangularity discharge #75529 (a) and in the positive triangularity case #75530 (b). Three TPCI rays are illustrated in black and the region selected with the spatial filters are shown in red.

be applied in the $\delta > 0$ case to keep the profiles the same, whereas the heat flux is very similar for these two discharges.

A comparison between the PSD in the $\delta > 0$ and $\delta < 0$ cases is shown in Fig. 5.9 for four overlapping radial locations where there are TPCI measurements in both discharges ($\rho_\psi = 0.59, 0.62, 0.64, 0.67$). We also show the two extremes with only measurement for $\delta < 0, \rho_\psi = 0.45$ and only measurement for $\delta < 0, \rho_\psi = 0.81$. These different radial locations correspond to different tangency points of the TPCI rays, where most of the contribution to the measurement is originating. Note that, in contrast to [83], here we have excluded fewer TPCI rays from the analysis and are therefore able to access a larger range in ρ_ψ.

In $\delta > 0$ there is a broad peak at $F = 75$ kHz that persists throughout all radial locations. In Fig. [83] this peak was suggested to be due to the QCM. By looking at Fig. 5.9, (d) $\rho_\psi = 0.64$ it indeed appears that the QCM at 75 kHz has been suppressed for $\delta < 0$. However, by looking at other radial positions the QCM-like fluctuation appears to persist also at $\delta < 0$, albeit at higher frequencies, $F \sim 120$ kHz at $\rho_\psi = 0.59$ and $\rho_\psi = 0.62$ (Fig. 5.9 (b) and (d)).

To analyse the QCM-like modes in further detail we assume invariance in the spatial coordinate
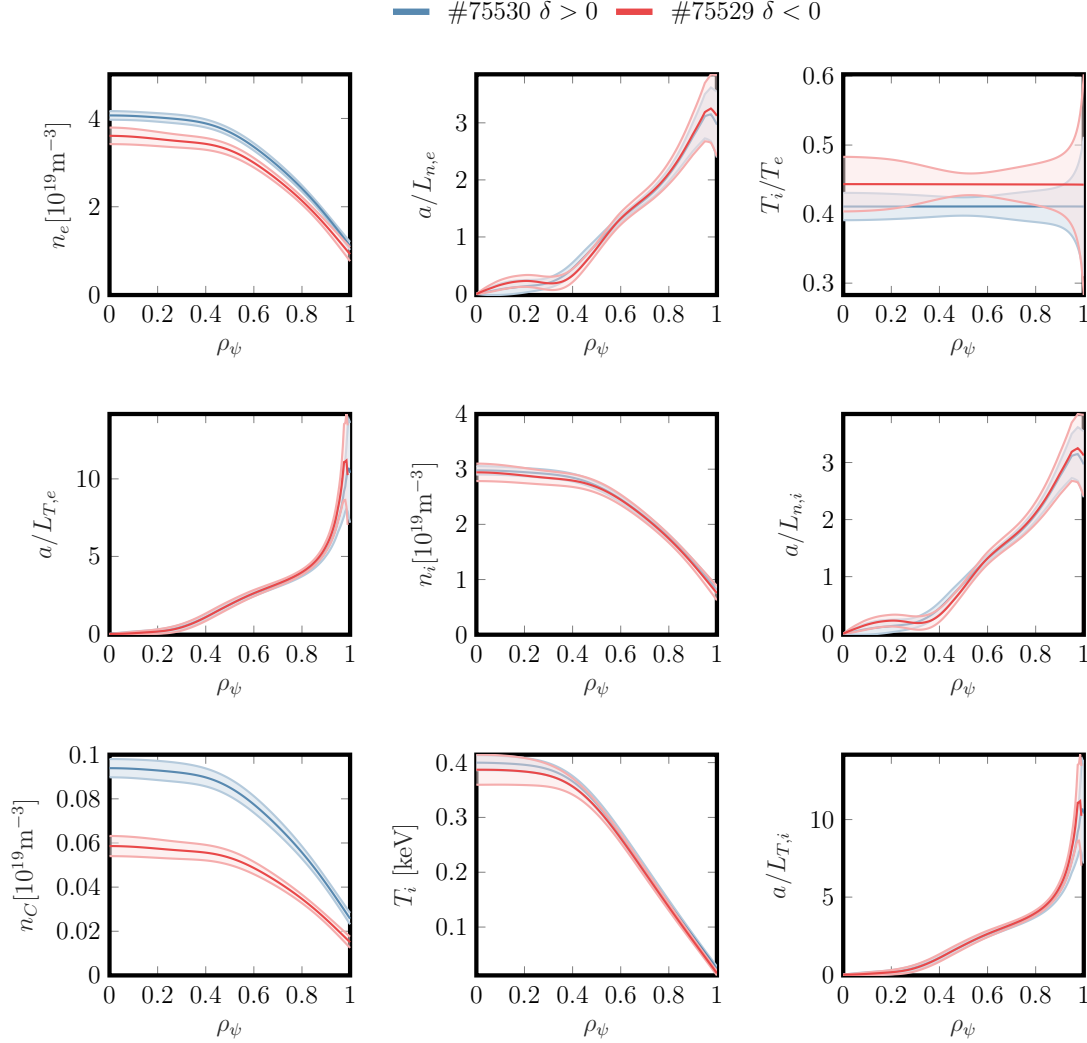
Figure 5.8 – Profiles for the $\delta > 0$ discharge #75530 (red) and the $\delta < 0$ discharge #75529 (blue).

r and evaluate the spatial Fourier-transform. The conditional spectra, shown in subfigure (a) in Fig. 5.10 reveal that $\delta > 0$ has a clear left band, corresponding to fluctuations propagating inward, with $k_r < 0$. In contrast, as can be see in subfigure (b) in Fig. 5.10, no clear structure is visible for $\delta < 0$, which could be an indication of reduced turbulent activity. However, instead of considering the whole laser beam, we can isolate a subset of detector elements that would in turn translate into a smaller range in ρ_ψ. Because the turbulence drive actually varies across the laser beam, due to radial variation in the profiles and their gradients, this approach could potentially provide a better estimate of the local wave-number spectra. However, the drawback is that fewer elements are now used for the estimates.

In Fig. 5.11 the conditional spectra are shown when considering only the first or the last 12 channels, out of the total 22 detector elements considered in the present analysis. This corresponds
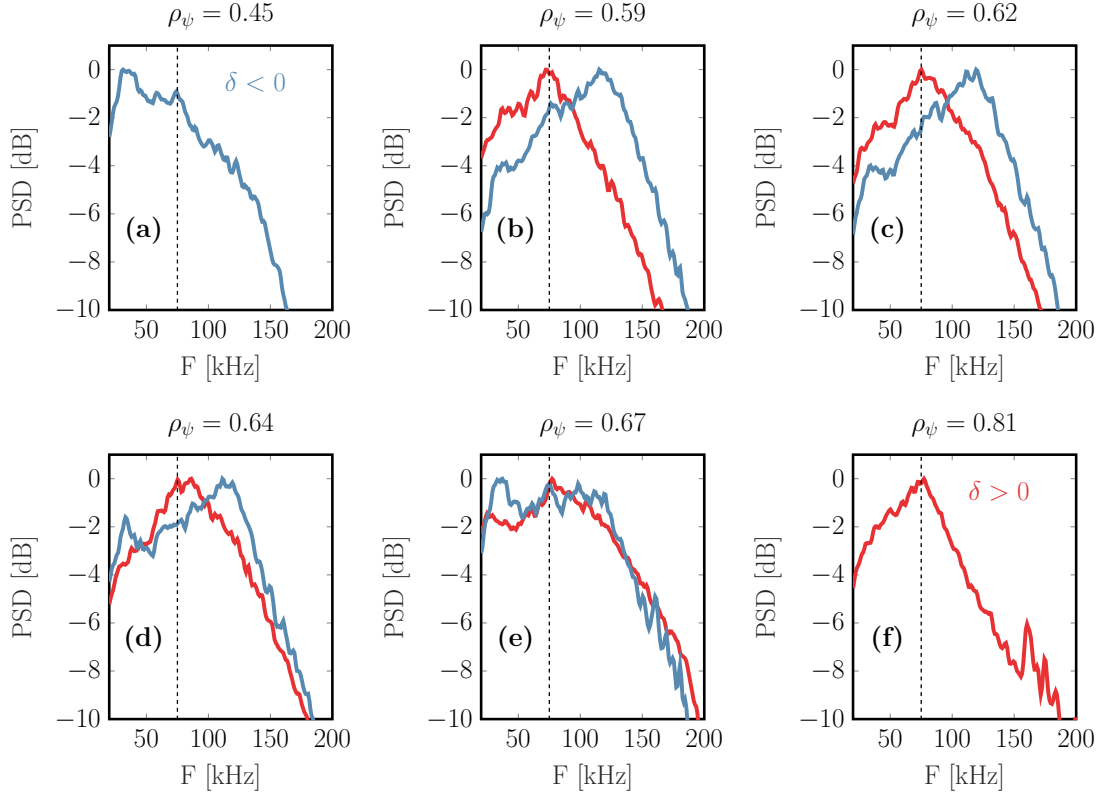
Figure 5.9 – The PSD for $\delta > 0$ (red) and $\delta < 0$ (blue). From left to right we illustrate the innermost $\delta > 0$ case (a), followed by overlapping measurements from both $\delta > 0$ and $\delta < 0$ at increased radial position in the plasma. The rightmost plot (f) shows the outermost $\delta > 0$ measurement.

to isolating the measurement around $\rho_\psi = 0.77$ and $\rho_\psi = 0.64$ at $\delta > 0$, and $\rho_\psi = 0.65$ and $\rho_\psi = 0.51$ at $\delta < 0$. In this case, much clearer structures are seen at $\delta < 0$, in contrast to Fig. 5.10. There is also striking similarity between the $\delta > 0$ and $\delta < 0$ cases, however not at the same radial locations, but when considering the same detector elements. This feature can be explained in two ways. The first is that the response of the detector elements strongly influences the measurement, thus leading to the similar conditional spectra in $\delta > 0$ as in $\delta < 0$. Another explanation could be that the measurement geometry is such that the fluctuations contributing to the TPCI measurement are similar at $\rho_\psi = 0.77$ and $\rho_\psi = 0.65$ for $\delta > 0$ and $\delta < 0$ respectively, and in $\rho_\psi = 0.64$ and $\rho_\psi = 0.51$. Both explanations are plausible, and without additional measurements, it is in the present difficult to reach a conclusion on what is the most probable explanation for the similarities observed in Fig. 5.11.

We move on and evaluate also the wave-number spectra for the two subsets of the TPCI channels for both discharges. As can be seen in Fig. 5.12, there is again a similarity between $\rho_\psi = 0.77$ ($\delta > 0$) and $\rho_\psi = 0.65$ ($\delta < 0$), both in terms of amplitude and shape. The ratio between the total power of modes with $k_r > 0$ and $k_r < 0$ is 1.15 in $\delta > 0$ and 1.5 in $\delta < 0$, indicating in both cases
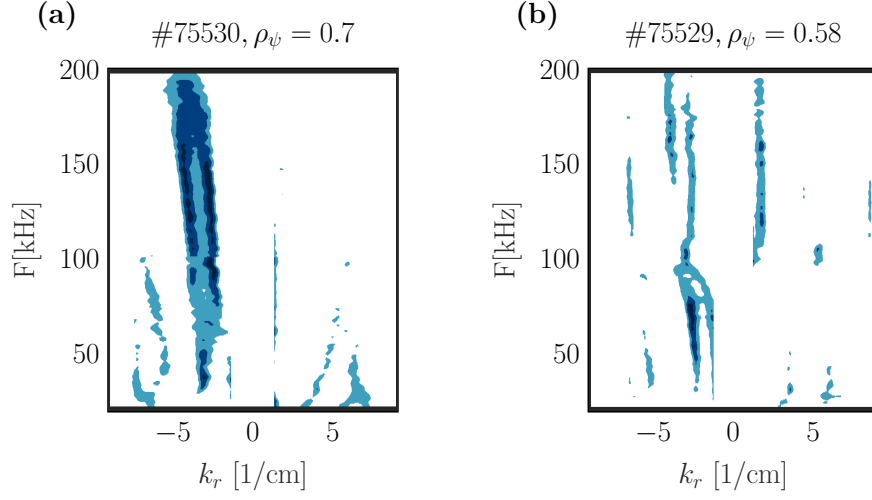
Figure 5.10 – Conditional spectra evaluated using all 24 TPCI channels for the $\delta > 0$ case (#75530, a) and for the $\delta < 0$ case (#75529, b).
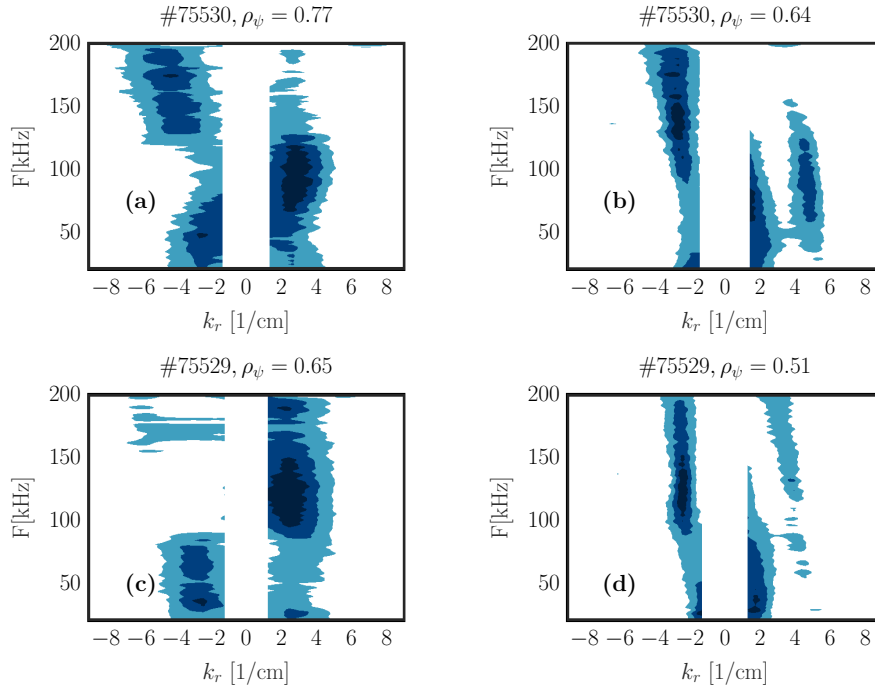

Figure 5.11 – The conditional wave-number and frequency spectra when considering only the first 12 TPCI channels (left) or only the last 12 channels (right). The $\delta > 0$ case is shown in (a,b) and the $\delta < 0$ case is shown in (c,d).
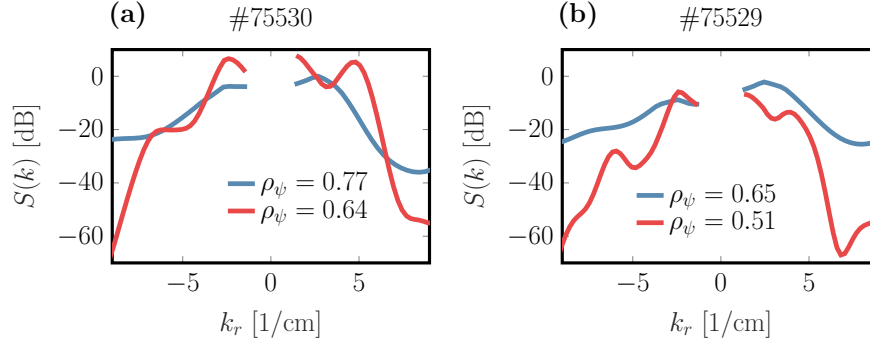
Figure 5.12 – Wave-number spectra of measurements for $\delta > 0$ (a) and $\delta < 0$ (b). We compare the case when only the first 12 TPCI channels are used in the analysis (blue) with the case when only the last 12 channels are used (red). This corresponds to measurements at larger and smaller ρ_ψ respectively.

that modes seem to propagate mostly radially outward. Following the discussion in chapter 4, this could mean either that zonal-type modes ($k_y = 0$) are more dominant in measurements at $\delta < 0$ than $\delta > 0$, or, if this contribution is not due to the zonal modes, that there might be an increased ITG-like activity at $\delta > 0$. As mentioned at the beginning, the filter configuration is focused on the radial contribution, but nevertheless still receives contributions from $k_y \neq 0$. Without a more optimised filter configuration, it is difficult to really conclude what could be responsible for the increased power of fluctuations with $k_r > 0$ relative to $k_r < 0$, in $\delta < 0$.

Regarding the other two radial locations, $\rho_\psi = 0.64$ ($\delta > 0$) and $\rho_\psi = 0.51$ ($\delta < 0$), it is seen that they are not as similar as the former two cases: in particular the amplitude at $\delta < 0$ is much smaller. The ratio between $k_r > 0$ and $k_r < 0$ has slightly increased to 1.5 for $\delta > 0$ and slightly decreased to 1.17 for $\delta < 0$.

Further details on the roles of $k_r > 0$ and $k_r < 0$ fluctuations are shown via the frequency spectra, in Fig. 5.13. The blue curves show the frequency spectra when taking into account all k_r modes, the red curves only take into account $k_r > 0$ and the green curve, only $k_r < 0$. The dashed black line indicates the same frequency, $F = 75$ kHz, that was previously shown in Fig. 5.9 and from Fig. 5.13 (a) it is clear that this potential QCM, originates from fluctuations with $k_r > 0$. The increased ratio between $k_r > 0$ and $k_r < 0$ previously mentioned for the $\delta > 0$ case is here clearly shown through an increase in power of $k_r > 0$ at lower frequencies. At $\delta < 0$ when moving radially inwards (Fig. 5.9 c to d) the dominance of the $k_r > 0$ modes is, similarly to $\delta > 0$, pushed to lower frequencies. Also the transition from a slightly steeper to a flatter spectrum that stems from fluctuations with $k_r < 0$ is seen both at $\delta > 0$ (green, a,b) and $\delta < 0$ (green, c,d).

Note that no clear GAM signatures are visible in the TPCI measurement. The very marginal peak near 28 kHz, especially visible in Fig. 5.13 (c, red curve) could potentially be interpreted as a GAM however it is clear that this GAM does not dominate the measurement, as was previously the case in the $\delta > 0$ discharge, #49052, analysed in section 4.1. On the other hand, in
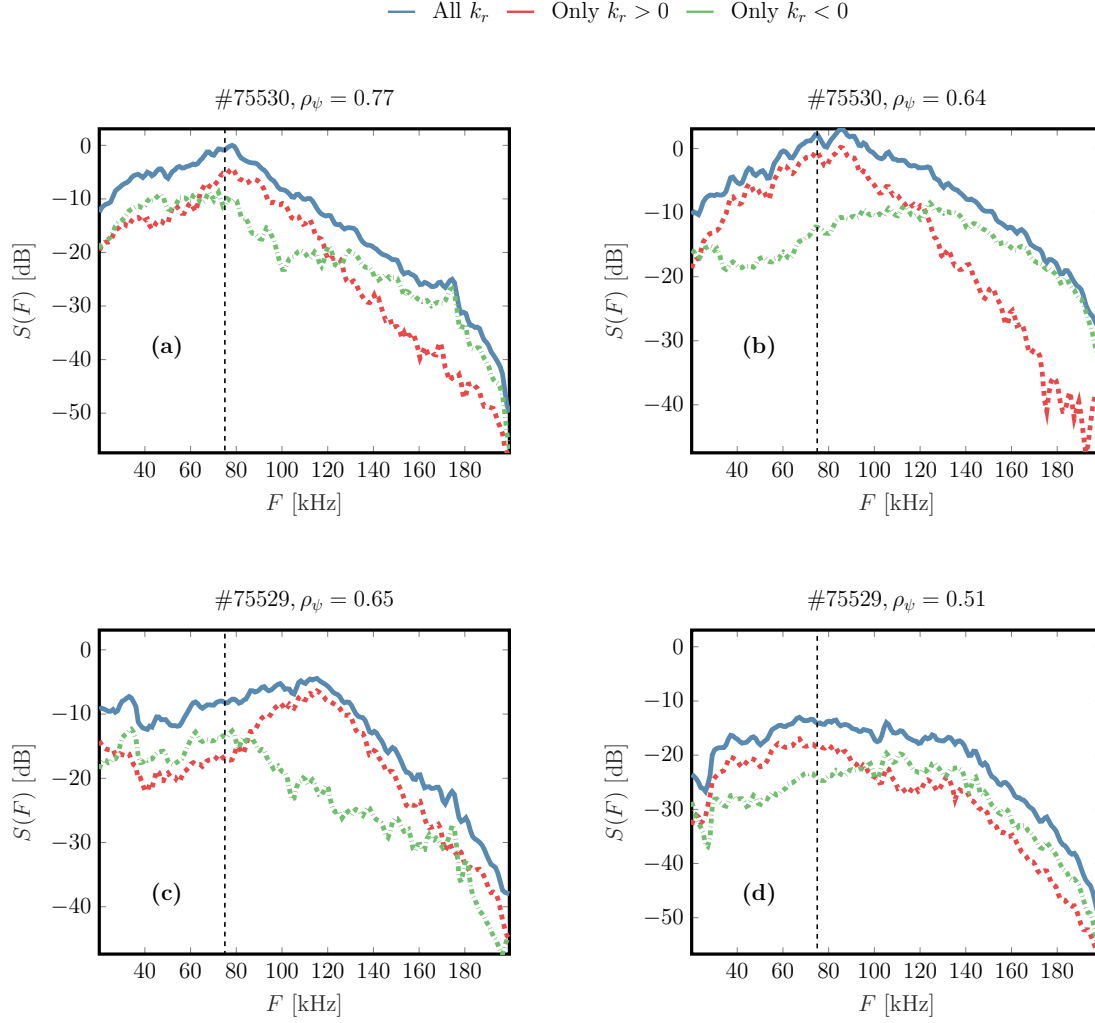
117

Figure 5.13 – The frequency spectra for $\delta > 0$ (a,b) and $\delta < 0$ (c,d) showing the case when only the first 12 TPCI channels are used in the analysis (a,c) or the last 12 (b,d). We compare the case when all k_r fluctuations are taken into account (blue), only $k_r > 0$ (red) and only $k_r < 0$ (green).

Ref. [83] a clear GAM structure near $\rho_\psi = 0.8$ and with $F \sim 28$ kHz was identified in the short pulse reflectometry signals. For a spatial filter configuration that should capture the effect of purely radial modes, it is surprising that no clear GAM like fluctuation can be observed in the TPCI signals. This again could be an indication that, despite the filter orientation, the observed fluctuations mainly come from non-zonal modes, with $k_y \neq 0$.

Finally we evaluate the relative density fluctuations at the different radial locations, and compare them with the average, evaluated over the whole laser beam, taking into account all 22 elements. The result is shown in Fig. 5.14 and shows that the only potential reduction in the TPCI signals when moving from $\delta > 0$ to $\delta < 0$ is due to a measurement closer to the core in $\delta < 0$. When the two measurements overlap, near $\rho_\psi = 0.65$, both $\delta < 0$ and $\delta > 0$ show similar fluctuation amplitudes.
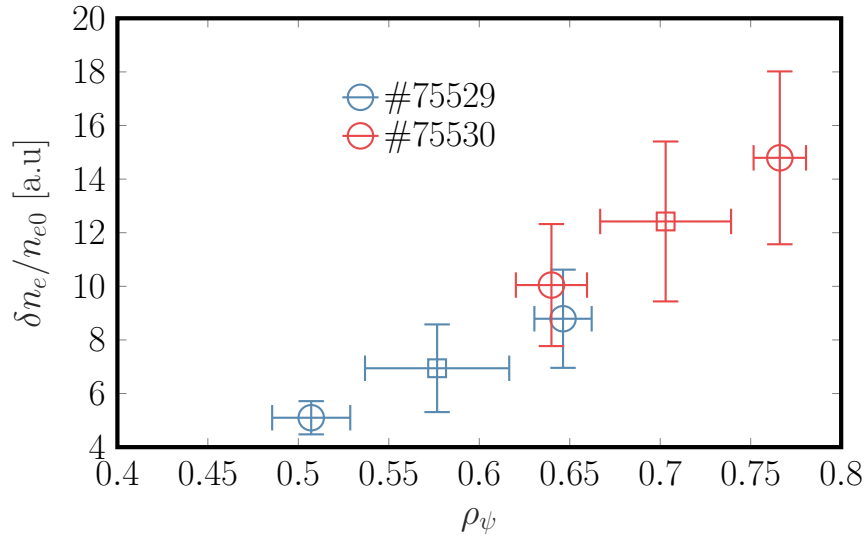

Figure 5.14 – Relative density fluctuations for $\delta > 0$ (red) and $\delta < 0$ (blue), when considering all 22 TPCI channels (squares) or divide the analysis into the first/last 12 TPCI channels (circles).

In summary, our results, which are consistent with those of the earlier study [83], suggest that δ has little effect on the fluctuation amplitude in diverted plasma configurations. However as mentioned above, this could be a consequence of the high collisionality in both scenarios rather than evidence that δ has no effect in diverted plasma configurations. Similar experiments with lower collisionality should be performed to test this hypothesis. Nevertheless, a change in the nature of the underlying modes could be observed: QCM-like fluctuations are stronger in $\delta > 0$ than in $\delta < 0$, and the mixture of modes with $k_r > 0$ and $k_r < 0$ is different in the two scenarios.

Before finishing this subsection, we comment on the results from linear modelling of the two discharges. Surprisingly, the linear simulations of these Ohmic discharges, where the electron temperature is larger compared to the ion temperature, as was shown in Fig. 5.8, are dominated by ITG-like modes, propagating in the ion direction. The quasilinear ratio R_{QL}, defined in

Eq. (4.10), is larger than one at the radial positions of the TPCI measurement in the plasma, ranging from $\rho_\psi = 0.8$ to $\rho_\psi = 0.45$. The ratio increases for lower ρ_ψ and is generally slightly larger for the $\delta < 0$ case. Although, indeed, this is different from the typical Ohmic TCV discharges that normally are dominated by TEM, it would be consistent with the observation of dominant $k_r > 0$ contribution seen in the TPCI signals. It would then suggest that the QCM is in fact due to the ITG-like modes present in the scenario. We stress again, however, that these conclusions are merely suggestions for an interpretation of the observed features in the TPCI signals. More measurements, with different filter configurations, supported by gyrokinetic simulations, are necessary to be able to better understand the role of triangularity in diverted plasma configurations.

5.2.2   Effect of EC heating on turbulence

It has been suggested that EC heating of a plasma drives turbulence. A publication with theoretical and experimental results on the role of ECH on plasma turbulence is in preparation by J. Cazabonne. TPCI measuremente of electron density fluctuations in plasmas with and without ECH have been performed in support of that study. In this subsection we will provide more detail on the results from the TPCI measurements in these ECH experiments.

Two TCV discharges were considered: the Ohmic case #75526 and a EC heated case #75528, both with nearly circular plasmas. In #75528 the ECH power is modulated between low ~ 150kW and high power 600 kW with a 2 ms duty cycle, as illustrated in subfigure (a) of Fig. 5.15. The vertical position of the plasma is such that the TPCI measurement is near the core, slightly below the midplane, as shown in subfigure (b) of Fig. 5.15. The measurement is, as in the last section, mainly from purely radial fluctuations, but with a non-negligible contribution from poloidal modes.

To analyse the turbulence in the EC heated discharge #75528 we consider different parts of the EC modulation: the low power flat-top phase, the high power flat-top phase, the ramp-up segment and the ramp-down segment. The TPCI signals are conditionally sampled to include all EC modulations in the discharge when analysing the different phases. The different phases will be compared with each other, as well as with the Ohmic discharge #75526.

In general, an analysis of the TPCI signals shows that the characteristics of the turbulence are very similar between the two discharges, and the four phases in #75528. The difference is most pronounced when comparing the high power phase of #75528 and the Ohmic discharge #75526. The conditional spectra for these two cases are shown in Fig. 5.16. Both scenarios show a band of turbulence with $k_r < 0$. This band is broader in the high power case, indicating a reduced correlation length of the turbulence. Low frequency components with $k_r \sim 1.8$ cm^{-1} are seen in both cases, but are more pronounced in the high power discharge. The frequency and wave number of these fluctuating components coincide with the typical characteristics of the GAM mode, seen in past TCV experiments [21, 36].
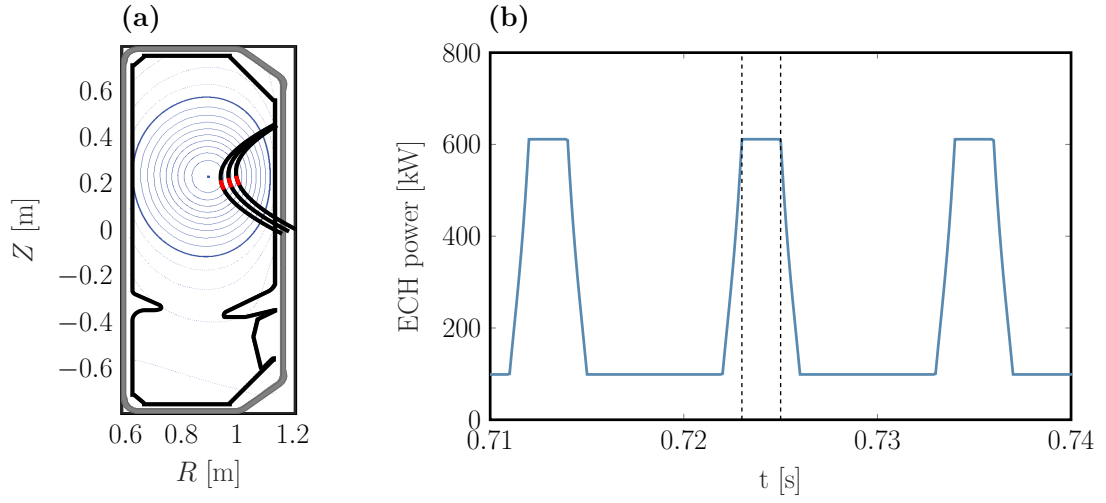
(a)

(b)

Figure 5.15 – An illustration of the TPCI measurement geometry (a) in the experiments considered in this section. Th measurement geometry is the same for both #75526 and #75528. A modulated ECH power (shown in (b)) is applied to #75528 with a 2 ms high-power phase followed by a low power phase. The vertical black dashed lines delimit an example of a high power segment that is used for the conditional averaging of the TPCI signals.

#75526 **no ECH**
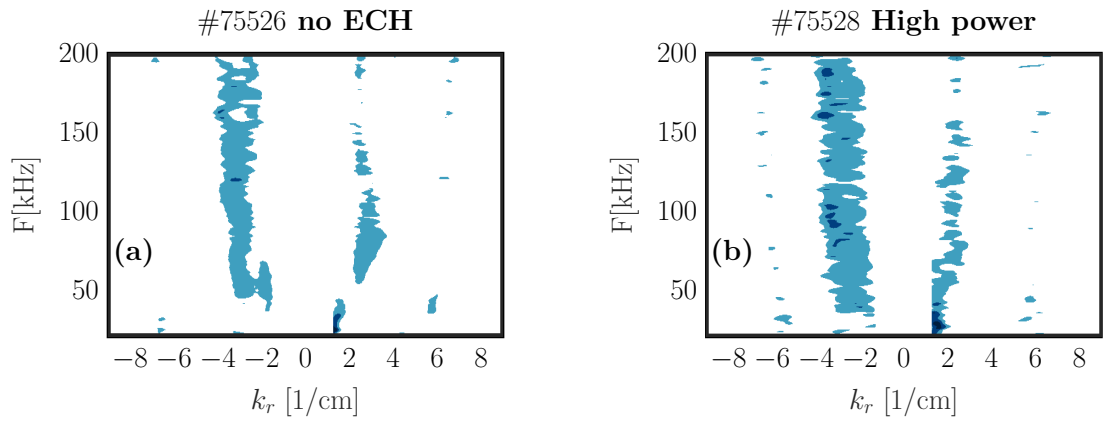
#75528 **High power**

(a)

(b)

Figure 5.16 – Conditional wave-number and frequency spectra for the Ohmic discharge #75526 (a) and for the high-power flat-top phases of #75528 (b).
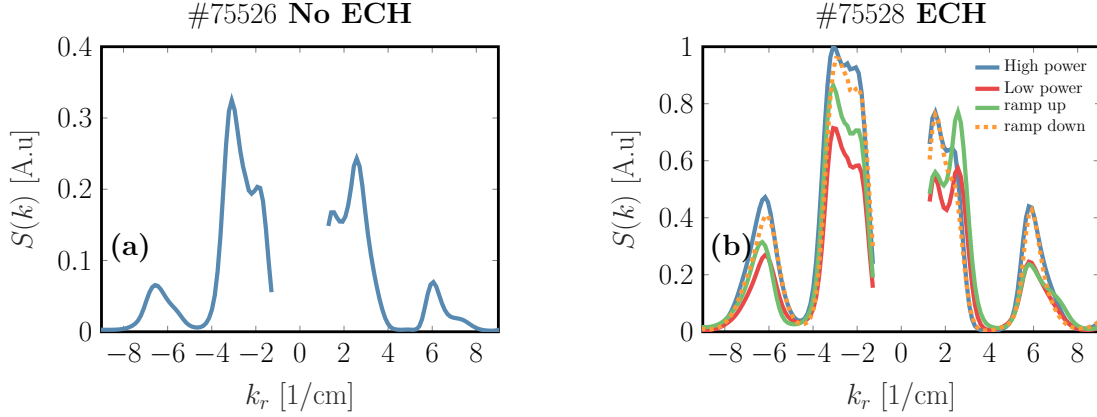
Figure 5.17 – Wave-number spectra for the Ohmic discharge #75526 (a) and the different phases in the EC heated discharge #75528 (b), separating between the high power flat-top (blue), low power segments (red), the ramp up phases (green) and finally the ramp down phases (dashed, orange).

The wave-number spectra for the Ohmic discharge as well as all four phases of the EC heated case, are shown on the left and right subfigures, respectively, in Fig. 5.17. The spectra are normalised to the maximum of the high powered case. Similarities between the various cases are observed, but there is clearly an increase in the fluctuation amplitude between the low and the high-powered case. Fluctuations with $k_r < 0$ are most affected by the EC beam; the ratio between components with $k_r > 0$ and $k_r < 0$ decreases from 0.7 for the Ohmic and low powered case, to 0.5 for the high-powered case. The frequency spectra, comparing the Ohmic and high-power cases, are shown in Fig. 5.18 and are also similar, although, in the high-power case the amplitude has increased substantially and the frequency peak has shifted slightly from 60 kHz for the Ohmic case to near 70 kHz for the high power case. It is also clear, by studying the red curve in Fig. 5.18, that $k_r > 0$ modes are less important in the high power case, consistent with the observations related to the wave-number spectra in Fig. 5.17.

Finally, we can study the relative fluctuation amplitudes for all five cases. In Fig. 5.19 we show the relative density fluctuations versus the electron temperature at the tangency point. It is clear, as was already seen in the other analyses, that increasing ECH power leads to more turbulent fluctuations. The reason seems to stem from the increased electron temperature, potentially suggesting an increased drive of TEM turbulence. From the discussion in chapter 4, the decreasing ratio, in the wave-number spectra, between fluctuations with $k_r > 0$ and $k_r < 0$, could be consistent with increased TEM drive. However, as was pointed out in chapter 4, it is important to note the diamagnetic direction with respect to the TPCI rays. Since the plasma is below the midplane, the diamagnetic direction, with respect to the filter axis, is reversed. Thus, an increased TEM would manifest itself with increasing fluctuation amplitude of components with $k_r > 0$, whilst here, instead, an increased amplitude of components with $k_r < 0$ is observed. We should also recall that the measurement is strongly affected by the radial fluctuations, and it is therefore difficult to draw conclusions regarding the ITG/TEM transport. As was discussed in
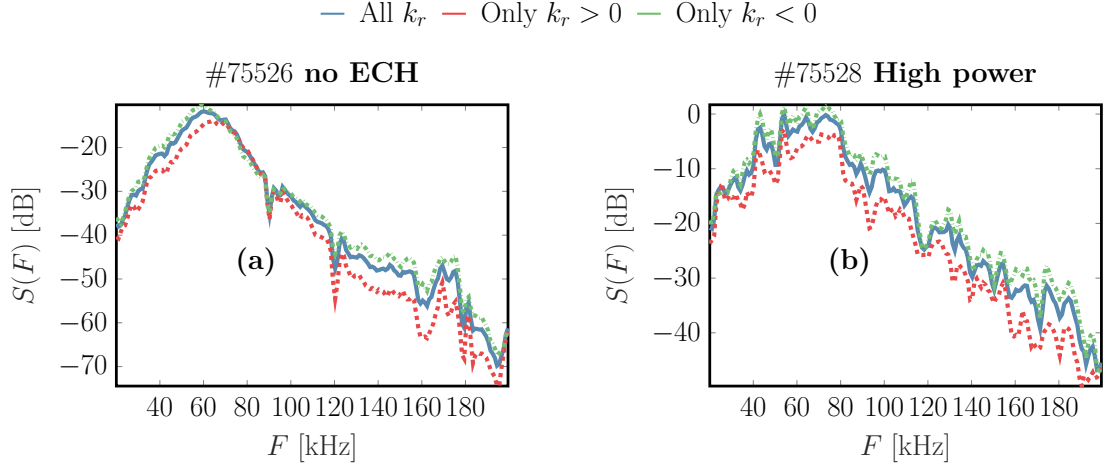
Figure 5.18 – The frequency spectra for the Ohmic discharge (a) and the high power phase in #75528 (b). We compare the case when all k_r fluctuations are taken into account (blue), only $k_r > 0$ (red) and only $k_r < 0$ (green).

chapter 4, a more optimised filter would be required for this task. Also support with gyrokinetic modelling would be very valuable to understand the change in the characteristics of the underlying fluctuations when applying EC heating. For now, we conclude that the effect of the beam is indeed to increase the fluctuation amplitude, mostly due to a local increase in the electron temperature.

5.3 Chapter summary

This chapter presented the upgrade of the TPCI diagnostic on TCV. The original plan was to implement a high bandwidth PV detector for electron-scale measurements, but due to a sequence of problems it could not be commissioned in the time available. Instead, a PC detector was implemented for performing ion-scale turbulence measurements. Due to technical problems with the recommissioning of the diagnostic, only data from four discharges in two different experiments could be analysed: one on the study of the effect of negative plasma triangularity on turbulence, in diverted configurations, and one on the role of ECH on turbulence. It is difficult to draw clear conclusions, but in general, a small effect of plasma triangularity on turbulence amplitudes, in diverted plasma configurations, was found. As suspected in previous studies, this small effect could be explained by the high collisionality in the considered scenarios. Nevertheless, a change in the nature of the underlying instabilities could be observed, when the plasma changes from positive to negative triangularity. Despite very limited data, a clear increase in the fluctuation amplitude was observed when the plasma is heated with ECH, most likely due to the local increase in the background electron temperature.
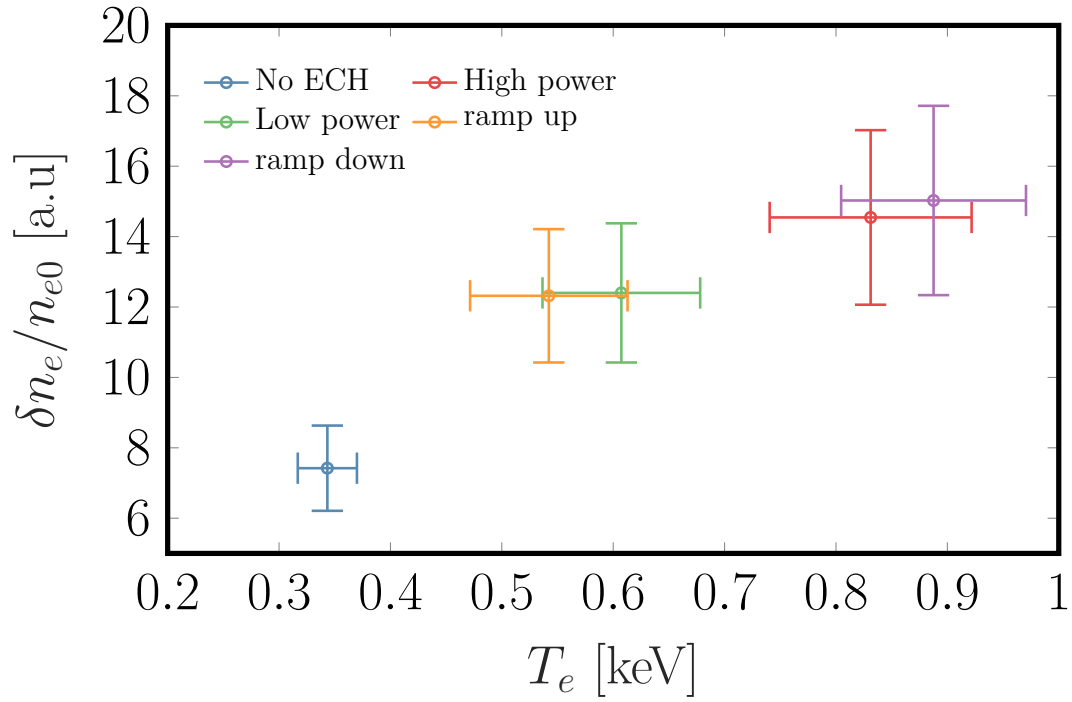
Figure 5.19 – The relative fluctuation amplitude as a function of the electron temperature at the tangency point for the Ohmic discharge (blue), ramp-up and low power phases (yellow and green) and finally the high power and ramp-down phases (red and purple).

6 JT-60SA simulations and prediction of TPCI signals

The focus so far has been on the study of turbulence in the TCV machine. In this final part of the thesis work turbulence in the JT-60SA machine is also investigated and predictions are made of future TPCI measurements.

The purpose of the JT-60SA tokamak is to provide substantial contributions for optimizing performance in ITER and DEMO [90, 91]. Its large size $R \sim 3$ m and high field $B \sim 3$T, provided by superconducting magnets, will allow JT-60SA to explore reactor-relevant regimes. The machine has the performance capability to surpass break-even, achieve high β conditions, and operate in steady state using non-inductive current drive. Furthermore, the machine can explore different diverted geometries and investigate the effect of plasma shape in reactor-relevant regimes by varying triangularity and elongation. A total of 41 MW of heating is installed, coming mostly from NBI and some ECH [92].

The study of turbulence and anomalous transport is an important part of the JT-60SA research plan [93]. Several fluctuation diagnostics to study turbulence in future JT-60SA experiments are already planned, including PCI [34], Beam Emission Spectroscopy [94] and Doppler reflectometry [95], all of which respond to local density fluctuations in the plasma. However, in preparation for these measurements, it is already important to start characterising the turbulent fluctuations in JT-60SA. First of all it is necessary for properly designing the fluctuation diagnostics. By modelling the turbulence and applying a synthetic diagnostic, it would be possible to assess the capability of the planned diagnostics to measure turbulence in JT-60SA. Secondly, it is necessary for testing whether the reduced transport models used to predict the profiles and plasma geometry for future JT-60SA operation properly account for turbulent transport. Finally, it is important for the general understanding of how simulations of turbulence should be performed in reactor-relevant regimes, which is becoming more relevant as we are approaching ITER operation.

This chapter presents the first predictions of turbulence in a representative JT-60SA plasma discharge, using profiles and magnetic geometry of scenarios that have been developed for future JT-60SA operation. The aim is to characterise the fluctuations and extrapolate our findings to reactor-relevant regimes. The predictions of the kinetic profiles from reduced transport models are

tested against the heat fluxes from gyrokinetic simulations. Finally, a reference case is generated that can be used to assess the capability of the fluctuation diagnostics planned for JT-60SA to measure turbulence in the machine. In particular, the electron density fluctuations generated from the gyrokinetic simulations are used for predicting TPCI signals in JT-60SA by applying the synthetic tool described in chapter 3.

The gyrokinetic simulations are first described in section 6.1 and then the predictions of the TPCI signals are presented in section 6.2.

6.1 Gyrokinetic turbulence modelling for JT-60SA

In this section we will present the first predictions of turbulence in a representative JT-60SA plasma discharge, using profiles and magnetic geometry of scenarios that have been developed for future JT-60SA operation. This section is organised as follows. In subsection 6.1.1 we present the details of the considered JT-60SA scenario, including the input parameters for the gyrokinetic GENE simulations. As will be shown, the scenario contains a vast range of competing electrostatic and electromagnetic modes that can only be properly modelled with fully electromagnetic effects. Impurities and fast ions also affect the instabilities and are therefore retained to ensure realistic modelling. In subsection 6.1.2 we show the results from linear GENE simulations of the most unstable modes. These results illustrate the importance of retaining all four kinetic species and full electromagnetic effects to ensure proper modelling of the scenario. Next, we show the results from the nonlinear simulations; first in subsection 6.1.3 we include kinetic ions and electrons only, and then in subsection 6.1.4 we include also kinetic carbon impurities and fast deuterium ions.

6.1.1 Details of the considered JT-60SA scenario

We focus on a reference JT-60SA scenario with 41MW of injected NBH and ECH, featuring a plasma current of 5.5 MA, toroidal field on axis of 2.25 T, safety factor at 95% of the minor radius $q_{95} = 3.24$, and a normalised ratio of the plasma kinetic to magnetic pressure $\beta_N = 3.14$. The scenario has a double-null separatrix and a large value of $\beta_e = 2\mu_0 n_e T_e / B_0^2 < 7\%$ as shown in Fig. 6.1. The profiles and equilibrium have been estimated with reduced transport modelling, using the TOPICS [96], ACCOME [97] and TOSCA [98] suite of codes. The density and temperature profiles are shown in Fig. 6.2. The magnetic equilibrium, as illustrated in Fig. 6.1, is consistent with the predicted total kinetic pressure. However, in the simulations presented in the following sections, we vary the total pressure and change β_e, but make the simplification of not recomputing the magnetic equilibrium, which will be held fixed. The density and temperature profiles are shown in Fig. 6.2

This work on simulating turbulence for JT-60SA originally started as a modelling support in view of developing a TPCI diagnostic that is planned for JT-60SA with the purpose of measuring
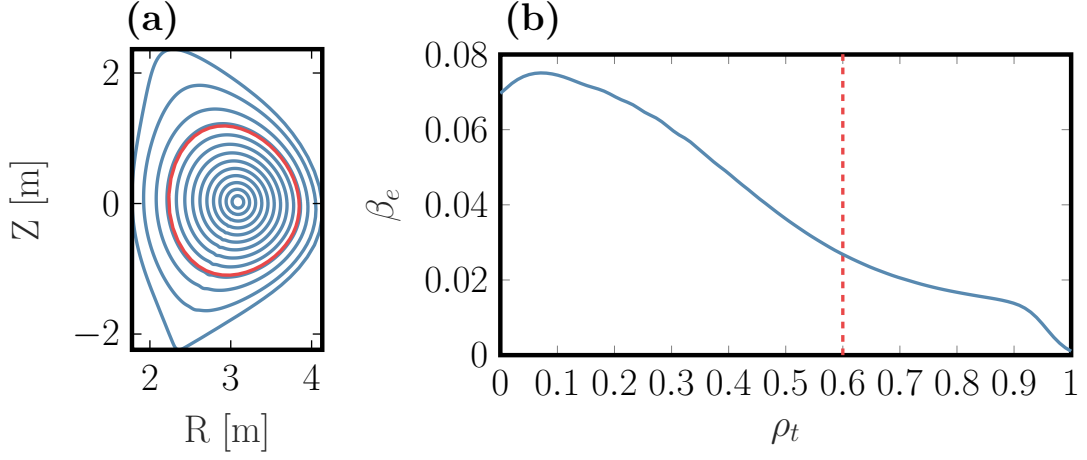
Figure 6.1 – Double-null equilibrium (a) and β_e profile (b) for the considered JT-60SA scenario. Local gyrokinetic simulations are carried out near the flux surface with $\rho_t = 0.6$, indicated by the red flux surface (a) and the red dashed line (b). The value of β_e is very high, $\beta = 2.7\%$ at the considered flux surface with $\rho_t = 0.6$.
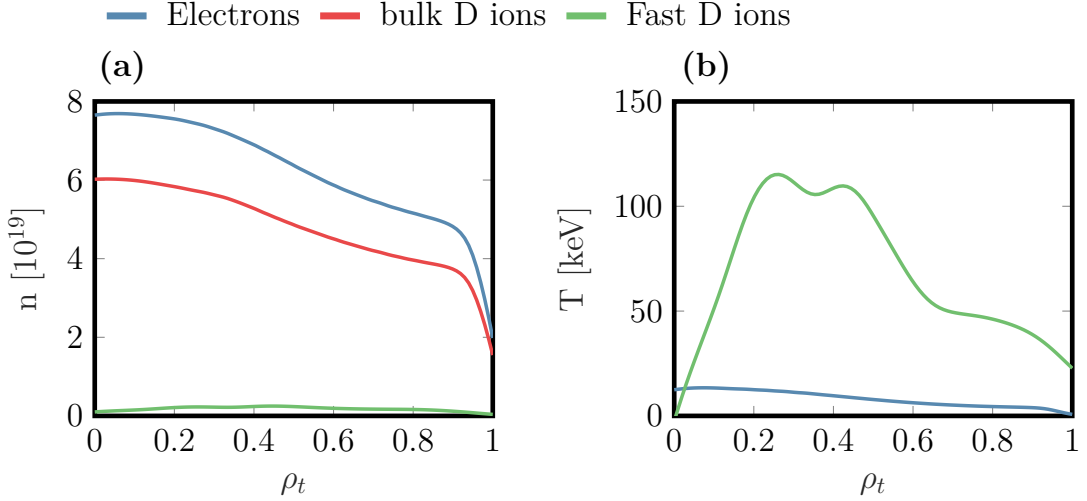

Figure 6.2 – Density profile (a) for electrons (blue) main D ions (red) and fast D ions (green), and the temperature profile (b) for electrons (blue) and fast D ions (green).

Table 6.1 – Input parameters for the considered JT-60SA scenario at $\rho_t = 0.6$. Here R is the major radius.

T_D/T_e	1	$a/L_{n,C}$	0.7224	q_0	1.1571
$a/L_{T,e}$	2.094	$a/L_{n,\mathrm{FD}}$	1.7231	$\hat{s}$	1.5528
n_D/n_e	0.7671	$a/L_{T,D}$	2.094	T_{FD}/T_e	10.21
$\varepsilon = r/R$	0.51	n_C/n_e	0.033	$a/L_{n,e}$	0.7224
Z_{eff}	2	n_{FD}/n_e	0.033	$a/L_{n,i}$	0.6794
β_e	2.7 %	$a/L_{T,\mathrm{FD}}$	4.25	v_i^*, v_e^*	0.052, 0.0074

electron density fluctuations [34]. In order to facilitate later comparison with future TPCI measurements, the radial location for the simulations in this section was chosen on the basis of the measurement locations. The regions of optimal TPCI localization are the pedestal and the magnetic axis, the former typically requiring prohibitively large computational resources, and the latter featuring small pressure gradients and broadly stable conditions; we thus chose the innermost region with sufficient turbulence levels, $\rho_t = 0.6$, roughly corresponding to mid-radius.

Given the density and temperature distribution of the fast species, as shown with the green curve in Fig. 6.2, we assume that most of the heating power is deposited within the $\rho_t = 0.6$ flux surface. In the following we will therefore compare the simulated heat flux obtained from local simulations at $\rho_t = 0.6$ with the total heating power of 41 MW.

We consider collisions, modelled with a linearised Landau collision operator, impurities and fast ions modelled with an equivalent Maxwellian, as well as electromagnetic effects, which in particular include compressional magnetic field fluctuations. Importantly, when including $\delta B_\parallel$, we use full ∇B and curvature drifts [99]. Whenever we neglect the compressional magnetic field fluctuations we also erase the pressure gradient from the ∇B drifts.

The considered input parameters to the GENE simulations are summarized in Table 6.1. There, $a/L_{T,n}$ is the normalised temperature and density gradient, respectively, where a is the minor radius, $Z_{\mathrm{eff}} = (n_D + n_{FD} + 36n_C)/n_e$ is the effective charge, and v_i^*, v_e^* are the normalised ion and electron collision frequencies [100]. The subscript D refers to main deuterium ions, e is the electrons, FD is the fast deuterium ions and C denotes the carbon impurity. The reference electron density and temperature at $\rho_t = 0.6$ are $n_e = 5.87 \times 10^{19}$ m^{-3} and $T_e = 6.27$ keV, respectively, and the reference magnetic field is $B_0 = 2.35$ T.

6.1.2 Linear simulations to find most important effects

We begin by investigating the dominant modes that exist in the considered JT-60SA scenario.
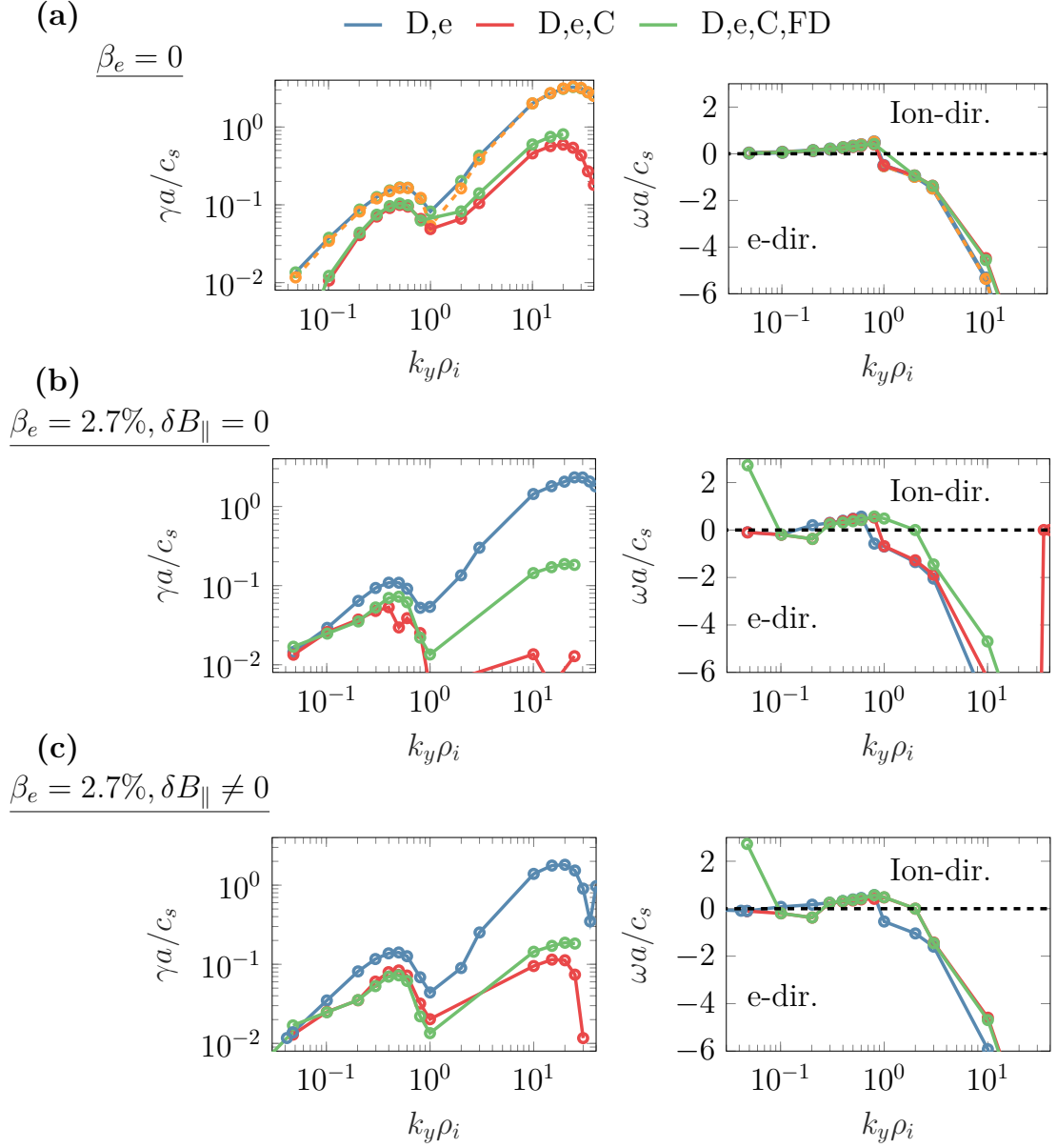
Figure 6.3 – Growth rate γ (left column) and frequency ω (right column) of the most unstable mode as a function of the binormal wave number k_y. We show the electrostatic case, $\beta_e = 0$ (a), electromagnetic with $\beta = 2.7\%$ but $\delta B_\parallel = 0$ (b) and finally, with $\delta B_\parallel \neq 0$ and using the full drift velocity (c). We compare the cases when only two kinetic species are considered in the simulations (blue), two kinetic species but including the effect of impurities in the collision operator through Z_{eff} (dashed orange in (a)), fully including impurities (red) and finally also fast ions (green). It is clear from these results that electromagnetic effects, and considering all four kinetic species, is necessary for properly modelling the considered scenario.

.

Linear growth rates and frequencies as functions of the binormal wave number k_y of the most unstable mode are shown in Fig. 6.3. We first consider the electrostatic limit, by setting $\beta_e = 0$. When including two kinetic species only, bulk deuterium ions and electrons, we see that the scenario is dominated up to $k_y \rho_i \approx 1$ by ITG modes that propagate in the ion diamagnetic direction ($\omega > 0$). For larger wave numbers, the dominant modes become of TEM or ETG type ($\omega < 0$). It is known that impurities can have an effect on the turbulent transport [101–104]. As shown by the orange dashed line in Fig. 6.3 (a), impurities have a negligible effect through the collision operator. Their main effect instead comes from diluting the main ion density, leading to a stabilisation of both ITG and TEM/ETG type fluctuations. When including fast deuterium ions, we observe a weak destabilisation at all scales. This is mostly seen at larger wave numbers, $k_y \rho_i \gtrsim 10$.

When including the projected $\beta_e = 2.7\%$, but still neglecting compressional magnetic field fluctuations $\delta B_{\parallel}$, the growth rates are reduced, as can be seen in Fig. 6.3 (b). Compared to the electrostatic case, the fast ions are slightly more destabilising while the stabilisation due to impurities is much more pronounced. The destabilisation due to fast ions can be theorised to arise from the larger fast-ion temperature gradient compared to its density gradient, $a/L_{T,FD} > a/L_{n,FD}$, which has been shown to counteract the otherwise stabilising effect of dilution of the main ion species [105].

Including electromagnetic effects changes the type of the underlying instabilities. Notably, for the four-species case at very low wave number $k_y \rho_i = 0.05$, finite β introduces in addition to the electrostatic modes a high-frequency mode with $\omega \approx 3c_s/a$. As will be seen later, this mode is driven by fast ions, and may resonate with the motion of the fast species. In addition to this high-frequency mode, a large-scale ($k_y \rho_i = 0.05$) and low frequency ($\omega \approx 0.1c_s/a$) electromagnetic mode arises. This is the most unstable mode for the two and three-species case in Fig. 6.3, and eigenfunction structures for Φ and $A_{\parallel}$ suggest that it is a micro-tearing mode. Finally, in subfigure (c) in Fig. 6.3, we additionally include compressional magnetic field fluctuations, which leads to a slight increase in the growth rate, in particular at ETG scales $k_y \rho_i \sim 10$ for the three-species case.

As shown in Fig. 6.3, electron-scale modes are present for all cases however, when including kinetic impurities and fast ions, the ratio between the growth rate and the binormal wave number becomes much smaller for electron scale modes compared to ion scale modes, $\max(\gamma_{ITG}/k_{y,ITG}) \gg \max(\gamma_{ETG}/k_{y,ITG})$, see Fig. 6.4. Following Ref. [33, 106], it is therefore expected that ETGs have little effect in the present scenario or at least are decoupled from ion-scale turbulence, and will therefore be neglected henceforth.

To better understand the role of finite β we compute the frequencies and growth rates for varying β_e. As mentioned in subsection 6.1.1, the background magnetic geometry is held fixed for simplicity and not recalculated to be consistent with varying pressure. We consider $k_y \rho_i = 0.6$, corresponding to the most unstable mode at the ion scales. As can be seen in Fig. 6.5, stabilisation occurs when increasing β_e until the Kinetic Ballooning Mode (KBM) limit at $\beta_e \approx 5\%$, above which growth rates increase. For comparison, the MHD estimate of the ballooning limit is
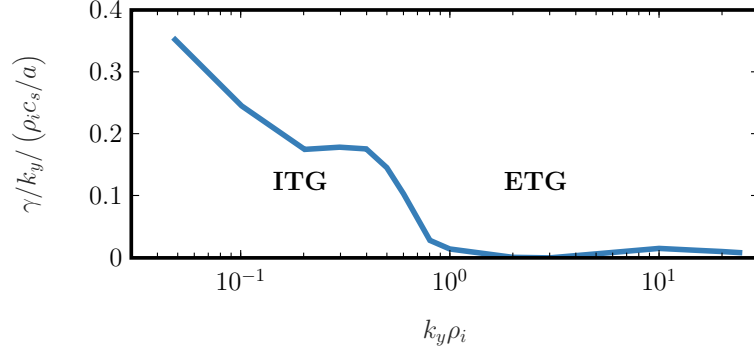
Figure 6.4 – Ratio of the growth rate γ over the corresponding wave number k_y, from ion to electron scales, for the four-species fully electromagnetic case. Since $\max(\gamma_{ITG}/k_{y,ITG}) \gg \max(\gamma_{ETG}/k_{y,ITG})$, it is expected that ETGs have negligible impact in the considered scenario.

$\beta_{crit}^{MHD} \approx \alpha_{crit}^{\mathrm{MHD}} R/(q_0^2 \nabla P) = 6\%$, based on the simple estimate $\alpha_{crit}^{\mathrm{MHD}} = 0.6\hat{s}$. At β below the KBM limit, stabilisation is due to the standard suppression of ITG turbulence [107]. For the two-species case, we investigate the role of compressional magnetic field fluctuations $\delta B_\parallel$ (compare blue and red lines). As expected, at low β_e, there is essentially no effect, but as β_e increases there is a destabilising effect. At the nominal value of $\beta_e \approx 2.7\%$, there is a significant destabilising effect. This destabilising effect of $\delta B_\parallel$ near the KBM limit is in agreement with Refs. [108–110], and neglecting $\delta B_\parallel$ underestimates the growth rates of the underlying modes. If we include the remaining two kinetic species, impurities reduce the growth rates, while fast ions have very little effect, except at large β_e above the KBM limit, where they are also stabilising. Just before the transition to KBM, a mode of electromagnetic nature, propagating in the electron diamagnetic direction becomes dominant. This is shown in Fig. 6.5 (c), where we have evaluated the ratios between the exponentially growing electromagnetic heat flux and the total heat flux. When β_e is above or substantially below the KBM threshold the most unstable mode, propagating in the ion diamagnetic direction, is dominated by the electrostatic component of the heat flux.

To summarise, these linear simulations have illustrated that four species and fully electromagnetic effects are important to retain for proper modelling of the considered JT-60SA scenario. We will use this information in the next subsection, where we proceed with nonlinear simulations for predicting the turbulent transport, and compare simulated heat fluxes to the 41 MW of planned injected power. We will retain fully electromagnetic effects, including compressional magnetic field fluctuations in the nonlinear simulations. Although collisionality is small and the effect of collisions on the underlying instabilities is moderate in linear simulations, they are included for completeness.
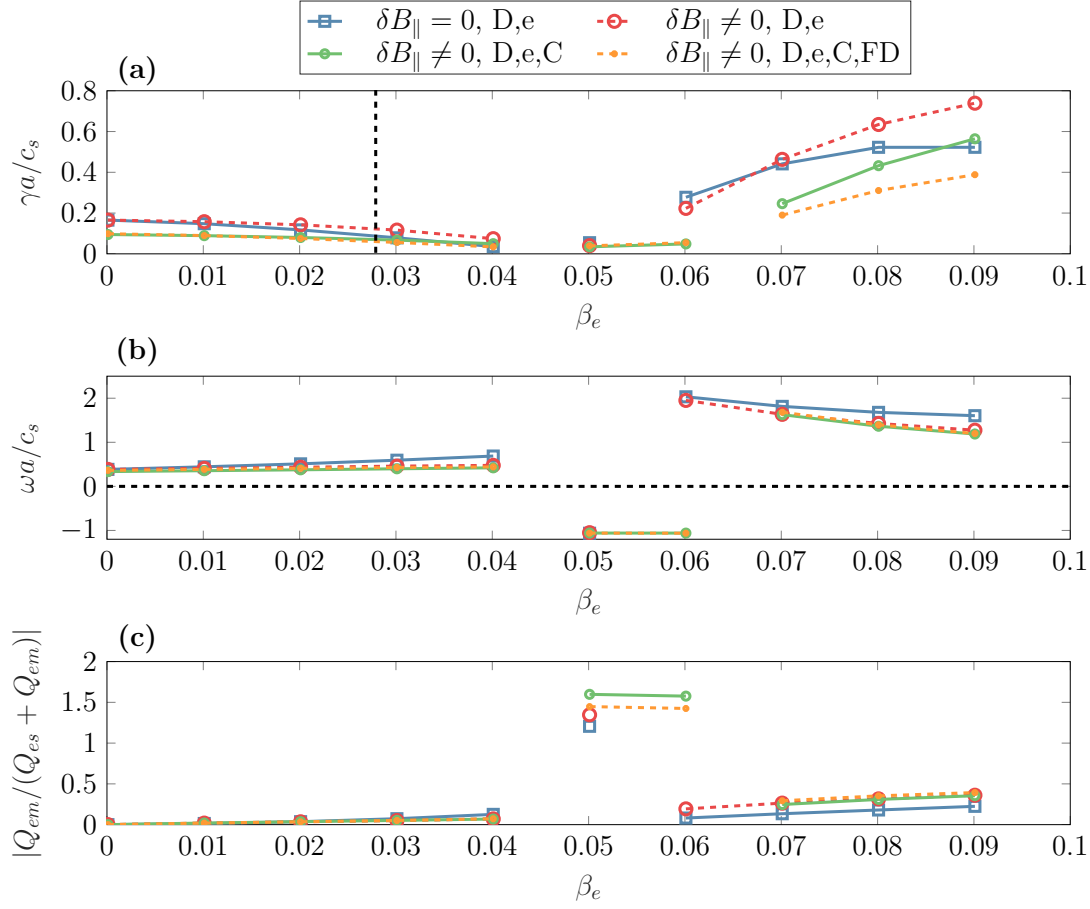
Figure 6.5 – Growth rate (a), frequency (b) and ratio of the electromagnetic to the total heat flux (c) as functions of β_e. The black dashed vertical line in (a) indicates the nominal value of $\beta_e = 2.7\%$. Here $k_y \rho_i = 0.6$, corresponding to the most unstable growth rate at the ion scales.

6.1.3 Nonlinear simulations with bulk electron and deuterium ions

A first set of simulations of the JT-60SA scenario was carried out considering only two kinetic species: bulk electrons and deuterium ions. When performing a simulation at the nominal parameters given in Table 6.1, simulations predict a far lower total heat flux than the value expected based on plasma heating and profiles predicted with reduced transport models, for which the simulated heat flux should match the injected power of 41 MW. Instead, after an initial transient phase, see Fig. 6.6 (a), the electrostatic heat flux decreases to very small values. The electromagnetic flutter transport is even smaller and therefore not shown.

A decay of turbulent amplitudes to near-zero levels after a robust linear growth phase and saturation onset at substantial fluxes is a strong indication that the simulation is in the so-called Dimits regime [111], i.e above the linear but below the nonlinear critical gradient. There, profiles can become very stiff, and transport may depend very sensitively on e.g. driving gradients.
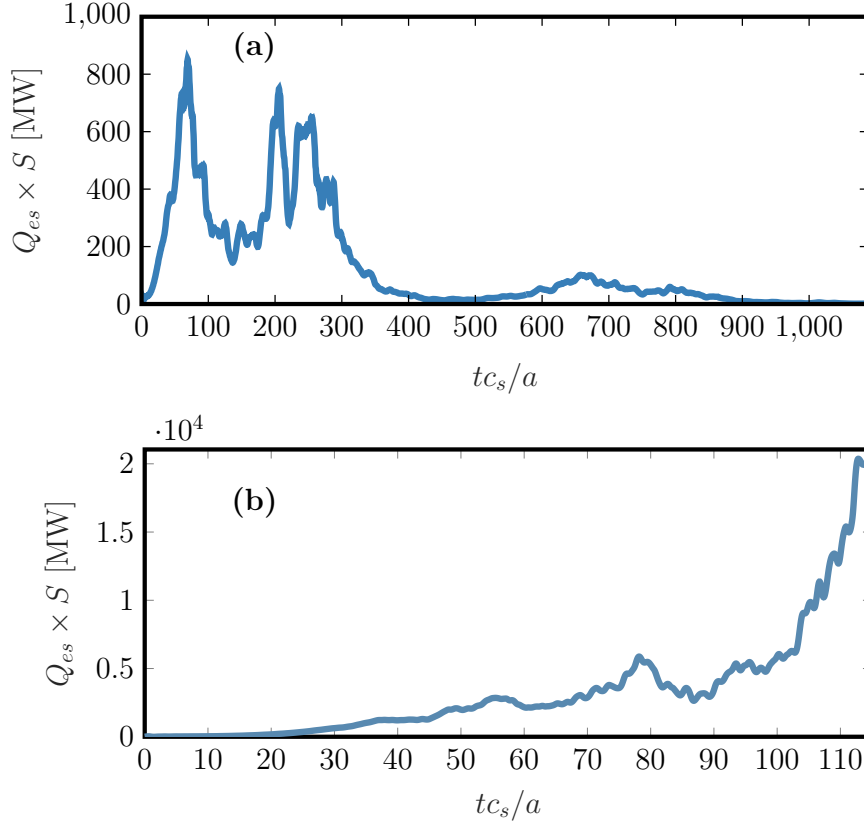
Figure 6.6 – Electrostatic heat flux for ions (a) for nominal parameters and (b) for a case with 10% increased background gradients, demonstrating a heat flux runaway due to a NZT. For comparison, the experimental heat flux level is 41 MW. The low heat flux seen in (a) suggests that the nominal parameters are in the Dimits-shifted regime.

Even though the scenario lies close to the nonlinear critical gradient, a moderate increase by 10% in the gradients leads to a runaway as illustrated in Fig. 6.6 (b). This is the consequence of a Non-Zonal Transition (NZT), where zonal-flow-based saturation is disabled due to enhanced magnetic stochasticity at large β and of the profile gradients [20]. A signature of the NZT is that the radial displacement of a perturbed field line $\Delta r_{1/2}$, after half a poloidal turn, exceeds the radial correlation length λ_{Bxx} of the radial magnetic fluctuation. Thus, flux surfaces break, causing decay of zonal flows, and runaway amplitudes. For example, in the case of the runaway shown in Fig. 6.6 (b), $\lambda_{Bxx} \approx 13\rho_i$ while $\Delta r_{1/2} \approx 10\rho_i$. Thus $\lambda_{Bxx} > \Delta r_{1/2}$ which confirms that the runaway seen in Fig. 6.6 (b) is due to a NZT. If instead, as is the case in most turbulence studies, the radial displacement of a given field line is smaller than the radial correlation length, the field lines travel only very small distances after one full poloidal turn, and the zonal modes and associated shear flows remain at sufficiently high amplitude to efficiently saturate the turbulence.

The threshold for the NZT was evaluated by varying both β_e and changing the ion and electron temperature gradients, with results summarized in Fig. 6.7. We normalise β_e with the KBM limit
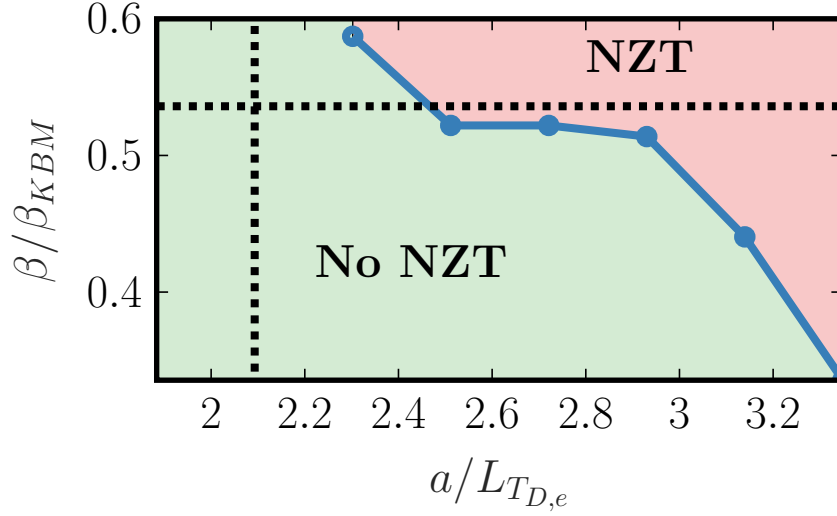
Figure 6.7 – The NZT threshold as a function of normalized β_e and the ion/electron temperature gradient. The dashed vertical line indicates the nominal temperature gradient, and the dashed horizontal line corresponds to the nominal β_e. The green/red regions correspond to parameters when a NZT occurs/does not occur.

as obtained from the corresponding linear simulations, at $k_y\rho_i = 0.3$, which roughly corresponds to the wave number where the nonlinear k_y spectra peak. Clearly, the NZT threshold occurs far below the KBM threshold in all cases. As seen in Fig. 6.7, increasing the gradients means that we simultaneously need to decrease β_e to avoid the NZT. For the nominal value of β_e, increasing the temperature gradients by only 10% leads to a NZT. In contrast to Ref. [20], we do not find a strictly linear decrease in the NZT β-threshold with the background gradients, possibly due to the mixed ITG/TEM regime in which we operate.

For experiments, closely approaching a NZT threshold implies a sudden and drastic increase in stiffness, and the gradients in temperature and density will remain the same irrespective of the injected heat. The proximity of the considered JT-60SA scenario to the NZT threshold could thus have the consequence of reducing the efficacy of NBI and EC heating in reaching high plasma pressure.

It needs to be tested explicitly whether these findings from the two-species simulations, in particular if the NZT threshold appears at similar gradients and β_e, remain the same when including kinetic carbon impurities and fast ions in our simulations. While the latter seemed to have a small effect linearly; it is known that their effect might be enhanced in high-β_e nonlinear simulations [105, 112]. Therefore, we proceed to the four-species case before further adjusting parameters towards matching the injected power.
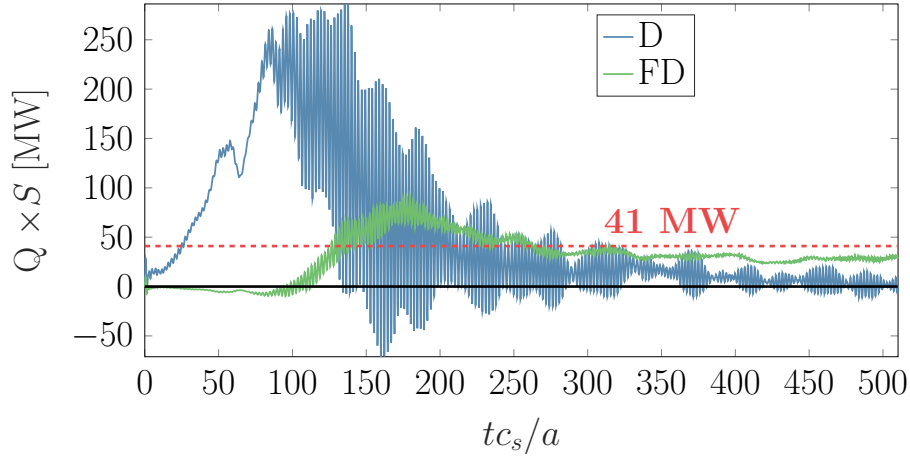
Figure 6.8 – Time trace of the heat flux for main ions (blue) and fast ions (green), from a four-species nonlinear simulation with 10% increased background temperature and density gradients. The red dashed line indicates the 41 MW of injected heat in the scenario.

6.1.4 Four-species simulations with carbon impurities and fast deuterium ions

When including carbon impurities and fast ions in nonlinear simulations, we find that a high-frequency oscillation $\omega \simeq 3c_s/a$ develops that dominates the heat flux time trace, as illustrated in Fig. 6.8. This oscillation is due to a resonance between the high-frequency, low-$k_y\rho_i$ mode, already seen in Fig. 6.3, and the fast ions, which produce most of the total heat flux. The high frequency of this mode is clearly visible from an analysis of the power-spectral density for each k_y, as shown in Fig. 6.9, as a clear signal at $k_y\rho_i = 0.1$. To better understand the characteristics of this mode, we carried out linear simulations where we vary the fast-ion parameters. As is shown in Fig. 6.10, the high-frequency mode is very sensitive to variation of these parameters, especially the fast-ion temperature T_{FD} and temperature gradient $a/L_{T,FD}$. By changing these parameters only slightly from the nominal values, the high-frequency mode can change from dominant to subdominant in the linear simulations. The linear simulations shown in Fig. 6.10 were performed at $k_y\rho_i = 0.08$, slightly lower than the smallest k_y in the nonlinear simulations, i.e $k_y\rho_i = 0.1$, as the eigenvalue solver did not return any high-frequency mode at $k_y\rho_i = 0.1$ which thus appears to be stable. In the nonlinear simulation, there are no candidate modes that would satisfy the frequency and wave number matching conditions to support destabilisation as a result of a three-wave interaction. An alternative explanation is that the mode may be destabilised in the nonlinear simulations due to the evolution of the fast-ion profiles [113–115]. However, these variations were found to be small (±0.3 and ±0.2 variation in the fast-ion density gradient and temperature gradient-scale length respectively, corresponding to a 18% respectively 5% variation compared to the nominal values) and not sufficient to destabilise the mode. One may speculate that the nonlinear energy transfer to a stable mode may account for the observed frequency features in the turbulence, although additional study is required on this topic. Furthermore, the fast-ion velocity distribution may need to be taken into account in order to model with greater
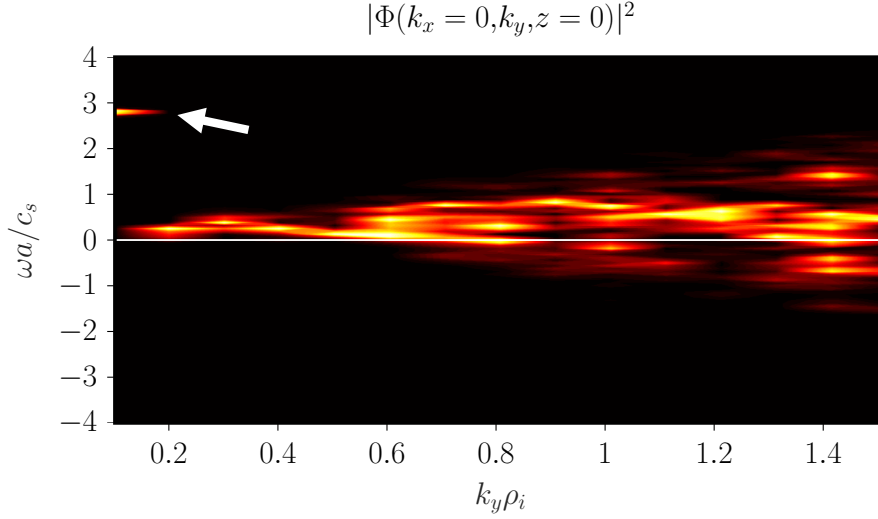
Figure 6.9 – Nonlinear frequency of the electrostatic potential vs the wave number, with the power normalised separately for each k_y. The white arrow is there to direct the attention to the high-frequency mode that is observed in the simulation.

accuracy the resonance between the fast particles and the high-frequency mode [116]. Here, we model the fast ions with a simple equivalent Maxwellian distribution function, at a higher temperature compared to the temperature of the bulk particles $T_F/T_i = 10.21$, but a more correct slowing-down distribution, falling outside the scope of this work, should be examined in future work. Similarly to the NZT, this high-frequency mode could pose a limitation on NBH efficacy. The injected fast ions could resonate with the high-frequency mode and, consequently, carry most of the heat away instead of depositing it in the core to the bulk particles. A better understanding of the nature of this mode, is therefore important and should be considered in future work.

Based on the linear properties of the high-frequency mode, we lower the fast-ion temperature to $T_f = 8T_e$ in another nonlinear simulation, which indeed removes the resonant oscillation in the heat-flux time trace. However, similarly to the two species case shown in subsection 6.1.3, Fig. 6.6 (a) the heat flux remains small, and very sensitive to variation in the grid parameters. To be able to properly carry out a convergence study, we thus additionally increase the gradients above the nominal values, moving away from marginal stability. The NZT is less ubiquitous when considering the two additional species and only appears at 40% increased ion temperature gradient. This is not surprising as ITG turbulence is stabilised by the complementary dilution of the bulk ion species occuring when adding fast ions and impurities in the simulations. For the convergence study we finally chose the following final parameters in addition to the nominal values shown in Table 6.1: $T_f = 8T_e$, $a/L_{T,i} = 2.93$, $a/L_{T,e} = 2.51$, $a/L_{n,i} = 0.87$, $a/L_{n,e} = 0.87$ and $n_e = 5.28 \times 10^{19}$ m^{-3} leading to $\beta_e = 2.4\%$, which corresponds to 90% of the nominal value. The following resolution parameters ensure converged nonlinear results (30% difference threshold upon doubled resolution; velocity space resolutions were taken from converged linear simulations) for the electrostatic heat flux (which remains the dominant contribution to the total
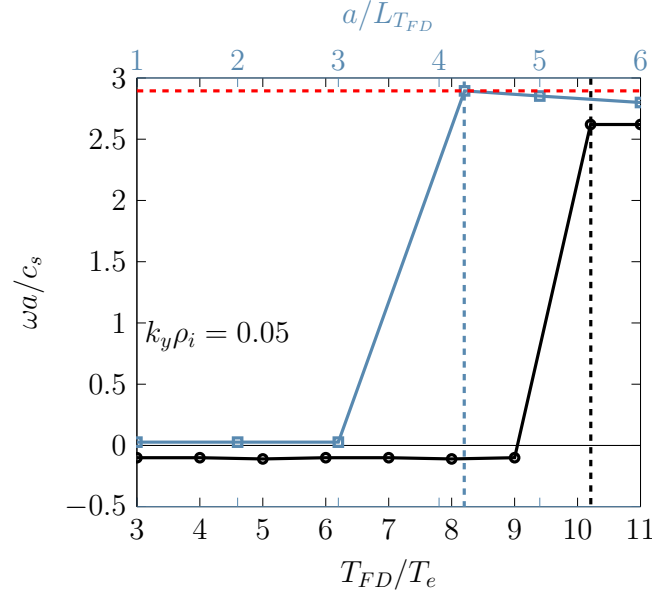
Figure 6.10 – Frequency of the most unstable mode when varying fast-ion temperature (black squares, lower scale) or fast-ion temperature gradient (blue circles, upper scale). The dashed red line indicates the frequency $\omega = 2.62a/c_s$ of the high-frequency mode seen in the nonlinear simulations. Results for $k_y\rho_i = 0.08$. The vertical dashed black/blue lines indicate the nominal fast-ion temperature/temperature gradient.

heat flux) $N_x \times N_{k_y} \times N_z \times N_{v_\parallel} \times N_\mu = 384 \times 16 \times 48 \times 32 \times 10$. The flux tube has a radial length $L_x = 256\rho_i$ and a binormal length $L_y = 62\rho_i$.

A summary of various turbulence related quantities for this case is given in Table 6.2, where we show the root mean square, flux surface averaged, density fluctuations δn, and parallel and perpendicular temperature fluctuations $T_\parallel$ and $T_\perp$, respectively. Fig. 6.11 displays nonlinear frequencies for this scenario (also compare Fig. 6.9), which no longer exhibit the low-k_y fast-ion feature. In the frequency range with the highest turbulent amplitudes ($k_y\rho_i \approx 0.3$), ion-direction frequencies around 50 kHz are accompanied by a narrower electron-direction frequency, which may be the result of a stable drift wave (compare Refs. [117, 118]). The k_y spectra of the density fluctuations are shown in Fig. 6.12, which has a dominant contribution around $k_y\rho_i = 0.3$, providing a testable prediction for future experiments. Corresponding temperature spectral data (not shown) has very similar properties.

In Table 6.2 we also show the electrostatic and electromagnetic (combining $A_\parallel$ and $B_\parallel$ contributions) heat fluxes for each of the four species, both in SI units and in GyroBohm units. Even though β_e is large, the electrostatic heat flux contribution is dominating, the largest contribution coming from bulk ions, with another sizable contribution from the electrons. Interestingly, the electrostatic fast-ion heat flux is negative. The electromagnetic heat flux is comparable between electrons, ions and and fast ions. Density and temperature fluctuations are substantial and should

Table 6.2 – Summary of saturated fluctuation amplitudes and fluxes for the new reference simulation for each species. The heat flux values are given in MW as well as in GyroBohm units.

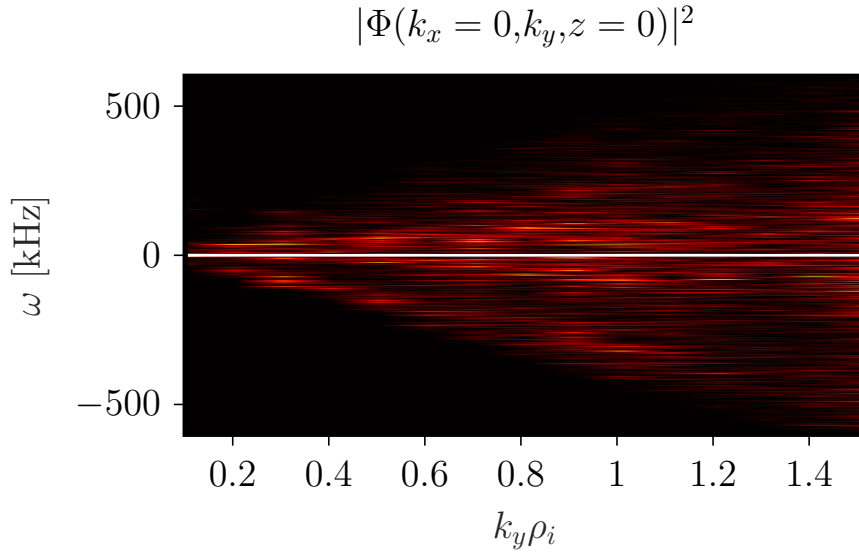| Parameter	e	D	C	FD
$\sqrt{\langle|\delta n|^2\rangle}/n_0$	1.2%	1.8%	2.1%	1.8%
$\sqrt{\langle|\delta T_\parallel|^2\rangle}/T_0$	1.3%	2.5%	4.2%	1.6%
$\sqrt{\langle|\delta T_\perp|^2\rangle}/T_0$	2%	4.7%	6.3%	1.3%
$\langle Q_{es}\rangle$ [MW]	121	485	18	-16
$\langle Q_{es}\rangle$ [Q_{GB}]	4	16	0.61	-0.53
$\langle Q_{em}\rangle$ [MW]	32	19	-0.3	21
$\langle Q_{em}\rangle$ [Q_{GB}]	1.1	0.63	-0.01	0.77

$$|\Phi(k_x = 0, k_y, z = 0)|^2$$

Figure 6.11 – Frequency spectrum of the electrostatic potential for each k_y. The high-frequency features visible in Fig. 6.9 has disappeared, whereas an electron-frequency branch with $\omega \propto k_y$ is now visible.
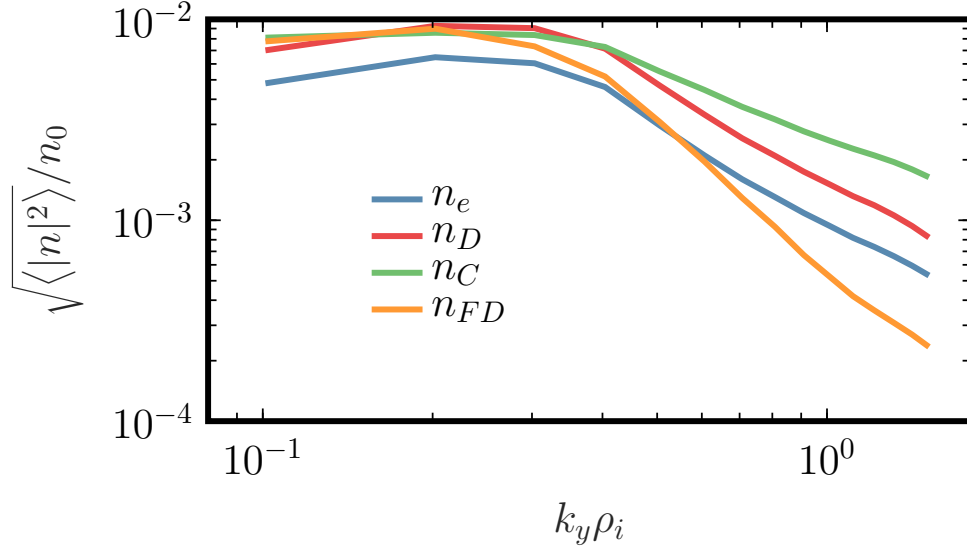
Figure 6.12 – Spectra of density fluctuations for each species, showing peak values at $k_y\rho_i = 0.3$ and different fall-off rates.

be detectable by JT-60SA diagnostics. The heat fluxes in GyroBohm units show that, even though we substantially increased the profile gradients, the transport remains relatively low.

Given this reference case, we attempt to identify the main-ion temperature gradient that matches the predicted heat flux of 41 MW. The result is shown as the blue circles in Fig. 6.13. The high stiffness of the profiles is evident: increasing the gradient by 16% (from $a/L_{T,D} = 2.5$ to $a/L_{T,D} = 2.93$) increases the heat flux by almost a factor of 10. Consequently, the gradients that would be consistent with a heat flux of 41 MW are in very close proximity to the nonlinear critical gradient. For comparison, the green dotted line shows an estimate of the linear critical gradient at the nonlinear spectral peak of $k_y\rho_i = 0.3$, see Fig. 6.12. The linear critical gradient is much lower, around $a/L_{T,D} = 1$. By implication, it is expected that the ion temperature profile in the experiment will largely be limited by the nonlinear critical gradient of $a/L_{TD}^{\text{crit}} \approx 2.4$. As a consequence, transport modelling will benefit substantially from precise knowledge of the Dimits shift [111] - i.e., the linear-to-nonlinear upshift of the critical gradient - which can be recovered by quasilinear models [119–121] when accounting for saturation efficiency.

Finally, in the linear simulations we noted the importance of retaining compressional magnetic field fluctuations, which turns out to be the correct approach in nonlinear simulations as well: In Fig. 6.14, we show that removing $\delta B_\parallel$ completely stabilises the turbulent transport. The nonlinear destabilising effect of $\delta B_\parallel$ is thus clearly enhanced, in comparison with the effect seen in the linear simulations in Fig. 6.5, as a consequence of nonlinear near-criticality. It is interesting to note that, the fully electromagnetic simulations with $\beta = 2.4\%$ yield a higher heat flux than the low-β case. Thus, in agreement with Ref. [122], we find that there is no decrease of ITG-driven heat transport with increasing β in the present scenario, although in Ref. [122],
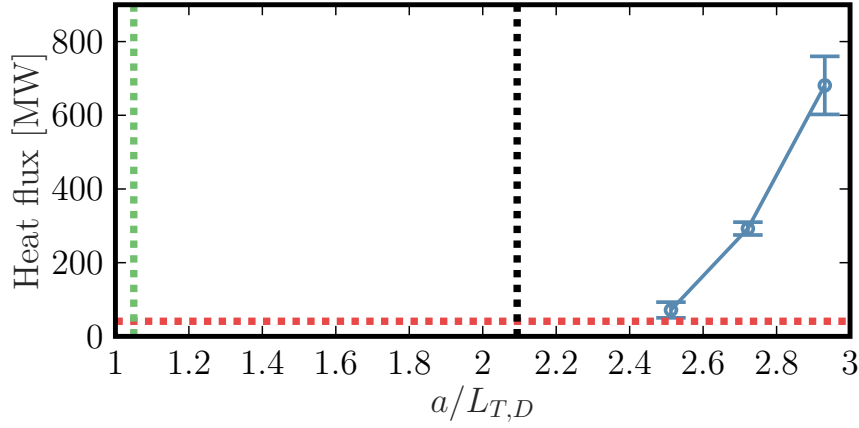
Figure 6.13 – Estimate of the nonlinear main-ion critical temperature gradient. The blue circles correspond to nonlinear simulations and the error bars denote a standard deviation. The dashed green vertical line indicates an estimate of the linear critical gradient, using $k_y\rho_i = 0.3$. The dashed vertical black line shows the nominal value of the bulk ion temperature gradient. Finally, the dashed red line corresponds to the nominal power of 41 MW. Matching the nominal flux requires very close proximity to the nonlinear critical gradient.

this result was a consequence of the self-consistent magnetic equilibrium, which is not the case here. While β alone is stabilising, adding $\delta B_\parallel$ counteracts this effect, and eventually, at large enough β, overtakes the β stabilisation. This again, highlights the importance of retaining $\delta B_\parallel$ when carrying out simulations of high-β scenarios.

This concludes the gyrokinetic study of the turbulence in the considered JT-60SA scenario. In the next section we will use the results obtained in this section to predict the signals from the TPCI diagnostic, using the set-up that is planned for future fluctuation measurements in JT-60SA.

6.2   First prediction of TPCI measurements for JT-60SA

In a recent publication [34] a design for a TPCI system for the JT-60SA tokamak was proposed. The proposed TPCI design features a tangentially viewing geometry, similar to TCV, but with a laser beam that passes deeper into the plasma cross-section. The optical path of the proposed TPCI diagnostic is shown in Fig. 6.15 as well as in Fig. 6.16.

The corresponding radial coordinate ρ along the laser beam is shown in Fig. 6.17 (a). In contrast to TCV, the beam in JT-60SA passes entirely, and multiple times, across the entire cross-section, leading to multiple locations $\ell_\perp$ where the considered k_x and k_y fluctuation component is perpendicular to the laser beam. These locations are illustrated in Fig. 6.17 (b) for a $k_y = 0$ (solid curve) and a $k_y\rho_i \neq 0$ (dashed curve) mode, and correspond to when the angle between the laser beam and the wave vector of the fluctuations is $\theta_{k_\perp,B,k_0} \sim 90$ degrees. Two of these locations are near the core, $\rho \sim 0.1$, positioned on the LFS and HFS respectively, and a third is at
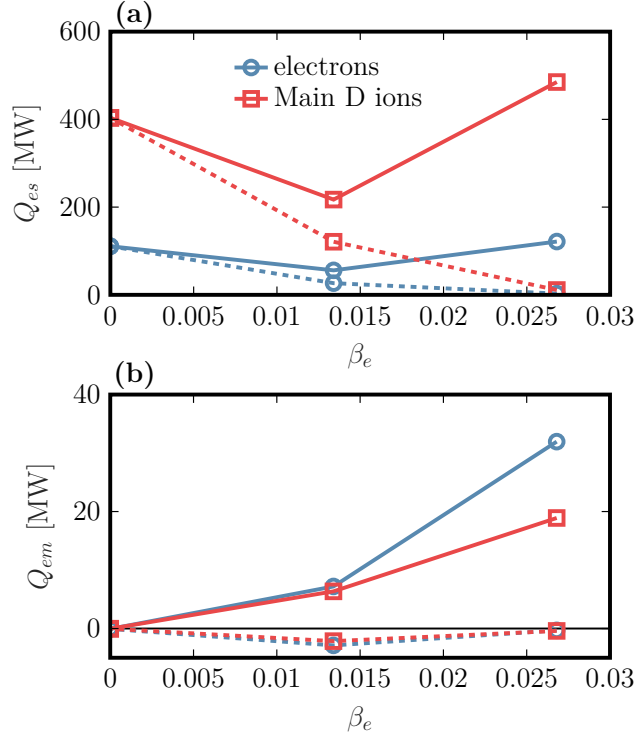
Figure 6.14 – The total electrostatic heat flux (a) and electromagnetic heat flux (b) for varying β_e, shown for electrons (blue) and main deuterium ions (red). Solid lines show data from simulations that include the effect of $\delta B_\parallel$, while dashed lines correspond to simulations which do not.

$\rho \sim 0.8$ on the HFS. These different regions are also illustrated in Fig. 6.16. In Fig. 6.17 (c) we show the angle between the filter axis and the wave vector of the fluctuations $k_{\perp,B}$, $\theta_{k_{\perp,B},f}$. In the optimal case of a narrow straight filter a fluctuating k_x, k_y component requires $\theta_{k_{\perp,B},f} \sim 0$ to scatter the laser light into the filter. In theory, to contribute to the TPCI measurement we need to simultaneously satisfy $\theta_{k_{\perp,B},f} \sim 0$ and $\theta_{k_{\perp,B},k_0} \sim 90$ degrees. By changing the filter orientation this means that we can either include the two regions near $\rho \sim 0.1$ (see blue line) or the single region near the plasma edge (see green line). In reality, as we will see in the following, for a given filter configuration there can still be a non-negligible contribution simultaneously from all three segments. However, the dominant contribution is still coming from either the two double segments or the single segmented region. In Fig. 6.17 (b) and (c) we can note that the single segmented region, selected by choosing $f_a = 0°$, mainly includes $k_y = 0$ contributions (the solid blue curve reaches simultaneously 90° in Fig. 6.17 (b) and 0° in Fig. 6.17 (c)). The double segmented regions will instead contain a mix of $k_y = 0$ and $k_y \rho_i \neq 0$ contributions.

Notice the very sharp variation of both angles in Fig. 6.17 (b) and (c) in the double segmented regions. A very sharp variation in $\theta_{k_{\perp,B},f}$ means that the fluctuating component quickly falls outside the filter and the localisation is therefore very good. However, a very sharp variation in $\theta_{k_{\perp,B},k_0}$ means, in principle, that unless $k_{\perp,B}$ is sufficiently large, the contribution from that
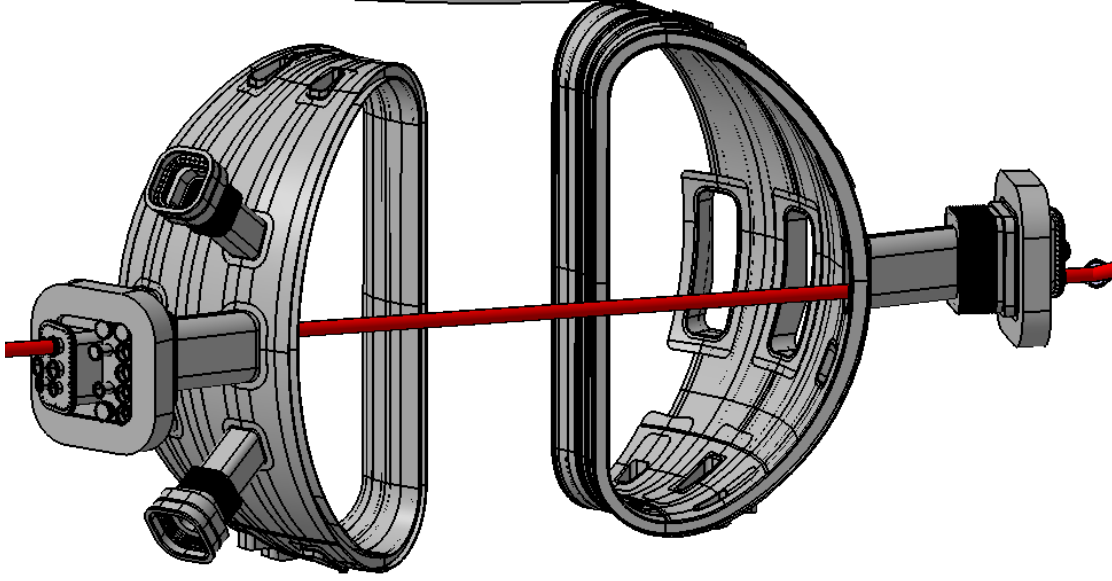
141

Figure 6.15 – Optical path of the proposed TPCI diagnostic. Source: [34].

location (either of the double segmented regions) will average out. In contrast, there is a much slower variation in both angles for the single segmented region near the HFS edge. This segment is thus better defined both in terms of the localisation length and in terms of the directions of $k_\perp$ that contribute to the measurement.

To study the localisation properties and generate first predictions of TPCI measurements in JT-60SA we use the results from the gyrokinetic simulations presented in the last section. We take the four-species case with modified parameters, as was discussed in subsection 6.1.4.

First, we estimate the localisation and compute the contribution from the different k_x and k_y fluctuating components to the PSD of the TPCI signals. We apply the same method as in section 3.2.2 for a given k_x and k_y component and consider the central ray only, $r = r_0$. We consider the two filter orientations already presented in Fig. 6.17 when the contribution to the TPCI signals is coming mostly from the single segmented region ($\theta_f = 0$) or from the two double segmented regions ($\theta_f = 90$ degrees). To simplify, we will only study the effect of geometry, thus using density fluctuations of the form (3.42), and compare it to the case when using the actual simulated density fluctuations of the form of Eq. (3.46).

Note that the passage of the TPCI laser beam through the inner midplane leads to a jump in the χ and y coordinates. However both $k_{\perp,B}$, given by Eq. (3.39), and the synthetic signal in Eq. (3.35) are made continuous through the parallel boundary condition and the connection of the k_x modes. Since the localisation is computed for each k_x and k_y mode, a meaningful estimate of the localisation can only be derived for the k_x and k_y components for which there exists a k_x connection. In the considered GENE simulation the maximum binormal wave number that still has a connection between different k_x values is $k_y\rho_i = 0.91$. Note, however, that fluctuating
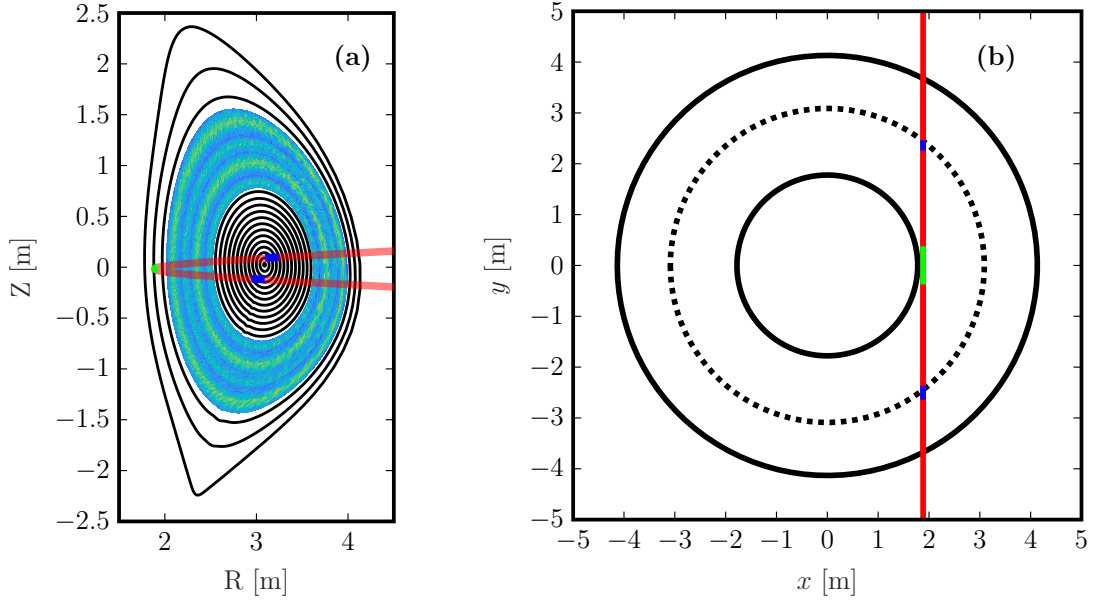
Figure 6.16 – The double-null geometry of the considered JT-60SA scenario together with the central ray of the TPCI laser beam path shown in red. We show the poloidal cross-section (a) with an overlaid snapshot of turbulent density fluctuations obtained with GENE simulations in section 6.1.4. In (b) we also show a toroidal cross-section, where the dashed black line indicates the magnetic axis and the solid black lines indicate the plasma boundary. In both (a) and (b) the blue segments illustrate the location of the double segmented regions while the green segment shows the single segmented region.

components with large k_x and k_y have very low fluctuating amplitudes and thus make a negligible contribution to the TPCI signals. In any case they can thus safely be ignored when analysing the localisation properties of TPCI.

The PSD levels without applying any filter are shown in Fig. 6.18. The result is only shown for the k_x, k_y modes with an existing connection, whereas the other components are set to zero. As just mentioned, in any case these components only make a small contribution to the synthetic TPCI signals due to their low fluctuation amplitudes. The remaining components have a dominant contribution around $k_y \rho_i \sim 0.4$. From the actual case, Fig. 6.18 (b) we see that the simulation is dominated by modes at $k_y \rho_i \sim 0.3$.

We apply then a wedge filter, with a 30 degree half angle (thus the same as has been generally used in TCV thus far), as well as the straight filter with a width equal to the width of the focal spot, thus yielding the optimal localisation as in the case of TCV in section 3.2.2. First, we choose the filter angle $\theta_f = 0$ such that we focus on the single segmented region. The PSD for this case is shown in Fig. 6.19. Of all the unfiltered components we see that this filter configuration favours purely radial modes, when the amplitude of each mode is equal (case (a) in Fig. 6.19).
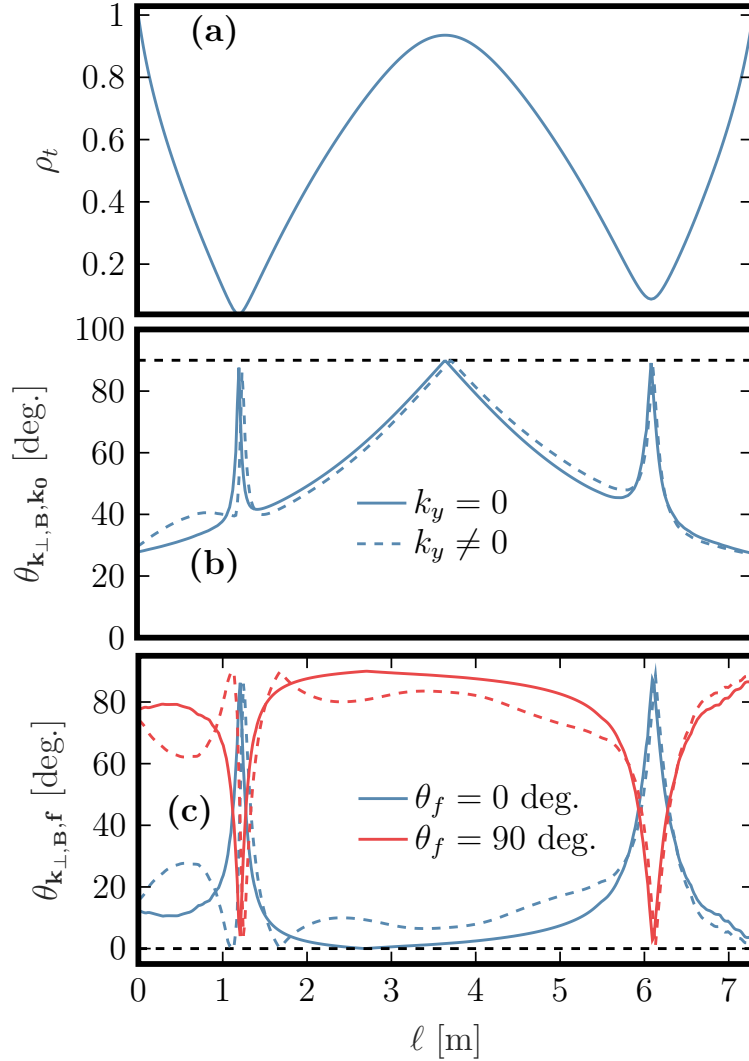
Figure 6.17 – The radial flux coordinate ρ_t as a function of the linear coordinate ℓ along the proposed JT-60SA TPCI laser beam path (a). In (b) we show the angle $\theta_{\mathbf{k}_{\perp,B},\mathbf{k_0}}$ between the wave vector of the fluctuations $\mathbf{k}_{\perp,B}$ and the laser beam direction $\mathbf{k_0}$. The black dashed line indicates a 90 degree angle. Finally (c) shows the angle $\theta_{\mathbf{k}_{\perp,B},\mathbf{f}}$ between the filter axis and the wave vector of the fluctuations. Here the dashed black line indicates a 0 degree angle. The latter is shown for two filter orientations, $\theta_f = 0$ (red) and $\theta_f = 90$ degrees (blue). The angles in (b) and (c) are illustrated for an example mode with $k_y = 0$ (solid curves) and a mode with $k_y \rho_i \neq 0$ (dashed curves).
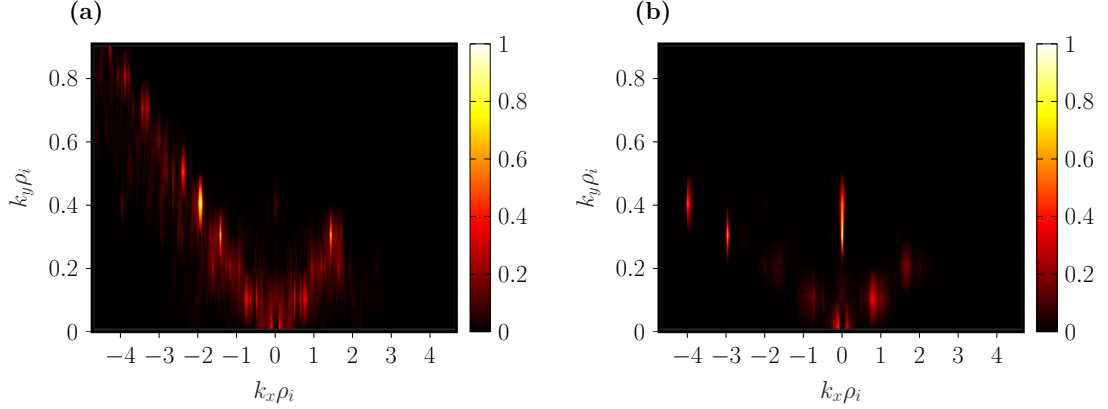
Figure 6.18 – PSD of each k_x, k_y component when integrating over the full JT-60SA laser beam path in the unfiltered case. Subfigure (a) shows the effect of the phase θ only, thus a density fluctuation of the form of Eq. (3.42) while (b) shows the actual simulated case, using Eq. (3.46). Only k_x, k_y modes with a connection are shown whereas the other components are set to zero.
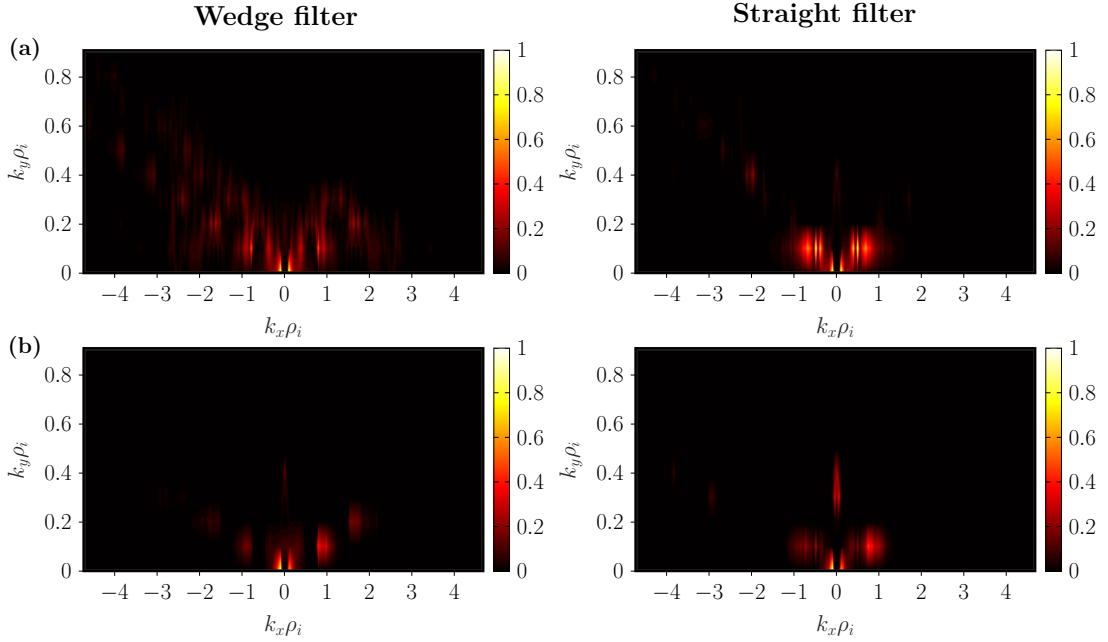
Figure 6.19 – PSD of each k_x, k_y component when integrating over the full JT-60SA laser beam path, when applying a 30 degree wedge filter (left column) or a straight filter (right column). The top row (a) shows the effect of the phase θ only, thus a density fluctuation of the form of Eq. (3.42) while the bottom row (b) shows the actual simulated case, using Eq. (3.46). Here the filter orientation is $\theta_f = 0$, focusing on the single segmented region. Only k_x, k_y modes with a connection are shown whereas the other components are set to zero.

Figure 6.20 – Same as 6.19 but with $\theta_f = 90$ degrees, thus focusing on the double segmented regions.
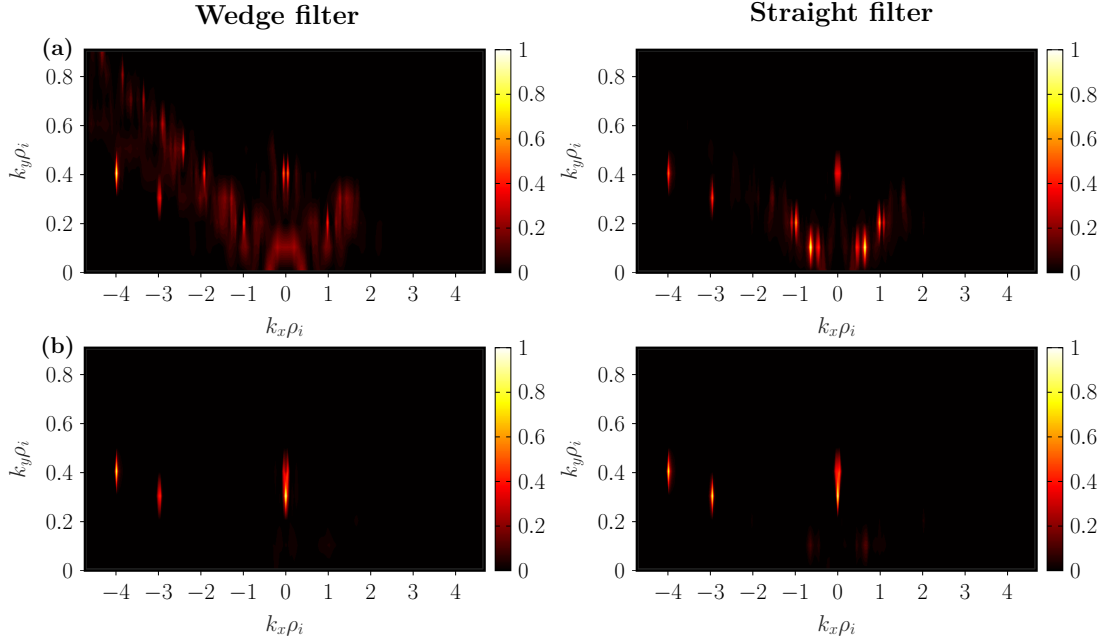
The straight filter, as expected, is more restrictive and only allows a few of the modes seen in Fig. 6.18 to contribute to the measurement.

If instead we orient the filter to focus on the double segmented regions, thus $\theta_f = 90$ degrees, we find the PSD shown in Fig. 6.20. For a density fluctuation with uniform amplitude, this filter configuration seems to slightly favour $k_y \rho_i \sim 0.4$ in the wedge filter case, and $k_y \rho_i \sim 0.1 - 0.2$ in the straight filter case. For the actual GENE simulation we see that mainly $k_y \neq 0$ modes remain. These results for the single segmented and double segmented cases are in agreement with the results from the conceptual design of TPCI at JT-60SA [34]. There it was shown that the TPCI measurement in the single segmented case essentially consists of the contribution from purely radial modes while the direction of $k_{\perp,B}$ is less constrained in the double segmented case.

To estimate the localisation we apply the same method as in section 3.2.2 for a given k_x and k_y component. The integration, Eq (3.40), is performed separately around each value of $\ell_\perp(k_x, k_y)$ to compute the contribution from either the double segmented regions, or the single segmented region. Due to the multiple values of $\ell_\perp(k_x, k_y)$ it is much more challenging to compute the localisation as it is difficult to properly distinguish the different segments from each other. To simplify we therefore limit the analysis to the unfiltered and straight filter configuration only. The latter yields in fact the optimal localisation that can be achieved in JT-60SA. Furthermore we relax the criterion in Eq. (3.41) and choose ε such that the combined power from the different segments is at least 70% of the PSD when integrating over the full laser beam length (instead of 90 % as was used for TCV). If ε is too large we otherwise, wrongly, end up connecting the different

segments together. Finally, we also limit the analysis to the 6 smallest k_y modes considered in the simulation, $k_y\rho_i = 0, 0.1, 0.2, 0.3, 0.4$ and $k_y\rho_i = 0.5$. Finally, we limit the integration length around each segment to ~ 2 m, again to avoid connecting the different segments together.

We group the localisation into the three following categories: single segmented region with $\ell_\perp \in [2.5, 5]$ m as seen in Fig. 6.17, the first double segmented region with $\ell_\perp \in [1, 1.5]$ m, and finally the second double segmented region, $\ell_\perp \in [5.5, 6.5]$ m. As was mentioned before, $\theta_{k_{\perp,B}, k_0}$ undergoes a sharp variation in the two double segmented regions. To properly satisfy the criterion $\boldsymbol{k}_{\text{meas}} \perp \boldsymbol{k}_0$ we need sufficiently large values of $k_{\perp,B}$ that the phase in Eq. (3.42) varies more rapidly than the variation of $\theta_{k_{\perp,B}, f}$ and $\theta_{k_{\perp,B}, k_0}$ in the double segmented regions. In the current GENE simulation of JT-60SA the largest value $k_{\perp,B}$ is still too low and we therefore discard the double segmented regions from the analysis in the unfiltered cases. However, it is still possible to include them in the analysis of the straight filtered cases, as will be done later.

The localisation for the single segmented region, in terms of $\Delta\rho_{k_x,k_y}$ for the unfiltered and straight filtered cases, is shown in Fig. 6.21. As before, the unfiltered case tests the property $\boldsymbol{k}_{\text{meas}} \perp \boldsymbol{k}_0$. In the case of a density fluctuation of the form of Eq. (3.42), (top plot, a) we see that this property is well satisfied for large enough values of k_x, which corresponds to larger values of $k_\perp$. We find very good localisation for $k_\perp > 5$ cm^{-1} with $\Delta\rho_{k_x,k_y} < 0.1$. At lower values of $k_\perp$ most components saturate at $\Delta\rho_{k_x,k_y} \approx 0.35$ which is the maximum value of $\Delta\rho_{k_x,k_y}$ corresponding to the maximum integration length $\Delta L_{k_x,k_y} \sim 2$ m considered in the analysis. The actual integration length for the low values of $k_\perp$ might actually be longer. There is a slight spread in the localisation due to imprecision of the underlying algorithm. We therefore include a cubic spline fit, with tension, through the points (solid lines) to more clearly illustrate the integration length at each value of $k_\perp$.

In the next step we apply the straight filter, using a 0 degree filter angle so that we only capture contributions to the TPCI measurement from the single segmented region. We see that we clearly mainly obtain contributions from very low k_y type modes, as the larger values of k_y lead to negligible contributions and are therefore not shown. The localisation for the remaining low k_y components is very similar to the corresponding result in the unfiltered case, with very good localisation for $k_\perp > 5$ cm^{-1}. This means that the averaging effect from the integration is in fact more restrictive compared to the size of the filter. That is, a fluctuating component is being averaged out sooner than it falls outside the filter.

If we use the actual form of the density fluctuation, using the GENE simulations described in the section 6.1, we get the corresponding results for the unfiltered and the filtered cases, shown in the third (c) and fourth row (d) in Fig. 6.21 respectively. We can see that only a few fluctuating components have a non-negligible contribution to the TPCI measurement, and these components have relatively low values of $k_\perp$ and are therefore poorly localised. Normally components with higher k_x have lower amplitudes which explains the low $k_\perp$ values of the components that remain in the two bottom plots in Fig. 6.21.

Figure 6.21 – Localisation in terms of the radial coordinate $\Delta\rho_{k_x,k_y}$, in JT-60SA, after applying Eq. (3.40) and using the criterion in Eq. (3.41) for the components. The localisation is shown for 6 different values of the binormal wave number $k_y\rho_i$ (circles) and a cubic spline fit (solid lines) is shown to more clearly illustrate the integration lengths. The localisation is shown for the case of a density fluctuation of the form of Eq. (3.42), (a,b) and when including the actual simulated density fluctuations (c,d). We show the unfiltered cases (a,c) and the cases when we apply the straight filter (b,d), using a 0 degree filter angle to focus on the single segmented regions.

We then rotate the filter and use a filter angle $f_a = 90$ degrees to focus instead on the two double segmented regions. The corresponding localisation for these cases is shown in Fig. 6.22. The top row shows the case of a density fluctuation of the form of Eq. (3.42) while the bottom row shows the case when including the actual simulated density fluctuations taken from GENE. Due to the very fast rotation of the wave vector of the fluctuations, the fluctuations quickly fall outside the narrow straight filter and are consequently very well localised. Already for $k_\perp > 1$ cm^{-1} we have a very short integration length with $\Delta\rho_{k_x,k_y} < 0.1$. The localisation in the second double segment is slightly better than in the first double segment. In contrast to the single segmented case, the double segmented regions include contributions from larger values of k_y, as was already shown in Fig. 6.20. Just as in the case of the single segmented region in Fig. 6.21, when considering the actual GENE-simulated case, Eq. (3.46), we see that fewer components remain, and these components have lower values of $k_\perp$. However, unlike the single segmented region, due to the fast rotation of the wave vector of the fluctuations, these components remain very well localised. The only exception are some very large scale modes with $k_\perp < 0.5$ cm^{-1} that have $\Delta\rho_{k_x,k_y} > 0.5$ in the first double segmented region.
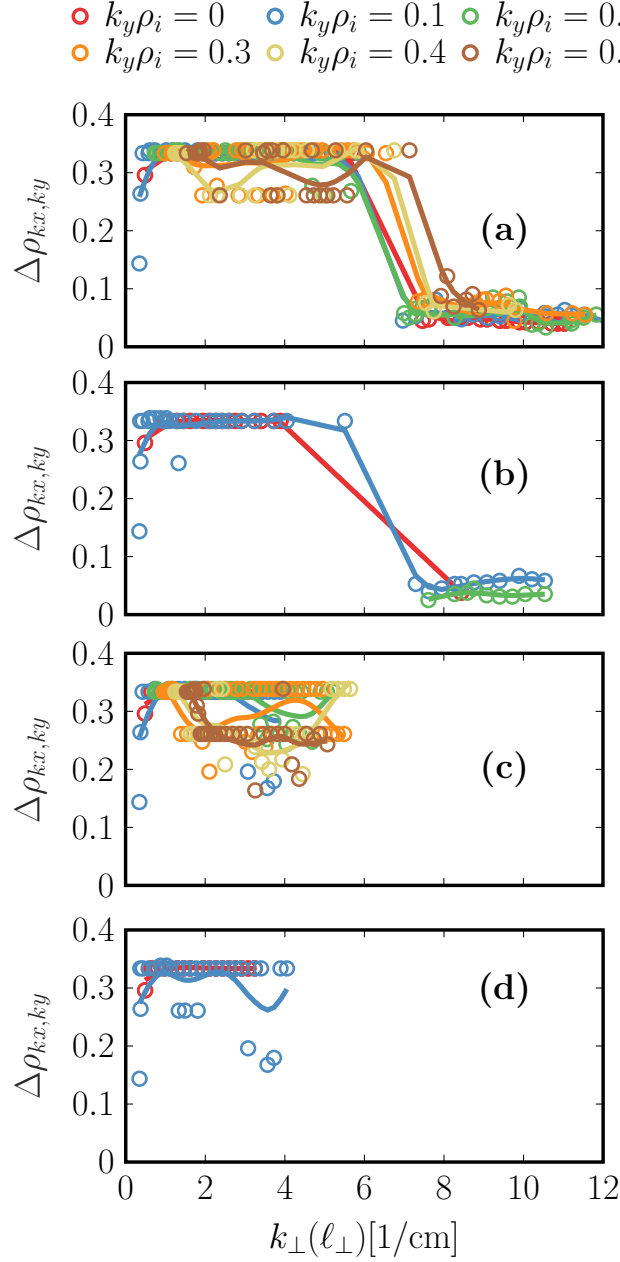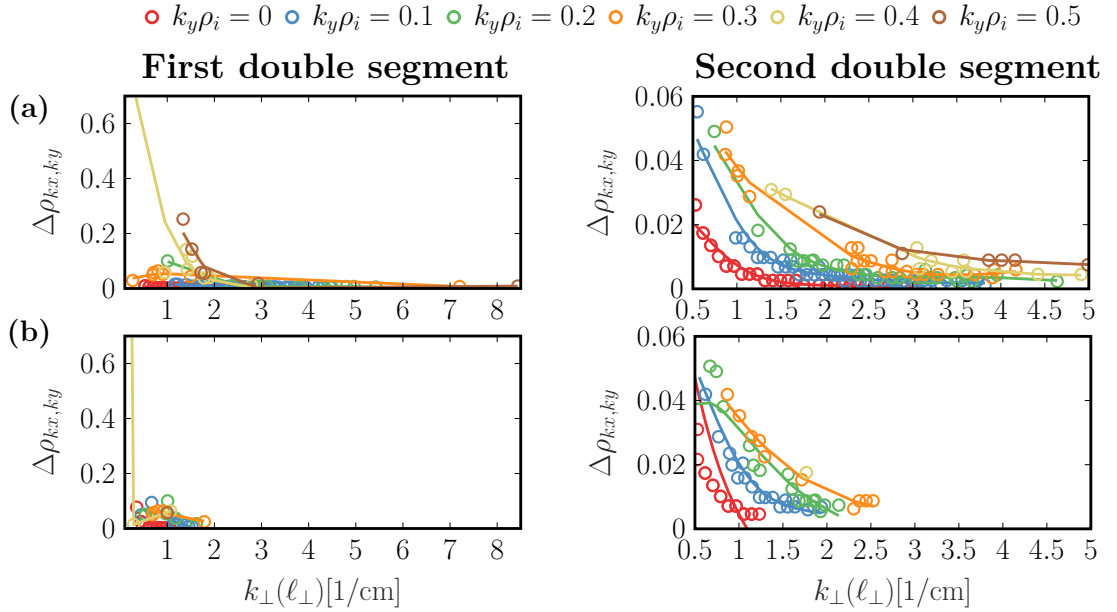

Figure 6.22 – Localisation in terms of the radial coordinate $\Delta\rho_{k_x,k_y}$, in JT-60SA, after applying Eq. (3.40) and using the criterion in Eq. (3.41) for the components. Only the results when we apply the straight filters are shown, using a 90 degree filter angle to focus on the first (left column) and second (right column) double segmented regions. The localisation is shown for 6 different values of the binormal wave number $k_y\rho_i$ (circles) and a cubic spline fit (solid lines) is used to more clearly illustrate the integration lengths. The localisation is shown for the case of a density fluctuation of the form of Eq. (3.42), (top row, a) and when including the actual simulated density fluctuations (bottom row, b).

To conclude, we find that in the single segmented region we obtain well defined segments that are

mainly defined by how rapidly a fluctuating k_x, k_y component is being averaged out, due to the line integration. We also have a well defined direction of the wave vector, mostly purely radial, that contributes to the measurement. When the filter is oriented to mostly focus on the fluctuating contribution from the two double segments instead, the localisation is achieved purely by how fast a given k_x, k_y component falls outside the spatial filter. Due to the rapid variation of $\theta_{k_{\perp,B},f}$ in the double segmented regions, as seen in Fig. 6.17 (c), the $k_\perp$ values in the present GENE simulation are too to small to be able to see an effect of line averaging of the fluctuations. The contribution now is dominated by poloidal modes $k_y \neq 0$ rather than $k_y = 0$.

We should again stress that these estimates of the localisation, obtained using a local simulation with the flux tube centred at one radial position, are by no means final. A more proper estimate of the localisation could be performed with a global simulation that would take into account the radial variation in the phases and amplitudes of the fluctuations. This is planned for future work. The equations presented in this section 3.2.1 are fully applicable also to a global case when using the Gaussian beam approach described in subsection 3.2.1. The plane wave approach described in subsection 3.2.1 can also be applied after estimating the k_x wave numbers. If we look back at the definition of the perpendicular wave number in eq. (3.39), we see that in a tokamak only k_y corresponds to an exact mode number while k_x follows from the periodic boundary conditions used in the flux tube representation. In experiments, however, k_x can be estimated by computing $k_{x,\text{eff},\ell_\perp}$, for example by computing the Fourier-transform of the spatial measurement at the TPCI image at a given poloidal angle χ. From the knowledge of the magnetic shear and the toroidal mode number of the considered mode one could then use the relationship, $k_{x,\text{eff}}(\ell, r) = k_x + \chi(\ell)\hat{s}k_y$ to infer k_x. This would also be the approach for generalising the equations shown here for a global gyrokinetic simulation, and potentially establishing a link between the k_x representation and the radial wave numbers measured in experiments.

Finally, we will compute the actual synthetic signals for the two filter orientations and generate a first prediction of the turbulence measurement with TPCI at JT-60SA. However, since we are already very limited in the number of components in the GENE fluctuations we will use a 30 degree wedge filter instead of the narrow straight filter that otherwise would lead to very low signal levels. The conditional spectra for the two filter orientations are shown in Fig. 6.23. For both filter orientations we see two narrow legs that are essentially straight, which indicates a large phase velocity $\Delta F / \delta k_r$ of the measured fluctuations. The legs are slightly wider in the double segmented case than in the measurement in the single single segment near the HFS edge.

The corresponding wave number spectrum is shown in Fig. 6.24. We see that the signal amplitudes are essentially similar for both filter orientations. However, clearly the single segmented case has a higher contribution from the purely radial fluctuating components while the double segmented case is more dominated by modes with $k_y \neq 0$. This is in agreement with the PSD levels seen already in Fig. 6.19 and Fig. 6.20

To conclude, we have made first predictions of the TPCI signals in JT-60SA, illustrating a measurement when the contribution is mainly coming from the single segmented region at the
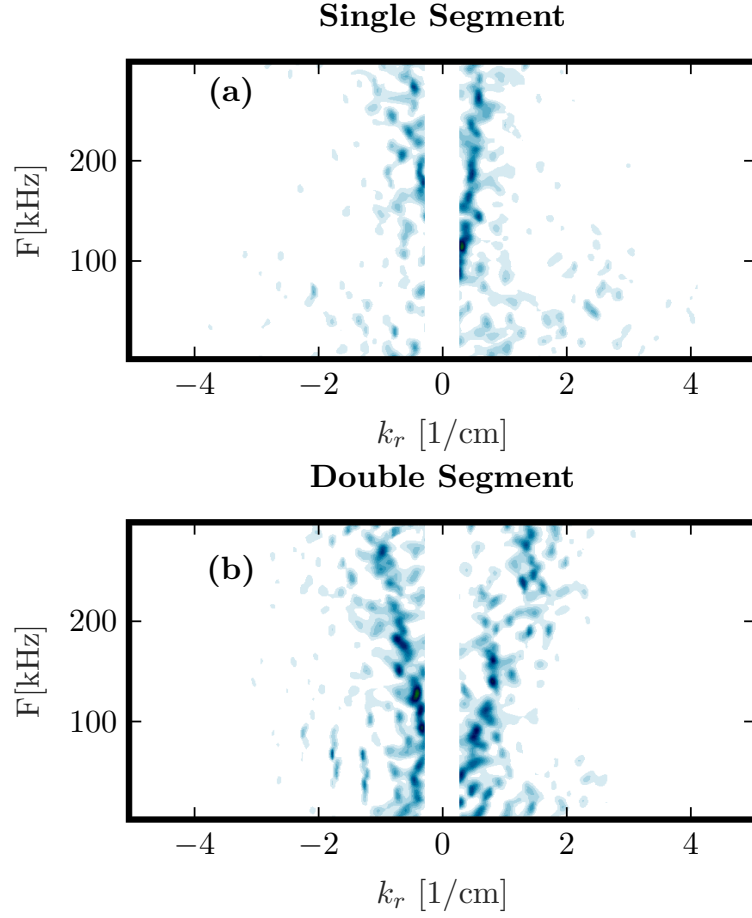
Single Segment

Double Segment

Figure 6.23 – The conditional spectrum calculated for the JT-60SA TPCI measurement, when using a wedge filter with a 30 degree half angle, with $\theta_f = 0$ thus focusing on the single segmented region (a) or $\theta_f = 90$ degrees that focuses on the double segmented regions instead (b).

edge of the plasma, or from the two double segmented regions near the core. In practice, the measurement will always be a mix of the two contributions (however with one dominating over the other depending on the selected filter angle). If the synthetic diagnostic would give an accurate picture of the fluctuations, in principle the contribution from the two different regions could be separated by artificially suppressing either contribution. Another way to distinguish the two contributions from each other, in practice, could be through the Doppler shifted frequencies due to poloidal $\boldsymbol{E} \times \boldsymbol{B}$ rotation of the plasma.

6.3   Chapter summary

In this chapter we have presented gyrokinetic modelling of turbulence, as well as the prediction of TPCI signals, in the JT-60SA machine. In section 6.1 we first showed the results from the gyrokinetic simulations of a reference JT-60SA scenario, including four kinetic species and full
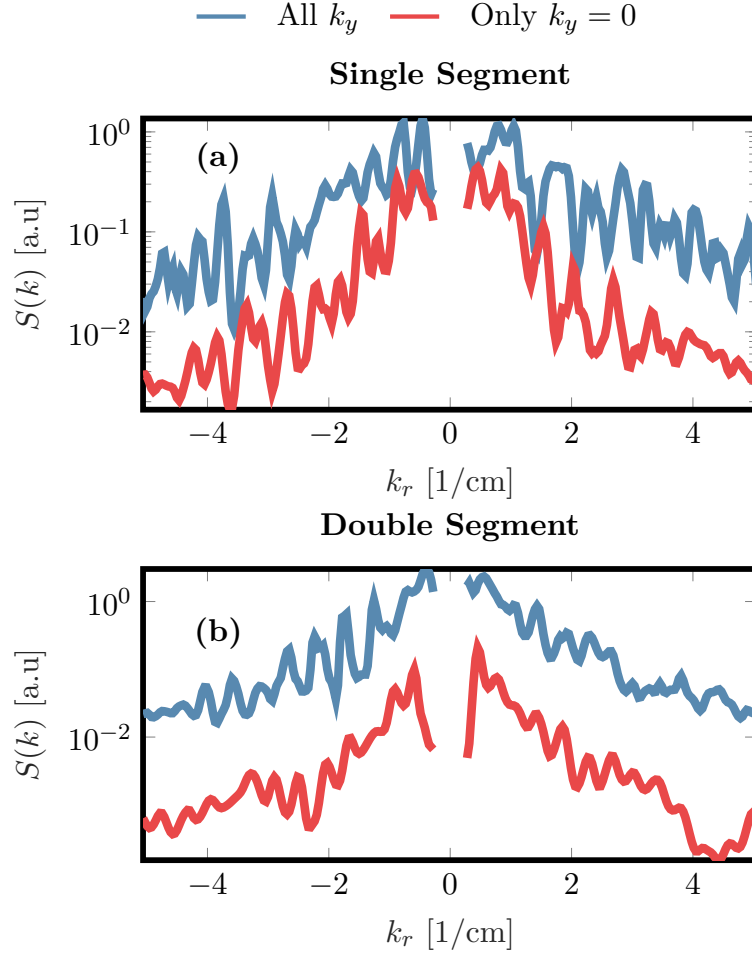
Figure 6.24 – Synthetic JT-60SA wave-number spectrum for the single segmented case (a) and the double segmented case (b) The result is shown when including all k_y contributions in Eq. (3.35) (blue) and only $k_y = 0$ (red).

electromagnetic effects. The scenario is very particular: on one hand simulations at nominal parameters predict an insufficient heat flux, well below the 41 MW of injected heat, and on the other hand, slightly increasing the background gradients leads to a runaway heat flux. The latter effect is due to the Non-Zonal Transition, which could be avoided by lowering the value of β.

We considered four kinetic species in our simulations and generated a first reference case of the considered JT-60SA scenario. In addition to increasing the gradients and lowering β we also had to slightly lower the fast-ion temperature to avoid resonating with a very high frequency mode that would otherwise dominate the heat flux time trace, with most of the heat flux being carried away by the fast ions.

We varied the gradients and demonstrated the high stiffness of the profiles. Also, in agreement with previous studies, we showed the importance of retaining, properly, compressional magnetic

field fluctuations and correctly treating the pressure gradient term, which has a strong destabilising effect on the underlying turbulence at high β.

Finally, in section 6.2, we also analysed the localisation properties of TPCI on JT-60SA and made first predictions for TPCI measurements, which in the future might be compared with experiments.

7 Summary and Conclusions

A study of turbulent fluctuations in the core of magnetised fusion plasmas using the TPCI diagnostic and gyrokinetic simulations has been carried out. Computational methods and results as well as experimental work have been presented in the different chapters of this thesis to improve our understanding of the turbulence phenomena.

7.1 Summary

The methodology for modelling PCI measurements was presented in chapter 3. First, electron density fluctuations have to be generated; the gyrokinetic framework can be used for this task. Here local flux-tube gyrokinetic GENE simulations were carried out to simulate the electron density fluctuations, which where then fed to the synthetic diagnostic. The synthetic diagnostic calculates the fluctuating intensity that would be measured by square-law detectors, by processing the code-generated fluctuations through the real diagnostics's transfer function, including the appropriate volume integration, frequency response, and wave-vector selection using a spatial filter - the latter in particular leading to the localisation of the measurement.

Two different approaches have been considered. The first, Gaussian approach, takes into account a Gaussian distribution of the electric field of the laser beam and a finite optical aperture. While this is the proper way of modelling the signals, it is complicated to use for understanding how different types of modes affect the TPCI signals. Therefore, a second approach was presented, where by taking the infinite plane wave approximation and neglecting the effect of the aperture, it is possible to write the synthetic signal as a sum over GENE k_x and k_y modes. This can then be used to conveniently trace the contribution from different types of modes to the TPCI signals. This approach was used in section 3.2.2 to estimate the localisation length from first principles. We found that the property $k_{meas} \perp k_0$ is poorly satisfied and therefore the localisation is worse than previously expected. The wide wedge filter, used in past TPCI measurements in TCV, in particular, did not lead to additional localisation. The narrow straight filter, on the other hand, leads to very good localisation of the signals. The localisation depends on the orientation of the

spatial filter, and is optimal when purely radial fluctuation directions are selected.

The synthetic diagnostic was applied to studying past TPCI measurements in a pair of positive and negative triangularity TCV discharges, finding that the $\delta > 0$ case is dominated by an outward propagating GAM. Due to a change in the measurement geometry as well as the characteristics of the fluctuations, the $\delta < 0$ case did not contain the GAM, and as a result the measurement became dominanted by fluctuations propagating inward, with $k_r < 0$.

Section 4.2 explored the idea of rotating the spatial filter and making the TPCI measurement mostly sensitive to ITG/TEM fluctuations instead of purely radial modes. Using several gyrokinetic simulations with varying ITG and TEM content, it was demonstrated that a transition from an ITG to a dominantly TEM-driven plasma could be identified by studying the direction of propagation of the most dominant modes. In particular, by taking the ratio in the wave-number spectral power $S(k_r)$, of contributions with $k_r > 0$ over contributions with $k_r < 0$, it is possible to identify if a scenario is more or less driven by ITG or TEM type turbulence. We stressed the importance of selecting an appropriate filter angle for measuring $k_y \neq 0$ modes, since if zonal type modes with $k_y = 0$ contribute to the measurement, they might pollute the contributions from ITG/TEM fluctuations, making it very difficult to identify the characteristics of the turbulence from the TPCI signals.

In the next part of chapter 4, in section 4.2.4, we showed that when the TPCI measurement is sensitive to $k_y \neq 0$ modes, certain aspects of the TPCI signals can to some extent already be seen in computationally inexpensive linear gyrokinetic simulations. After applying the quasilinear model, it was shown that the fluctuation wave number that gives the largest contribution to the TPCI signals, the asymmetry in the $S(k_r)$ wave-number spectra computed from the measurement, and finally the relative change in the amplitude of the TPCI signals, could already be, to some extent, predicted from linear simulations. The procedure for using linear simulations to predict TPCI signals was demonstrated by applying the described method to a plasma undergoing a LOC-SOC transition, featuring a transition from TEM to ITG.

The following chapter 5 contained the experimental part of this thesis work. We discussed the upgrade of the TPCI diagnostic, the tests of the PC and PV detectors in the lab, and finally the final TPCI set-up that was implemented for measurement of ion scale turbulence. Issues with mechanical vibrations constituted one of the main setbacks that prevented us from taking measurements with TPCI. Nevertheless, data in four discharges could still be acquired. Two of these were carried out within a study on the effect of plasma triangularity on plasma turbulence, in a diverted configuration. We found that the only variation in the fluctuation amplitude was due to lower values of ρ_ψ that were measured in the $\delta < 0$ case. Despite similar amplitudes, the spectral features, however, were different between $\delta > 0$ and $\delta < 0$. Signatures of Quasi-Coherent Modes (QCMs) were identified for $\delta > 0$, but not as clearly for $\delta < 0$, suggesting a stabilisation of TEM turbulence in the latter. However, with linear simulations, both $\delta > 0$ and $\delta < 0$, despite no external heating, were found to be already ITG dominated, thus suggesting that the QCMs are actually not due to TEM. A dominant contribution from ITG could be in agreement

with a dominant $k_r > 0$ contribution seen in the $S(k_r)$ spectra. However, since the orientation of the spatial filter was not optimised for measurements of $k_y \neq 0$, it is difficult to draw clear conclusions.

A second pair of TCV discharges with TPCI measurements were also carried out for studying the role of electron-cyclotron heating on turbulence. We found that the characteristics of the turbulence are very similar, but the amplitude is clearly increased. We found that the main difference between these two cases without and with EC heating was an increase in the local electron temperature in the latter, which leads to an increased drive of the underlying instabilities.

Chapters 3-5 focused on the study of turbulence in TCV. In the final part, chapter 6, we instead looked at the turbulent fluctuations that could be expected in the JT-60SA tokamak. The JT-60SA tokamak is much larger than TCV and will operate in a very different parameter regime. In particular, while electromagnetic effects could be neglected in TCV, in JT-60SA they play a crucial role because of the high β that can be reached. Using local gyrokinetic GENE simulations we explored this electromagnetic turbulence in a representative, planned, high-performance JT-60SA plasma discharge. We found first that the nominal parameters, generated from reduced transport models, predict a very low turbulent heat flux, well below the injected 41MW from NBH and ECH. In an attempt to match the total heat flux with the injected power we increased the ion and electron temperature and density gradients, but encountered then the Non-Zonal Transition causing heat fluxes to no longer saturate. We characterised the threshold of the NZT and found that, while increasing the background density and temperature gradients, one has to reduce β to avoid the heat-flux runaway. We included also carbon impurities and fast ions in our simulations and generated a first reference case of the considered JT-60SA scenario. We found that including compressional magnetic field fluctuations $\delta B_\parallel$ is crucial, together with a proper treatment of the pressure gradient term in the simulations. If this parameter is not considered, the high-β completely suppresses the heat flux, even when the background gradients are increased. Finally, we found very high stiffness in the ion temperature profile, so that modifying the ion temperature gradient even slightly has a very large effect on the simulated heat flux. It was also clear that the nominal parameters predicted with the reduced transport models are clearly below nonlinear critical gradients.

The final part of chapter 6 was dedicated to using the results from the gyrokinetic simulations and the synthetic PCI diagnostic to predict the PCI signals in future experiments. The actual diagnostic set-up planned for JT-60SA was taken into account. We showed the synthetic signals and demonstrated the good localisation that can be achieved.

7.2 Suggestions for Future Work

The synthetic diagnostic already includes the most important physics, and yet could be improved further by including the divergence of the laser beam and by treating scattering in the Bragg regime. Also, it would be desirable to make the calculations of the synthetic signals more efficient,

potentially parallelizing the codes to simultaneously handle several diagnostic rays. However, the main next step would be to calculate the synthetic signals using global turbulence simulations. This is particularly important in the case of TCV, but even in JT-60SA it is necessary for more properly calculating the localisation of the TPCI signals, and to identify where in the plasma the main contribution to the signals comes from. Instead of global simulations, a different approach could also be to find a way of combining the results from several local flux-tube simulations. This would be beneficial in larger machines, to more accurately predict the TPCI signals, while avoiding the high computational cost of global simulations.

The synthetic tool could be actively used for predicting and interpreting TPCI measurements in different conditions. In this work we only explored a few scenarios, which were mainly geared towards demonstrating the principles of the synthetic diagnostic and better understanding the measured TPCI signals, rather than studying the physics of turbulence and actively comparing synthetic signals with actual experiments. Several scenarios would be interesting to explore, including the LOC-SOC transition that was discussed in section 4.3. Other suggestions are scenarios with internal transport barriers, with strong electron scale turbulence and with different mixes of ITG and TEM fluctuations, all in varying plasma geometry, to mention a few. Finally, it would also be desirable to continue exploring the role of the EC beam on turbulence as well as the effect of plasma triangularity in diverted configurations.

On the hardware side, the most crucial improvement would be to properly damp the vibrations and recover the past performance of the diagnostic. Next, the planned PV high bandwidth detector should be employed for measuring electron scale turbulence. It would also be of interest to implement the heterodyning components and combine measurements of turbulence with high frequency MHD modes. Finally, an optical set-up that would allow to quickly change the filter orientation would be very valuable to investigate the contribution from different types of fluctuations. For example, measurements first of the zonal $k_y = 0$ components and then separately of the $k_y \neq 0$ fluctuations, in the same scenario, would provide useful information on the coupling between zonal modes and ITG/TEM, and improve our understanding on how changes in the plasma parameters affects these different type of fluctuations.

7.3   Conclusions

Turbulence is an intriguing phenomenon that dictates the behaviour of many physical systems, such as fusion plasmas, where it leads to large cross-field transport, ultimately limiting the performance of the fusion reactors. The complexity of turbulence makes it very difficult to understand the underlying physics of the fluctuations, however, by combining the measurements of turbulence with simulations and modelling we can improve our understanding of the turbulence phenomena. One day, perhaps, we shall have enough confidence to stay calm *...in the midst of so much turbulence.*

A The transfer function in GENE coordinates

The goal is to prove the following relation

$$\tilde{\mathscr{E}}(Mr, Mp, t) = \frac{\sqrt{\rho} c E_{p0}^2}{4\pi M^2} r_e \lambda_0 \int_L d\ell \, [T \circ \delta n_e](r, p, t) \tag{A.1}$$

$$= \frac{\sqrt{\rho} c E_{p0}^2}{4\pi M^2} r_e \lambda_0 \int_L d\ell \tag{A.2}$$

$$\times \sum_{k_x} \sum_{k_y} \hat{G}(k_r(k_x, k_y, r, p, \ell), k_p(k_x, k_y, r, p, \ell)) \delta n_e(k_x, k_y, z(r, p, \ell), t)$$

$$\times e^{ik_x x(r,p,\ell) + ik_y y(r,p,\ell)}, \tag{A.3}$$

meaning that the convolution operator can be written as a sum over k_x, k_y modes

$$[T \circ \delta n_e](r, p, t) =$$

$$\sum_{k_x} \sum_{k_y} \hat{G}(k_r(k_x, k_y, r, p, \ell), k_p(k_x, k_y, r, p, \ell)) \delta n_e(k_x, k_y, z(r, p, \ell), t) e^{ik_x x(r,p,\ell) + ik_y y(r,p,\ell)}, \tag{A.4}$$

for some function $\hat{G}(k_r(k_x, k_y, r, p, \ell), k_p(k_x, k_y, r, p, \ell))$. The meaning of the function $\hat{G}$ is that is should capture the effect of the phase plate and spatial filters on each k_x and k_y mode.

Each k_x and k_y is related to k_r, k_p via the following equations

$$k_r = \mathbf{e}_r \cdot \mathbf{k}_\perp(k_x, k_y, r, p, \ell),$$
$$k_p = \mathbf{e}_p \cdot \mathbf{k}_\perp(k_x, k_y, r, p, \ell), \tag{A.5}$$

where $\mathbf{e}_r$ and $\mathbf{e}_p$ are the unit vectors pointing in the r or p direction respectively, and perpendicular wave vector equals to $\mathbf{k}_\perp = k_x \nabla x(r, p, \ell) + k_y \nabla y(r, p, \ell)$.

The convolution in k_r, k_p space reads

$$[T \circ \delta n_e](r, p, t) = \int dk_r \int dk_r \hat{T}(k_r, k_p) \delta n_e(k_r, k_p, \ell, t) e^{ik_r r + ik_p p}. \tag{A.6}$$

Appendix A. The transfer function in GENE coordinates

Consider the representation of $\delta n_e(k_r, k_p, \ell, t)$ via the Fourier transform

$$\delta n_e(k_r, k_p, \ell, t) = \int \int \mathrm{d}r \, \mathrm{d}p \, \delta n_e(r, p, \ell, t) e^{-ik_r r - ik_p p} =$$
$$\int \mathrm{d}x \, \mathrm{d}y \, \delta n_e(x, y, z, t) e^{-ik_r r(x,y,z) - ik_p p(x,y,z)} J(x, y, z) \qquad (A.7)$$

where in the second step we have done a coordinate transformation from the cartesian r, p, ℓ to the field aligned GENE coordinates x, y, z by using the Jacobian $J(x, y, z)$, such that $\mathrm{d}r \, \mathrm{d}p = J(x, y, z) \, \mathrm{d}x \, \mathrm{d}y$. Now, $\delta n_e(x, y, z, t)$ can then be represented in Fourier k_x, k_y space

$$\delta n_e(x, y, z, t) = \int \mathrm{d}k_x \int \mathrm{d}k_y \, \delta n_e(k_x, k_y, z, t) e^{ik_x x + ik_y y}. \qquad (A.8)$$

Plugging this into Eq. (A.7) gives

$$\delta n_e(k_r, k_p, \ell, t) =$$
$$\int \mathrm{d}x \int \mathrm{d}y \int \mathrm{d}k_x \int \mathrm{d}k_y \, \delta n_e(k_x, k_y, z, t) e^{ik_x x + ik_y y} e^{ik_r r(x,y,z) + ik_p p(x,y,z)} J(x, y, z) \qquad (A.9)$$

We can reorganise the integrals and write

$$\delta n_e(k_r, k_p, \ell, t) = \int \int \mathrm{d}k_x \, \mathrm{d}k_y \, \delta n_e(k_x, k_y, z, t) \int \int \mathrm{d}x \, \mathrm{d}y \, e^{ik_x x + ik_y y} e^{ik_r r(x,y,z) + ik_p p(x,y,z)} J(x, y, z)$$
$$= \int \int \mathrm{d}k_x \, \mathrm{d}k_y \, \delta n_e(k_x, k_y, z, t) F(k_x, k_y, k_r, k_p),$$

where in the last stage we have represented the integral over x and y as the function $F(k_x, k_y, k_r, k_p)$.

Plugging in this result into Eq. (A.6) gives

$$[T \circ \delta n_e](r, p, t) =$$
$$\int \mathrm{d}k_r \int \mathrm{d}k_r \hat{T}(k_r, k_p) \int \int \mathrm{d}k_x \, \mathrm{d}k_y \, \delta n_e(k_x, k_y, z, t) F(k_x, k_y, k_r, k_p) e^{ik_r r + ik_p p} =$$
$$\int \int \mathrm{d}k_x \, \mathrm{d}k_y \, \delta n_e(k_x, k_y, z, t) \int \int \mathrm{d}k_r \, \mathrm{d}k_p \hat{T}(k_r, k_p) F(k_x, k_y, k_r, k_p) e^{ik_r r + ik_p p}, \qquad (A.10)$$

where in the second step we took out $\delta n_e(k_x, k_y, z, t)$ from the integral over k_r and k_p since it does not depend on these wave numbers. Multiplying and dividing by $\exp[ik_x x(r, p, \ell) + ik_y y(r, p, \ell)]$ yields

$$[T \circ \delta n_e](r, p, t) =$$
$$\int \int \mathrm{d}k_x \, \mathrm{d}k_y \, \delta n_e(k_x, k_y, z, t) e^{ik_x x(r,p,\ell) + ik_y y(r,p,\ell)} e^{-ik_x x(r,p,\ell) - ik_y y(r,p,\ell)}$$
$$\times \int \int \mathrm{d}k_r \, \mathrm{d}k_p \hat{T}(k_r, k_p) F(k_x, k_y, k_r, k_p) e^{ik_r r + ik_p p} =$$
$$\int \int \mathrm{d}k_x \, \mathrm{d}k_y \, \delta n_e(k_x, k_y, z, t) e^{ik_x x(r,p,\ell) + ik_y y(r,p,\ell)} \hat{G}(k_x, k_y, r, p, \ell) \qquad (A.11)$$

Where in the second step we introduced yet another function $\hat{G}(k_x, k_y, r, p, \ell)$ which is equal to

$$\hat{G}(k_x, k_y, r, p, \ell) = e^{-ik_x x(r,p,\ell) - ik_y y(r,p,\ell)} \int \int \mathrm{d}k_r \, \mathrm{d}k_p \hat{T}(k_r, k_p) F(k_x, k_y, k_r, k_p) e^{ik_r r + ik_p p}. \quad \text{(A.12)}$$

Finally, we have the relationship between k_x, k_y and k_r, k_p given by Eq. (A.5) which means that we can write $\hat{G}(k_x, k_y, r, p, \ell) = \hat{G}(k_r(k_x, k_y, r, p, \ell), k_p(k_x, k_y, r, p, \ell))$. Thus we have proved that Eq. (A.11) is valid under the assumption that the transfer function $\hat{T}(k_r, k_p)$ is sufficiently nice such that the kernel in Eq. (A.12) remains integratable.

B Updating the synthetic diagnostic MATLAB routines to use a different coordinate system

The synthetic PCI diagnostic presented in this work is based on the field-aligned coordinate system employed in the GENE code, thus using

$$x = \rho_t - \rho_{t,0},$$
$$y = C_y \left[q(\rho_t)\chi - \varphi \right],$$
$$z = \chi,$$

with associated boundary conditions, as discussed in subsection 3.1.1. Given the Cartesian r, p, ℓ coordinates, defining the PCI detector volumes, we compute the GENE coordinates $x(r,p,\ell), y(r,p,\ell)$ and $z(r,p,\ell)$ which are then used to map the simulated density fluctuations in the GENE coordinate system onto the diagnostic volumes, thus

$$\delta n_e(x,y,z) \rightarrow \delta n_e(x(r,p,\ell),y(r,p,\ell),z(r,p,\ell)) \rightarrow \delta n_e(r,p,\ell), \tag{B.1}$$

following the method described in section 3.2.1.

In the plane-wave approximation presented in subsection 3.2.1, the synthetic TPCI signals were further written as a sum over k_x and k_y modes. The spatial filters and the effect of the phase plate is then applied by mapping each k_x and k_y mode onto k_r and k_p according to

$$k_r = \mathbf{e}_r \cdot \mathbf{k}_\perp (k_x, k_y, r, p, \ell),$$
$$k_p = \mathbf{e}_p \cdot \mathbf{k}_\perp (k_x, k_y, r, p, \ell),$$

where $\mathbf{k}_\perp = k_x \nabla x(r,p,\ell) + k_y \nabla y(r,p,\ell)$.

The synthetic diagnostic tool has been written in MATLAB, and consists of various subroutines. The script `feed_PCI.m` is used to define the diagnostic volumes, to carry out the coordinate transformation, and in the case of the plane wave approach, to define the filter functions. The transformation from the Cartesian coordinate system r, p, ℓ to the field-aligned system x, y, z is handled by the subroutine `compute_diag_coords.m`. As input it takes r, p, ℓ

Appendix B. Updating the synthetic diagnostic MATLAB routines to use a different coordinate system

and as output it gives $x(r,p,\ell), y(r,p,\ell), z(r,p,\ell)$. The filters are defined in the subroutine `compute_filter_matrix.m` where each part of the PCI transfer function, including the effect of the phase plate $\hat{G}_G$, the spatial filters $\hat{G}_W$ (case of wedge filter) or $\hat{G}_S$ (case of straight filter) and the averaging function $\mathscr{T}_{av}(k_r, k_p)$, is each represented as a matrix $M(k_x, k_y, \ell)$.

Once the diagnostic volumes have been defined we run the routine `start_synth_diag.m` that calculates and saves the synthetic signal for each PCI detector volume. For each time-step in this routine we run the function `build_fluct_maps.m` that loads the electron density fluctuations from GENE. The data is provided both in real space $\delta n_e(x,y,z)$ after carrying out the inverse Fourier transform, and by taking directly the output from GENE in Fourier space, $\delta n_e(k_x, k_y, z)$. In the case of the Gaussian beam approach, the first is provided to the function `pci_signal_gaussian.m` where the GENE data in the field-aligned coordinate system is transformed onto the PCI detector coordinates, after which we calculate the PCI signal by computing the Fourier transform in r, p, ℓ and then applying the various filter functions in k_r, k_p space. In the case of the plane wave approach, we use the density fluctuation in the Fourier representation $\delta n_e(k_x, k_y, z)$ and then apply the filter functions in the routine `pci_signal_plane.m`, by a simple multiplication with the matrix $M(k_x, k_y, \ell)$ computed before.

To use a different coordinate system, an additional sub-module has to be added to the subroutine `compute_diag_coords.m` to transform the diagnostic volumes to the new coordinate system, $x'(r,p,\ell), y'(r,p,\ell), z'(r,p,\ell)$. Then, a new routine for reading the simulated density fluctuations (which we here assume to be still represented in Fourier-space) $\delta n_e(k_{x'}, k_{y'}, z')$ and the evaluation of the inverse Fourier-transform to give $n_e(x', y', z')$, has to be added to `build_fluct_maps.m`. Updating these two routines is sufficient to use the Gaussian beam approach.

To use the plane-wave approach requires also an update of the routine `compute_filter_matrix.m` by adding the new form of the perpendicular wave vector, $\mathbf{k}_\perp = k_{x'} \nabla x'(r,p,\ell) + k_{y'} \nabla y'(r,p,\ell)$. This is sufficient to calculate the new matrices $M(k_{x'}, k_{y'}, \ell)$ that are then used to multiply $n_e(k_{x'}, k_{y'}, z')$ in the function `pci_signal_plane.m`.

Note that in the Gaussian beam approach, x', y', z' do not have to correspond to a field-aligned coordinate system. This is in contrast to the plane-wave approach, where a field-aligned coordinate system has been assumed.

Bibliography

[1] R. J. Hawryluk, "Results from deuterium-tritium tokamak confinement experiments," *Rev. Mod. Phys.*, vol. 70, pp. 537–587, 2 Apr. 1998.

[2] G. Bateman, A. H. Kritz, V. V. Parail, and J. G. Cordey, "Effect of isotope mass on transport simulations of Joint European Torus high-mode plasmas with Edge Localized Modes," *Physics of Plasmas*, vol. 6, no. 12, pp. 4607–4614, 1999.

[3] A. J. Creely, M. J. Greenwald, S. B. Ballinger, D. Brunner, J. Canik, J. Doody, T. Fülöp, D. T. Garnier, R. Granetz, T. K. Gray, and et al., "Overview of the SPARC tokamak," *Journal of Plasma Physics*, vol. 86, no. 5, p. 865 860 502, 2020.

[4] M. Hoppe and A. Iantchenko and I. Strandberg, "Simulation of Charged Particle Orbits in Fusion Plasmas," Bachelors's thesis, Chalmers University of Technology, 2015.

[5] V. D. Shafranov, "Plasma Equilibrium in a Magnetic Field," *Reviews of Plasma Physics*, vol. 2, p. 103, Jan. 1966.

[6] S. Coda, M. Agostini, R. Albanese, S. Alberti, E. Alessi, S. Allan, J. Allcock, R. Ambrosino, H. Anand, Y. Andrèbe, H. Arnichand, F. Auriemma, J. Ayllon-Guerola, F. Bagnato, and J. Ball, "Physics research on the TCV tokamak facility: from conventional to alternative scenarios and beyond," *Nuclear Fusion*, vol. 59, no. 11, p. 112 023, Aug. 2019.

[7] W. Horton, D. Choi, and W. M. Tang, "Toroidal drift modes driven by ion pressure gradients," *The Physics of Fluids*, vol. 24, no. 6, pp. 1077–1085, 1981.

[8] B. Kadomtsev and O. Pogutse, *Zh.EKsp.Teor.Fiz*, vol. 51, 1966.

[9] G. Merlo, "Flux-tube and global grid-based gyrokinetic simulations of plasma microturbulence and comparisons with experimental tcv measurements," *Ph.D. Thesis, EPFL*, 2016.

[10] A. Marinoni, S. Brunner, Y. Camenen, S. Coda, J. P. Graves, X. Lapillonne, A. Pochelon, O. Sauter, and L. Villard, "The effect of plasma triangularity on turbulent transport:modelling TCV experiments by linear and non linear gyrokinetic simulations," *Plasma Phys. Control. Fusion*, vol. 51, p. 055 016, 2009.

[11] F. Jenko, W. Dorland, M. Kotschenreuther, and B. N. Rogers, "Electron temperature gradient driven turbulence," *Physics of Plasmas*, vol. 7, no. 5, pp. 1904–1910, 2000.

[12] T. Görler and F. Jenko, "Scale separation between electron and ion thermal transport," *Phys. Rev. Lett.*, vol. 100, p. 185 002, 18 May 2008.

[13] N. T. Howard, C. Holland, A. E. White, M. Greenwald, and J. Candy, "Synergistic cross-scale coupling of turbulence in a tokamak plasma," *Physics of Plasmas*, vol. 21, no. 11, p. 112 510, 2014.

[14] S. Maeyama, Y. Idomura, T.-H. Watanabe, M. Nakata, M. Yagi, N. Miyato, A. Ishizawa, and M. Nunami, "Cross-scale interactions between electron and ion scale turbulence in a tokamak plasma," *Phys. Rev. Lett.*, vol. 114, p. 255 002, 25 Jun. 2015.

[15] N. Bonanomi, P. Mantica, J. Citrin, T. Goerler, and B. T. and, "Impact of electron-scale turbulence and multi-scale interactions in the JET tokamak," *Nuclear Fusion*, vol. 58, no. 12, p. 124 003, Sep. 2018.

[16] W. Dorland, F. Jenko, M. Kotschenreuther, and B. N. Rogers, "Electron temperature gradient turbulence," *Phys. Rev. Lett.*, vol. 85, pp. 5579–5582, 26 Dec. 2000.

[17] H. Doerk, F. Jenko, M. J. Pueschel, and D. R. Hatch, "Gyrokinetic microtearing turbulence," *Phys. Rev. Lett.*, vol. 106, p. 155 003, 15 Apr. 2011.

[18] M. J. Pueschel, Ph.D. dissertation, University of Münster, 2009.

[19] P. H. Diamond, S.-I. Itoh, K. Itoh, and T. S. Hahm, "Zonal flows in plasma—a review," *Plasma Physics and Controlled Fusion*, vol. 47, no. 5, R35–R161, Apr. 2005.

[20] M. J. Pueschel, P. W. Terry, F. Jenko, D. R. Hatch, W. M. Nevins, T. Görler, and D. Told, "Extreme heat fluxes in gyrokinetic simulations: a new critical β," *Phys. Rev. Lett.*, vol. 110, p. 155 005, 15 Apr. 2013.

[21] C. A. De Meijere, "An Experimental Study of Plasma Fluctuations in the TCV and TEXTOR Tokamaks," Ph.D. dissertation, No. 5610, EPFL, 2013.

[22] Z. Huang, S. Coda, G. Merlo, S. Brunner, L. Villard, B. Labit, and C. Theiler, "Experimental observations of modes with geodesic acoustic character from the core to the edge in the TCV tokamak," *Plasma Physics and Controlled Fusion*, vol. 60, no. 3, p. 034 007, Feb. 2018.

[23] J. P. Freidberg, *Plasma Physics and Fusion Energy*. Cambridge University Press, 2007, Cambridge Books Online, ISBN: 9780511755705.

[24] S. Coda, M. Porkolab, and T. N. Carlstrom, "A phase contrast interferometer on DIII-D," *Review of Scientific Instruments*, vol. 63, no. 10, pp. 4974–4976, 1992.

[25] S. Coda, "An experimental study of turbulence by phase-contrast imaging in the DIII-D tokamak," *Ph.D. Thesis, MIT Plasma Science and Fusion Center*, 1997.

[26] E. Nelson-Melby, M. Porkolab, P. T. Bonoli, Y. Lin, A. Mazurenko, and S. J. Wukitch, "Experimental observations of mode-converted ion cyclotron waves in a tokamak plasma by phase contrast imaging," *Phys. Rev. Lett.*, vol. 90, p. 155 004, 15 Apr. 2003.

[27] A. Marinoni, "Plasma fluctuation studies in the TCV tokamak modeling of shaping effects and advanced diagnostic development," Ph.D. dissertation, No. 4516, EPFL, 2009.

[28] K. Tanaka, C. A. Michael, L. N. Vyacheslavov, A. L. Sanin, K. Kawahata, T. Akiyama, T. Tokuzawa, and S. Okajima, "Two-dimensional phase contrast imaging for local turbulence measurements in large helical device (invited)," *Review of Scientific Instruments*, vol. 79, no. 10, 10E702, 2008.

[29] E. M. Edlund, M. Porkolab, Z. Huang, O. Grulke, L.-G. Böttger, C. von Sehren, and A. von Stechow, "Overview of the Wendelstein 7-X phase contrast imaging diagnostic," *Review of Scientific Instruments*, vol. 89, no. 10, 10E105, 2018.

[30] P. A. Molina Cabrera, "Tokamak plasma edge studies by microwave short-pulse reflectometry and backscattering," Ph.D. dissertation, No. 9515, EPFL, 2019.

[31] Z. Huang, "Experimental study of plasma turbulence in the TCV tokamak," Ph.D. dissertation, No. 7715, EPFL, 2017.

[32] *GENE web page*, http://genecode.org/, Accessed: 2018-04-25.

[33] T. Görler, X. Lapillonne, S. Brunner, T. Dannert, F. Jenko, F. Merz, and D. Told, "The global version of the gyrokinetic turbulence code GENE," *Journal of Computational Physics*, vol. 230, no. 18, pp. 7053–7071, 2011, ISSN: 0021-9991.

[34] S. Coda, A. Iantchenko, S. Brunner, M. Toussaint, and K. Tanaka, "A phase-contrast-imaging core fluctuation diagnostic and first-principles turbulence modeling for JT-60SA," *Nuclear Fusion*, vol. 61, p. 106 022, 2021.

[35] H. Weisen, "The phase contrast method as an imaging diagnostic for plasma density fluctuations (invited)," *Review of Scientific Instruments*, vol. 59, no. 8, pp. 1544–1549, 1988.

[36] Z. Huang and S. Coda, "Dependence of density fluctuations on shape and collisionality in positive- and negative-triangularity tokamak plasmas," *Plasma Physics And Controlled Fusion*, vol. 61, no. 1, p. 014 021, 2019.

[37] C. A. de Meijere, S. Coda, Z. Huang, L. Vermare, T. Vernay, V. Vuille, S. Brunner, J. Dominski, and P. Hennequin, "Complete multi-field characterization of the geodesic acoustic mode in the TCV tokamak," *Plasma Physics and Controlled Fusion*, vol. 56, no. 7, p. 072 001, Jun. 2014.

[38] C. Marini, "Poloidal CX visible light plasma rotation diagnostics in TCV," Ph.D. dissertation, No. 8031, EPFL, 2017.

[39] F. Bagnato, "Study of impurity ion transport using charge exchange spectroscopy on TCV," Ph.D. dissertation, No. 9550, EPFL, 2022.

[40] J.-M. Moret, B. Duval, H. Le, S. Coda, F. Felici, and H. Reimerdes, "Tokamak equilibrium reconstruction code liuqe and its real time implementation," *Fusion Engineering and Design*, vol. 91, pp. 1–15, 2015, ISSN: 0920-3796.

[41] F. Carpanese, "Development of free-boundary equilibrium and transport solvers for simulation and real-time interpretation of tokamak experiments," Ph.D. dissertation, No. 7914, EPFL, 2021.

[42] J. Candy and R. E. Waltz, "An Eulerian gyrokinetic-Maxwell solver," *Journal of Computational Physics*, vol. 186, no. 2, pp. 545–581, Apr. 2003.

[43] E. Highcock, "The zero turbulence manifold in fusion plasmas," Ph.D. dissertation, University of Oxford, 2012.

[44] *Gyrokinetic simulations project*, http://gyrokinetics.sourceforge.net/, Accessed: 2021-10-11.

[45] E. Lanti, N. Ohana, N. Tronko, T. Hayward-Schneider, A. Bottino, B. McMillan, A. Mishchenko, A. Scheinberg, A. Biancalani, P. Angelino, S. Brunner, J. Dominski, P. Donnel, C. Gheller, R. Hatzky, A. Jocksch, S. Jolliet, Z. Lu, J. Martin Collar, I. Novikau, E. SonnendrÃŒcker, T. Vernay, and L. Villard, "Orb5: a global electromagnetic gyrokinetic code using the pic approach in toroidal geometry," *Computer Physics Communications*, vol. 251, p. 107 072, 2020, ISSN: 0010-4655.

[46] A. Peeters, Y. Camenen, F. Casson, W. Hornsby, A. Snodin, D. Strintzi, and G. Szepesi, "The nonlinear gyro-kinetic flux tube code gkw," *Computer Physics Communications*, vol. 180, no. 12, pp. 2650–2672, 2009, 40 YEARS OF CPC: A celebratory issue focused on quality software for high performance, grid and novel computing architectures, ISSN: 0010-4655.

[47] Y. Idomura, M. Ida, T. Kano, N. Aiba, and S. Tokuda, "Conservative global gyrokinetic toroidal full-f five-dimensional vlasov simulation," *Computer Physics Communications*, vol. 179, no. 6, pp. 391–403, 2008, ISSN: 0010-4655.

[48] Y. Chen and S. E. Parker, "Electromagnetic gyrokinetic îžf particle-in-cell turbulence simulation with realistic equilibrium profiles and geometry," *Journal of Computational Physics*, vol. 220, no. 2, pp. 839–855, 2007, ISSN: 0021-9991.

[49] Z. Lin, S. Ethier, T. S. Hahm, and W. M. Tang, "Size scaling of turbulent transport in magnetically confined plasmas," *Phys. Rev. Lett.*, vol. 88, p. 195 004, 19 Apr. 2002.

[50] A. J. Wootton, B. A. Carreras, H. Matsumoto, K. McGuire, W. A. Peebles, C. P. Ritz, P. W. Terry, and S. J. Zweben, "Fluctuations and anomalous transport in tokamaks," *Physics of Fluids B: Plasma Physics*, vol. 2, no. 12, pp. 2879–2903, 1990.

[51] E. Mazzucato, "Spectrum of small-scale density fluctuations in tokamaks," *Phys. Rev. Lett.*, vol. 48, pp. 1828–1830, 26 Jun. 1982.

[52] R. J. Fonck, G. Cosby, R. D. Durst, S. F. Paul, N. Bretz, S. Scott, E. Synakowski, and G. Taylor, "Long-wavelength density turbulence in the tftr tokamak," *Phys. Rev. Lett.*, vol. 70, pp. 3736–3739, 24 Jun. 1993.

[53] X. Lapillonne, "Local and global eulerian gyrokinetic simulations of microturbulence in realistic geometry with applications to the tcv tokamak," Ph.D. dissertation, No. 4684, EPFL, 2010.

[54] D. Told, "Gyrokinetic microturbulence in transport barriers," en, Ph.D. dissertation, Universität Ulm, 2012.

[55] J. Ball, S. Brunner, and B. F. McMillan, "The effect of background flow shear on gyrokinetic turbulence in the cold ion limit," *Plasma Physics and Controlled Fusion*, vol. 61, no. 6, p. 064 004, Apr. 2019.

[56] B. F. McMillan, J. Ball, and S. Brunner, "Simulating background shear flow in local gyrokinetic simulations," *Plasma Physics and Controlled Fusion*, vol. 61, no. 5, p. 055 006, Mar. 2019.

[57] F. Merz, "Gyrokinetic simulation of multimode plasma turbulence," en, Ph.D. dissertation, Universität Münster, 2008.

[58] G. H, "Gyrokinetic simulations of microtearing turbulence," en, Ph.D. dissertation, Universität Ulm, 2012.

[59] C. P, "Collisional and electromagnetic physics in gyrokinetic models," en, Ph.D. dissertation, UCLA, 2019.

[60] A. Chandrarajan Jayalekshmi, "Studying the effect of non-adiabatic passing electron dynamics on microturbulence self-interaction in fusion plasmas using gyrokinetic simulations," Ph.D. dissertation, No. 8206, EPFL, 2020.

[61] M. A. Beer, "Gyrofluid models of turbulent transport in tokamaks," Ph.D. dissertation, Princeton University, 1995.

[62] J. Ball, S. Brunner, and A. C.J., "Eliminating turbulent self-interaction through the parallel boundary condition in local gyrokinetic simulations," *Journal of Plasma Physics*, vol. 86, Apr. 2020.

[63] D. R. Mikkelsen and W. Dorland, "Dimits shift in realistic gyrokinetic plasma-turbulence simulations," *Phys. Rev. Lett.*, vol. 101, p. 135 003, 13 Sep. 2008.

[64] J. W. Connor, R. J. Hastie, and P. Helander, "Stability of the trapped electron mode in steep density and temperature gradients," *Plasma Physics and Controlled Fusion*, vol. 48, no. 6, p. 885, May 2006.

[65] F. L. Hinton and M. N. Rosenbluth, "Dynamics of axisymmetric and poloidal flows in tokamaks," *Plasma Physics and Controlled Fusion*, vol. 41, no. 3A, A653, Mar. 1999.

[66] M. N. Rosenbluth, W. M. MacDonald, and D. L. Judd, "Fokker-planck equation for an inverse-square force," *Phys. Rev.*, vol. 107, pp. 1–6, 1 Jul. 1957.

[67] S. Brunner, T. Tran, and J. Hittinger, "Review of the landau collision operator and approximate linearized forms for numerical implementation," *LLNL-CRPP internal report*, 2010.

[68] H. Sugama, T.-H. Watanabe, and M. Nunami, "Linearized model collision operators for multiple ion species plasmas and gyrokinetic entropy balance equations," *Physics of Plasmas*, vol. 16, no. 11, p. 112 503, 2009.

[69] A. Iantchenko, S. Coda, S. Brunner, G. Merlo, J. Ball, and F. Margairaz, "A synthetic phase-contrast imaging diagnostic with spatial filtering for gyrokinetic simulations," *Plasma Physics and Controlled Fusion*, 2022.

[70] H. Lütjens, A. Bondeson, and O. Sauter, "The CHEASE code for toroidal MHD equilibria," *Computer Physics Communications*, vol. 97, no. 3, pp. 219–260, 1996, ISSN: 0010-4655.

[71] M. Pueschel, T. Dannert, and F. Jenko, "On the role of numerical dissipation in gyrokinetic vlasov simulations of plasma microturbulence," *Computer Physics Communications*, vol. 181, no. 8, pp. 1428–1437, 2010, ISSN: 0010-4655.

[72] Z. Huang, S. Coda, and the TCV Team, "Dependence of density fluctuations on shape and collisionality in positive- and negative-triangularity tokamak plasmas," *Plasma Physics and Controlled Fusion*, vol. 61, no. 1, p. 014 021, Nov. 2019.

[73] A. Marinoni, S. Coda, R. Chavan, and G. Pochon, "Design of a tangential phase contrast imaging diagnostic for the tcv tokamak," *Review of Scientific Instruments*, vol. 77, no. 10, 10E929, 2006.

[74] Z. Huang and S. C. and, "Dependence of density fluctuations on shape and collisionality in positive- and negative-triangularity tokamak plasmas," *Plasma Physics and Controlled Fusion*, vol. 61, no. 1, p. 014 021, Nov. 2018.

[75] F. I. Parra, M. Barnes, and A. G. Peeters, "Up-down symmetry of the turbulent transport of toroidal angular momentum in tokamaks," *Physics of Plasmas*, vol. 18, no. 6, p. 062 501, 2011.

[76] G. Merlo, S. Brunner, O. Sauter, Y. Camenen, T. Görler, F. Jenko, A. Marinoni, D. Told, and L. Villard, "Investigating profile stiffness and critical gradients in shaped tcv discharges using local gyrokinetic simulations of turbulent transport," *Plasma Physics and Controlled Fusion*, vol. 57, no. 5, p. 054 010, Apr. 2015.

[77] J. L. V. Lewandowski, G. Rewoldt, S. Ethier, W. W. Lee, and Z. Lin, "Global particle-in-cell simulations of microturbulence with kinetic electrons," *Physics of Plasmas*, vol. 13, no. 7, p. 072 306, 2006.

[78] A. Mariani, S. Brunner, J. Dominski, A. Merle, G. Merlo, O. Sauter, T. Görler, F. Jenko, and D. Told, "Identifying microturbulence regimes in a tcv discharge making use of physical constraints on particle and heat fluxes," *Physics of Plasmas*, vol. 25, no. 1, p. 012 313, 2018.

[79] E. Fable, C. Angioni, and O. Sauter, "The role of ion and electron electrostatic turbulence in characterizing stationary particle transport in the core of tokamak plasmas," *Plasma Physics and Controlled Fusion*, vol. 52, no. 1, p. 015 007, Dec. 2009.

[80] T. Dannert and F. Jenko, "Gyrokinetic simulation of collisionless trapped-electron mode turbulence," *Physics of Plasmas*, vol. 12, no. 7, p. 072 309, 2005.

[81] A. Casati, C. Bourdelle, X. Garbet, F. Imbeaux, J. Candy, F. Clairet, G. Dif-Pradalier, G. Falchetto, T. Gerbaud, V. Grandgirard, Ö. Gürcan, P. Hennequin, J. Kinsey, M. Ottaviani, R. Sabot, Y. Sarazin, L. Vermare, and R. Waltz, "Validating a quasi-linear transport model versus nonlinear simulations," *Nuclear Fusion*, vol. 49, no. 8, p. 085 012, 2009.

[82] F. Jenko, T. Dannert, and C. Angioni, "Heat and particle transport in a tokamak: advances in nonlinear gyrokinetics," *Plasma Physics and Controlled Fusion*, vol. 47, no. 12B, B195, Nov. 2005.

[83] S. Rienäcker, "Characterization of Core Turbulence in the TCV Tokamak," Master's thesis, Swiss Plasma Center, EPFL, 2022.

[84] M. Fontana, L. Porte, and P. Molina Cabrera, "Correlation electron cyclotron emission diagnostic in tcv," *Review of Scientific Instruments*, vol. 88, no. 8, p. 083 506, 2017.

[85] P. Molina Cabrera, S. Coda, L. Porte, and A. Smolders, "V-band nanosecond-scale pulse reflectometer diagnostic in the TCV tokamak," *Review of Scientific Instruments*, vol. 90, no. 12, p. 123 501, 2019.

[86] Y. Camenen, A. Pochelon, R. Behn, A. Bottino, A. Bortolon, S. Coda, A. Karpushov, O. Sauter, G. Zhuang, and the TCV team, "Impact of plasma triangularity and collisionality on electron heat transport in TCV l-mode plasmas," *Nuclear Fusion*, vol. 47, no. 7, pp. 510–516, Jun. 2007.

[87] H. Arnichand, R. Sabot, S. Hacquin, A. Krämer-Flecken, X. Garbet, J. Citrin, C. Bourdelle, G. Hornung, J. Bernardo, C. Bottereau, F. Clairet, G. Falchetto, and J. Giacalone, "Quasi-coherent modes and electron-driven turbulence," *Nuclear Fusion*, vol. 54, no. 12, p. 123 017, Nov. 2014.

[88] H. Arnichand, R. Sabot, S. Hacquin, A. KrÃ€mer-Flecken, C. Bourdelle, J. Citrin, X. Garbet, J. Giacalone, R. Guirlet, J. Hillesheim, L. Meneses, and J. Contributors, "Discriminating the trapped electron modes contribution in density fluctuation spectra," *Nuclear Fusion*, vol. 55, no. 9, p. 093 021, Aug. 2015.

[89] H. Arnichand, J. Citrin, S. Hacquin, R. Sabot, A. KrÃ€mer-Flecken, X. Garbet, C. Bourdelle, C. Bottereau, F. Clairet, J. C. Giacalone, Z. O. GuimarÃ£es-Filho, R. Guirlet, G. Hornung, A. Lebschy, P. Lotte, P. Maget, A. Medvedeva, D. Molina, V. Nikolaeva, D. Prisiazhniuk, the Tore Supra, and the ASDEX Upgrade teams, "Identification of trapped electron modes in frequency fluctuation spectra," *Plasma Physics and Controlled Fusion*, vol. 58, no. 1, p. 014 037, Nov. 2015.

[90] P. Barabaschi, Y. Kamada, H. Shirai, and the JT-60SA Integrated Project Team, "Progress of the JT-60SA project," *Nuclear Fusion*, vol. 59, no. 11, p. 112 005, Jun. 2019.

[91] G. Giruzzi, M. Yoshida, N. Aiba, J. F. Artaud, J. Ayllon-Guerola, O. Beeke, A. Bierwage, T. Bolzonella, M. Bonotto, C. Boulbe, M. Chernyshova, S. Coda, R. Coelho, D. Corona, N. Cruz, S. Davis, C. Day, G. D. Tommasi, M. Dibon, D. Douai, D. Farina, A. Fassina, B. Faugeras, L. Figini, M. Fukumoto, S. Futatani, K. Galazka, J. Garcia, M. Garcia-Muñoz, L. Garzotti, L. Giudicotti, N. Hayashi, M. Honda, K. Hoshino, A. Iantchenko, S. Ide, S. Inoue, A. Isayama, E. Joffrin, Y. Kamada, K. Kamiya, M. Kashiwagi, H. Kawashima, T. Kobayashi, A. Kojima, T. Kurki-Suonio, P. Lang, P. Lauber, E. de la Luna, G. Marchiori, G. Matsunaga, A. Matsuyama, M. Mattei, S. Mazzi, A. Mele, Y. Miyata, S. Moriyama, J. Morales, A. Moro, T. Nakano, R. Neu, S. Nowak, F. Orsitto, V. Ostuni, N. Oyama, S. Paméla, R. Pasqualotto, B. Pégourié, E. Perelli, L. Pigatto, C. Piron, A. Pironti, P.

Platania, B. Ploeckl, D. Ricci, M. Romanelli, G. Rubino, S. Sakurai, K. Särkimäki, M. Scannapiego, K. Shinohara, J. Shiraishi, S. Soare, C. Sozzi, T. Suzuki, Y. Suzuki, T. Szepesi, M. Takechi, K. Tanaka, H. Tojo, M. Turnyanskiy, H. Urano, M. Valisa, M. Vallar, J. Varje, J. Vega, F. Villone, T. Wakatsuki, T. Wauters, M. Wischmeier, S. Yamoto, and R. Zagórski, "Advances in the physics studies for the JT-60SA tokamak exploitation and research plan," *Plasma Physics and Controlled Fusion*, vol. 62, no. 1, p. 014 009, Oct. 2019.

[92] M. Yoshida, G. Giruzzi, N. Aiba, J. F. Artaud, J. Ayllon-Guerola, L. Balbinot, O. Beeke, E. Belonohy, P. Bettini, W. Bin, A. Bierwage, T. Bolzonella, M. Bonotto, C. Boulbe, J. Buermans, M. Chernyshova, S. Coda, R. Coelho, S. Davis, C. Day, G. D. Tommasi, M. Dibon, A. Ejiri, G. Falchetto, A. Fassina, B. Faugeras, L. Figini, M. Fukumoto, S. Futatani, K. Galazka, J. Garcia, M. Garcia-Muñoz, L. Garzotti, L. Giacomelli, L. Giudicotti, S. Hall, N. Hayashi, C. Hoa, M. Honda, K. Hoshino, M. Iafrati, A. Iantchenko, S. Ide, S. Iio, R. Imazawa, S. Inoue, A. Isayama, E. Joffrin, K. Kamiya, Y. Ko, M. Kobayashi, T. Kobayashi, G. Kocsis, A. Kovacsik, T. Kurki-Suonio, B. Lacroix, P. Lang, P. Lauber, A. Louzguiti, E. de la Luna, G. Marchiori, M. Mattei, A. Matsuyama, S. Mazzi, A. Mele, F. Michel, Y. Miyata, J. Morales, P. Moreau, A. Moro, T. Nakano, M. Nakata, E. Narita, R. Neu, S. Nicollet, M. Nocente, S. Nowak, F. P. Orsitto, V. Ostuni, Y. Ohtani, N. Oyama, R. Pasqualotto, B. Pégourié, E. Perelli, L. Pigatto, C. Piccinni, A. Pironti, P. Platania, B. Ploeckl, D. Ricci, P. Roussel, G. Rubino, R. Sano, K. Särkimäki, K. Shinohara, S. Soare, C. Sozzi, S. Sumida, T. Suzuki, Y. Suzuki, T. Szabolics, T. Szepesi, Y. Takase, M. Takech, N. Tamura, K. Tanaka, H. Tanaka, M. Tardocchi, A. Terakado, H. Tojo, T. Tokuzawa, A. Torre, N. Tsujii, H. Tsutsui, Y. Ueda, H. Urano, M. Valisa, M. Vallar, J. Vega, F. Villone, T. Wakatsuki, T. Wauters, M. Wischmeier, S. Yamoto, and L. Zani, "Plasma physics and control studies planned in JT-60SA for ITER and DEMO operations and risk mitigation," *Plasma Physics and Controlled Fusion*, vol. 64, no. 5, p. 054 004, Mar. 2022.

[93] JT–60SA Research Unit, *JT–60SA Research Plan, Version 4.0*, 2018.

[94] O. Asztalos, G. Pokol, D. Dunai, G. Boguszlavszkij, A. Kovacsik, M. Hellermann, K. Kamiya, T. Suzuki, and A. Kojima, "Feasibility study on the JT-60SA tokamak beam emission spectroscopy diagnostics," *Fusion Engineering and Design*, vol. 123, pp. 861–864, 2017, Proceedings of the 29th Symposium on Fusion Technology (SOFT-29) Prague, Czech Republic, September 5-9, 2016, ISSN: 0920-3796.

[95] D. Carralero, T. Happel, T. Estrada, T. Tokuzawa, J. Martínez, E. de la Luna, A. Cappa, and J. García, "A feasibility study for a Doppler reflectometer system in the JT-60SA tokamak," *Fusion Engineering and Design*, vol. 173, p. 112 803, 2021, ISSN: 0920-3796.

[96] N. HAYASHI, M. HONDA, K. HOSHINO, K. HAMAMATSU, K. SHIMIZU, T. TAKIZUKA, T. OZEKI, and A. FUKUYAMA, "Integrated modeling of whole tokamak plasma," *Plasma and Fusion Research*, vol. 6, pp. 2 403 065–2 403 065, 2011.

[97] K. Tani, M. Azumi, and R. Devoto, "Numerical analysis of 2d mhd equilibrium with non-inductive plasma current in tokamaks," *Journal of Computational Physics*, vol. 98, no. 2, pp. 332–341, 1992, ISSN: 0021-9991.

[98] K. Shinya, "Equilibrium analysis of tokamak plasma," *J. Plasma Fusion Res*, vol. 76, no. 5, pp. 479–488, 2000.

[99] R. E. Waltz and R. L. Miller, "Ion temperature gradient turbulence simulations and plasma flux surface shape," *Physics of Plasmas*, vol. 6, no. 11, pp. 4265–4271, 1999.

[100] F. L. Hinton and R. D. Hazeltine, "Theory of plasma transport in toroidal confinement systems," *Rev. Mod. Phys.*, vol. 48, pp. 239–308, 2 Apr. 1976.

[101] F. Jenko and W. Dorland, "Nonlinear electromagnetic gyrokinetic simulations of tokamak plasmas," *Plasma Physics and Controlled Fusion*, vol. 43, no. 12A, A141–A150, Nov. 2001.

[102] M. Porkolab, J. Dorris, P. Ennever, C. Fiore, M. Greenwald, A. Hubbard, Y. Ma, E. Marmar, Y. Podpaly, M. L. Reinke, J. E. Rice, J. C. Rost, N. Tsujii, D. Ernst, J. Candy, G. M. Staebler, and R. E. Waltz, "Transport and turbulence studies in the linear ohmic confinement regime in alcator c-mod," *Plasma Physics and Controlled Fusion*, vol. 54, no. 12, p. 124 029, Nov. 2012.

[103] I. Pusztai, A. Mollén, T. Fülöp, and J. Candy, "Turbulent transport of impurities and their effect on energy confinement," *Plasma Physics and Controlled Fusion*, vol. 55, no. 7, p. 074 012, Jun. 2013.

[104] P. Ennever, M. Porkolab, J. Candy, G. Staebler, M. L. Reinke, J. E. Rice, J. C. Rost, D. Ernst, C. Fiore, J. Hughes, and J. Terry, "The effects of dilution on turbulence and transport in c-mod ohmic plasmas and comparisons with gyrokinetic simulations," *Physics of Plasmas*, vol. 22, no. 7, p. 072 507, 2015.

[105] G. Wilkie, A. Iantchenko, I. Abel, E. Highcock, and I. P. and, "First principles of modelling the stabilization of microturbulence by fast ions," *Nuclear Fusion*, vol. 58, no. 8, p. 082 024, Jun. 2018.

[106] G. Staebler, N. Howard, J. Candy, and C. Holland, "A model of the saturation of coupled electron and ion scale gyrokinetic turbulence," *Nuclear Fusion*, vol. 57, no. 6, p. 066 046, May 2017.

[107] G. G. Whelan, M. J. Pueschel, and P. W. Terry, "Nonlinear electromagnetic stabilization of plasma microturbulence," *Phys. Rev. Lett.*, vol. 120, p. 175 002, 17 Apr. 2018.

[108] N. Joiner, A. Hirose, and W. Dorland, "Parallel magnetic field perturbations in gyrokinetic simulations," *Physics of Plasmas*, vol. 17, no. 7, p. 072 104, 2010.

[109] A. Zocco, P. Helander, and J. W. Connor, "Magnetic compressibility and ion-temperature-gradient-driven microinstabilities in magnetically confined plasmas," *Plasma Physics and Controlled Fusion*, vol. 57, no. 8, p. 085 003, Jul. 2015.

[110] M. Kotschenreuther, W. Dorland, Q. Liu, M. Zarnstorff, R. Miller, and Y. Lin-Liu, "Attaining neoclassical transport in ignited tokamaks," *Nuclear Fusion*, vol. 40, no. 3Y, p. 677, Mar. 2000.

Bibliography

[111] A. M. Dimits, G. Bateman, M. A. Beer, B. I. Cohen, W. Dorland, G. W. Hammett, C. Kim, J. E. Kinsey, M. Kotschenreuther, A. H. Kritz, L. L. Lao, J. Mandrekas, W. M. Nevins, S. E. Parker, A. J. Redd, D. E. Shumaker, R. Sydora, and J. Weiland, "Comparisons and physics basis of tokamak transport models and turbulence simulations," *Physics of Plasmas*, vol. 7, no. 3, pp. 969–983, 2000.

[112] J. Citrin, F. Jenko, P. Mantica, D. Told, C. Bourdelle, J. Garcia, J. W. Haverkort, G. M. D. Hogeweij, T. Johnson, and M. J. Pueschel, "Nonlinear stabilization of tokamak microturbulence by fast ions," *Phys. Rev. Lett.*, vol. 111, p. 155 001, 15 Oct. 2013.

[113] B. N. Rogers, W. Dorland, and M. Kotschenreuther, "Generation and stability of zonal flows in ion-temperature-gradient mode turbulence," *Phys. Rev. Lett.*, vol. 85, pp. 5336–5339, 25 Dec. 2000.

[114] R. E. Waltz, M. E. Austin, K. H. Burrell, and J. Candy, "Gyrokinetic simulations of off-axis minimum-q profile corrugations," *Physics of Plasmas*, vol. 13, no. 5, p. 052 301, 2006.

[115] M. J. Pueschel, M. Kammerer, and F. Jenko, "Gyrokinetic turbulence simulations at high plasma beta," *Physics of Plasmas*, vol. 15, no. 10, p. 102 310, 2008.

[116] A. Di Siena, T. Görler, H. Doerk, R. Bilato, J. Citrin, T. Johnson, M. Schneider, and E. Poli, "Non-Maxwellian fast particle effects in gyrokinetic GENE simulations," *Physics of Plasmas*, vol. 25, no. 4, p. 042 304, 2018.

[117] B. J. Faber, M. J. Pueschel, J. H. E. Proll, P. Xanthopoulos, P. W. Terry, C. C. Hegna, G. M. Weir, K. M. Likin, and J. N. Talmadge, "Gyrokinetic studies of trapped electron mode turbulence in the helically symmetric experiment stellarator," *Physics of Plasmas*, vol. 22, no. 7, p. 072 305, 2015.

[118] M. J. Pueschel, B. J. Faber, J. Citrin, C. C. Hegna, P. W. Terry, and D. R. Hatch, "Stellarator turbulence: subdominant eigenmodes and quasilinear modeling," *Phys. Rev. Lett.*, vol. 116, p. 085 001, 8 Feb. 2016.

[119] P. W. Terry, P.-Y. Li, M. J. Pueschel, and G. G. Whelan, "Threshold heat-flux reduction by near-resonant energy transfer," *Phys. Rev. Lett.*, vol. 126, p. 025 004, 2 Jan. 2021.

[120] P.-Y. Li, P. W. Terry, G. G. Whelan, and M. J. Pueschel, "Saturation physics of threshold heat-flux reduction," *Physics of Plasmas*, vol. 28, no. 10, p. 102 507, 2021.

[121] M. Pueschel, P. Li, and P. Terry, "Predicting the critical gradient of itg turbulence in fusion plasmas," English, *Nuclear Fusion*, vol. 61, no. 5, Apr. 2021, Publisher Copyright: © 2021 Institute of Physics Publishing. All rights reserved., ISSN: 0029-5515.

[122] A. Ishizawa, D. Urano, Y. Nakamura, S. Maeyama, and T.-H. Watanabe, "Persistence of ion temperature gradient turbulent transport at finite normalized pressure," *Phys. Rev. Lett.*, vol. 123, p. 025 003, 2 Jul. 2019.

Acknowledgements

Acknowledgements

This thesis would have been in a much worse state without the detailed comments of Stefano and Stephan, despite their very busy schedule. I would also like to thank Justin for his help with chapter 3, Samuele, Claudia Colandrea, Matteo Vallar, Lorenzo Martinelli and Filippo Bagnato per aiuto con l'abstract italiano et Jessica Chaves, Stephan et Stefano pour l'aide avec la version française. Thank you Gabriele for Fig. 1.4 and to Sascha Rienäcker for Fig. 5.1.

The JT-60SA simulations were by far more challenging than we expected, but thanks to Moritz Pueschel we finally managed to get through this electromagnetic-non zonal-dimits-shifted jungle. Thank you for the guidance and for answering our questions so quickly.

All the simulations I have done would have been useless without the IT support of Joan Decker, Pierre Etienne, Antoine Merle and Mateusz Gospodarczyk. A special thanks goes to Joan, who, in desperate times, provided me with the storage I needed to save my ridiculously large gyrokinetic data.

Thank you Blaise Marletaz, Steve Couturier, Thierry Leresche, Maxime Erpen, Pierre Lavanchy and others in the electronics group. Countless of times I have come to you with yet another request to construct a special cable, repair amplifiers or just for general advice. I learned a lot from you. Christian Moura, thank you for the clever water-cooling solutions and to Frédéric Dolizy for helping to pump-down the detectors.

Thank you, Yanis Andrebe, for assisting us with the problems we were facing in the lab and for helping me and Sascha with the optics-related questions. Sascha, it was a pleasure working with you here. Our project certainly accelerated with your help.

Many thanks also to Olivier Sauter, Antoine, Francesco Carpanese, Matteo, Patrick Blanchard, Yann Camenen, Matteo Fontana, and Filippo for their help with the experimental profile measurements and the preparation of the data for my simulations.

The DDJ was a very useful experience to learn about experiments and the various diagnostic systems on TCV. Arigato to my fellow ninjas: Kevin, Pedro, and especially Mirko. Thank you also to Umar, Patrick, Duccio and PF, and Cenk, Luke and Federico for their help with gitlab. I am very grateful to Francesco for taking over as lead ninja, together with ... (we will see, yes I still remember !). Managing the DDJ schedule and fixing the DDJ codes would have been much more difficult without the selfless support of the DDJs themselves. There was always someone to offer their help when a DDJ was suddenly requested, even at inconvenient times. I am also indebted to Filippo and Lorenzo who saved the day countless times when (rather than if ...) the DDJ codes failed.

I consider myself very lucky to have spent my years here at the SPC. It is an incredible environment characterised by the highest level of research, collaboration, humour and inspiration.

When I started this journey, I first met Filippo, but was quickly accompanied by Dario, Paolo and then also by Lorenzo. Even though we no longer shared an office, and I was banished from

176

Filippo's and Paolo's office (maybe in my ignorance I mentioned something about pizzas in Sweden ... Now I know better !), we had many great moments together that I will remember fondly. Thank you for the coffee breaks, the dinners, the climbing and running sessions, the sfogilatelle, and for answering my Italian questions (dov'è il vulcano ?). Thank you also to Claudia for correcting my Italian and for your support, and to Arsène and Samuele for your constant encouragement. Justin, I hope we will run many more kilometers together!

I could not have wished for better office mates, Simon and Nico. Thank you for the office trips, the laughs and the talks.

Five years ago I only walked on mountains. Thank you to Mateusz, Matteo and Nico for teaching me how to also climb and ski down them too.

Everyone at the SPC: thank you for your constant support and encouragement. For the coffee breaks, for showing me my limits (of various kinds, I now know better how to handle the fondue ...!), for your competitive spirit, for your commitment and zealous concern for the environment, for help with using the poster printer, for the skiing weekends, for the cycling adventures, for the scientific and non-scientific discussions.

Many thanks to Eric, Vidit, Sourabh and Illaria. Meeting you always puts me in a good mood! I always look forward to discussing with you, whatever the topic.

Finally, I am in immense debt to my family and Jessica. Without your love, support and selfless care, none of this would have been possible and I would never have reached the end of this journey. I do not know how I can ever repay you.

Lausanne, March 9, 2023   A.I

Aylwin Iantchenko | Curriculum Vitae

Avenue de l'Eglise Anglaise 12 – 1006, Lausanne, Switzerland

📞 +41786262009 • ✉ aylwin.iantchenko@epfl.ch

Research Experience

PhD candidate in plasma physics   **Lausanne, Switzerland**
École Polytechnique Fédérale de Lausanne (EPFL), Swiss Plasma Center   *2018 – present*
Experimental and computational study of turbulence in fusion plasmas using the
Phase-Contrast Imaging (PCI) diagnostic

Project Assistant   **Gothenburg, Sweden**
Chalmers University of Technology, Division of Subatomic and Plasma physics   *2017*
Included poloidal variations in the collision operator in the FORTRAN code SFINCS

Project Assistant   **Gothenburg, Sweden**
Chalmers University of Technology, Division of Subatomic and Plasma physics   *2016 – 2017*
Computational study on the effect of fast ions on plasma turbulence

Selected publications

- A. Iantchenko *et al.*, "*A synthetic phase-contrast imaging diagnostic with spatial filtering for gyrokinetic simulations*", Plasma Phys. Control. Fusion in press https://doi.org/10.1088/1361- 6587/aca4f7
- S. Coda *et al.*, Nuclear. Fusion **61** 106022 (2021)
- G. J. Wilkie, *et al.*, Nuclear Fusion **58**, 082024 (2018)

Selected conference contributions

- 6th Asia Pacific Conference on Plasma Physics, 9-14, October, 2022 (online)
  Invited talk with the title: Gyrokinetic simulations of turbulence in JT-60SA with the GENE code
- 47th EPS Conference on Plasma Physics (online), 21 - 25 June 2021
  Poster with the title: On the modelling of experimental results on plasma shaping with a synthetic diagnostic and nonlinear gyrokinetic GENE simulations
- Virtual 25th Joint EU-US TTF Meeting, 6-10 September 2021 (online) *Poster with the title: Gyrokinetic simulations of turbulence in JT-60SA with the GENE code*

Education

MSc in Physics and Astronomy   **Gothenburg, Sweden**
Chalmers University of Technology,   *2015 – 2017*
Master's thesis in computational plasma physics with the title :
"The role of fast ions in stabilising the ion temperature gradient mode"

Exchange studies   **Lausanne, Switzerland**
École polytechnique fédérale de Lausanne (EPFL),   *2015 – 2016*
Studied the first year of my master's degree at École polytechnique fédérale de Lausanne

BSc in Engineering physics   **Gothenburg, Sweden**
Chalmers University of Technology,   *2011 – 2015*

Upper secondary School   **Gothenburg, Sweden**
Social science program with sports specialisation, Aspero idrottsgymnasium   *2009 – 2011*

Upper secondary School   **Malmö, Sweden**
The Natural Science Programme with mathematical specialisation, Malmö borgarskola   *2008 – 2009*

Work Experience

Teaching Assistant   **Lausanne, Switzerland**
École Polytechnique Fédérale de Lausanne (EPFL), Swiss Plasma Center   *2018 – 2022*
Computational Physics I, Computational Physics II, General Physics

179

Teaching Assistant   **Gothenburg, Sweden**
Chalmers University of Technology   *2015 – 2016*
Linear algebra, Multivariable analysis
Study Coach   **Gothenburg, Sweden**
My Academy,   *2014 – 2015*

Languages

Languages: Swedish (mother tongue), Russian (mother tongue), English (fluent), French (intermediate), Italian (basic).
Softwares (basic): JAVA, PYTHON, C, C++, FORTRAN
Softwares (experienced): MATLAB, LaTeX, INKSCAPE

Awards

Dean's Award for Excellence in teaching, EPFL, 2022.

Other

TCV diagnostics administrator   **Lausanne, Switzerland**
École Polytechnique Fédérale de Lausanne (EPFL), Swiss Plasma Center   *2018 – present*
Responsible for organising TCV diagnosticians, overseeing a team of ≥ 25 people involved in TCV
daily operation. Coordinating and working with the team for maintenance and upgrade of TCV diagnostics tools
Archaeological Field School   **Menorca, Spain**
Sanisera Acheology Institute   *2017*
Driver's licence
Category B   *2014*

180